THE UNIVERSITY OF CHICAGO

MOLECULAR AND INSTRUMENTAL ASPECTS OF BRIGHTNESS IN FLUORESCENCE-ENCODED INFRARED SPECTROSCOPY

A DISSERTATION SUBMITTED TO
THE FACULTY OF THE DIVISION OF THE PHYSICAL SCIENCES
IN CANDIDACY FOR THE DEGREE OF
DOCTOR OF PHILOSOPHY

DEPARTMENT OF CHEMISTRY

BY
ABHIRUP GUHA

CHICAGO, ILLINOIS
JUNE 2024

To Late Prof. Ashish Kumar Nag, from whom I have learned to appreciate Science...

Contents

List of Figures

List of Tables

Acknowledgements

I would like to take this space to reflect on the journey I began six years ago. It was September 2018, when I left the comfort of my home, and arrived in Chicago to start school here at the University. Despite the challenges of adapting to an entirely new culture, a new life surrounded by new faces, I found comfort in the Tokmakoff Group. Back then, I had only heard about the great works of the group, which would often engulf me in a realm of imagination. It is from my colleagues in the group that I have come to this realization: Spectroscopy is a form of art. Every feature in a spectrum is like a brush stroke, which can only be admired by a true connoisseur.

I would like to thank Andrei for his role as my supervisor. Moreover, I would like to thank him for being the Teacher I will always look up to. It was a great pleasure being advised by Andrei. His innovative attitude towards Science and scientific inquisition has been a source of inspiration for my efforts and endeavors in the group. Scientific discussions with Andrei always involved a humongous amount of brainstorming, and I do not remember an instance when I left his office not engulfed in thoughts. Like every project in Andrei's group, the FEIR project involved a massive level of imagination and innovation. Andrei taught me to push my limits to think out of the box to address the questions I discussed in this thesis. I thank him for everything I have learned during my time in the group.

I would like to thank the members of my thesis committee, Prof. Greg Engel and Prof. Allison Squires for their valuable advice and guidance during the different phases of my PhD. I would especially like to acknowledge Prof. Greg Engel for instilling in me the sense of necessity to put forth a general description of the FEIR selection rules from the perspective of group theory, which inspired me to write the sixth chapter of this thesis.

I consider myself lucky to be blessed with amazing colleagues. Especially, I am ever-grateful to Lukas Whaley-Mayda for his mentorship through most of my time in the group. I would do injustice calling him just a mentor to me. I believe Lukas fits the definition of the Master. Be it preparation for my candidacy exam, learning to align the laser, approaching a scientific problem, my BGM talks, or writing a manuscript for communication, Lukas guided me selflessly, and I cannot ever thank him enough for that. Although I could never think like him, the standard that he set for the group in general, and the FEIR project in particular, kept me motivated. He has shown me what it is like to be a perfectionist, a great scientist, a great mentor, and above all, a great human being.

It has been a great pleasure working with Seung Yeon Lee. Seung Yeon's unwavering efforts in the extremely difficult experiments in the lab kept inspiring me. It has always been exciting to discuss different aspects of the project with her, and team up with her to build the visible OPA. I will dearly miss the chats we had in the office, the jokes we shared, and the amazing time we spent in Providence during GRC 2022. With Chih-Tsun Yang joining the FEIR project, I am happy to see that FEIR is in capable hands, and I cannot wait to see the results that come out of the Flour Lab in the future. I wish Seung Yeon and Chih-Tsun all the best. Furthermore, I thank Seung Yeon for her feedback on my thesis, and Chih-Tsun for sharing his DFT calculations on Fluorescein with me.

I thank Yumin Lee for the constant encouragement she provided during my time in the group. I remember the day Yumin visited the group for her postdoc interview. It was the first time I collected a good-quality FTIR spectrum. From that day to now, as I grew up as a member of the group, I have cherished her presence, and have always been inspired by her hard work and positivity towards research. I am thankful to her for her constant support and valuable advice on my thesis chapters.

I am grateful to Nick Lewis for his precious feedback on various aspects of research throughout my time in grad school, especially during Andrei's absence. I have immensely benefited from his suggestions on experimental design and construction of the visible OPA and his valuable suggestions on manuscripts and thesis chapters.

I would like to thank Brennan Ashwood for teaching me the true meaning of tenacity. His awe-inspiring personality and his attitude towards research are exemplary, and I always look up to him as a senior and a role model for hard work. Besides research, Brennan has been my neighbor in the office. We bonded a lot over tea, cricket, and baseball. Sharing my morning cup of 'chai' with him during his thesis-writing phase is a piece of memory that I will always cherish. I have seen a great teacher in John Hack. His pedagogic approach to explaining Science would make even the most complex topics of physical chemistry and spectroscopy exciting and easy to understand. I will not be surprised to see John as a great teacher of the subject in the future. The time in the group was always great when Ram Itani was around (not that it isn't now...). Ram's jovial nature, a positive attitude, and immense respect towards his project, despite the extreme technical hurdles he faced, have been a source of inspiration for me. Outside work, we have shared good times (and great jokes!), biking along the lakefront trail and enjoying our free time together in Providence during GRC 2022. I will cherish every bit of it.

I found a great friend in Melissa Bodine, and it was a pleasure being her colleague too. She is an extremely talented researcher. Scientific discussions with her are always exciting. I wish her all the best for her upcoming graduation. We have spent great times in the office, most of which would be Melissa being sarcastic about me not designing her candidacy bottle, or something else. Outside the lab, we have had great fun at the Christmas parties, game nights, and dinners Melissa would host. I would be delighted if I ever get the chance to be her colleague in the future.

It was a pleasure to be colleagues with Sam Knight and Liv Mumma. Sam has an inquisitive mind, and his curiosity for science is bound to take him far. Oftentimes, our discussions would be drawn to the whiteboard, with Sam trying to explain something he recently figured out, or me trying to think something out by discussing with him. Liv has taken the social dynamics of the group to the next level. I cannot help but admire their skill in engaging the group in various kinds of activities, bringing vibrance to the office, and making life at work exciting. I have seen an extremely talented researcher in Josh Edwards, as he took on the microfluidics project, and am eager to see his future endeavors bear fruit in his grad school career. It was a pleasure being acquainted with Jakob Schauss. He is an amazing neighbor, and an ever-smiling person, with whom, I have shared many a fond memory. I wish him all the best for his career ahead, especially research in the Big lab, which recently had Jill Belluomini join. I would love to see some exciting results from their research together. I am happy to have been associated with Ian Bongalonta, whose work bears the potential of some great collaboration between theory and experiments to approach the most complex questions in biophysics. Very recently, I got the opportunity to have Anuj Pennathur as my colleague. His enthusiasm towards science and his jovial nature have brought a huge amount of positive impact on the overall group culture.

Chicago would not have been home without Aritrajit Gupta. I could keep writing pages about my times with him, as the memories we made seem endless. In him, I have found a friend, and a slightly younger, wiser brother. I deeply cherish the times we spent together in Chicago, and I cannot wait to join him as his colleague in Portland.

I thank Shankar G Menon for being a great friend, and an amazing roommate during most of my time in grad school, and I eagerly wait to see him achieve great milestones in his PhD. I thank Kavya Pillai, Alok Anand, Poojya Ravishankar, Vinay Shirhatti, and Kruthika Maheshwar for making life outside the lab fun and exciting, keeping alive a tiny bit of India by celebrating the festivals together. Additionally, I would like to thank Sneha

Paul, Mandira Dutta, Debaleen Biswas, and Titli Nargis for providing me with a homely atmosphere right here in Hyde Park. Life in Chicago is incomplete without them.

I thank Anchita Addhya for her company, primarily during the tough times of the pandemic. She has a lovable and compassionate personality that makes her stand out as one of the most approachable persons at every point of time. Anchita has the unique ability to try her best to make others' dreams come true, as she did for me. I cannot express enough gratitude for her.

I wouldn't have come to the US for grad school if Raktim Sen did not inspire me. From a great Masters student at IITD to an exemplary scientist from USC, Raktim's path towards excellence has always enthralled me. Along with Shubhangi Aggarwal, an exceptional organic chemist, they form the power-couple I always look up to.

I was lucky to make some great friends during my undergrad days at St. Xavier's, those who bring back old and fond memories whenever we meet. I thank Nikita Chiripal, Sayan Palui, Jyotirban Dey, Tannistha Bhattacharya and Souvik Sarkar for being the reason to cherish the memories of the days I spent in 30 Park Street.

It is a boon to have a few constants in one's life, which, in my case, are my childhood friends, Rohan Bhaumik, Akash Ghosh, and Baidurya Tarafder, who make me realize the value of friendship and brotherhood. I cannot help but admire the strong bonds that bind the Core4 together. It is for them I feel homesick, and long to go back to Kolkata every year.

I thank my parents Keya Chakraborty Guha and RK Guha, for supporting me all through my journey, helping me at every step to pursue my dreams, without giving me a hint of the struggle they undertook to ensure a good quality of life for me. I have been blessed to have my sister, Meghna by my side through all thick and thin, comforting me with her calm and thoughtful personality.

Finally, I would like to thank my friend, partner, and wife, Sraddha Agrawal for everything. She is the only person who has seen all ups and downs in my life, and has been a constant strong pillar of support throughout my academic career. I cherish every moment I spent with her, and look forward to starting a fresh new chapter of life together.

Funding

The work presented in this thesis received support through two grants CHE-1856684 and CHE-2155027 from the National Science Foundation (NSF). Furthermore, all steady-state electronic absorption and fluorescence measurements were performed at the shared facilities in the Materials Research Science and Engineering Center (MRSEC) of the University of Chicago, which is funded by the NSF under Award No. DMR-2011854. The work highlighted in Chapters 5 and 6 were presented in two conferences, namely Gordon Research Conference on Vibrational Spectroscopy 2022 (RI, USA) and American Chemical Society Conference Fall 2022 (IL, USA), participation in which was partially funded through the Windt Travel Award 2022 from the Department of Chemistry, University of Chicago.

Abstract

Single-molecule measurements represent a remarkable frontier in spectroscopy, offering unparalleled insights into the heterogeneity and dynamics of individual molecules that are often obscured in ensemble measurements. Techniques like vibrational spectroscopy, which detect structural changes at the scale of a chemical bond, are challenging to perform with single-molecule sensitivity. However, near-field strategies enable single-molecule vibrational measurements, though their application in solution remains a challenge.

Fluorescence-Encoded Infrared Spectroscopy (FEIR) uses sequential absorption of IR and visible photons, creating a double resonance condition that excites molecular vibrations in its electronic ground state, followed by selective up-conversion to a higher-lying fluorescent electronic state. The resulting fluorescence is encoded with vibrational information of the molecular ground state. FEIR combines the single-molecule sensitivity of fluorescence with the structural specificity of vibrational spectroscopy, enabling solution-phase vibrational measurements in the optical far field with single-molecule sensitivity.

This thesis describes the factors that collectively contribute to achieving single-molecule sensitivity with FEIR. Instrumental factors play a vital role in determining the signal-to-noise ratio at the single-molecule level, resulting from a combination of FEIR brightness and contrast. An FEIR spectrometer employing high-energy sub-picosecond ultrafast infrared and visible pulses at a 1 MHz repetition rate, generated from home-built optical parametric amplifiers pumped with a Yb-fiber laser source, and a microscope for high-sensitivity fluorescence detection are described. Proof-of-principle experiments using Coumarin 6 as the model system are discussed, along with the impact of FEIR resonance condition on molecular brightness, through a comparative study across a series of coumarin chromophores. The effect of tuning the visible encoding frequency on the FEIR brightness and contrast is explored using Rhodamine 6G as the model system, demonstrating the need for precise tuning of the resonance condition when setting up an FEIR experiment.

The thesis further presents a discussion on the collective role played by various factors intrinsic to the electronic structure of the chromophore, in shaping the FEIR selection rules. These molecular factors include the magnitudes and relative orientation of vibrational and electronic transition dipoles, vibronic coupling, and fluorescence quantum yield. A computational model based on electronic structure calculations is described, which predicts the FEIR activity of a normal mode within a chromophore. The impact of these molecular factors on the mode-specific FEIR activities is demonstrated through correlations with measured FEIR cross-sections. The discussion includes an illustration of the effect of vibrational dynamics and interaction with finite light pulses on these correlations, and a description of FEIR selection rules from the perspective of normal mode symmetry, supported by an illustrative example of a comparative study of FEIR cross-sections of a symmetric and an asymmetric molecule with similar FEIR resonance condition.

The work concludes by defining a "good FEIR probe" and provides computational tools to guide the choice of a chromophore with an FEIR-active vibrational reporter for single-molecule applications to study the dynamics of chemical interactions in solution by probing structural changes down at the length-scale of a chemical bond.

Chapter 1

Introduction

1.1 The single-molecule perspective of chemical dynamics

In the exploration of molecular landscapes, single-molecule spectroscopy (SMS) emerges as a pivotal innovation, casting light on the complexities of individual molecules and unveiling the obscured heterogeneity inherent in ensemble-averaged measurements. This transformative technique has redefined our approach to molecular studies, offering unparalleled insights into the dynamics, mechanisms, and interactions at the molecular level. The transition from bulk to single-molecule analyses represents a paradigm shift, revealing an unprecedented level of detail in molecular behavior.[1]

1.1.1 A brief history of single-molecule spectroscopy

The history of single-molecule spectroscopy (SMS) is a fascinating journey of scientific innovation and discovery that spans over several decades, providing researchers the necessary tools to observe and understand the behavior of individual molecules, breaking away from the limitations of ensemble measurements that mask the otherwise inherent heterogeneity of a system. The practical realization of observing individual molecules was hindered by the technological limitations of the time. It wasn't until the development of more sensitive detectors capable of detecting single photons, like photomultiplier tubes (PMT) in the 1940s and 1950s[2,3] and eventually, solid-state based detectors like avalanche photodiodes (APD) in 1980s,[4–6] and the advent of laser technology in the 1960s and 1970s that the foundational work for single-molecule spectroscopy could begin in earnest.

The 1980s marked a pivotal period for SMS, with significant technological advancements enabling the first observations of single molecules. In 1989, Moerner and Kador made a groundbreaking discovery by observing the absorption spectrum of a single molecule at low temperatures.[7] This achievement demonstrated that it was possible to detect and analyze the properties of individual molecules, setting the stage for the rapid development of the field.

The 1990s saw an explosion of interest and progress in SMS, driven by improvements in laser technology, fluorescence microscopy, and computational methods.[7,8] Techniques such as near-field scanning optical microscopy (NSOM)[9] and confocal microscopy[10–15] became powerful tools for single-molecule detection. Researchers began to apply SMS to study a wide range of phenomena, including the dynamics of biomolecules, the heterogeneity of chemical reactions, and the properties of semiconductors and nanomaterials.[16–18]

The early 2000s were characterized by the diversification of SMS applications and the development of new techniques. Single-molecule fluorescence spectroscopy, in particular, became a staple in biological research, providing insights into the mechanisms of enzymes, the folding of proteins, and the dynamics of nucleic acids.[16,19–22] Techniques such as FRET (Förster Resonance Energy Transfer) allowed researchers to probe the distances and interactions between different parts of molecules, revealing the intricacies of molecular machines.[14,23]

Today, single-molecule spectroscopy stands at the forefront of molecular science, with its applications extending into quantum computing, nanotechnology, and materials science. The integration of SMS with other cutting-edge technologies, such as super-resolution microscopy and nanopore sequencing, continues to push the boundaries of what can be observed and understood at the molecular level.[24–33]

1.1.2 Complementary insights beyond bulk measurements

One of the most significant advantages of SMS is its unique ability to access molecular heterogeneity. By isolating and examining individual molecules, SMS uncovers behaviors and properties that ensemble measurements blend into an average, often masking critical variations.[8] This granularity is essential for dissecting the diversity within molecular populations, revealing subpopulations and a spectrum of conformations, states, or reactions that are critical for understanding the complexity of biological systems, where function often hinges on molecular diversity.[34]

Furthermore, SMS offers a window into the dynamic processes of molecules, allowing for real-time monitoring of transformations, interactions, or state transitions. This real-time observation is a stark contrast to ensemble measurements, which average out transient states and sequences of events, obscuring the dynamic nature of molecular processes.[35] SMS elucidates the pathways and intermediates of chemical reactions and biological mechanisms, shedding light on the rare events and underlying dynamics that drive molecular behavior.[36]

The spatial and temporal resolution afforded by SMS exceeds that of traditional methods, enhancing our ability to observe molecular systems. High spatial resolution enables the detailed study of molecular structures and interactions, while temporal resolution captures the evolution of molecular states over time, offering a detailed chronology of molecular interactions and transformations.[29] This high resolution is instrumental for the direct quantification of molecular properties, including distances, orientations, and energy transfer efficiencies, and for determining stoichiometry and binding affinities with unparalleled precision.[37]

Central to the utility of SMS is its ability to provide mechanistic insights into the workings of biological systems. Observations of conformational changes and the folding dynamics of biomolecules offer insights into their functional mechanisms. Similarly, the detailed examination of molecular machines through SMS uncovers the stepwise motions and interactions that underlie biological processes, offering a glimpse into the molecular machinery of life.[22]

Additionally, the minimal sample requirements of SMS present a practical advantage, especially for studies involving precious or hard-to-obtain materials. This efficiency, coupled with the experimental versatility of SMS, underscores its wide applicability across various scientific disciplines. SMS facilitates investigations under diverse environmental conditions, including in vivo measurements within living cells, providing a realistic context for understanding molecular function.[38]

1.2 Fluorescence as a popular observable for single-molecule spectroscopy

Fluorescence has established itself as a cornerstone observable in single-molecule spectroscopy (SMS), revered for its unparalleled sensitivity and specificity in probing the intricacies of individual molecules. This prominence stems from fluorescence's fundamental principles, which involve the absorption of light by a molecule and the subsequent emission of light at a longer wavelength upon spontaneous relaxation of the molecule to its electronic ground state. From the perspective of measurements at the single-molecule level, it provides a huge advantage over absorption spectroscopy. Unlike the latter, which involves detection of a small "dip" in the incident light intensity, fluorescence is detected as photon bursts in an otherwise dark background, thus enabling background-free data acquisition. Together with its distinct spectral signatures for different molecules, and the availability of commercial single-photon detection modules, it enables highly sensitive detection at the single-molecule level, making fluorescence a preferred method in SMS.

Fluorescence is celebrated for its versatility, allowing for adaptation across a wide array of environments, from test tubes to living cells. This adaptability enables researchers to explore molecular processes in their native contexts, providing insights that are more physiologically relevant.

However, the sensitivity of fluorescence is limited to molecular interactions that result in large change in the electronic structure at the length-scale of the molecule. Examples of such changes include, but are certainly not limited to, changes in oxidation state,[39] change of conformation,[40] or a complete conversion to a product by formation/breaking of chemical bonds.[41] In the event of probing dynamics of molecular interactions mediated through non-covalent bonding, or chemical exchange, primarily resulting in structural changes at the length-scale of a chemical bond, fluorescence is rendered practically insensitive.

1.3 Vibrational spectroscopy as a tool to probe changes in chemical structure

Vibrational spectroscopy, encompassing the realms of both infrared (IR) and Raman analyses, serves as a quintessential instrument in the elucidation of molecular structural dynamics with remarkable sensitivity and specificity. Esteemed for its ability to delve into the perturbations and alterations within molecular frameworks, this technique facilitates an advanced understanding of chemical interactions, bonding mechanisms, and material characteristics, surpassing conventional analytical methods in both depth and breadth.

The application of vibrational spectroscopy in observing real-time molecular dynamics stands as a testament to its unparalleled capabilities. Time-resolved techniques like time-resolved IR spectroscopy (TRIR) and 2-dimensional IR spectroscopy (2D IR) provide a window into the evolving structural changes of molecules during reactions, phase transitions, and under external stimuli, shedding light on reaction mechanisms, energy transfer, and the emergence of transient species.[42–44] This, along with computational simulations further enriches this landscape, offering a potent combination for the validation of theoretical models, delve into intricate details such as anharmonicity, alteration in the shape of the potential energy surfaces upon certain interactions with the surrounding media, and the exploration of intricate reaction pathways.[45,46]

A hallmark of vibrational spectroscopy is its intrinsic sensitivity to the minutiae of molecular geometry and the electronic environment, enabling the differentiation between structural isomers, conformers, and tautomers with exceptional precision.[47] This attribute proves indispensable in the realms of complex biological systems, polymer science, and materials engineering, where minor structural nuances can significantly influence functional outcomes. Its proficiency in capturing the subtle intricacies of biophysical phenomena such as protein dynamics and hybridization mechanisms for nucleic acids.[48–50]

Despite its extensive utility, the sensitivity of vibrational spectroscopy, encompassing both infrared (IR) and Raman spectroscopy, is inherently limited by the fundamental physical interactions that these techniques rely on. Specifically, the small absorption cross-sections of IR light, which is typically of the order of $\sim 10^{-18}$ cm^2, and the inherently weak

Raman scattering cross-sections ($\sim 10^{-30}$ cm^2) contribute to this limitation. This is in stark contrast to the large electronic absorption cross-sections of visible light $\sim 10^{-16}$ cm^2, which are exploited in UV/visible absorption spectroscopy. Furthermore, the short-lived nature of excited vibrational state and the presence of a myriad of non-radiative relaxation pathways makes it practically impossible to acquire fluorescence signal from vibrational relaxation at room temperature, thus precluding the opportunity of background-free data acquisition. To add to the difficulty, it is daunting to detect IR photons above the thermal noise at room temperature with conventional IR detectors. As a result of the several layers of associated challenges and limitations, conventional vibrational spectroscopy to high-concentration bulk measurements.

1.4 Single-molecule vibrational spectroscopy in the near field

Realizing the depth of information that single-molecule measurements reveal, the quest to materialize vibrational spectroscopy at the single-molecule level was imminent. This led to the emergence of vibrational spectroscopy in the near-field. The methodology includes the sophisticated techniques of Surface-Enhanced Raman Spectroscopy (SERS) and Tip-Enhanced Raman Spectroscopy (TERS), for example. These techniques capitalize on the principles of plasmonic enhancement to probe the vibrational characteristics of individual molecules, thus making it possible to get an unparalleled glimpse into the molecular structure, dynamics, and interactions at the nanoscale.

SERS harnesses the phenomenon of localized surface plasmon resonances induced in metal nanoparticles under illumination. These resonances intensify the electromagnetic field at the nanoparticle surface, dramatically amplifying the Raman scattering signal of molecules situated in close proximity. This amplification allows for the detection and analysis of vibrational modes of single molecules, providing the much desired single-molecule sensitivity to vibrational measurements.[51–56]

Building on the concept of enhanced vibrational signal, TERS combines the spatial resolving power of scanning probe microscopy (SPM) with the chemical specificity of Raman spectroscopy. A metallic tip, brought near to a sample surface, concentrates the electromagnetic field to a nanoscopic point, significantly boosting the Raman signal of molecules directly underneath. TERS not only achieves the high sensitivity required for single-molecule detection but also provides spatial resolutions at the sub-nanometer level. This capability has opened new avenues for the detailed investigation of molecular structures, enabling scientists to visualize the distribution of chemical species on surfaces and to delve into the dynamics of chemical reactions at an unprecedented scale.[57,58]

Despite the excellent spatial resolution and single-molecule sensitivity, such near-field techniques enable measurements on the surface, localized to the nanoscopic proximity of the probe (metal tip in case of TERS, for example). The perturbation introduced is strong enough to preclude measurements in solution, which can be thought of as the native environment of the molecule. This called for a certain level of innovation that would allow vibrational measurements with single-molecule sensitivity in the optical far field.

1.5 Enhancing the sensitivity of vibrational measurements through fluorescence-detection

We have discussed how fluorescence plays a pivotal role in single-molecule spectroscopy, celebrated for its unparalleled ability to detect signals against a noise-free backdrop, coupled with the extraordinary sensitivity inherent in conventional single-photon detection technologies. On the other hand, vibrational spectroscopy introduces a distinct advantage by providing precise specificity to molecular structural alterations, even at the diminutive scale of chemical bonds. This advocates for a pioneering approach within the realm of single-molecule vibrational spectroscopy—an approach that seeks to couple the sensitivity found in fluorescence detection at the single-molecule level with the meticulous structural discernment offered by vibrational spectroscopy. Such an innovative technique promises to unlock new possibilities for observing chemical dynamics at the single-molecule level in solution environments, allowing for probing "fine" structural changes that would remain undetected to conventional fluorescence methodologies. Furthermore, a critical requirement for methods that permit solution-phase measurements is to avoid the strong perturbations introduced by near-field strategies, implying that the hypothetical fluorescence-detected vibrational spectroscopy would involve detection in the optical far-field. A confluence of single-molecule fluorescence spectroscopy and vibrational spectroscopy would therefore bridge the gap between fluorescence sensitivity and vibrational specificity, and pave the way for unprecedented insights into molecular dynamics in solution.

1.5.1 Inception

Research into fluorescence-detected vibrational spectroscopy precedes the advent of single-molecule spectroscopy.[59,60] It was then that Kaiser and co-workers devised a method to merge molecular fluorescence with vibrational insights of the electronic ground state. Their technique involved a double-resonance excitation scheme that selectively up-converts a vibrationally pre-excited state to a higher-lying fluorescence state. Population in the excited vibrational state is initially created through interaction with an incident infrared pulse. Then, it is excited to a higher-lying fluorescence state through interaction with a subsequently incident visible light pulse.

The choice of frequency for the visible pulse was crucial. It was selected to make up for the remaining energy for the $|g, 0\rangle \rightarrow |e, 0\rangle$ resonance, bringing about a transition from $|g, 1\rangle$ to $|e, 0\rangle$ vibronic states (illustrated in Figure 1.1). Because the electronic excited state is populated with species initially in the excited vibrational state prior to the second excitation, the resulting fluorescence carries vibrational information of the electronic ground state.

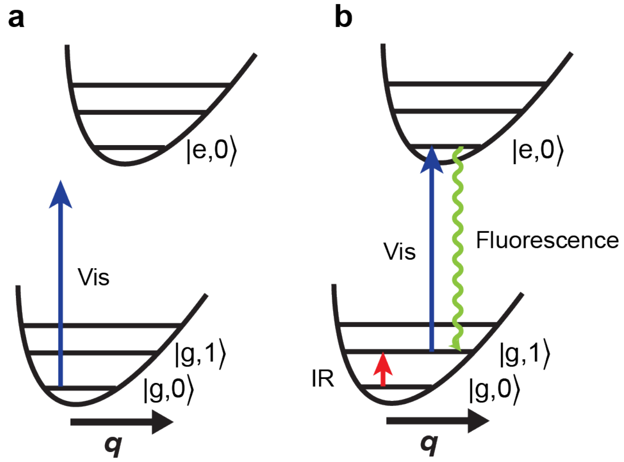

Figure 1.1: Excitation scheme for fluorescence-detected infrared vibrational spectroscopy. (a) The visible excitation frequency is chosen such that it falls off-resonance for $|g, 0\rangle \rightarrow |e, 0\rangle$ transition. (b) In the event of vibrational pre-excitation ($|g, 0\rangle \rightarrow |g, 1\rangle$)by interaction with an IR pulse, the visible pulse makes up for the remaining $|g, 1\rangle \rightarrow |e, 0\rangle$ transition energy. The fluorescence signal obtained as a result of spontaneous relaxation is coupled with vibrational information of molecular ground state.

A measurement of the fluorescence signal as a function of the IR-visible time delay showed an exponential decay profile, indicating that the fluorescence state was indeed populated from a vibrationally excited state. The decay was characterized by two characteristic decay timescales. The short time $\sim 1-2$ ps was interpreted to represent intramolecular vibrational relaxation, creating a global hot ground state, while the long time $\sim 7-10$ ps represented the energy relaxation of the hot molecule to the solvent bath. This was followed by subsequent experiments by the same group[60,61] that gave further insights into the vibrational modes that gave rise to the fluorescence response, in addition to useful information about the molecular factors such as the Franck-Condon overlaps that shaped the signal levels.

Kaiser and co-workers' experiments paved way to extrapolate the potential of this "indirect" detection method to various vibrational spectroscopy techniques. Wright introduced a Stimulated Raman Scattering (SRS) version of this approach in the early 1980s,[62] coining it as double resonance excitation. Subsequently, in 1983, Wright and co-workers undertook the initial experimental exploration of double resonance fluorescence facilitated by SRS.[63] This initial foray, unfortunately, encountered challenges due to significant two-photon fluorescence background noise from the perylene dye they were working with, resulting in the inability to detect the anticipated SRS-mediated double resonance fluorescence signal. Despite this early setback, researchers remained hopeful about the technique's promise. In 2011, drawing inspiration from the achievements in room-temperature single-molecule fluorescence spectroscopy, it was suggested that applying this SRS-mediated double resonance fluorescence technique with contemporary optical microscopy could potentially unlock unparalleled sensitivity in single-molecule vibrational spectroscopy within the optical far-field.[64] The double-resonance excitation introduced by Wright was later revived by Min and co-workers in 2019, who termed it as Stimulated Raman Excited Fluorescence (SREF) where they demonstrated imaging of a single nitrile strech in a rhodamine 800 molecule by employing high repetition rate excitation, sample illumination techniques relevant to single-molecule fluorescence, and sophisticated single-photon level fluorescence detection mechanisms.[65–67]

1.5.2 Fluorescence-Encoded Infrared Vibrational spectroscopy

Despite the manifold enhancement of sensitivity brought about by the coupling of vibrational information with molecular fluorescence, we did not see any further developments in the infrared spectroscopy side of the field past the 20^{th} century. It was in 2016 that Mastron and Tokmakoff revived the technique, employed excitation with broadband ultrafast laser pulses to observe vibrational dynamics at sub-ps timescales.[68] This technique was named as Fluorescence-Encoded Infrared Spectroscopy, or FEIR. Soon, with the incorporation of interferometric IR excitation, frequency-resolved FEIR measurements were performed, that helped resolve population and coherence pathways constituting the non-linear molecular response, giving useful information of vibrational dynamics, including coherence between vibrational mode pairs and the corresponding timescales.[69]

1.5.3 Single-molecule sensitivity with FEIR spectroscopy

At this stage, FEIR was established as a technique capable of unraveling detailed information about vibrational states and the dynamics associated with them, indirectly from molecular fluorescence signal. However, we were still far from the goal of enabling vibrational measurements at the single-molecule level in solution. A key challenge in the path to single-molecule detection was to be able to acquire fluorescence signals at the single-molecule level with sufficient signal-to-noise ratio that would enable a distinction of the FEIR signal from the background. Widely popular single-molecule experiments, primarily in the field of single-molecule fluorescence spectroscopy, employ high repetition rate excitation modules, typically in the range of 40 - 80 MHz. Besides this, detection at the single-molecule level requires tight-focusing of incident beams to create the smallest illumination volume under the diffraction limit. This calls for invoking excitation and detection techniques relevant to confocal microscopy. Keeping these requisites in mind, our group designed a next-generation version of the FEIR spectrometer, where, for the primary excitation source, an Yb-fiber laser was used to generate 1033 nm sub-ps NIR pulses at a repetition rate of 1MHz. A part of this output was used to generate tunable mid-IR pulses using optical parametric amplification, and another small part was frequency-doubled to form the visible excitation pulses centered at 516.5 nm. These pulses were tightly focused at the sample position, satisying the conditions for confocal microscopy, and the molecular fluorescence was detected in a time-tagged-time-resolved manner with a Si-based avalanche photodiode. With the ultrafast excitation pulses, confocal microscopy, and time-tagged time-resolved single-photon detection mechanisms, the sensitivity of FEIR underwent a manifold enhancement to enable vibrational measurements on small molecular ensembles,[70]. Subsequently, with further improvements in fluorescence signal collection efficiency and the employment of fluctuation correlation measurements of the FEIR signal trajectory (analogous to fluorescence correlation spectroscopy (FCS) from a nanomolar level solution of Coumarin 6, we were finally able to demonstrate single-molecule sensitivity with FEIR.[71] Subsequently, the visible excitation line was replaced with an OPA capable of delivering tunable narrow-band visible pulses across the majority part of the visible spectrum. This enabled an expansion of the applicability of FEIR to chromophoric systems across the visible spectrum.

The single-molecule sensitivity of a molecular vibration in FEIR is a result of a multiple factors, part of which are instrumental, while the rest being factors intrinsic to the electronic structure of the molecule. Instrumental factors include–but are not limited to –a proper choice of the visible excitation frequency (which we call as the "encoding" frequency) to ensure the most efficient up-conversion of the vibrationally excited state, improvements in the fluorescence collection and detection efficiencies, and striking a balance between a high repetition rate to ensure large signal-to-noise ratios at the single-molecule level and high mid-IR pulse energies to ensure efficient vibrational excitation. The molecular factors, on the other hand are beyond one's control. These factors include vibrational and electronic transition dipoles, their relative orientations in space, the coupling between the initial and final vibronic states, the symmetry of the vibrational modes, and fluorescence quantum yield. Understanding the roles played by these individual factors in shaping the overall FEIR response of a vibration is therefore expected to guide the choice of vibrational probes for FEIR experiments at the single-molecule level.

1.5.4 Recent advances in fluorescence-detected vibrational measurement strategies

The recent years have seen a huge enhancement in interest in the field of fluorescence- detected vibrational measurements, evident through the works of various research groups across different parts of the world. Particularly, the excitation scheme of FEIR was employed in several experimental setups to achieve different goals. Sakai and co-workers have demonstrated how we can think of the IR-visible double excitation as a way to bring about effective vibrational excitation of molecules in a volume much smaller than the diffraction limit of IR light.[72]. Jeremy Baumberg's group demonstrated a very interesting application of this technique, confining mid-IR excitation to nanoplasmonic cavities, thus demonstrating single-molecule detection of mid-IR transduced fluorescence signal.[73] Contemporarily, Wei Xiong's group developed a multidimensional widefield imaging technique employing the same principle, demonstrating vibrational imaging of Rhodamine 6G.[74]. Most interesting is the work communicated by Lu Wei's group, where they employed the FEIR excitation scheme, incorporated high laser repetition rates of 80 MHz, and sophisticated microscopy to demonstrate bond-selective imaging of single-molecule probes in biological tissue, demonstrating the bond-scale level of sensitivity such techniques can achieve.[75] These works have certainly proved to be inspiring for further developments in the FEIR project, paving the path forward to study real-time single-molecule chemical dynamics in solution, mediated through bond-scale changes in molecular structure–changes that would otherwise pass undetected under the lens of single-molecule fluorescence spectroscopy.

1.6 Thesis outline

The single-molecule sensitivity of FEIR spectroscopy is a result of an interplay of a set of instrumental factors and properties that stem from the intrinsic electronic structure of the molecule. The instrumental factors include the establishment of a suitable resonance condition, determined by the choice of encoding frequency, given the choice of the IR pump frequency is driven by the vibrational mode of interest. A suitable choice of the encoding frequency is necessary to establish an adequate balance between the FEIR brightness and contrast. While the optimization of the experimental factors is necessary to ensure the brightest FEIR signals from a given chromophore, the overall FEIR signal strength is determined by an interplay of multiple molecular factors that shape the FEIR activity, which is a quantity directly proportional to the probability of excitation in an FEIR experiment. These molecular factors include the strengths and relative orientations of the vibrational and electronic transition dipole moments, the strength of vibronic coupling between the initial and final states of the molecule, and the symmetry of the normal mode. The overall FEIR activity of a normal mode within a chromophore is further modulated by vibrational dynamics including population relaxation and multimode coherences (which is a consequence of simultaneous excitation of multiple vibrations with the broadband IR pump), besides the modulations brought about by interactions with excitation pulses that are finite in time.

The primary goal of this thesis is to discuss the interplay of the aforesaid instrumental and molecular factors in shaping the FEIR response from a normal mode within a chromophore, with an aim to establish the definition of a "good FEIR probe", which is a molecular vibration that is predicted to have a strong FEIR activity, and shows high sensitivity for the chemical interaction of interest by either a shift in its resonance frequency or a modulation of its FEIR intensity. The discussion is aimed to provide a systematic approach to choosing a suitable FEIR probe, or to predict the structure of a designer chromophore, containing a normal mode with a strong predicted FEIR activity and high sensitivity to structural changes, to facilitate the study of dynamics of chemical interactions in solution at the single-molecule level.

This thesis is divided into six chapters. Chapter 2 describes the FEIR spectrometer, highlighting the considerations that determine its design, description of the individual components, and details about signal acquisition and data processing. Chapter 3 discusses the proof-of-principle experiments, description of brightness, cross-section and contrast from the perspective of FEIR spectroscopy, and the instrumental factors, primarily the optical resonance condition that determines FEIR signal strength from a chromophore. Chapter 4 discusses a minimalistic description of FEIR activity under the displaced harmonic oscillator model. It includes descriptions of the different molecular factors, including magnitudes and relative orientation of vibrational and electronic transition dipole moments, and Franck-Condon factors, that collectively play a role in determining the FEIR activity of a normal mode within a chromophore. It also gives establishes a back-of-the-envelope description of the FEIR selection rule, and describes a computational model used to predict the FEIR activities of individual normal modes within a chromophore. Chapters 5 and 6 are written to help the reader choose a chromophore for a specific single-molecule level FEIR experiment, or even predict the structure of a hypothetical designer chromophore using the computational tools discussed in Chapter 4, that would promise strong FEIR signals from the desired vibrational probe. Chapter 5 reports the correlation between the computationally predicted FEIR activities and experimentally measured FEIR cross-sections of a series of ten coumarin dyes to describe the roles played by individual molecular factors in shaping the FEIR activity of a vibrational, and to demonstrate the quality of prediction the computational model can perform. Chapter 6 discusses the FEIR selection rule from the perspective of normal mode symmetry. The thesis is concluded with Chapter 7, which provides an outlook for the future of FEIR spectroscopy, discussing some potential experiments with different molecular probes to study various flavors of chemical dynamics by probing molecular vibrations. These proposed experiments are based on the computational predictions done on candidates from different dye families.

Chapter 2

Description of the FEIR spectrometer

2.1 Requisites to build an FEIR spectrometer

FEIR spectroscopy is developed with a goal to surpass the limitation in sensitivity of conventional infrared vibrational spectroscopy by encoding vibrational information of the electronic ground state into molecular fluorescence. This requires a pre-excitation of a molecule's vibration by an incident IR-pulse, followed by the selective up-conversion of the excited vibrational state to a higher-lying electronic state by a subsequent interaction with an incident visible pulse. The frequency of the visible pulse is chosen such that it is sufficient to promote the molecule from $|g,1\rangle$ to $|e,0\rangle$, just falling short of the $|g,0\rangle \rightarrow |e,0\rangle$ bare electronic transition. We call the latter transition as the "encoding" transition. This is followed by a spontaneous relaxation of the molecule to its ground state through the emission of fluorescence signal.

Owing to the much smaller IR absorption cross-section compared to the electronic absorption cross-section, an efficient vibrational excitation would require IR pulses with sufficiently high pulse energies. Furthermore, to ensure an efficient up-conversion, duration of both IR and visible pulses must be shorter than the vibrational relaxation timescales, which are typically in the range of $\sim 1-2$ ps. Therefore, the pulses must be of sub-ps duration.

Measurements down at the single-molecule level require high throughput averaging to reduce the signal averaging time for a high signal-to-noise ratio, sufficient for resolving the FEIR signal from any background fluorescence. This calls for a high laser repetition rate. Researchers performing single-molecule fluorescence measurements routinely use repetition rates typically between 40 - 80 MHz. However, given a fixed laser output power, the pulse energy is inversely proportional to the repetition rate. Hence, striking a balance between the two factors is of significant pertinence.

Additionally, we would require continuous frequency tunability of both the IR and visible pulses, without which, the applicability of FEIR would be drastically limited. The tunability can be achieved through various strategies, including parametric amplification of the fundamental output from the primary laser source. Furthermore, the bandwidth of the visible pulse, which we call as the "encoding" pulse, must be very small, of the order of $\sim 1 - 2$ nm to ensure a minimization of one-photon absorption at the red tail of the absorption spectrum of the chromophore.

Once the pulses of desired characteristics, that is, center frequency, bandwidth, and pulse duration, are generated, the pulse delivery mechanism is to be designed. A small amount of math would give us an idea of the size of the illumination volume we need. If we work with a sample solution of $\sim$ 1 nM concentration, which amounts to $\sim 6 \times 10^{14}$ molecules per liter of sample, we need the illumination volume to be of the order of 10^{-15} liters, or $\sim$ 1µm^3, to ensure that we have $<$ 1 molecule in the illumination volume on an average. This requires incorporating tight-focusing and detection conditions relevant to confocal microscopy. Performing non-linear infrared spectroscopy typically requires 1-10 GW/cm^2 pulse energy density at the sample position. This is achieved by tight-focusing 50 nJ IR pulses with about $\sim$ 140 fs pulse duration to a focal spot size of $\sim$ 9 µm. An efficient encoding transition at the single-molecule level requires the visible pulse energy density of $\sim 30-50$ GW/cm^2, which is ensured by tight-focusing the 30-50 pJ visible pulses of ~ 315 fs pulse duration to a spot size of about 450 μm. We will discuss this in detail in the description of the probe volume in Section 2.6. Fluorescence intensity at the single-molecule level is expected to be very low, which means that every single photon is precious. Therefore, we must strive towards achieving the highest collection efficiency possible under practical considerations.

With all the considerations described above, Figure 2.1 represents an illustration of the full FEIR spectrometer, the different parts of which are discussed in the next few sections of this chapter.

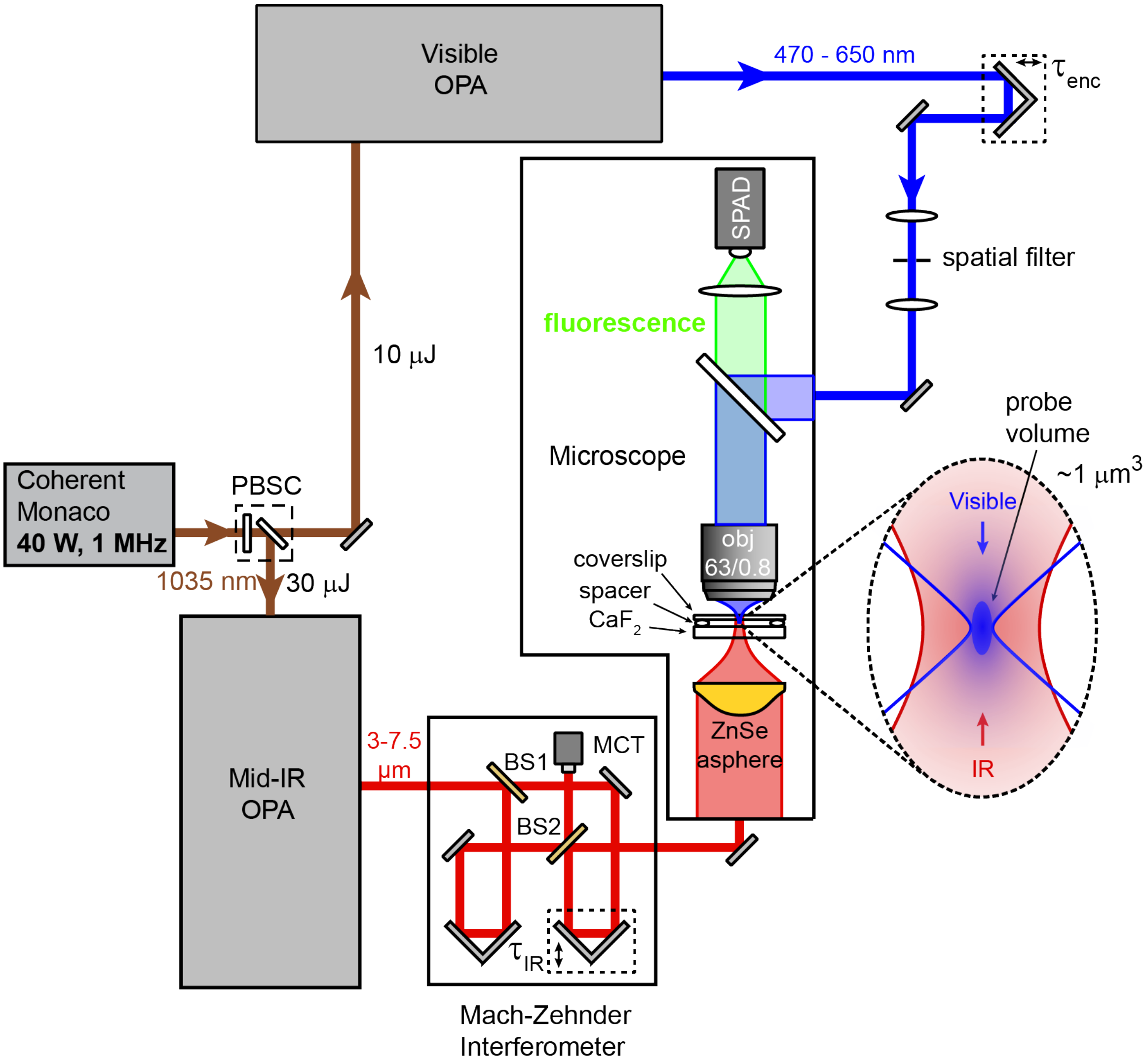

Figure 2.1: Schematic of the FEIR spectrometer showing its different components–The primary laser source (Coherent Monaco Yb fiber laser) delivers 40 µJ pulses centered at 1033 nm at a 1MHz repetition rate used to pump the the mid-IR and the visible OPAs to generate tunable excitation pulses. The Mach-Zehnder interferometer generates two copies of the IR pulse for frequency-resolved measurements. The FEIR microscope is an upright confocal fluorescence microscope where IR and visible pulses are co-focused at the sample position, creating an effective probe volume of ∼ 1 µm^3. The fluorescence is collected by the objective used to focus the visible pulses, and eventually focused on the 50 µm active area of the SPAD detector. PBSC: Polarizing beam-splitting cube, OPA: Optical parametric amplifier, BS: Beam Splitter, MCT: Mercury Cadmium Telluride IR detector, obj: Objective, SPAD: Single-photon avalanche photodiode

2.2 Primary laser source

The recent years have seen significant development in the field of fiber laser technology. Fiber based lasers are capable of delivering pulses with high repetition rate and high enough energies for performing optical parametric amplification. Specifically, Yb-doped gain media enable more efficient direct diode pumping as compared to the widely popular Ti:Sapphire lasers. This enables operation at higher repetition-rates while maintaining large pulse energies.[76] Furthermore, fiber-based gain media operate at higher average powers due to the favorable thermal dissipation properties as a result of an increased surface-to-volume ratio, which makes it possible to operate at MHz repetition rates.[77] While a high repetition rate is a key requisite for signal acquisition at the single-molecule level, high pulse energies are crucial for generating mid-IR pulses, which suffer from a lack of sensitivity. Of late there have been several reports of the use of Yb:KGW and Yb-doped fiber laser systems to generate mid-IR pulses at a 100 kHz repetition rate.[78–84] These laser systems are also routinely used for generating visible pulses at repetitions rates as high as 2 MHz.[85,86] A combination of high pulse energies and a high repetition rate is naturally the most desirable for the choice of the primary laser source. The laser system that we use is a Yb-fiber laser (Coherent Monaco 1035-40) delivering near IR pulses centered at 1033 nm at a repetition rate of 1 MHz with pulse energy of 40 µJ and pulse duration of < 230 fs. The pulses are p-polarized with a $1/e^2$ diameter of ~ 3 mm.

2.3 Generation of tunable mid-IR pulses

The mid-IR pulses are generated from a home-built single-stage optical parametric amplifier (OPA).[87] A schematic of the setup is shown in Figure 2.2. The full output power from the Monaco (40 W) is split into two arms of 30W and 10W using a combination of a half waveplate (Thorlabs WPH05M-1030) and a high-power polarizing beamsplitting cube (Thorlabs CCM1-PBS25-1064-HP). The 30 W arm is used to pump the mid-IR OPA. It is further split into two arms using a combination of a second half waveplate and a thin film polarizer (Eksma 420-1298). The p-polarized arm (24 W) forms the OPA-pump which passes through a delay stage (DS, Newport 423) that ensures proper timing between the two arms, and is focused slightly behind the OPA crystal position for Type I phase matching, using a 250 mm focusing lens (L1, Thorlabs LA1252-B), after reflecting off a longpass dichroic mirror (DCM1). At the crystal position, the pump beam fwhm is $\sim$ 250 µm, and the power is measured to be 22 W after 2W of cumulative loss from all the optics upstream in the pump line.

The s-polarized arm (6 W) is passed through an ND wheel (ND, Thorlabs NDC-50C-2-B), adjustable iris aperture (IA, Thorlabs SM1D12C-SM1), and 100 mm lens (L1, Thorlabs LA1509-B) that focuses the 1033 nm fundamental on a 10 mm Yttrium-Aluminum-Garnet crystal (YAG, Newlight Photonics) for supercontinuum generation (SCG). The focusing conditions used for SCG have been previously reported by Calendron et. al.[88] Post SCG, a 1150 nm longpass dichroic mirror (DCM2, Edmund Optics 87-043) is used to reflect and reject the visible part of the spectrum in a water-cooled beam dump (WCBD), while the near-IR part (1150 - 1700 nm) is transmitted, which is focused at the OPA crystal position using a 40 mm achromat lens (Thorlabs AC254-040-C-ML).

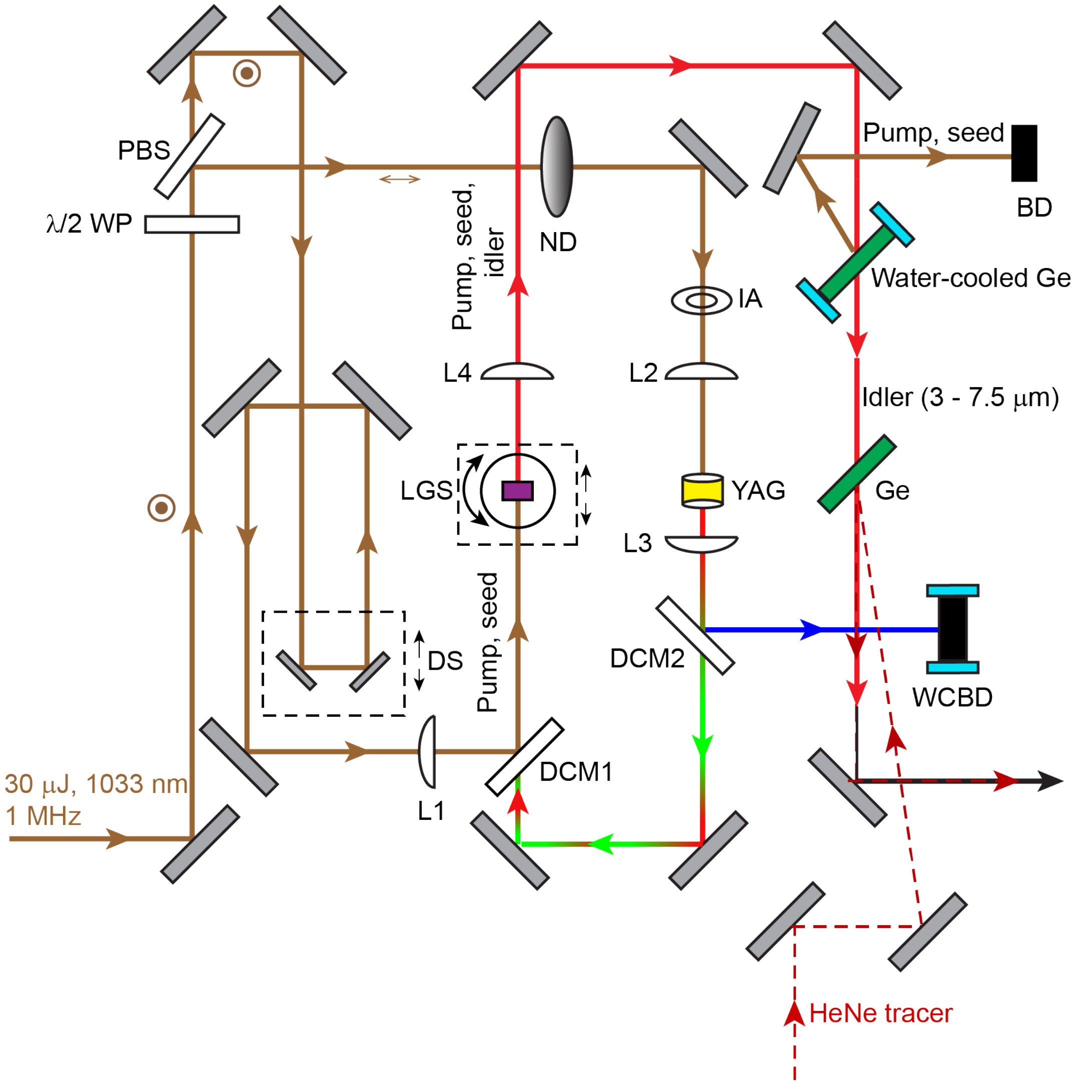

Figure 2.2: Schematic of the mid-IR OPA. WP = Waveplate, PBS = Polarizing beamsplitter, ND = Neutral density wheel, IA = adjustable iris aperture, YAG = Yttrium Aluminum Garnet crystal, L1-L4 = Focusing and collimating lenses, LGS = Lithium Gallium Sulfide crystal

Parametric amplification is performed under Type I phase matching condition ($\phi = 0°$) in a $LiGaS_2$ crystal (LGS) of size $5 \times 5 \times 4$ mm, cut at a phase-matching angle $\theta = 48°$ (for phase-matching at 4.5 μm at normal incidence) or 45° (for phase-matching at 7 μm at normal incidence). The crystal is sourced from Ascut UG & Co. KG.

The choice of LGS as the medium for OPA was made after a careful analysis of all commercially available non-linear materials for phase-matching at 3–8 µm region with a 1033 nm pump source.[87] Amongst various candidates, Li-based materials offer large bandgaps, high damage thresholds, and significant transparency out to 10 µm, although the effective nonlinear coefficient (d_{eff}) is much lower than the Ge and Ag based materials.[89] Due to this, comparatively long crystals are required, which limits the bandwidth of the amplified pulse. Amongst the Li-based materials, LGS provides the best possible combination of large bandgap and d_{eff}. Additionally, amongst all Li-based materials, LGS is predicted to produce the steepest angle-tuning curve for Type I phase-matching, enabling idler generation in the range of 3–7.5 µm over a ∼ 7° range of internal angles, as shown in the phase-matching curve in Figure 2.3.

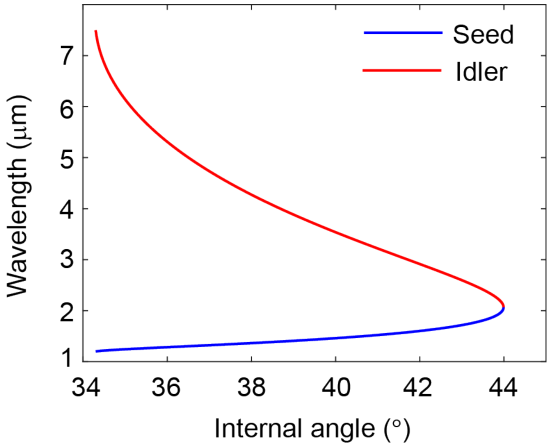

Figure 2.3: Type I phase-matching curve for LGS.

To minimize pump loss, the front and back surfaces are AR coated for the pump frequency. Any back reflection from the crystal is collected on a beam block. Past the crystal position, the generated s-polarized idler is collimated using a 75 mm BaF_2 lens (L4, ISP Optics BF-PX-25-75). The three pulses (pump, seed and idler) are passed through an

AR-coated Ge window (Edmund Optics 83-349) which reflects the pump and the seed and transmits the mid-IR idler pulses. Additionally, the Ge window is housed in a water-cooled mount to avoid thermal lensing effects. The reflected pump and seed are routed to a beam block (BD) Following this, the idler is passed through a second Ge window, which acts as a reflector for the HeNe tracer, overlapping with the mid-IR idler for alignment purposes. All mirrors in the OPA pump line and the seed line upstream of the YAG crystal are dielectric high reflectors for the fundamental (Newport 10D20DM.10).The OPA is enclosed in a dry N_2-purged box.

The mid-IR pulses generated by the OPA are sent to a home-built Mach-Zehnder interferometer to generate two copies for frequency-resolved measurements. The intensity in the dark arm is monitored on a room-temperature HgCdTe detector (MCT) and is used to collect the reference spectrum of the IR pulse either slightly before or after the FEIR experiment. The beam in the bright arm is fed into the FEIR microscope (described in section 2.6)

The experiments presented in this thesis are performed with the IR pulses tuned at 6 µm.

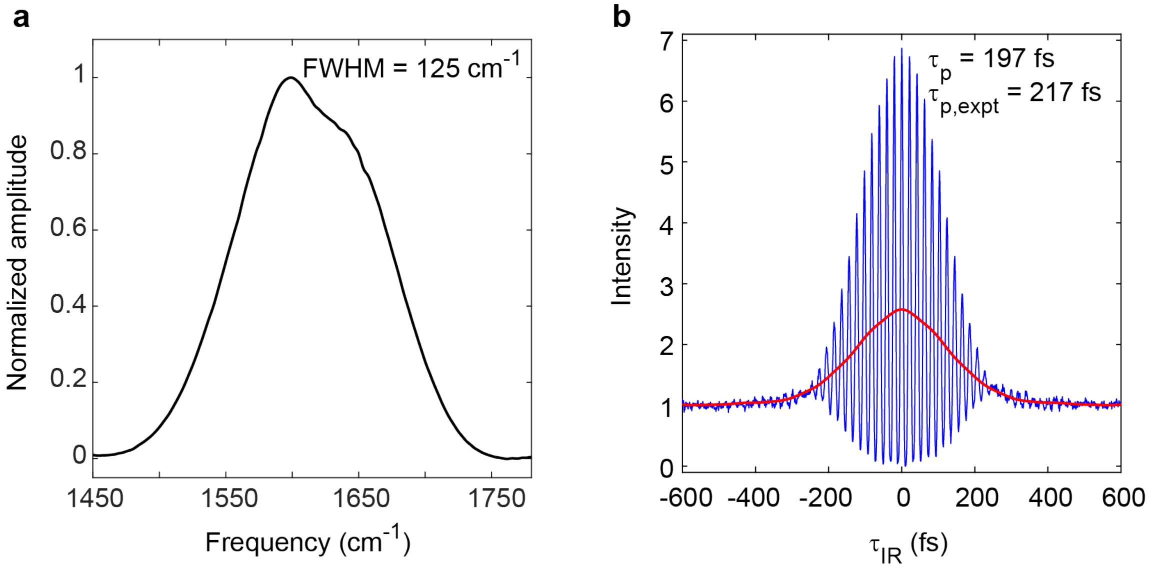

Figure 2.4: IR pump pulse characterization. (a) The spectrum of the IR pump pulse centered at 1620 cm^{-1}. (b) Interferometric autocorrelation. The extracted zero-frequency component is shown in red overlaid on the IAC shown in blue.

The pulse duration is measured by interferometric autocorrelation (IAC) using the second harmonic generated by focusing the pulses on an $AgGaS_2$ crystal (AGS) placed at the sample position on the microscope stage. The generated 3 µm pulses and the transmitted 6 µm pulses are passed through two glass microscope cover slides, which block the 6 µm pulses. The transmitted 3 µm pulses are sent to the MCT detector. The pulse duration (τ_p) is determined from the FWHM of the zero-frequency component extracted from the IAC according to $\tau_p = \mathtt{FWHM}/\sqrt{2}$. The pulse duration is determined to be 197 fs, by directly focusing the IR pulses on the AGS crystal. To account for the experimental conditions for FEIR measurements, a 1 mm CaF_2 window is added before the AGS, which brings about a certain amount of dispersion, lengthening the pulses to 217 fs.

2.4 Fixed frequency visible pump source

For most of the experimental data presented in this thesis, primarily on all coumarins and proflavin, the visible pump or "encoding" line features a fixed frequency of 516.5 nm, which is the frequency double of the 1033 nm fundamental output from the Yb fiber laser source. The schematic is shown in Figure 2.5.

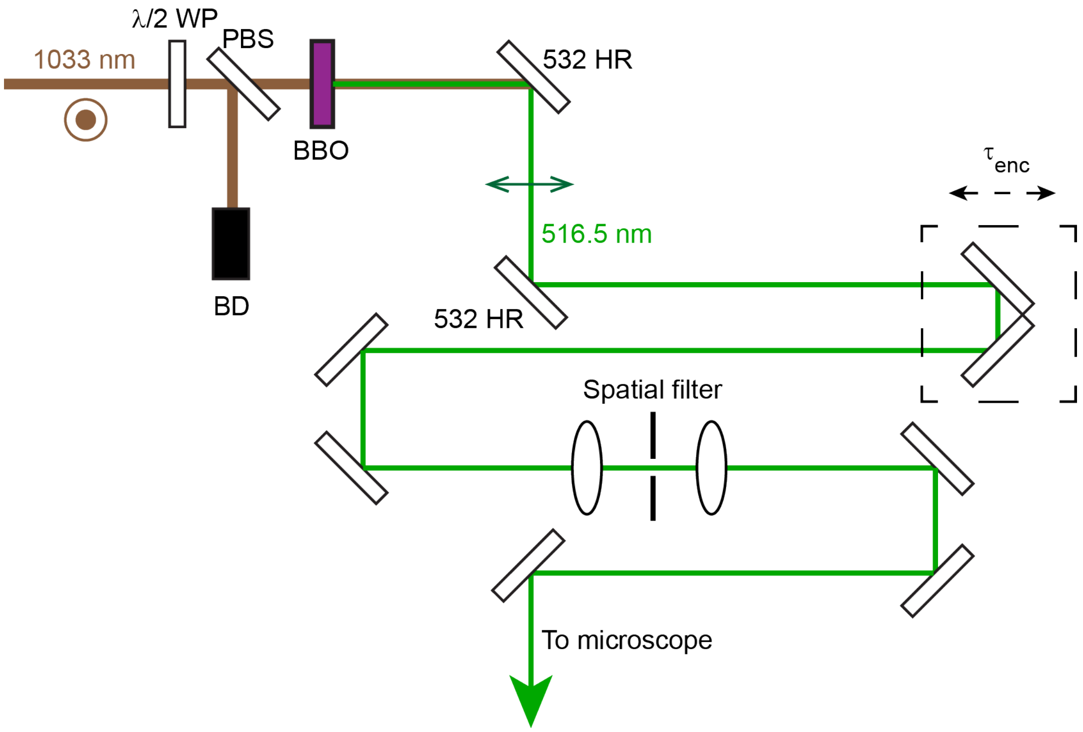

Figure 2.5: Schematic of the fixed frequency visible encoding line.

To generate this, about 2W of the total 40 W of laser power was split off using a 90:10 beamsplitter. A combination of a half waveplate (λ/2 WP, Thorlabs WPH05M-1030) and a high-power polarizing beamsplitting cube (PBS, Thorlabs CCM1-PBS25-1064-HP) is used to set the total input power to pump a 3mm thick Beta-Barium Borate (BBO) crystal for second harmonic generation (SHG). The remaining fundamental is routed to a beam dump

(BD). The input fundamental pulses are p-polarized and the resultant SHG pulses are s-polarized. Post SHG, the visible pulses are filtered out of the fundamental by reflection off 532 nm high-reflector mirrors (532 HR) and eventually routed to a retro-reflector mounted on a motor-controlled precision delay stage (Aerotech ANT95-50L-MP) to regulate the time-delay between the IR and the visible pulses, which we call the "encoding delay" or τ_{enc}. Following the delay stage, the beam is passed through a spatial filter to produce a $\sim$ 6 mm circular mode to slightly overfill the back aperture of the visible objective in the microscope. The pulse energy can be regulated between $\sim$ 10 fJ and 2.2 µJ, measured by a visible power detector (Coherent LM2-VIS).

The duration of the visible encoding pulse was measured indirectly from the fluorescence induced by vibrationally non-resonant IR+visible two-photon absorption. The IR pulse is tuned to 2235 cm^{-1}, which is non-resonant with any vibration of Coumarin 6. The visible pulse duration is back-calculated from the pulse overlap region with the knowledge of the IR pulse duration from the IAC. The visible pulse duration was calculated to be $\sim$ 315 fs.

2.5 Generation of frequency-tunable visible pulses

The fixed frequency visible encoding line imposes some serious limitations on the FEIR experiments. Firstly, it limited the choice of chromophores to a handful of dyes. Secondly, the FEIR resonance condition plays a vital role in determining the overall fluorescence signal strength. The consequences of resonance tuning and the description of brightness and contrast in the context of FEIR is discussed in Ref. [90] and Chapter 3. The dearth of a tunable resonance therefore precludes the option to optimize the experimental conditions to ensure the best possible combination of signal and contrast in an FEIR experiment. To overcome this problem, an optical parametric amplifier (OPA) was built to generate sub-ps narrowband pulses tunable across the visible range of the spectrum.

2.5.1 Strategy

The key considerations for building the visible OPA were similar to those for the single-stage mid-IR OPA discussed before. Specifically, the design must be suitable for operating at a high repetition rate of 1 MHz and generate high-stability visible pulses of sub-ps duration. The schematic of the OPA is shown in Figure 2.6.

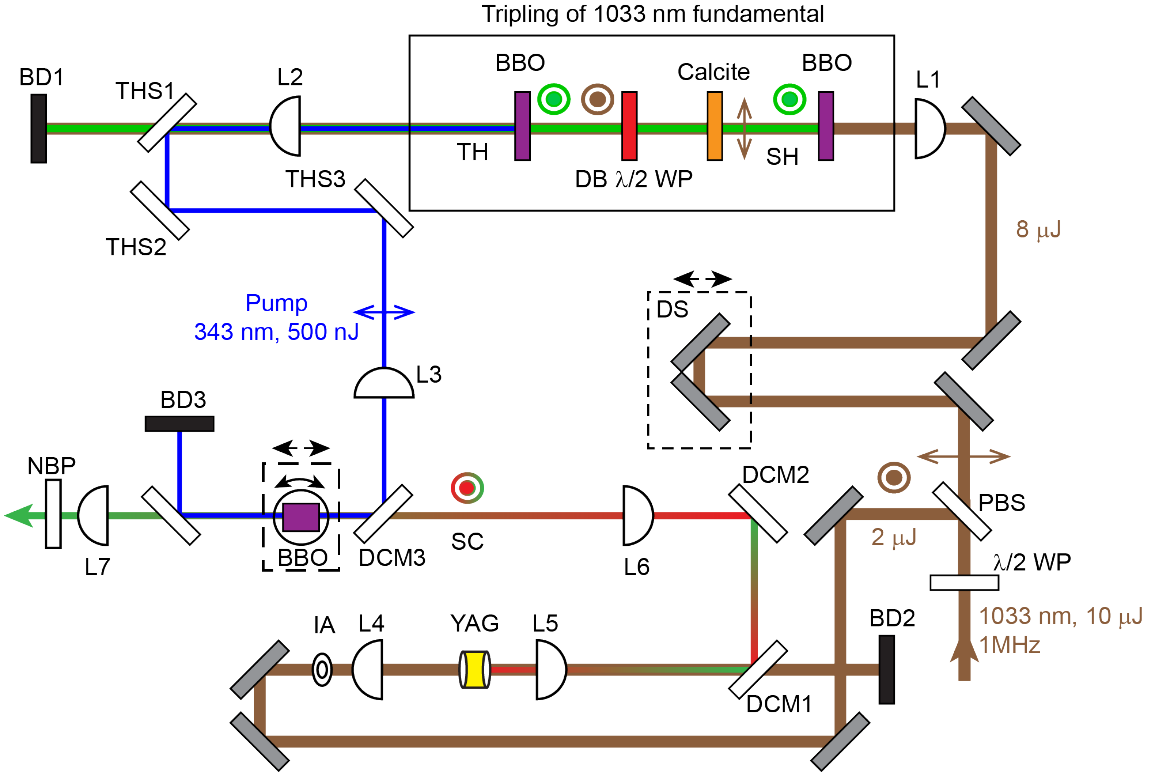

Figure 2.6: Schematic of the visible OPA. The abbreviations and specifications of the optics are given in the main text.

This strategy was adopted from a previous design of a non-collinear OPA (NOPA) published by Riedle and co-workers,[85] where the triple harmonic of a Yb-fiber laser (343 nm) was used to pump a BBO crystal seeded by a supercontinuum generated by focusing part of the 1033 nm fundamental on a continuously rotating sapphire crystal. The pump and the seed are phase-matched at the BBO in a non-collinear geometry to generate ultrashort tunable visible pulses with broad bandwidth. The NOPA was demonstrated to operate at a repetition rate as high as 2 MHz.

One of our key requisites is to generate visible pulses that are narrowband, to avoid unwanted one-photon excitation at the red absorption tail of the chromophore (see Chapter 3). Additionally, the requisite for pulse duration is not stringent, as long as the generated pulses are shorter than the vibrational relaxation timescale, which is often of the order of $\sim 1 - 2$ ps. Keeping these requisites in mind, we chose a collinear geometry for the OPA, which is pumped by a total of 10 W of power from the primary Yb-fiber laser source.

2.5.2 Generation of the ultraviolet pump for OPA

A total of 10 W of the output from the Yb-fiber laser (s-polarized) is divided into two arms of 8 W (s-polarized) and 2 W (p-polarized) using a combination of a half waveplate ($\lambda/2$ HP, Thorlabs WPH05M-1030) and a high-power polarizing beamsplitting cube (PBS, Thorlabs CCM1-PBS25-1064-HP). The 8 W arm is retro-reflected off two mirrors mounted on a manual delay stage (DS, Newport 423). After bouncing off 1030 nm high-reflector mirrors (Eksma 042-1030HHR), the beam is focused between two BBO crystals using a 250 mm UVFS lens (L1, Thorlabs LA4158-B). The first BBO crystal has the dimensions of $6 \times 6 \times 3$ mm, with both surfaces AR-coated for 1030 nm and 515 nm, and is cut at a phase-matching angle of 23.4° for Type I second harmonic generation. The group delay dispersion of 1033 nm fundamental pump and the resultant 516.5 nm second harmonic (SH) is matched by passing them through a natural calcite plate of size 16×14 mm, with a delay compensation range of 295-463 fs (Eksma 225-2212), both sides of which are AR-coated for 500-530 nm and 1000-1060 nm. Following this, the s-polarized fundamental and the p-polarized SH are passed through a dual band half-waveplate (Eksma, 465-4212) that rotates the polarization of the fundamental, while retaining the polarization of the SH. Following this, the p-polarized pulses are incident on the second BBO crystal of size $6 \times 6 \times 0.3$ mm, cut at a phase-matching angle of 32.5° for third harmonic generation. The two BBOs, the dual-band half waveplate and the natural calcite plate are mounted on an optical rail (Eksma 810-0005-02) with the help of rail carriers for precision adjustment of their relative positions. The resultant 343 nm third harmonic (TH) is used as the pump for subsequent parametric amplification downstream.

The pulses are s-polarized, and the beam is collimated by passing through a 250 mm UV-AR coated UVFS lens (L2, Thorlabs, LA4158-UV), and filtered out from the fundamental and SH by reflecting off three high-reflector UVFS third harmonic separator mirrors (THS1, THS2, THS3, Eksma 042-3535). The fundamental and the SH are routed to a beam dump (BD1) after transmitting through THS1. Any residual beam that transmits through THS2 and THS3, has significantly low power, and is dumped on the edge of the respective mirror mounts. The UV pulse energy after THS1 is $\sim$ 519 nJ as measured by the UV power detector (Coherent, LM2-UV). After reflection off THS3, the TH passes through a 150 mm UVFS lens AR-coated for UV (L3, Thorlabs LA4874-UV), which focuses the beam slightly before the OPA crystal position, after reflecting off a 425 nm longpass dichroic mirror (DCM3, Thorlabs DMLP425).

2.5.3 Supercontinuum generation

The p-polarized 2 W arm is used to generate a supercontinuum by self phase modulation in a non-linear medium. The key requisite for the supercontinuum was that it has enough intensity across the maximum range of the visible spectrum. We tested two materials, YAG and sapphire for this purpose. Both are sourced from Newlight Photonics. The fundamental beam was sent through a variable iris aperture (IA) and focused on the non-linear crystal. For sapphire, we used a 8 mm long c-cut window, set the iris aperture to 4.0 and focused the fundamental onto it by a 75 mm UVFS lens (L4, Thorlabs LA4725-B). For the YAG, the iris aperture was set to 6.2, and the same focusing lens was used. The spectra of the two supercontinuua were acquired on a CCD spectrometer (Thorlabs CCS200), and are shown in Figure 2.7. The spectra are normalized with respect to maximum intensity, shown on a log-scale to better visualize the intensities at the higher frequencies.[85]

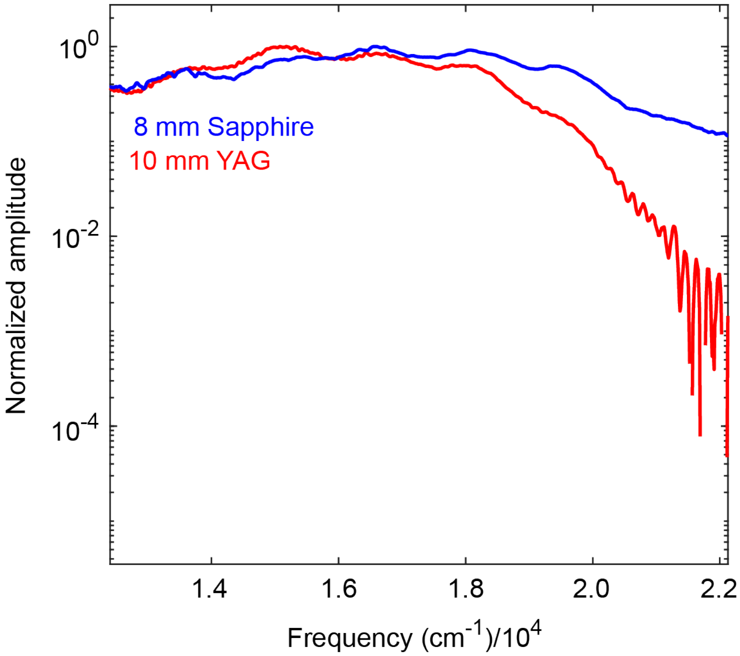

Figure 2.7: Spectra of supercontinuua generated by focusing 1033 nm fundamental in 8 mm sapphire and 10 mm YAG. The intensity is normalized, and shown on a log scale for clear visualization of the intensitites at high-frequencies.

Both supercontinuua exhibit a plateau in the range of 12500 - 18000 cm^{-1} region (550 - 800 nm). Sapphire does give a better spread in the blue frequencies, especially past 21000 cm^{-1} (470 nm), where the intensity of the YAG-generated supercontinuum is negligible.

However, YAG has a much higher laser damage threshold than sapphire, resulting in very stable SCG, without the need for any rotatory or translational motion of the crystal, which is a common practice while using sapphire or CaF_2.[85,91] Furthermore, the high stability of the SC generated in YAG is well-established in our mid-IR OPA. Therefore, we finalized YAG as the material for SCG in the visible OPA. The generated SC is collimated using a 40 mm achromatic doublet, AR-coated for the visible (L5, Thorlabs AC254-040-A-ML). The collimated beam is then made incident on a 900 nm longpass dichroic mirror (DCM1, Thorlabs DMLP900) which transmits the 1033 nm fundamental and the near-IR part of the SC, and reflects the visible part of the spectrum. The transmitted beam is routed to a beam dump (BD2). The reflected beam is reflected off a second dichroic mirror (DCM2), and sent through an AR-coated 300 nm achromatic doublet (L6, Thorlabs AC254-300-A-ML), to focus it at the OPA crystal position after transmitting through DCM3.

2.5.4 OPA in Beta Barium Borate with Type I phase-matching

The pulse energies at the OPA crystal position are $\sim$ 390 nJ for the pump and $\sim$ 12.6 nJ for the the full visible part of the seed, as measured by respective power detectors (Coherent, LM2-UV for the pump and LM2-VIS for the seed). The focusing conditions for the pump and the seed are set such that the seed beam diameter at the OPA crystal position is slightly smaller than the pump beam diameter, with the transmission ratio through a 50 µm pinhole being Seed/Pump= 1.13.

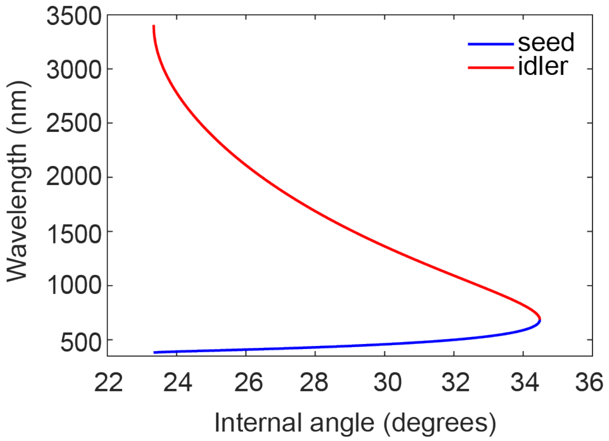

Figure 2.8: Type I phase-matching curve for BBO.

The OPA is performed under Type I phase-matching conditions in a 15mm long BBO crystal (Newlight Photonics) cut at $\theta = 32.3°$, phase-matching for 509 nm at normal incidence. Both surfaces of the crystal are AR-coated for 300-700 nm. BBO exhibits high damage threshold, large bandgap (6.2 eV)[92], and a fairly large nonlinear coefficient ($d_{eff} = 1.99$ pm/V for 343 nm pump, calculated using SNLO), making it a very popular choice for medium in visible OPAs. Additionally, BBO exhibits a steep phase-matching curve (shown in Figure 2.8) that allows for amplification across almost the entire visible spectrum in merely $\sim 8°$ of angle tuning range. BBO exhibits high transmissivity in the range of 190 nm to 3500 nm.

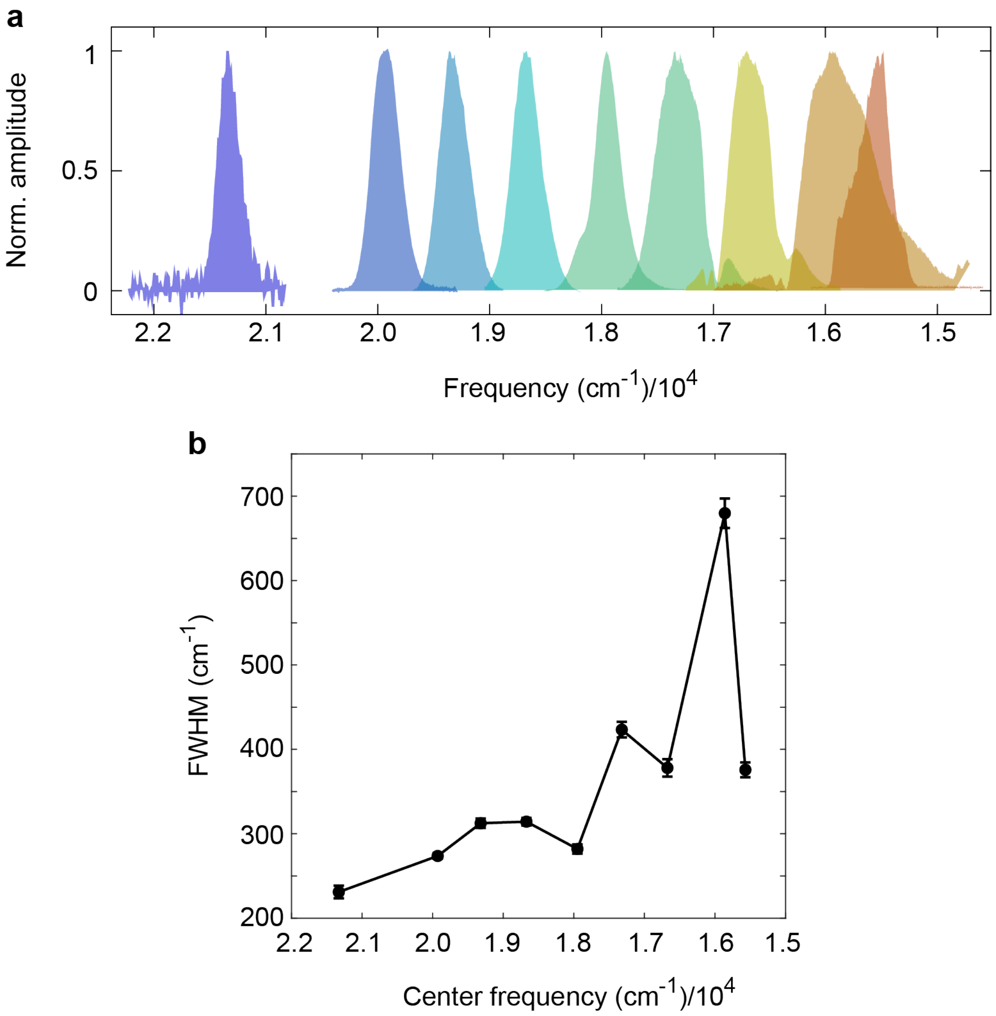

Figure 2.9: Demonstration of frequency tunability with the visible OPA. (a) Spectra of visible pulses tuned across 15500 - 21500 cm^{-1}. (b) FWHM of the amplified pulses across the tuning range.

The BBO is mounted on a manual rotating stage for angle tuning (OptoSigma KSP-656MUU). The entire assembly is further mounted on a manual delay stage (Optosigma TADC-651S25UU) for adjusting the foci positions of the pump and the seed relative to the crystal. The amplification is limited to 3500 nm in the red due to absorption at lower frequencies by BBO. The blue frequency limit is set to 470 nm due to low spectral intensity of the SC generated in YAG. At the wavelength of 680 nm, the seed and the idler become degenerate, resulting in unwanted broadening of the amplified pulses. We have been able to demonstrate effective tuning for amplification of seed wavelengths with reasonable pulse bandwidths in the range of 470 nm to 625 nm, as shown in Figure 2.9a.

The best possible amplification of the visible pulses so far has yielded pulse energies ranging from ~ 1 nJ at 470 nm to ~ 12 nJ at 620 nm. The comparatively low amplification at the blue frequencies is primarily due to the low intensity at the blue region of the seed spectrum. However, since the optimum pulse energies employed for the single-molecule level measurements ranges from $30 - 50$ pJ, we have sufficient pulse energies out of the OPA. The amplified pulses have their FWHM ranging from 220 cm^{-1} for the highest center frequency to 720 cm^{-1} towards low center frequency, as shown in Figure 2.9b. Although a linear geometry for the amplification gives us fairly narrowband pulses compared to NOPA, they are still broader than the desirable FWHM for the encoding pulses ($\sim$ 100 cm^{-1}). Using these pulses in an FEIR experiment would result in unwanted 1-photon fluorescence from increased absorption by the chromophore in the red absorption tail. For this, we take an additional step of transmitting the amplified beam through ultra-narrow bandpass filters (NBP) to reduce the FWHM to $<$ 100 cm^{-1}.

Tuning across a smaller range of frequency is brought about by changing the angle of incidence on the bandpass filter between 0 and $\sim 60°$, which acts as an etalon, blue-shifting the frequency of maximum transmission upon tuning away from 0° angle of incidence. Such tuning across a small frequency range is demonstrated in Figure 2.10.

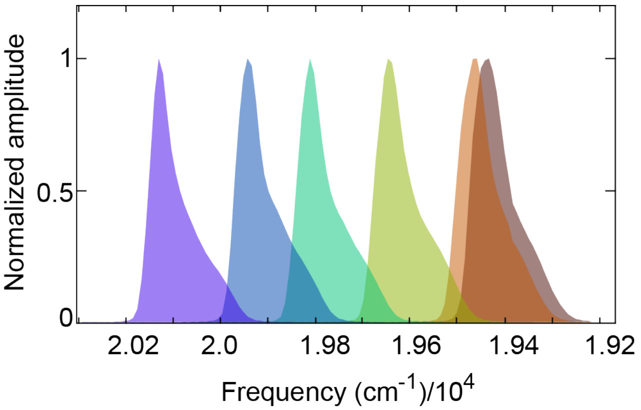

Figure 2.10: Generation of narrowband visible pulses by transmission of amplified seed through a narrow bandpass filter. The tunability is brought about by changing the angle of incidence on the filter.

The resulting pulses are narrower than the instrument response function of the CCD spectrometer, which convolves itself with the spectrum of the pulses, resulting in their apparent asymmetry. Table 2.1 summarizes the narrow bandpass filters used to reduce the bandwidths of the pulses out of the OPA, and the corresponding ranges of wavelength spanned by tuning the angle of incidence. For the wavelength ranges of $570 - 585$ nm and $585 - 591$ nm, there was a dearth of a commercially available bandpass filter with a bandwidth as narrow as $2-3$ nm. Hence, to work around the problem, a combination of two bandpass filters, each with a bandwidth of 10 nm was used, and the angle of incidence on both the filters were tuned to generate pulses with bandwidths of $\sim 2 - 3$ nm. For spanning the range of $570 - 585$ nm, a combination of two bandpass filters centered at 580 nm and 590 nm was used, while for the range of $585 - 590$, the combination of filters had center wavelengths of 590 nm and 600 nm.

Table 2.1: Narrow bandpass filters used to reduce the bandwidth of the amplified pulses and the corresponding wavelength tuning ranges

Vendor	Part No.	λ (nm)	$\Delta\lambda$ (nm)	Tuning range (nm)
Chroma	27006 - OIII 500.7/3	500.7	3	470 – 500
Semrock	FF01-514-12.5	514	3	500 – 514
Semrock	FF01-532-12.5	532	2	514 – 532
Semrock	LL01-568-12.5	568	2	540 – 568
Thorlabs	FBH580-10	580	10	570 – 585
Thorlabs	FBH590-10	590	10	
Thorlabs	FBH590-10	590	10	585 – 591
Thorlabs	FBH600-10	600	10	

The pulses out of the OPA box bounce off two mirrors before being incident on the retro-reflector mounted on the motorized delay stage mentioned previously, which controls the encoding delay. Following this, the beam is sent through a spatial filter to generate a collimated beam with a roughly circular mode with a beam diameter of $\sim$ 7 mm to slightly overfill the back aperture of the visible objective described in the next section. The polarization of the visible pulses relative to the IR pulses is controlled by a half waveplate right before the entry to the microscope.

2.5.5 Visible pulse characterization

The duration of the visible (or encoding) pulses are back-calculated from the temporal overlap of the IR and visible pulses, which is in turn determined from the fluorescence induced by vibrationally non-resonant two-photon absorption (TPA).[93] Ideally, the pulse duration should be measured as a function of the encoding frequency, but, for this thesis, the characterization was performed only on the pulse with the frequency tuned to 19342 cm^{-1}, which corresponds to 517 nm. This was done to enable a direct comparison with the encoding pulses used previously, generated by frequency doubling the 1033 nm Monaco fundamental. The measurement was performed on Coumarin 6, with the encoding pulse tuned to 19342 cm^{-1}. The IR pulse was tuned to 2235 cm^{-1} to facilitate vibrationally non-resonant TPA. The results of the experiment are summarized in Figure 2.11 below.

Figure 2.11a shows the two-pulse transient resulting from the fluorescence induced by the vibrationally non-resonant TPA, and therefore, appears only during the pulse overlap. The width of this response is therefore interpreted as the duration of overlap between the IR and visible pulses, and is derived by fitting the response to a Gaussian function. The FWHM of the resultant fit is determined to be 586 fs.

Figure 2.11b shows the TPA spectrum measured as a function of the encoding delay. The projection of the spectrum along the IR frequency axis (top panel) appears to be slightly red-shifted from the IR pump spectrum, while the projection along the encoding delay axis (right panel) should, in principle reproduce the two-pulse transient response. A Gaussian fit to this projection yields an FWHM of 582 fs. With the prior knowledge of the IR pulse duration at 2235 cm^{-1} to be 182 fs,[93] the encoding pulse duration is back-calculated using the relation $\tau_{enc} = \sqrt{\tau_{TPA}^2 - \tau_{IR}^2}$, which gives $\tau_{enc} = 557$ fs from the projection of the TPA spectrum along the encoding delay axis, and $\tau_{enc} = 553$ fs from the two-pulse transient signal. The duration of the encoding pulse is taken to be the average of these two values: $\tau_{enc} = 555$ fs. This is much longer in duration than the encoding pulses used in the previous setup, generated by frequency-doubling the 1033 nm Monaco fundamental (315 fs). However, since the pulse is still much shorter than the vibrational relaxation timescales, the efficiency of the encoding transition is not expected to be compromised with the use of the visible OPA.

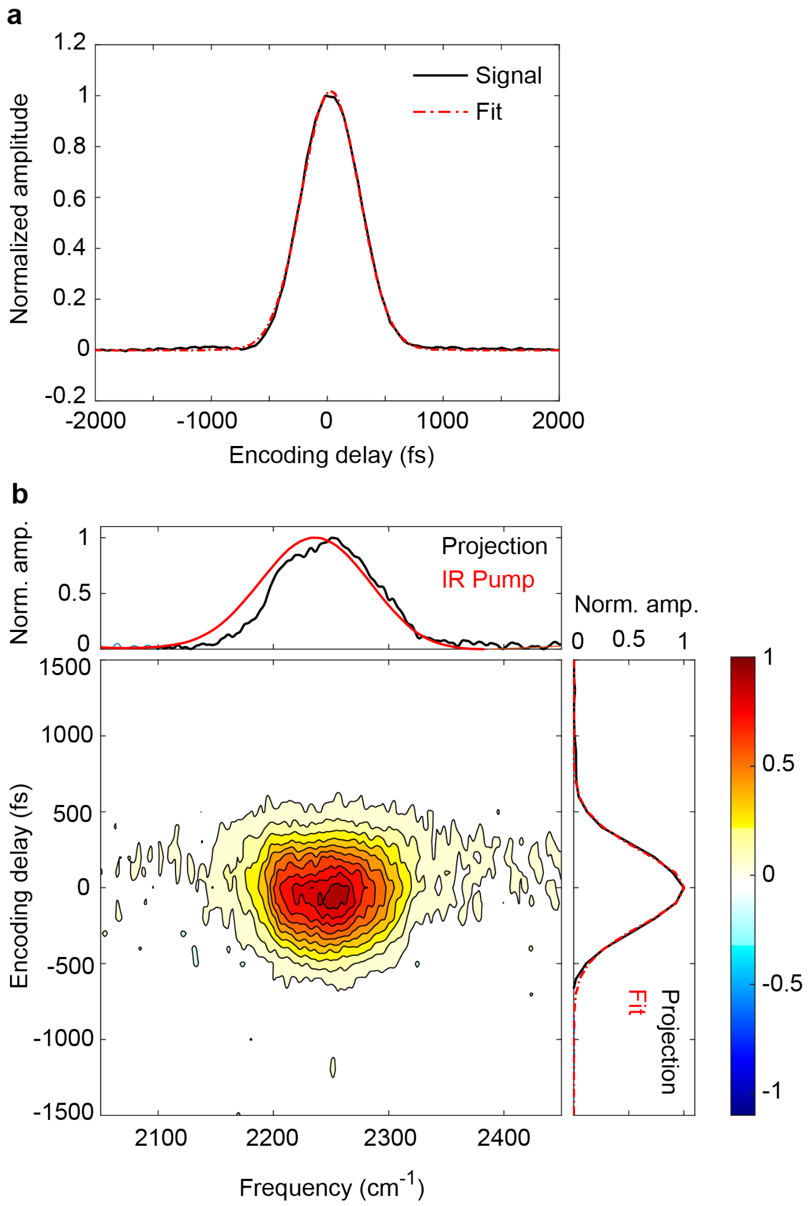

Figure 2.11: Determination of the encoding pulse duration from fluorescence induced by vibrationally non-resonant two photon absorption. (a) Two-pulse transient fluorescence induced by vibrationally non-resonant two photon absorption (TPA) (black). A gaussian fit (red) is used to determine the duration of the pulse overlap as 586 fs. (b) Frequency-resolved TPA spectrum of Coumarin 6. (Top panel) The projection of the surface along the frequency axis (black) is shown overlaid on the IR pump spectrum (red). (Right panel) The projection along the encoding delay axis (black) is shown with a Gaussian fit yielding FWHM = 582 fs.

2.6 Description of the FEIR microscope

The FEIR microscope is a modified upright confocal fluorescence microscope, the schematic of which is shown in Figure 2.1. The linearly polarized visible pulses, after passing through the half waveplate, are brought to the top of the microscope with the help of a periscope. After bouncing off two mirrors on the microscope top, the beam is made incident on either a shortpass or a longpass dichroic mirror, depending on the spectral properties of the chosen chromophore. After reflecting off the dichroic mirror, the collimated visible beam is sent through a high numerical aperture (NA) visible objective (Zeiss A-Plan 63x/0.8), that creates a tight focus with a spot size of 430 nm. The IR pulse pair out of the Mach-Zehnder interferometer is made incident on a ZnSe asphere (ISP Optics ASPH-ZC-25–12), which creates a tight focus of the size $\sim$ 10.5 µm, coincident with the visible focus, but incident in a counter-propagating manner. The IR pulse energy at the sample position is measured to be 50 nJ, and the tight focusing of the IR beam ensures sufficiently high peak field intensities at the sample. The characterization of the IR and visible foci is presented in Refs. [70] and [93]. The focal length of the asphere is 12.7 mm, and the clear aperture is reported as 90% of the 25.4 mm diameter. Based on this information, the NA of this lens is calculated to be

$$NA = n \sin\theta = n \sin\left[\tan^{-1}\left(\frac{D}{2f}\right)\right] \approx 0.68 \tag{2.1}$$

In the above equation, D is the effective diameter of the back aperture. The refractive index is denoted by n, which is 1 in case of air. The diameter of the beam incident on the asphere is $\sim 8 - 12$ mm, and therefore, slightly underfills the back aperture. The asphere is mounted on a manual translation stage capable of linear motion in X, Y and Z direction. The IR beam path leading to the asphere is enclosed in beam tubes that are purged with dry N_2 gas.

The sample solution is sandwiched between a 1 mm thick CaF_2 window at the bottom and a 150 µm CaF_2 coverslip at the top (Crystran), with a 50 µm teflon spacer in between, that determines the pathlength of the cell. The assembly is housed in a custom-machined aluminum holder which is placed on a motorized X, Y, Z translation stage. Upon excitation, the fluorescence from the solution is collected using the same objective used to focus the visible pulses, and transmitted through the dichroic. Past this, the fluorescence beam is sent through a tube lens of suitable focal length to match the focal spot size to the size of the 50 µm active area of the single-photon avalanche photodiode (SPAD, PicoQuant MPD PDM 50). This ensures that the active area acts as the pinhole itself, enabling the confocal condition.[94] The choice of the tube lens focal length is made based on the desirable size of the image of the focal volume on the detector. The diameter of the diffraction-limited spot is given by

$$d_{DL} \approx \frac{1.22\lambda}{\mathtt{NA}} \tag{2.2}$$

where, λ is the wavelength of the incident beam. We demonstrate it for 516.5 nm, which is the wavelength of the second harmonic generated from the fundamental output of the Yb-fiber laser. For 0.8 NA Zeiss objective, $d_{DL} = 0.788$ µm. The size of the image of this spot on the detector is determined by the magnification of the objective, which is in turn given by the ratio of the focal lengths of the tube lens and itself ($\frac{f_{TL}}{f_{obj}}$, which gives us

$$d_{\mathtt{image}} = \frac{f_{TL}}{f_{obj}} d_{DL} \tag{2.3}$$

The focal length of the Zeiss objective is determined to be 2.62 mm[93]. The focal length of the tube lens is chosen to be 150 mm to ensure an image size of $\sim$ 45 µm, which roughly matches the size of the detector active area. For all the wavelengths of the visible encoding beam used in the experiments reported in this thesis (516.5 nm to 591 nm), the image size at the detector ranges between 45 µm and 52 µm, thus satisfying the confocal conditions throughout.

To position the sample at the focus and aligning the beam through the scope, the beam reflected off a silver mirror housed in a microscope cube, and is then routed to a 125 mm tube lens that focuses it on a CMOS camera (Thorlabs DCC1545M). After alignment, the cube housing the mirror and the tube lens is removed, thus providing a clear path to the tube lens before the detector.

2.6.1 Considerations for choosing the microscope objective

Our choice for the visible objective is driven by the conditions imposed by the FEIR experiment. The primary consideration is shaped by two factors: First, maximizing the collection efficiency of the objective, which is determined by its NA. Under paraxial approximation, this is given as $CE = \mathtt{NA}^2/4$. The second factor is to make the setup compatible with the use of high energy IR pulses. Most microscopes in single-molecule fluorescence experiments employ immersion objectives, characterized by NA values typically > 1. However, the immersion media used in such objectives (hydrocarbon oils, silicone oils, water, etc.) have been observed to be incompatible with high energy IR pulses. In our current geometry, the IR beam is focused at the sample position, past which, it diverges and transmits right through the sample cell. This causes tremendous heating effect, deforming the surface of the immersion fluid, and therefore, bringing about a complete degradation of the focus.[93]. To avoid this, we limit ourselves to using dry air objectives. The experiments shown in this thesis are carried out using the Zeiss objective mentioned previously. Recently, we have installed a higher NA (0.95) air objective (Olympus PlanFL N 100x), which should in principle result in a 50% increase in the total collected fluorescence photon count rate relative to the Zeiss objective. This objective is currently being used for the ongoing FEIR experiments.

2.7 Data acquisition

The electronic architecture used in the acquisition of both IR and fluorescence signals are discussed in detail in Ref. [93]. The key points are summarized below.

2.7.1 IR signal detection

The mid-IR signal is detected by the MCT detector in a shot-to-shot manner, which is possible because the MCT detector has a fast response time of the order of nanoseconds, which allows the detector voltage response to fully relax between consecutive pulses. The mid-IR intensity is measured by sampling the peak detector response. A 1 MHz sync from the Monaco amplifer is used as an external trigger for a delay generator (Standord Research Systems DG 645), which outputs either a 1 MHz or a 2 MHz digital waveform with an electronic delay chosen to synchronize waveform with the detector response. This trigger serves as a sample clock for the data acquisition (DAQ) card (National Instruments PCIe-6361) This enables measurement of either the peak voltage (1 MHz trigger) or the difference between the peak and baseline voltages (2 MHz trigger). The difference between the peak and baseline voltage is used to measure the absolute voltage on the detector during alignment of the IR beam through the scope. The 1 MHz trigger is used during the measurements of the IR interferograms.

2.7.2 Fluorescence signal detection

Photon counting in SPAD is asynchronous with respect to the laser pulse train. The photon detection events registered by SPAD are fed into two separate electronic channels. One channel ues a transistor-transistor logic (TTL) waveform that is sent to the DAQ card, which has a counter that is increases on the incoming edges of the waveform. This counter is sampled either by an internal clock of the DAQ card or an external trigger. The difference in the counter value between two consecutive waves gives the number of photons recorded in that interval. In the experiments discussed in this thesis, the total fluroescence signal is measured from the sample, which uses the internal clock of the DAQ card, which has a time bin of 50 ms. The photon number per interval is converted to the intensity, or the photon count rate by multiplying by the sampling rate. The other channel uses a Nuclear Instrument Modules (NIM) waveform. It is used for TCSPC measurements and fluctuation correlation measurements, which are not discussed in this thesis.

Chapter 3

Quantification of FEIR signal and its modulation by resonance condition

3.1 Introduction

In the FEIR excitation scheme, the molecular vibration undergoes two interactions with a mid-IR light field, thereby creating an excited vibrational population state. This is followed by two subsequent interactions with a visible light field that creates an excited electronic population state. This implies that the molecular response in an FEIR experiment is described at the minimum of the fourth order of nonlinearity. In Ref. [95], we have shown how nonlinear response function formalism can be successfully used to describe the FEIR response, and upon further incorporation of the effects of interaction with finite electric fields, we can reach a near-quantitative level of agreement with the experimental results.[96].

While setting up an FEIR experiment, the frequency of the visible field is chosen such that it falls off-resonance in the absence of the IR excitation. However, in the event of a pre-excitation of molecular vibrations by the IR pulse, the visible excitation brings about a selective up-conversion of the excited vibrational state to a higher-lying fluorescent state. The fluorescence signal arising from the molecule's spontaneous relaxation to the ground state is what constitutes the FEIR signal. It originates from an excited vibrational state of the ground electronic state, or, in other words, is encoded with molecular vibrational information.

This chapter describes the proof-of-principle experiments of FEIR spectroscopy and provides a discussion of the FEIR signal, the primary observable in an FEIR experiment. From the perspective of single-molecule spectroscopy, this entails expressing the FEIR count rate based on per molecule per excitation cycle, thus leading to the description of FEIR brightness and cross-section, in a similar manner as their fluorescence analogs. Following the discussion on the different instrumental parameters that determine the FEIR count rate, such as the laser repetition rate, the average number of molecules in the probe volume, the photon detection efficiency, the fluorescence quantum yield, and the energy densities of the IR and visible pulses, the chapter provides a discussion on the impact of resonance condition on the FEIR brightness and contrast, and how it is optimized for a given experiment.

We choose Coumarin 6, a fluorescent dye from the coumarin family as our model system to describe the FEIR signal. The molecular structure is shown in Figure 3.1a The electronic absorption and fluorescence spectra of the molecule are shown in Figure 3.1b. The mid-IR pulse used in the FEIR experiment, shown as a grey shaded area in Figure 3.1, is centered at 1600 cm^{-1}. It excites four of its vibrations in the fingerprint region shown in the FTIR spectrum of the molecule in the same figure. Three of these, appearing at 1515, 1586, and 1616 cm^{-1}, describe conjugated ring stretches, primarily involving the C=C bonds. The peak at 1712 cm^{-1} denotes the lactone carbonyl stretch. The visible pulse, also called the "encoding pulse" is tuned to 19360 cm^{-1} or 516.5 nm, falling off-resonance in the absence of the IR pulse, as shown overlaid on the absorption spectrum of the molecule. However, pre-excitation by the IR pulse promotes it to the excited fluorescent state. The fluorescence signal then passes through a bandpass filter, shown as the green shaded area overlaid on the emission spectrum, and is finally acquired on the SPAD.

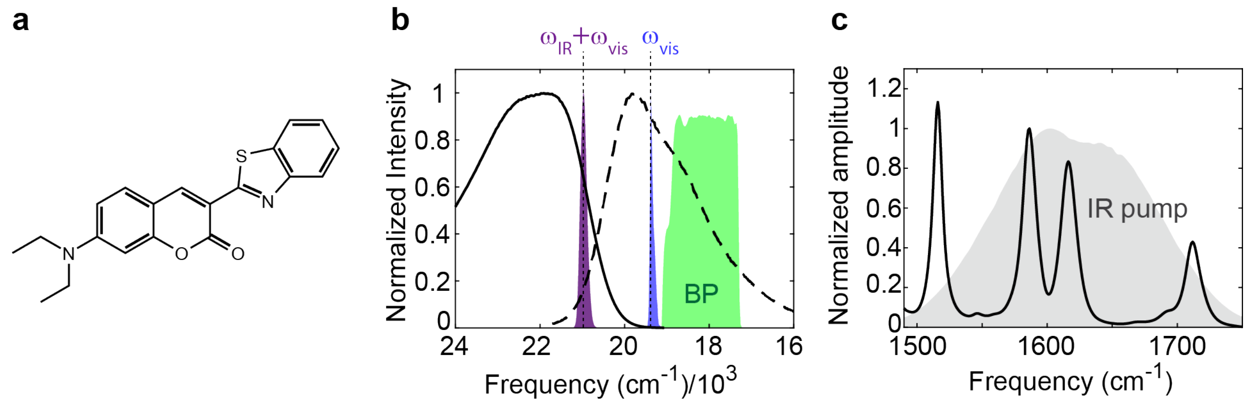

Figure 3.1: Steady-state electronic absorption, fluorescence, and IR spectra of Coumarin 6. (a) Molecular structure of Coumarin 6. (b) UV/vis absorption (solid) and fluorescence (dashed) spectra. The visible encoding frequency, set to 19360 cm^{-1}(blue) falls off-resonance for the electronic excitation of the molecule. The IR pulse is tuned to be centered at 1600 cm^{-1}, bringing the IR + visible frequency to 20960 cm^{-1} (purple). The fluorescence signal is passed through a bandpass filter, shown as a green-shaded area labeled BP. (c) FTIR spectrum of Coumarin 6, showing the four vibrations excited by the IR pulse (grey shaded area).

3.2 Materials and methods

Preparation of solutions: Stock solutions were prepared by weighing out the required masses of solid dyes in clear glass vials and dissolving in acetonitrile (CH_3CN) or methanol (CH_3OH). Sample solutions for UV/Vis, fluorescence, FTIR, and FEIR measurements were prepared by pipetting out the required volumes of stock solutions in clear glass vials, drying out the solvent by passing N2 and dissolving the solid residue in either acetonitrile (for UV/Vis and fluorescence measurements) or deuterated acetonitrile (CD_3CN) (for FTIR and FEIR measurements).

UV/vis and fluorescence measurements: The UV/vis spectra were acquired from 40 µM on an Agilent Cary 5000 UMA dual-beam spectrophotometer. The fluorescence excitation/emission surfaces were acquired from 2-5 µM solutions on a Horiba Fluorolog-3 spectrofluorometer. The samples were ensured to have an absorbance of less than 5% to avoid errors in the fluorescence measurements arising from inner filter effect.

FTIR measurements: Dye samples of 2-10 mM concentrations were used to measure the FTIR spectra on a Bruker Tensor 27 FTIR spectrometer. The sample cell was prepared by enclosing 60 µL of sample solution between two CaF2 windows with path length maintained between 50-500 µm using Teflon spacers. The measured absorption spectra are converted to the units of molar extinction coefficient according to Beer's Law.

FEIR measurements: FEIR spectra were acquired on 30 - 100 µM solutions using the instrument and methods described previously,[71,90,97], and in Chapter 2. The mid-IR excitation pulses were generated using the home-built mid-IR OPA[87], centered between 1600 - 1620 cm^{-1}, with a typical FWHM bandwidth of$\sim$ 140 cm^{-1}, and a pulse duration of 230 fs. For the experiments on coumarins, the visible excitation pulses were centered at 516.5 nm, with a bandwidth $<$ 2 nm and a pulse length of $\sim$315 fs.[93] For the experiments on rhodamine 6G, visible pulses were generated from the OPA described in Chapter 2, tuned in the range of 565 - 591 nm and filtered by passing through a combination of narrow bandpass filters to obtain a final bandwidth of $<$ 2nm. The pulse duration was measured to be $\sim$ 550 fs, as described in Section 2.5.5. For acquiring Fourier transform FEIR spectra, the IR pulses were sent through a Mach-Zehnder interferometer to generate collinear IR pulse pairs with the delay controlled by a nanopositioning stage and an identical stage is used to set the IR-visible encoding delay. The relative polarization between the IR and visible pulses was set by controlling the visible polarization with a half waveplate. The IR and the visible pulses focused at the sample position by the ZnSe asphere and the 0.8NA Zeiss objective, respectively, as discussed in Chapter 2. The fluorescence signal was collected with the same objective, passed through a long-pass dichroic optic, and focused onto the ∼50 µm active area of the SPAD.

3.3 Proof-of-principle experiments

3.3.1 Two-pulse FEIR experiment

In the first kind of FEIR experiment, we irradiate the sample with an IR pulse, followed by a visible pulse. The IR-visble pulse sequence is shown in Figure 3.2a. The variable time-delay separating the two pulses is termed as the "encoding delay" (τ_{enc}). The fluorescence signal as a function of the encoding delay is shown in Figure 3.2b. This is the two-pulse FEIR transient of the molecule. One can break down the total fluorescence signal into three different components. Following the two-pulse transient along the encoding delay axis, we see that the negative encoding delay regime shows a small fluorescence signal. A negative encoding delay implies that the molecule interacts with the visible pulse prior to vibrational excitation. The fluorescence in this regime is constituted of two different components: 1) the fluorescence resulting from one-photon visible excitation from the molecule at the frequency of the encoding pulse (F_0), and 2) the signal originating from non-molecular background (B).[90] The latter originates from autofluorescence from the coverslip, optical components and the solvent. As the encoding delay reaches positive values, that is, the visible pulse succeeds the IR pulse in time, the fluorescence gains intensity, and its peaked at a certain encoding delay ($\tau_{enc} = 600$ fs for Coumarin 6). The value at which the fluorescence response peaks is different for different molecules, and is dependent on multiple factors involving the effect coherence pathways due to simultaneous excitation of multiple vibrations by the broadband IR excitation pulses, and interactions with finite pulses.[90,96]. The fluorescence signal riding on top of the the one-photon fluorescence and non-molecular background is the

FEIR signal (F). The total fluorescence response can therefore be represented as:

$$F_{tot} = F + F_0 + B \tag{3.1}$$

A scan to the later encoding delays shows a decay in the fluorescence signal, indicating that the fluorescence indeed originates from excited vibrational state, and decays following the population relaxation of that state. This decay is bi-exponential in nature, characterized by a short and a long time constant. The short time constant is of the order of $\sim 1-2$ ps, and it describes the intramolecular energy redistribution to lower-energy vibrations. The long time constant, often of the order of $\sim 7-10$ ps is identified as energy relaxation to the solvent molecules.[59]

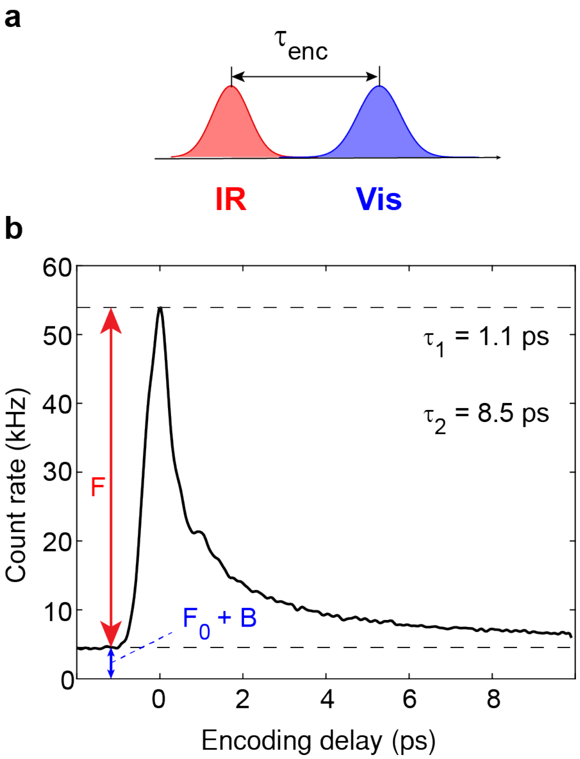

Figure 3.2: Two-pulse FEIR transient of Coumarin 6. (a) The IR-visible pulse sequence used in a two-pulse FEIR experiment, with the variable time-delay between the two pulses labeled as the encoding delay. (b) The two-pulse transient FEIR response from Coumarin 6, depicting the fluorescence count rate from the molecule as a function of the encoding delay. The negative encoding delays are characterized by a small signal level constituted of the one-photon fluorescence and non-molecular background ($F_0 + B$). The FEIR signal (F) onsets at positive encoding delays.

3.3.2 Frequency-resolved FEIR spectrum

To get our hands on frequency-resolved information of the molecule, we employ two copies of the IR pulse, labeled as IR1 and IR2 in Figure 3.3a with a variable time-delay between them (τ_{IR}). In this event, the total FEIR signal (F) is a function of both τ_{IR} and τ_{enc}, and can be expressed as follows:[93]

$$F(\tau_{IR}, \tau_{enc}) = F_1(\tau_{IR} + \tau_{enc}) + F_{12}(\tau_{IR}, \tau_{enc}) + F_2(\tau_{enc}) \tag{3.2}$$

The terms $F_1(\tau_{enc} + \tau_{IR})$ and $F_2(\tau_{enc})$ represent two-pulse FEIR excitation, involving two interactions with IR1 (F_1) or IR2 (F_2) and two interactions with the visible pulse. The term $F_{12}(\tau_{enc}, \tau_{IR})$ represents the three-pulse FEIR signal that involves one interaction each with the two IR pulses, and two interactions with the visible pulses.

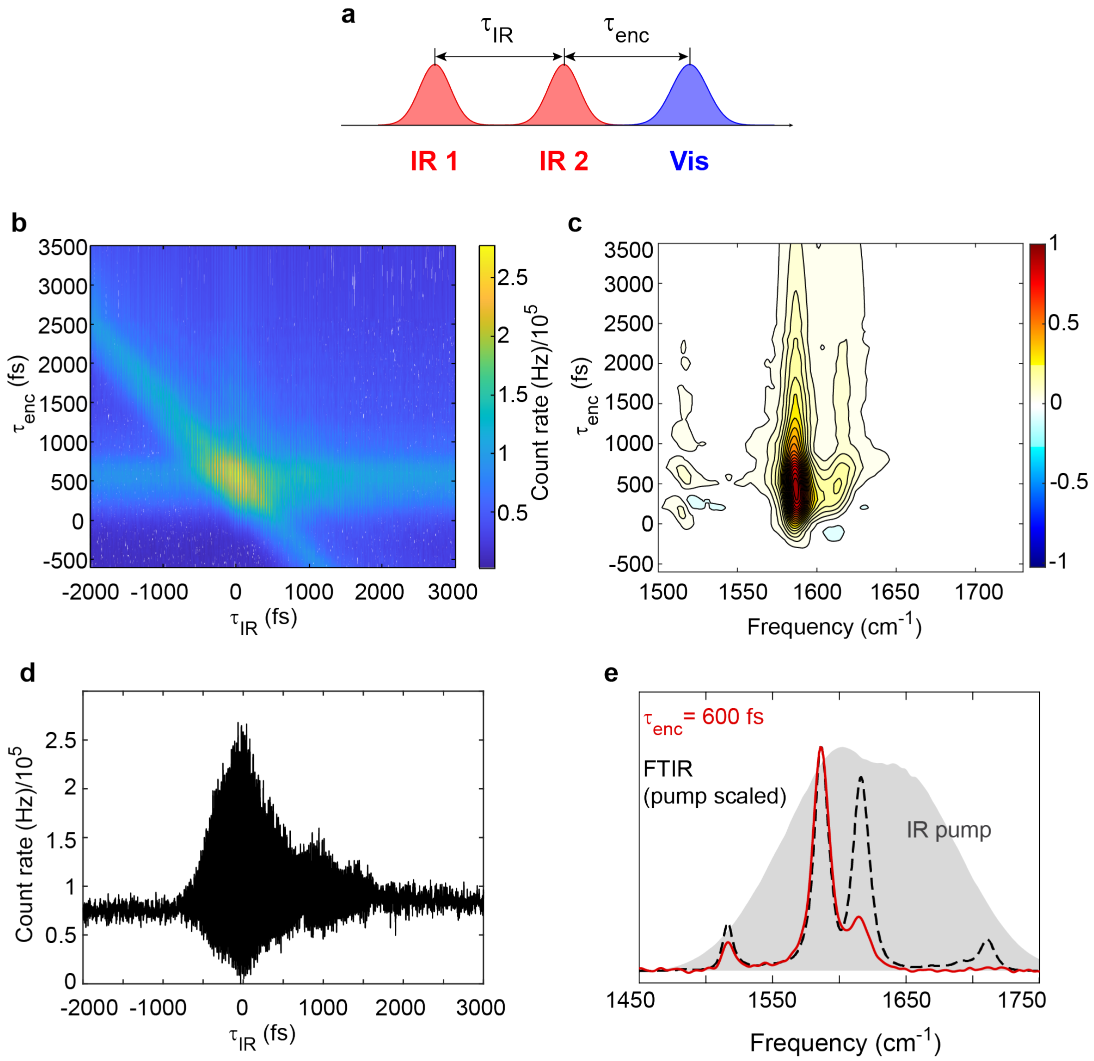

Figure 3.3: Fourier transform FEIR spectrum of Coumarin 6. (a) The pulse sequence used to collect frequency resolved FEIR data. (b) Time-domain three-pulse FEIR measurement showing the FEIR signal count rate as a function of τ_{IR} and τ_{enc}. The F_2 signal component represents interaction with IR2 and Vis pulses, and is visible as a stripe along $\tau_{enc} = 600$ fs. The F_1 component represents interaction with IR1 and Vis pulses, and appears as an anti-diagonal stripe along $\tau_{IR} + \tau_{enc} = 600$ fs. The F_{12} component represents the three-pulse interaction, and having a coupled dependence on both τ_{IR} and τ_{enc}, is visible as an rapidly oscillating signal. (c) The Fourier transform of the time-domain signal, after subtracting off the background, gives the frequency-resolved FEIR spectrum, shown as a function of τ_{enc}. (d) Time-domain FEIR signal at $\tau_{enc} = 600$ fs. (e) The intensity-normalized FEIR spectrum of C6 at $\tau_{enc} = 600$ fs (red), overlaid on the FTIR spectrum (dashed black), scaled by the intensity of the IR pump spectrum (grey shaded area).

Figure 3.3b represents the time-domain signal from Coumarin 6, as a function of both τ_{IR} (x-axis) and τ_{enc} (y-axis). The three components can be visualized separately in the background-subtracted time-domain signal. The F_2 component is a function of τ_{enc} only, and therefore shows up as a horizontal stripe along $\tau_{enc} = 600$ fs. The F_1 component is a function of $\tau_{IR} + \tau_{enc}$, and appears as an anti-diagonal stripe with $\tau_{IR} + \tau_{enc} = 600$ fs. The F_{12} component, being a three-pulse signal, has coupled dependence on both τ_{IR} and τ_{enc}, and shows up as an oscillating component along τ_{IR}. The frequency-resolved FEIR spectrum is obtained by a Fourier-transform along τ_{IR}.[93] For this, at first, the constant values –one-photon fluorescence and non-molecular background ($F_0 + B$) and the two-pulse F_2 signals –are subtracted off. This is followed by extracting the phase information from an IR reference, acquired from the dark arm of the MZI (generally averaged over 20 scans). This is used to determine the timing between the IR pulse pair. This is followed by a Fourier transform of both the fluorescence and the reference IR interferograms after necessary signal processing steps. The frequency domain FEIR spectrum is divided by the complex phase factor from the IR reference, followed by an inverse Fourier transform to the time domain. This is followed by the removal of the part of the interferogram corresponding to negative τ_{IR}, which leaves us with a one-sided positive FEIR interferogram. This is then followed by a Fourier transform, the real part of which gives us the frequency-resolved FEIR spectrum. In this step, the zero-frequency F_1 signal gets filtered out. A full FEIR surface is constituted of these FEIR spectra along a range of encoding delays, as shown in Figure 3.3c.

In principle, the projection of the FEIR spectrum along the τ_{enc} axis should give us the two-pulse FEIR transient shown in Figure 3.2b. Note that both the FEIR and IR reference interferograms are acquired under the same conditions while scanning across τ_{IR}, that is, bin size, range of positions, and scan speed are kept constant to ensure that the τ_{IR} axes are identical. The FEIR spectra we report are averages over the spectra acquired during forward and reverse scans of the τ_{IR} stage.

Shown in Figure 3.3d is the background-subtracted time-domain FEIR signal acquired at a fixed encoding delay of 600fs, which corresponds to the maximum amplitude in its two-pulse transient. The corrresponding frequency-domain FEIR spectrum is shown in Figure 3.3e. We observe a fully absorptive spectrum, with the frequencies and lineshapes of the peaks in agreement with the FTIR spectrum. This serves as proof of the fact that the fluorescence signal is encoded with the information about the vibrational states that were up-converted by the IR+visible double resonance. However, a qualitative comparison between the FEIR and the IR pump-scaled FTIR spectra shows that three of its vibrations at 1515, 1616, and 1712 cm^{-1} are suppressed relative to the vibration at 1586 cm^{-1}. The factors determining the relative intensities are discussed in detail in Chapters 4 and 5.

3.3.3 Pile-up correction to acquired FEIR signal

We employ single-photon counting to detect the FEIR signal, which has a common error associated with it, called the pile-up error. It is an important phenomenon to understand, as it can significantly affect the accuracy with which the photon count rate is determined. The pile-up effect arises due to the inherent limitation in the detection and processing speed of the detector system. When photons arrive very closely in time, the system might not be able to resolve them as separate events. As a result, when the fluorescence intensity is high, there's a higher chance that only the first of the series of photons is detected, while subsequent photons are missed.

The effect of pile-up error and its impact on the measured photon count rate in a typical time-correlated single-photon counting experiment has been illustrated in Ref. [98]. To get a complete picture of its consequences on the acquired FEIR count rates, we direct the reader to Section 4.5.4 of Ref. [93]. Briefly, pile-up error arises due to the contrast in the fluorescence lifetime of the molecule, which is of the order of a few nanoseconds, and the duty cycle of the excitation scheme, which is ~ 1 µs. This contrast indicates that only the first few of the series of fluorescence photons will be detected per duty cycle. Our detector has a dead time of 75 ns, which implies, only one photon is detected per excitation cycle, leading to an increasing error between the original and the measured photon count rate with increasing photons count rates. Considering a Poissonian distribution for the probability of photon detection, it can be shown that given a particular repetition rate, the measured photon count rate is related to the original value according to:

$$F_{meas} = r\left(1 - \exp\left(-\frac{F}{r}\right)\right) \tag{3.3}$$

where, r represents the repetition rate of the laser. As $F \rightarrow \inf$, $F_m eas \rightarrow r$, indicating that, as the original photon count rate increases, the measured photon count rate saturates at the laser repetition rate. To mitigate this error, we apply the pile-up correction to the measured photon count rate:

$$F_{corrected} = -r \ln\left(1 - \frac{F_{meas}}{r}\right) \tag{3.4}$$

In single-molecule level experiments, the measured photon count rates are way below the saturation limit ($\sim$ 200 Hz), and follow a linear relationship with the original photon count rates, making the pile-up correction unnecessary. However, it becomes crucial for high-concentration FEIR measurements like the ones presented in majority of this thesis. Figure 3.4a below illustrates the pile-up correction based on Eq. 3.4. The result of the pile-up correction on the acquired two-pulse FEIR transient of Coumarin 6 is illustrated in Figure 3.4b.

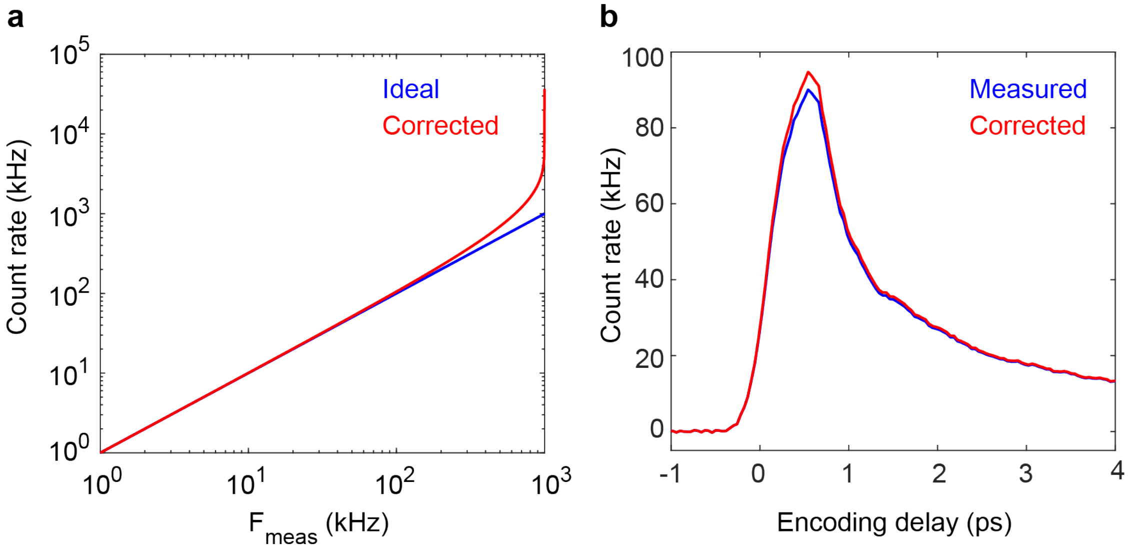

Figure 3.4: Demonstration of pile-up correction. (a) A comparison between the measured and pile-up corrected photon count rates based on Eq. 3.4.(b) Result of pile-up correction on the count rate acquired during a two-pulse FEIR measurement of Coumarin 6, showing a prominent increase in the corrected photon count rate at the maximum.

3.4 Description of FEIR brightness, cross-section, and contrast

From the perspective of single-molecule spectroscopy, it is necessary to understand the fluorescence count rate per molecule per excitation cycle. This leads us to describe FEIR brightness. Before delving into the formal description, let us first take a look at the factors that determine the fluorescence count rate in an FEIR experiment. Experimentally, the fluorescence count rate can be expressed as a number of factors:[90]

$$F = qr\langle N\rangle\eta I_{vis}I_{IR} \tag{3.5}$$

where, q is a proportionality constant, r denotes the repetition rate of the laser, $\langle N \rangle$ represents the average number of molecules in the focal volume, η represents the overall photon detection efficiency, which is in defined as $\eta = \eta_{coll} \times \eta_{det} \times \eta_{bp}$ where, η_{coll} is the collection efficiency of the visible objective, measured as the fraction of power transmitted through it. η_{det} is the quantum efficiency of the detector and η_{bp} is the bandpass fraction of the molecule. The latter is determined by the overlap of the transmission area of the bandpass filter and the fluorescence spectrum of the molecule. Additionally, the fluorescence count rate is directly proportional to the intensities of the IR and visible pulses, I_{IR} and I_{vis} respectively, at the sample position.

The proportionality constant is what we define as the FEIR brightness:

$$q = \frac{F}{r \langle N \rangle \eta I_{vis} I_{IR}}$$

This definition allows describing FEIR brightness as the number of photons obtained per molecule per excitation cycle, additionally normalized with respect to the excitation pulse energy density (expressed as GW cm^{-2}). Furthermore, to express the FEIR brightness in the units of directly measurable quantities, we express the average molecule number $\langle N \rangle$ in terms of concentration (C; mol L^{-1}), thus eventually being expressed in the units of L mol^{-1} GW^{-2} cm^{4}.

$$q = \frac{F}{r C \eta I_{vis} I_{IR}} \tag{3.6}$$

In analogy with the fluorescence brightness, that is defined as the product of the electronic absorption cross-section of the molecule (σ) and its fluorescence quantum yield(ϕ) ($q = \sigma \cdot \phi$), the FEIR brightness is expressed as

$$q = a \cdot \phi \tag{3.7}$$

where, a denotes the FEIR cross-section of the molecule, experimentally determined as the FEIR brightness normalized by the fluorescence quantum yield ($a = \frac{q}{\phi}$).

Similarly, the one-photon brightness is determined according to

$$q_0 = \frac{F_0}{rC\eta I_{vis}} \tag{3.8}$$

We report the FEIR brightness of a molecule as an average over a range of encoding delays beyond the pulse overlap region. Practically, this conforms to a 400 fs range from $400-800$ fs. The contrast in an FEIR experiment, termed as the modulation ratio (M), is determined from the ratio of the FEIR count rate (F) and the one-photon plus background fluorescence ($F_0 + B$) averaged over the same range.

$$M = \frac{F}{F_0 + B} \tag{3.9}$$

While at the high concentration regimes, the background fluorescence signal is dominated by the one-photon fluorescence ($F_0 + B \approx F_0$), making the modulation ratio measurable as F/F_0, the non-molecular background becomes an important contributing factor when approaching nM level concentrations, and eventually becomes the predominant term at the single-molecule level measurements. Since the non-molecular background is independent of the chromophore concentration, the modulation ratio falls off as we approach the nM concentration regime.[90]

3.5 Impact of resonance tuning on FEIR brightness

While setting up an FEIR experiment, probably one of the most important question that might arise is, given that we want to excite a specific vibration in a chromophore, what frequency of the visible encoding pulse should we choose to get the best possible combination of brightness and contrast? If the IR+visible double resonance picture holds true for FEIR excitation, it would imply that it is possible to approach larger and larger values of FEIR brightness upon tuning the visible encoding frequency such that the $\omega_{vis}+\omega_{IR}$ approaches the absorption maximum of the molecule. Simultaneously, it would also result in an increase in the one-photon fluorescence signal (F_0) as ω_{vis} rises along the red absorption edge, thus compromising the modulation ratio. Therefore, determining the dependence of FEIR brightness as a function of the encoding frequency becomes crucial.

3.5.1 Demonstration of resonance tuning with a series of coumarin-based chromophores

During the initial part of this project, we had not yet built the visible OPA, and therefore, were unable to tune the encoding frequency. We used the second harmonic of the fundamental output from the Yb fiber laser (1033 nm) as the visible encoding pulse with a fixed frequency of 516.5 nm. To work around the problem of determining the effect of resonance condition on FEIR brightness, we chose a series of ten structurally similar dyes –all belonging to the coumarin family, the structures of which are shown in Figure 3.5.

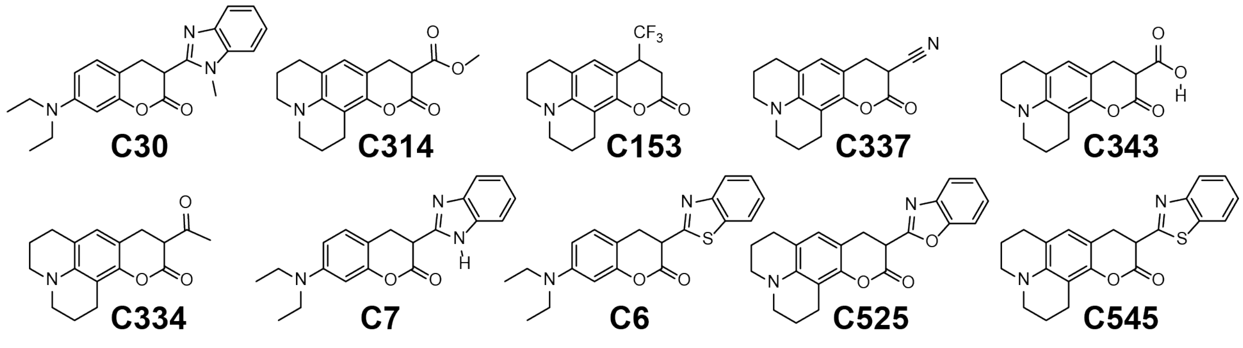

Figure 3.5: Molecular structures of the coumarins studied.

These dyes have their electronic absorption spectra covering a significant range of the visible spectrum, as seen in Figure 3.6, where C30 is the most de-tuned, while C545 is over-tuned, implying that the encoding frequency brings about significant one-photon excitation of the dye.

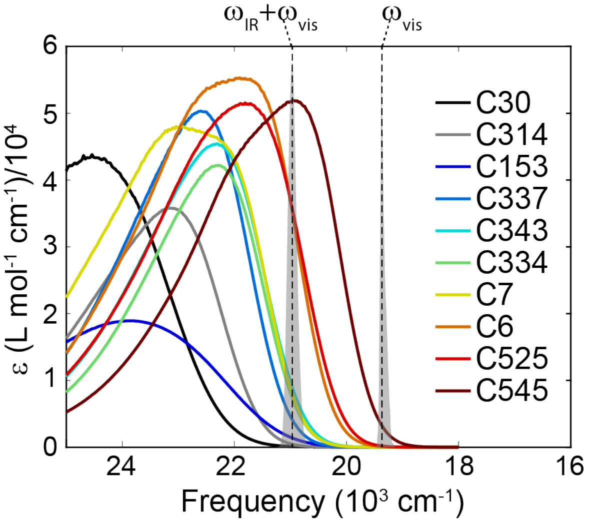

Figure 3.6: UV/Vis spectra of the coumarin series acquired in acetonitrile, demonstrating resonance tuning in FEIR. With reference to the visible and visible + IR frequencies (shown in grey), C30 represents the case of extreme resonance de-tuning while C545 represents resonance over-tuning.(Reproduced with permission from AIP Publishing)

Note that the units for the one-photon cross-section $a_0 = \frac{q_0}{\phi}$ are L mol^{-1} GW^{-1} cm^2 since it is a function of visible pulse energy density only, while the FEIR cross section a has a double-dependence on both the pulse energy densities. To make a head-to-head comparison between these two values, we make use of the FEIR cross-sections not normalized with respect to the IR pulse energy density.

$$a_{IR} = a \cdot I_{IR} \tag{3.10}$$

This effective FEIR cross-section makes sense since the IR pulse energy density is kept effectively constant across the series of measurements.We deduced the one-photon (a_0) and FEIR cross-sections (a_{IR}) from the corresponding F_0 and F count rates at the frequencies ω_{vis} and $\omega_{vis} + \omega_{IR}$ respectively in their two-pulse FEIR transients, and looked at the correlation between the cross-sections and the values of molar extinction coefficients at the corresponding frequencies. The results shown in Figure 3.7 are reproduced from Ref. [90].

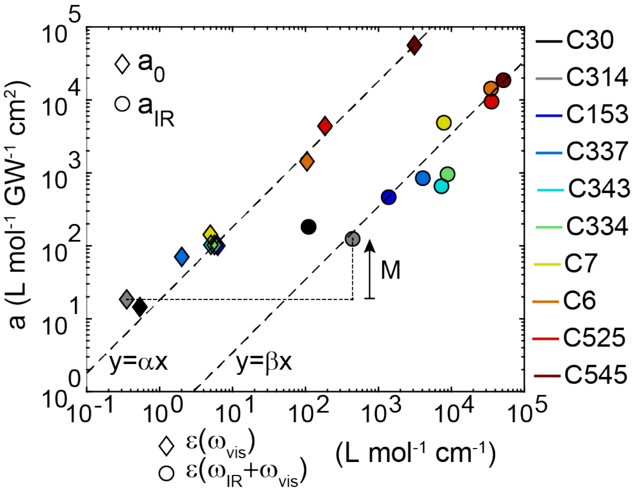

Figure 3.7: Correlation of a_{IR} against $\varepsilon(\omega_{vis} + \omega_{IR})$ (circles) and a_0 against $\varepsilon(\omega_{vis} + \omega_{IR})$ (diamonds). The slopes from linear fits to the correlations, α and β were determined to be 18.7 and 0.367 GW^{-1}cm^3 respectively, giving their ration as $\alpha/\beta = 50.9$. This highlights that the one-photon cross-section grows in with resonance tuning at a $\approx$ 50 times faster rate than the FEIR cross-section. (Reproduced with permission from AIP Publishing)

We observed a linear correlation in both cases. While the linear relationship between $\varepsilon(\omega_{vis})$ and F_0 validates the Beer's law, it is the correlation between $\varepsilon(\omega_{vis} + \omega_{IR})$ and F that is intriguing. A perfect linear correlation would imply that the lineshape function of the encoding transition is simply the equilibrium lineshape function red-shifted by the vibrational frequency.[90] This corroborates the double-resonance picture we invoke to describe the FEIR excitation. However, this is not entirely true because the initial and final states of the encoding transition are different from the electronic transition. Moreover, the equilibrium lineshape function is determined by several vibronic transitions, not only the ones pumped by the IR pulse. Also, there is lineshape broadening by overdamped solvent coordinates. However, since the excitation at $\omega_{vis} + \omega_{IR}$ falls on the red side of the absorption spectra of the coumarins, the lineshape of which is predominantly determined by the solvent coordinates, the aforesaid approximation stands reasonable. A similar correlation between the signal strength and resonance condition for $\omega_{vis} < \omega_{0-0} - \omega_{IR}$ of Coumarin 6 was found in the early experiments carried out by Kaiser and co-workers,[59] where, ω_{0-0} is the frequency of the $|g, 0\rangle \rightarrow |e, 0\rangle$ transition, although the vibrations interrogated were later determined to be combination bands.[61]

The observed scatter in the second correlation can be attributed to changes in multiple factors intrinsic to the molecular electronic structure, such as vibrational transition dipoles, Franck–Condon overlaps, and orientational factors, which we describe in chapters 4 and 5. It's quite surprising, then, that we still see a relatively strong linear trend, considering these components are overlooked. This can be explained from a couple of angles. For one, the 'a' values are constituted of the overall contributions of the response from all the vibrations that are simultaneously pumped, potentially evening out the differences in these ignored factors across dyes and thus shedding light on the electronic resonance's impact on an "average" coumarin. Additionally, the structural congruence among the dyes means drastic changes in these elements are unlikely for the skeletal vibrations, despite $\varepsilon_{el}(\omega_{vis} + \omega_{IR})$ showing a significant variation, nearly threefold.

A fairly strong linear correlation definitely suggests that it is important to be able to tune the visible resonance such that the IR + visible frequency lies as close to ω_{max} as possible without compromising too much on the modulation ratio. Another key point we observed is the difference in the rate at which the one-photon and FEIR cross-sections change with resonance. Comparing the slopes of the two linear fits, we get the relation $\alpha/\beta \approx 50$, indicating that the one-photon cross-section grows with resonance, at a rate 50 times faster than the FEIR cross-section. This implies that it in an attempt to maximize the FEIR cross-section with resonance tuning, the modulation ratio is easily compromised, which becomes extremely important in the single-molecule level experiments where the modulation ratios are much smaller than the corresponding high-concentration values, as briefly discussed in the above paragraphs, and shown in Ref. [90].

3.5.2 Demonstration of continuous tuning of electronic pre-resonance using the visible OPA

Having built the visible OPA, we were now in a position to be able to tune the electronic resonance with a precision of ~ 2 nm. This gave us a fine control knob on balancing FEIR brightness and modulation ratio. To demonstrate this, we chose Rhodamine 6G (R6G), a member of the xanthene family, as the model system. The molecular structure is shown in Figure 3.8a. The generation of tunable narrow-band visible pulses is described in Chapter 2. To demostrate the effect of resonance tuning on the FEIR cross-section of R6G, we measured the FEIR cross-sections of the molecule as a function of resonance tuning, which was done by changing the phase-matching angle of the BBO crystal to tune the encoding pulses in the frequency range of $16920 - 17700$ cm^{-1}, to make the IR+visible frequency rise the absorption edge, approach the absorption maximum, and eventually cross it ($\omega_{vis} = 17700$ cm^{-1}), as demonstrated in Figure 3.8b. For all the measurements, the IR pulse was tuned to 1535 cm^{-1}, which simultaneously excited five ring stretches of the molecule, shown in the FTIR spectrum in Figure 3.8c.

Here, it is pertinent to highlight a key difference in the experimental setup for the coumarins and R6G. The coumarins exhibit large Stokes shifts in general, an example of which (Coumarin 6) is shown in Figure 3.1b. For the FEIR measurements on the coumarins, we used a long-pass dichroic mirror that reflected the excitation beam to the microscope objective, and transmitted the fluorescence on the Stokes side. The fluorescence signal was then passed through a bandpass filter before it reached the SPAD. Additionally, a high OD notch filter centered at 517 nm was used to block any residual scatter of the encoding frequency light. R6G, on the contrary, exhibits a comparatively smaller Stokes shift, as seen from the comparison of the maxima of its electronic absorption (Figure 3.8b) and fluorescence spectra (Figure 3.8d). Using a longpass dichroic mirror result in much of the fluorescence getting rejected. Therefore, we used a 550 nm shortpass dichroic that would transmit the fluorescence photons on the anti-Stokes side, as shown by its transmission curve (red shaded area). Additionally, to ensure maximum blocking of any residual scatter of the visible pump frequency, we passed the fluorescence through a shortpass filter (blue shaded area), which acts as a continuous notch filter for all frequencies lying below 18000 cm^{-1}. Comparing the transmission curves of these two optics, it is apparent that the fluorescence transmitted by the shortpass dichroic is effectively entirely transmitted through the shortpass filter. Therefore the effective bandpass fraction (η_{bp}) is given by the overlap integral of the fluorescence spectrum and the transmission curve of the dichroic, and is calculated to be ≈ 0.17 for R6G.

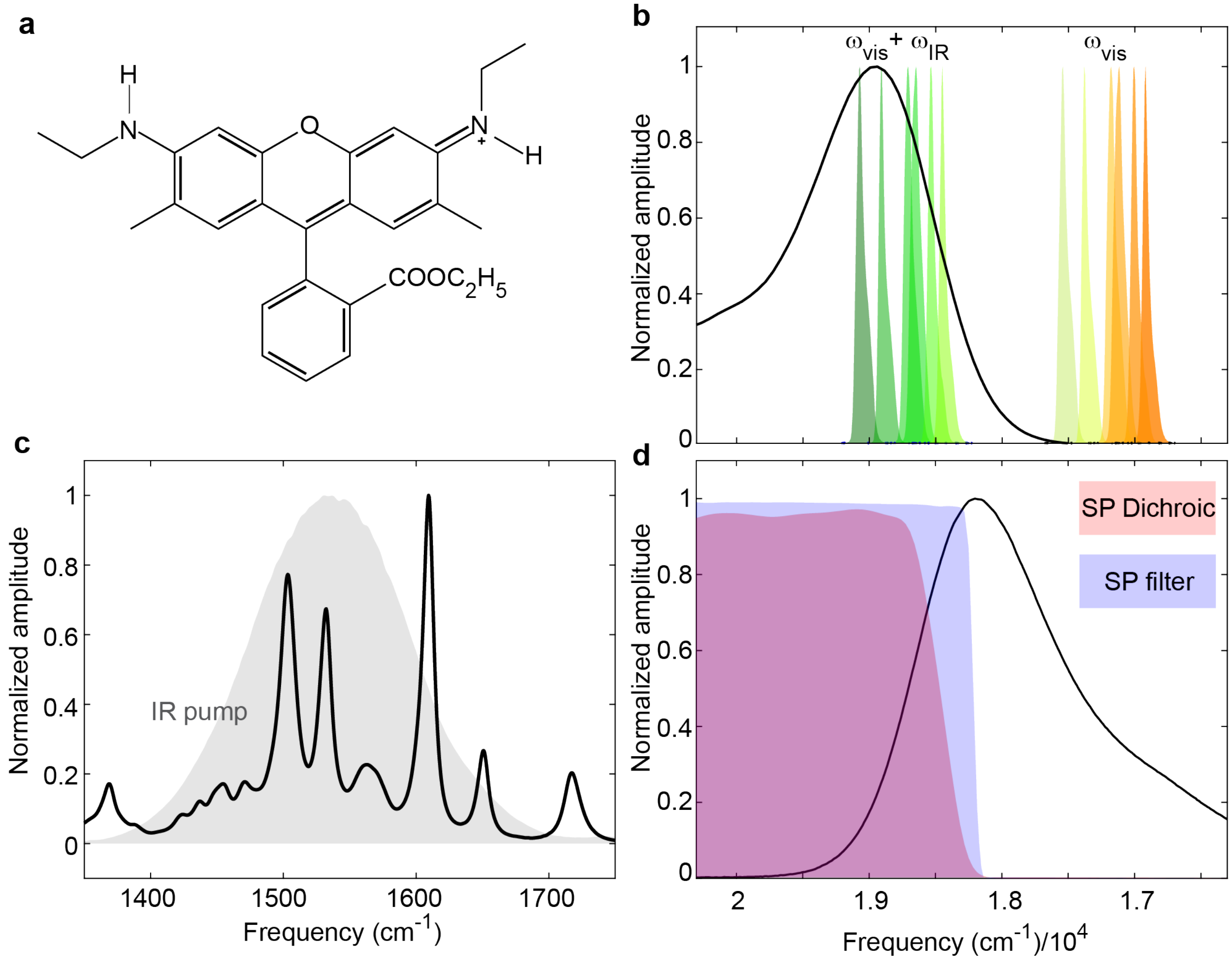

Figure 3.8: Demonstration of resonance tuning with tunable visible pulses using R6G as model system. (a) Molecular structure of R6G. (b) Tunable visible pulses in the range of 16920 – 17700 cm-1 and IR+visible frequencies shown overlaid on the normalized electronic absorption spectrum of R6G, demonstrating a continuous tuning of FEIR resonance until over-tuned. (c) FTIR spectrum of R6G with the IR pump pulse spectrum overlaid, tuned to 1535 cm-1, simultaneously exciting five ring stretches. (d) Normalized fluorescence spectrum of R6G with the transmission curves of the shortpass dichroic (red) and shortpass fluorescence filter (blue) overlaid.

The impact of such continuous tuning of the resonance condition on the FEIR brightness and contrast of R6G is demonstrated in Figure 3.9, which shows the FEIR and one-photon cross-sections, and the modulation ratios as a function of frequency. Intuitively, the one-photon cross-section is observed to rise systematically with blue-tuning the encoding frequency. Keeping the IR pump frequency tuned to 1550 cm^{-1}, the FEIR cross-section is also observed to rise uniformly as $\omega_{vis}+\omega_{IR}$ tunes to higher values, until $\omega_{vis}+\omega_{IR} \leq \omega_{max}$, where ω_{max} represents the frequency corresponding to the maximum of the UV/Vis spectrum of the chromophore. The modulation ratio is observed to drop systematically upon blue-tuning the encoding frequency. Especially, for $\omega_{vis} = 17699$ cm^{-1} (or, 565 nm), the $\omega_{vis} + \omega IR$ goes past the absorption maximum, resulting in the modulation ration being heavily compromised to a value < 1.

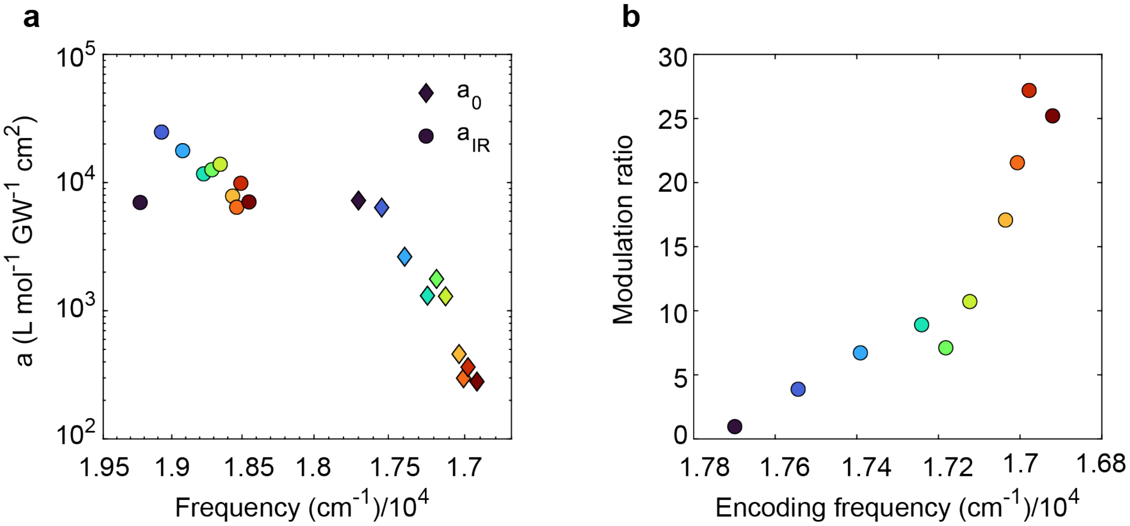

Figure 3.9: One-photon and FEIR cross-section, and modulation ration of R6G as a function of frequency. (a) One-photon (diamonds) and FEIR cross-sections (circles) of R6G plotted against ω_{vis} and $\omega_{vis} + \omega_{IR}$ respectively. The colors going from red to blue represent an increase in the frequency value. (b) The modulation ratios as a function of ω_{vis}.

We obtain a similar linear correlation between the two sets of cross-sections and the molar extinction coefficients at the corresponding frequencies, as we have seen for the coumarin series. The correlations for R6G are shown in Figure 3.10a below. As observed previously for the coumarins, the one-photon cross-section grows in at a much faster rate as compared to the FEIR cross-section, with the ratio of the slopes from linear fits to their correlations $\alpha/\beta \approx 30$.

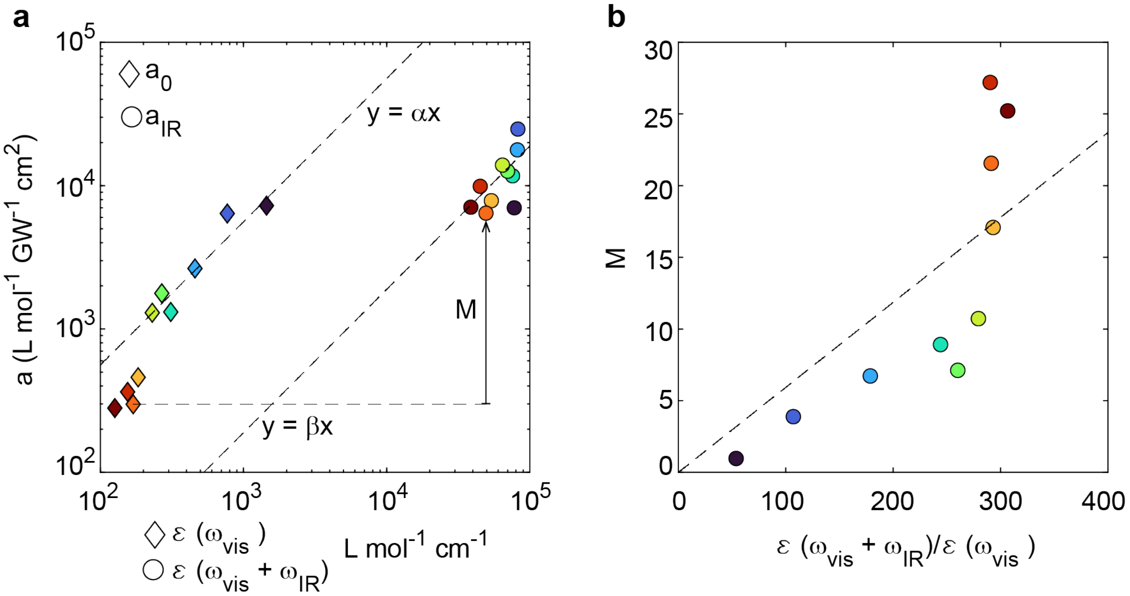

Figure 3.10: Impact of resonance tuning on the one-photon and FEIR cross-section of R6G. (a)Correlation of a_{IR} against $\varepsilon(\omega_{vis} + \omega_{IR})$ (circles) and a_0 against $\varepsilon(\omega_{vis})$ (diamonds). The ratio between the slopes from linear fits to the correlations, α and β was determined to be $\alpha/\beta \approx 30$, indicating the faster growth of one-photon brightness with more optimal tuning than the FEIR brightness, similar to the observation for coumarins. (b) Correlation of the modulation ratio against $\varepsilon(\omega_{vis} + \omega_{IR})/\varepsilon(\omega_{vis})$ showing a linear, yet diffuse relationship, indicated by the relatively poor $R^2 = 0.57$ value, similar to the observation for the coumarins. The colors represent the encoding frequencies (for a_0 and M) and the visible + IR frequencies (for a_{IR}), as shown in Figure 3.9.

The modulation ratios also exhibit a linear correlation with the corresponding ratios of the extinction coefficients $(\varepsilon(\omega_{vis}+\omega_{IR})/\varepsilon(\omega_{vis}))$, as shown in Figure 3.10b. However, the fit is much poor, with $R^2 = 0.57$, and the slope is reported to be 18, which is much smaller than the value of α/β. We had a similar observation for the coumarin measurements as well (not shown here).[99] This diffuse correlation might be a result of the previously mentioned mode-specific vibrational and vibronic factors that are not addressed here.

Chapter 4

Theoretical description of FEIR activity of normal modes

Parts of the material in this chapter are adapted from:

Guha, A; Whaley-Mayda, L; Lee, S.Y.; Tokmakoff, A. "Molecular factors determining brightness in Fluorescence-Encoded Infrared Vibrational Spectroscopy" *J. Chem. Phys.* **2024**, *160*, 104202.

Overview

Electronic transitions are bound by stringent selection rules that determine its overall response to the light-matter interaction. In the context of FEIR spectroscopy, the double-resonance condition involves promoting the system to an excited vibrational state, followed by its up-conversion to a higher-lying electronic state with the aid of vibronic coupling. Whether a normal mode is “FEIR active”, is determined jointly by the magnitude of the vibrational transition dipole and the strength of vibronic coupling, tying the selection rules of FEIR closely with those of IR spectroscopy and resonance Raman spectroscopy. This chapter presents a minimalistic description of FEIR activity of a normal mode within a chromophore, as a function of the different matrix elements that constitute the FEIR response, namely, the magnitudes and relative orientation of the vibrational and the electronic transition dipoles, vibronic couplings, and fluorescence quantum yield. The chapter also describes the computational methodology to calculate them, involving electronic structure calculations based on Density Functional Theory (DFT) and its time-dependent analog (TDDFT). The description of FEIR activity developed in this chapter aids the next chapter where we discuss the roles played these different molecular parameters in modulating FEIR activity.

4.1 Introduction

The overall sensitivity of FEIR spectroscopy is broadly determined by two classes of factors: the instrumental and the molecular factors. The instrumental aspects determine the overall brightness and contrast in an FEIR experiment, and are optimized by the choice of the encoding frequency, as described in Chapter 3. It is crucial to understand, given a specific set of instrumental parameters, what makes a particular vibrational mode on a molecule produce a strong FEIR signal, or, in other words, what molecular properties determine the FEIR selection rules? In the context of applying FEIR spectroscopy to probe chemical dynamics at the single-molecule level, a "good FEIR vibrational probe" is a molecular vibration that is strongly FEIR active, and exhibits high sensitivity towards chemical interactions in solution, manifested through large frequency shifts, or a large change in the oscillator strength.

FEIR brightness can be heuristically described as the joint probability of excitation by double resonance with IR and visible light fields, and subsequent emission of photons during relaxation of the excited electronic state.

$$\texttt{FEIR brightness} = A \cdot \phi$$

where the FEIR activity (A) represents the excitation probability, and the emission probability is phenomenologically described by the fluorescence quantum yield ϕ. This description bears a striking resemblance to the widely acknowledged fluorescence brightness, which is described as

$$\texttt{Fluorescence brightness} = \sigma \cdot \phi$$

where, σ represents the electronic absorption cross-section of the molecule. Despite the manner in which we try to draw an analogy between the FEIR activity and absorption cross-section, the both are set apart from each other by levels of complexity. While absorption cross-section is described in the linear regime of light-matter interaction, therefore having a rather simple picture, FEIR activity has a rather complicated picture owing to the non-linear nature of excitation involved.

The double resonance condition imposed in FEIR spectroscopy requires a minimum of two interactions with each of the IR and visible pulses, thus invoking a mininum of fourth-order of non-linearity in the description,[95]. Assuming a completely ordered light-matter interaction, that is, the visible pulses do not interact prior to the IR pulses, and a single vibrational mode is excited by the IR pulse, first, an excited vibrational state is created. This is followed by the up-conversion of this state to a higher-lying fluorescent electronic state. As described earlier in Chapter 1, we refer to this second transition as the “encoding transition”. Owing to the vibronic nature of this transition, the effective activity of vibration in FEIR spectroscopy is proportional to its IR transition dipole moment scaled by the corresponding vibronic coupling factor. Under the Condon approximation, this is described by the Franck-Condon factor (FCF). The overall strength of the encoding transition is correspondingly also proportional to the electronic transition moment, while the fluorescence quantum yield governs subsequent emission.

Our goal for this chapter is to present a minimalistic description of FEIR activity from the Displaced Harmonic Oscillator (DHO) model, discuss the matrix elements at length, especially the FCF and the orientational factor, and present a detailed description of the computational methodology used to calculate them. For the computations, we have employed electronic structure calculations using density functional theory (DFT). The chapter is broadly organized into two sections. Section 4.2 describes the theoretical construct for FEIR activity under the DHO model, with the constituting subsections containing a detailed mathematical description of the individual matrix elements, primarily the FCF and the orientational factors. We describe the FCF in detail under three levels of approximation with gradual increase in complexity. At level I, the FCFs are approximated as a function of the displacements of the excited state along the ground state normal coordinates. Level II introduces the effect of a change of curvature of the excited state potential, manifested through differences in the normal mode frequencies in the ground and the excited electronic state. At level III, mode mixing is taken into consideration through the incorporation of Duschinsky rotation. Section 4.3 describes the computational methodology we adopt to calculate these values, and appendix 4.A outlines the protocol we follow to perform these calculations.

4.2 Theory

4.2.1 FEIR activity

We consider the efficiency of FEIR fluorescence emission to be the product of probabilities for double-resonance excitation and fluorescence emission. In theory, we can describe these purely from the molecular perspective, neglecting experimental factors such as resonance detuning from the electronic lineshape and detection efficiencies, effects of which are discussed in detail in Ref. [90], and in Chapter 3. For the initial minimalistic description of FEIR activity, we also set aside its modulation by time-dependent vibrational dynamics of population relaxation, multimode vibrational coherences, and effects arising due to interactions with finite light pulses, which we have discussed at length in Refs. [95] and [96]. We will, however, build on this description of FEIR activity, and discuss how such time-dependent phenomena modulate it, later in the text. While the molecule's fluorescence quantum yield accounts for the emission probability, the excitation probability involves several factors owing to the nonlinear nature of the excitation process, which we compute here as a product of matrix elements.

Working in the Born-Oppenheimer approximation, we assume the system is initially in its global ground state $|g, \mathbf{0}\rangle = |g\rangle|\mathbf{0}\rangle$, where $|g\rangle$ is the ground-state electronic wavefunction, and $|\mathbf{0}\rangle$ denotes the vibrational wavefunction with zero quanta of excitation in each vibrational mode. The bold notation denotes a vector. This implies, for a molecule with N vibrations, $|\mathbf{0}\rangle$ is an N-dimensional product state. Resonant IR excitation promotes one of the vibrations (j) to its first excited state $|g, \mathbf{1}_j\rangle = |g\rangle|\mathbf{1}_j\rangle$, where, $|\mathbf{1}_j\rangle$ represents an N-dimensional product state where the j^{th} vibration is in the first excited state while the remaining $N - 1$ vibrations are in the ground vibrational state. The transition probability for this stem is proportional to the square of the vibraitonal transition dipole moment

$\left|\langle \mathbf{0}_j|\mu|\mathbf{1}_j\rangle\right|^2 = \left|\mu_j\right|^2$. In practice, FEIR experiments with broad bandwidth IR pulses can initially create vibrational coherences on the ground state which result in vibrational excitation probabilities that depend linearly on each transition moment, $\mu_i\mu_j$.

The visible encoding pulse subsequently promotes the system to the first excited electronic state with all vibrations in their respective ground states, $|e, \mathbf{0}'\rangle = |e\rangle|\mathbf{0}'\rangle$. A prime ($'$) is used to indicate vibrations on the excited electronic state. We restrict our analysis to transitions arriving in this zero-quantum level of the electronic manifold partly for simplicity, but also because we can always choose resonance conditions such that higher transitions are inaccessible. The encoding transition probability depends on the square of the vibronic transition dipole moment $\left|\langle g, \mathbf{1}_j|\mu|e, \mathbf{0}'\rangle\right|^2$. At this point, we explicitly write down the dipole moment operator as a Taylor series expansion about the equilibrium geometry of the ground or the excited electronic state. We choose the coordinates of the ground electronic state for our analysis.

$$\mu = \mu_0 + \sum_{j=1}^{N}\left(\frac{\partial \mu}{\partial Q_j}\right)_0 Q_j + \frac{1}{2}\sum_{i=1}^{N}\sum_{j=1}^{N}\left(\frac{\partial^2 \mu}{\partial Q_i \partial Q_j}\right)_0 Q_i Q_j + \cdots \tag{4.1}$$

Within the Condon approximation, we can truncate the series to the first term on the right-hand side of the equation, since the electronic transitions are assumed vertical, making the transition dipole moment independent of the motion along the nuclear coordinates. As a result, the vibronic transition dipole moment factors into the electronic transition dipole moment $\mu_{eg} = \langle g|\mu|e\rangle$ and the FCF $\langle \mathbf{1}_j|\mathbf{0}'\rangle$ that is, the vibrational wavefunction overlap integral. For most of the organic chromophores studied in this work exhibit vibronic couplings that can be described under the Franck-Condon approximation. To look at how nuclear motions can modulate vibronic couplings, we have to take the second term in Equation 4.1 into consideration. This is termed as Herzberg-Teller (HT) coupling, and, together with the higher order terms, forms the non-Condon contribution to vibronic coupling. In this chapter, we will particularly describe the system under the Franck-Condon approximation, truncating Eq. 4.1 to its first term and neglecting everything else.

Sticking to the Condon approximation, the overall FEIR excitation probability of the j^{th} vibration is proportional to the product of three molecular factors describing the sequential infrared and visible encoding transitions

$$A^{(j)} = \left|\mu_j\right|^2 \left|\langle \mathbf{1}_j | \mathbf{0}' \rangle\right|^2 \left|\mu_{eg}\right|^2 \tag{4.2}$$

We denote A as the FEIR activity. The activity is independent of experimental factors and can be computed directly at this level of description.

4.2.2 Franck-Condon factors

Most of the organic chromophores are molecules with number of normal modes of the order of 10^2. To get a clear picture of what the FCFs look like, we begin with the vibrational wavefunctions of the N-dimensional product states. For multi-atomic molecule, they are expressed as a product of orthogonal Hermite polynomials,[100]

$$\boldsymbol{\psi}(\mathbf{Q}) = \left(\frac{\det \boldsymbol{\Omega}}{\pi^N}\right)^{1/4} \prod_{j=1}^{N} \left(\frac{1}{2^{v_j} v_j!}\right)^{1/2} \exp{(-\frac{1}{2}\omega_j Q_j^2)} H^{(v_j)}(\omega_j^{1/2} Q_j) = |\psi_1 \psi_2 \cdots \psi_N\rangle \tag{4.3}$$

where, $\boldsymbol{\Omega}$ denotes a diagonal matrix of vibrational frequencies (ω_j) in a given electronic state. v_j represents the vibrational quantum number of the j^{th} normal mode, and $\mathbf{Q}$ represents the normal coordinate. $H^{(v_j)}(\omega_j^{1/2} Q_j)$ represents the Hermite polynomial of v_j^{th} order. The first few Hermite polynomials are given below:

$$\begin{aligned} H_0(x) &= 1 \\ H_1(x) &= 2x \\ H_2(x) &= 4x^2 - 2 \\ H_3(x) &= 8x^3 - 12x \end{aligned} \tag{4.4}$$

The FCFs are therefore large multidimensional integrals of the form,[101]

$$\text{FCF} = \int \boldsymbol{\psi}^*(\mathbf{Q})\boldsymbol{\psi}(\mathbf{Q}')d\mathbf{Q} = \langle \psi_1\psi_2...\psi_N|\psi'_1\psi'_2...\psi'_N\rangle \tag{4.5}$$

where ($'$) denotes the wavefunction in the excited product state, and ($*$) denotes the complex conjugate. The integral is arbitrarily over the normal coordinates of the ground electronic state. To compute the FCFs, we have taken the approach outlined in refs.[102, 103] that utilizes the recursion relations derived by Ruhoff[104] using the formalism of Sharp and Rosenstock,[105], and Lermé[106]. The N normal mode coordinates in the ground and excited electronic states are related according to the linear transformation

$$\mathbf{Q} = \mathbf{J}\mathbf{Q'} + \mathbf{K} \tag{4.6}$$

where $\mathbf{Q}$ and $\mathbf{Q'}$ are N-dimensional vectors containing the normal coordinates in the ground and excited electronic states. $\mathbf{J}$, the Duschinsky matrix, describes mixing between the ground and excited state normal coordinates. It is defined as follows,

$$\mathbf{J} = \mathbf{L}^{-1}\mathbf{L}' \tag{4.7}$$

where, $\mathbf{L}$ is a transformation matrix that relates the normal mode coordinates $\mathbf{Q}$ to the mass-weighted cartesian coordinates $\mathbf{q} = (q_1, q_2, ..., q_{3N})$ as,

$$\mathbf{Q} = \mathbf{L}^{-1}(\mathbf{q} - \mathbf{q}_0) \tag{4.8}$$

Here, the subscript $(_0)$ represents the coordinates of the equilibrium geometry. Thus, $\mathbf{J}$ represents mixing of the ground and the excited electronic states along the normal coordinates, and is non-diagonal in nature. In the event of no mixing, it is an identity matrix of dimensions $N \times N$. $\mathbf{K}$ is a vector of displacements of the electronic excited state potential minimum with respect to the ground state minimum along the normal coordinates. With respect to the normal modes in the ground state, it is defined as

$$\mathbf{K} = \mathbf{L}^{-1}(\mathbf{q}_0' - \mathbf{q}_0) \tag{4.9}$$

$\mathbf{K}$ may be transformed to the dimensionless displacement vector $(\boldsymbol{\delta})$ with respect to the ground state coordinates according to

$$\boldsymbol{\delta} = \mathbf{K}^T \boldsymbol{\Omega}^{1/2} \tag{4.10}$$

While computing these large multidimensional integrals in Eq. 4.5 might seem daunting, the work has been simplified to a great extent by the mathematical treatment of Ruhoff.[104] According to that, the multidimentional $\langle \mathbf{0} | \mathbf{0'} \rangle$ integral is exactly solvable.

$$\langle \mathbf{0} | \mathbf{0'} \rangle = (\det \boldsymbol{\Omega} \det \boldsymbol{\Omega}')^{1/4} \left(\frac{2^N \det \mathbf{J}}{\det \mathbf{X}} \right)^{1/2} \exp \left[-\frac{1}{2} \mathbf{K}^T \boldsymbol{\Omega} \mathbf{K} + \frac{1}{2} \mathbf{Y}^T \mathbf{X}^{-1} \mathbf{Y} \right] \tag{4.11}$$

Using this exactly solvable integral, the Franck-Condon factor between any two vibronic states can be calculated based on the following recursion relation,

$$\begin{aligned}
\langle \mathbf{v}_j | \mathbf{v}'_j \rangle = {} & \left(\frac{1}{2v_j} \right)^{1/2} B_j \langle \mathbf{v} - 1_j | \mathbf{v}' \rangle \\
& + \left(\frac{v_j - 1}{v_j} \right)^{1/2} E_{jj} \langle \mathbf{v} - 2_j | \mathbf{v}' \rangle \\
& + \sum_{k \neq j} \left(\frac{v_k}{v_j} \right)^{1/2} E_{jk} \langle \mathbf{v} - 1_j - 1_k | \mathbf{v}' \rangle \\
& + \sum_{k} \left(\frac{v'_k}{v_j} \right)^{1/2} F_{jk} \langle \mathbf{v} - 1_j | \mathbf{v}' - 1_k \rangle
\end{aligned} \tag{4.12}$$

There are elements from five matrices $\mathbf{X}, \mathbf{Y}, \mathbf{B}$, $\mathbf{E}$ and $\mathbf{F}$ used in the above equation, which we define below:

$$\begin{aligned}
\mathbf{X} &= \mathbf{J}^T \boldsymbol{\Omega} \mathbf{J} + \boldsymbol{\Omega}' \\
\mathbf{Y} &= \mathbf{J}^T \boldsymbol{\Omega} \mathbf{K} \\
\mathbf{B} &= 2\boldsymbol{\delta}(\mathbf{I} - \boldsymbol{\Omega}^{1/2} \mathbf{J} \mathbf{X}^{-1} \mathbf{J}^T \boldsymbol{\Omega}^{1/2}) \\
\mathbf{E} &= 2\boldsymbol{\Omega}^{1/2} \mathbf{J} \mathbf{X}^{-1} \mathbf{J}^T \boldsymbol{\Omega}^{1/2} - \mathbf{I} \\
\mathbf{F} &= 2\boldsymbol{\Omega}^{1/2} \mathbf{J} \mathbf{X}^{-1} \boldsymbol{\Omega}'^{1/2}
\end{aligned} \tag{4.13}$$

From here, we will treat these integrals at three different levels of approximation. At level I, we will treat them as functions of electronic state displacements along normal coordinates. At level II, we will add in the dependence on change in frequency, and finally, in level III, we include effects of mode mixing through the incorporation of a non-identity Duschinsky matrix.

4.2.2.1 Level I: FCF as a function of displacements

Let us begin our analysis of FCFs with the most simplistic, yet significant model for the physical chemists: the displaced harmonic oscillator (DHO). Within the description of this model, the FCFs are considered functions of the displacement of the excited state minimum relative to the ground state mininum, along the normal coordinates of the molecule. The first step we take under this approximation is to set $\mathbf{\Omega} = \mathbf{\Omega'}$, implying the vibrational frequencies are unchanged in $|g\rangle$ and $|e\rangle$. As the next step of approximation, we set $\mathbf{J} = \mathbf{I}$, implying, there is no mode mixing. It is pertinent to mention here that the absence of mode-mixing indicates that each oscillator is decoupled from the other. Therefore, we are able to express the N-dimensional FCF as a product of N one-dimensional integrals,

$$\langle \psi_1 \psi_2 \cdots \psi_N | \psi'_1 \psi'_2 \cdots \psi'_N \rangle = \langle \psi_1 | \psi'_1 \rangle \langle \psi_2 | \psi'_2 \rangle \cdots \langle \psi_N | \psi'_N \rangle \tag{4.14}$$

Setting these parameters in Eq. 4.11, and expressing $\mathbf{K}$ in terms of $\boldsymbol{\delta}$ using Eq. 4.10, we get the following simplified terms:

$$\mathbf{X} = 2\mathbf{\Omega}$$

$$\mathbf{Y} = \mathbf{\Omega}^{1/2}\boldsymbol{\delta}$$

Furthermore, the frequency matrix $\mathbf{\Omega}$ is a diagonal matrix, whose determinant is essentially the product of the diagonal elements. The expression in Eq. 4.11 is simplified to

$$\langle \mathbf{0} | \mathbf{0'} \rangle_I = \prod_{j=1}^{N} \exp\left[-\frac{1}{4}\delta_j^2 \right]$$

The subscript ($_I$) indicates first level of approximation. At this stage, we are in a position to represent the dimensionless displacements (δ_j's) in terms of Huang-Rhys factors (S). For any given normal mode, the Huang-Rhys factor is related to the dimensionless displacement of the excited state minimum with respect to the ground state minimum along the respective normal coordinate according to the following relation

$$S_j = \frac{1}{2}\delta_j^2 \tag{4.15}$$

This brings us to the simplified expression for the $\langle \mathbf{0}|\mathbf{0}'\rangle_I$ overlap integral

$$\langle \mathbf{0}|\mathbf{0}'\rangle_I = \exp\left[-\frac{1}{2}\mathbf{S}\right] \tag{4.16}$$

Next, for the calculation of the Franck-Condon factors for any two vibronic states, we need the simplified expressions for the relevant matrices, $\mathbf{B}$, $\mathbf{E}$, and $\mathbf{F}$

$$\mathbf{B} = \boldsymbol{\delta}$$

$$\mathbf{E} = \mathbf{0}$$

$$\mathbf{F} = \mathbf{I}$$

Substituting these in our master equation 4.12, we get

$$\langle \mathbf{v}_j|\mathbf{v}'_j\rangle = \left(\frac{1}{2v_j}\right)^{1/2}\delta_j\langle \mathbf{v}-1_j|\mathbf{v}'\rangle + \sum_k\left(\frac{v'_k}{v_j}\right)^{1/2}\langle \mathbf{v}-1_j|\mathbf{v}'-1_k\rangle$$

This equation can be further simplified for our purpose, based on the approximation that the encoding transition involves $|g, \mathbf{1}_j\rangle \rightarrow |e, \mathbf{v}'\rangle$, and the resonance condition employed in the FEIR experiment ensures that all vibrations end up in the vibrational ground state $|\mathbf{0}'\rangle$ in the excited electronic state. Under this approximation, the relevant FCF $\langle \mathbf{1}_j|\mathbf{0}'\rangle$ integral is expressed by the first term in the above equation, since the second term does not survive the integral.

$$\langle \mathbf{1}_j|\mathbf{0}'\rangle_I = \left(\frac{1}{\sqrt{2}}\right)\delta_j \exp\left[-\frac{1}{2}\mathbf{S}\right] \tag{4.17}$$

The transition probability within the population pathway is described by the square of the Franck-Condon factor. We note that it is a fairly common practice to denote the squared values as `FCF`. However, for this thesis, we will denote them separately as $\texttt{FCF}^2$, which is therefore expressed as,

$$\texttt{FCF}^2 = |\langle \mathbf{1}_j|\mathbf{0}'\rangle_I|^2 = S_j e^{-\mathbf{S}} \tag{4.18}$$

This expression demonstrates the well-known Poissonian distribution for the $\texttt{FCF}^2$ values.[107] Figure 4.1 illustrates the dependence of $\texttt{FCF}^2$ on S for two vibronic transitions, namely $|g, \mathbf{1}_j\rangle \rightarrow |e, \mathbf{0}'\rangle$, and $|g, \mathbf{1}_j\rangle \rightarrow |e, \mathbf{1}_j\rangle$.

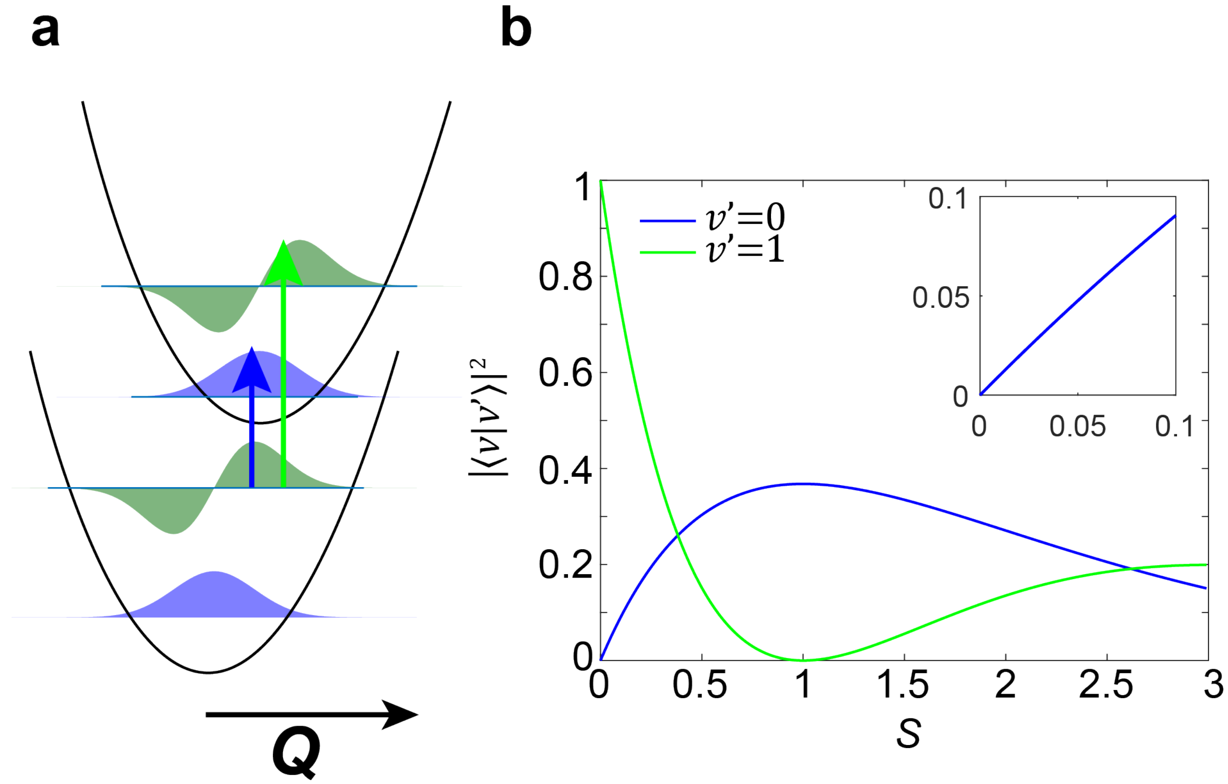

Figure 4.1: Dependence of Franck-Condon overlap integrals on the Huang-Rhys factor.(a) A graphical representation of three vibronic transitions originating from $v = 1$ in the ground electronic state to $v' = 0$ (blue) and $v' = 1$ (green) in the excited electronic state. (b) Plot showing the magnitude of the squares of FCF corresponding to the two transitions shown in (a) as a function of Huang-Rhys factor. In FEIR spectroscopy, the most relevant vibronic transition as per the assumptions made is $v = 1 \rightarrow v' = 0$ (blue) that shows a Poissonian distribution, maximizing at $S = 1$. The trend within $S = 0.1$ is near-linear (Inset).

Of particular interest in the context of FEIR spectroscopy is the $\langle 1|0'\rangle$ integral, that exhibits a Poissonian distribution, maximizing at $S = 1$. For organic molecules like the coumarins used in this work, the S values lie below 0.1 where the square of the FCF shows a near-linear dependence on S (Inset in Figure 4.1b). This makes it possible to represent the squares of FCFs in terms of their corresponding Huang-Rhys factors, $|\langle 1|0'\rangle|^2 \approx S$, thus allowing for a minimalistic description of the Franck-Condon factors solely in terms of the displacements of the excited state potential along the normal mode coordinates.

4.2.2.2 Level II: Incorporating vibrational frequency changes in the excited state

A change of vibrational frequency in the excited electronic state indicates a change in the curvature of its potential, as illustrated in Figure 4.2a. The relationship between frequency and curvature is directly proportional, wherein higher frequencies correspond to elevated curvatures. Predicting the directional shift of a specific vibrational mode's frequency in a molecule upon entering an excited electronic state lacks a universally applicable method. This necessitates the execution of requisite electronic structure calculations, specifically encompassing ground and excited electronic state geometry optimizations, along with corresponding frequency calculations. The determination of such frequency alterations requires a comprehensive computational approach and cannot be reliably inferred without conducting these intricate calculations.

Mathematically, incorporating the vibrational frequency changes manifests as $\boldsymbol{\Omega} \neq \boldsymbol{\Omega'}$. Consequently, the expression for $\langle \mathbf{0}|\mathbf{0'}\rangle$ is no longer as simplified as Eq. 4.16. We will derive the relevant expression by making the necessary substitutions in the master equation 4.11. First, we see what the relevant matrices defined in Eq. 4.13 look like when we set $\mathbf{J} = \mathbf{I}$, but $\boldsymbol{\Omega} \neq \boldsymbol{\Omega'}$.

$$\mathbf{X} = \boldsymbol{\Omega} + \boldsymbol{\Omega'}$$

$$\mathbf{Y} = \boldsymbol{\Omega}^{1/2}\boldsymbol{\delta}$$

$$\mathbf{B} = 2\boldsymbol{\delta}(\mathbf{I} - \boldsymbol{\Omega}^{1/2}\mathbf{X}^{-1}\boldsymbol{\Omega}^{1/2})$$

$$\mathbf{E} = 2\boldsymbol{\Omega}^{1/2}\mathbf{X}^{-1}\boldsymbol{\Omega}^{1/2} - \mathbf{I}$$

$$\mathbf{F} = 2\boldsymbol{\Omega}^{1/2}\mathbf{X}^{-1}\boldsymbol{\Omega'}^{1/2}$$

Since there is no mode mixing, Eq. 4.14 still holds. Substituting the expressions for $\mathbf{X}$ and $\mathbf{Y}$ in Eq. 4.11, we get

$$\langle \mathbf{0} | \mathbf{0'} \rangle_{II} = \prod_{j=1}^{N} (\zeta_{j,j'} \eta_{j,j'})^{1/4} \exp \left[-\frac{1}{2} S_j \eta_{j,j'} \right] \tag{4.19}$$

The subscript (II) indicates that this expression is valid under level II of approximation. The two new matrix elements introduced in the expression, $\zeta_{j,j'}$ and $\eta_{j,j'}$ are defined as,

$$\zeta_{j,j'} = \frac{2\omega_j}{\omega_j + \omega_{j'}} \qquad \eta_{j,j'} = \frac{2\omega_{j'}}{\omega_j + \omega_{j'}}$$

The impact of the change of curvature on the overall magnitude of overlap integral between the respective ground vibrational states of the two electronic states, as a function of the displacement of the excited state potential along the normal coordinate, is illustrated in Figure 4.2b. Intuitively, when the frequency change is negative with respect to the ground electronic state, the width of the Gaussian distribution is greater than for $\langle \mathbf{0} | \mathbf{0'} \rangle_I$, increasing as the frequency difference grows larger. On the other side, the distribution becomes narrower as the curvature of the excited state potential gets higher with more positive frequency differences. The magnitude of maximum overlap, unlike $\langle \mathbf{0} | \mathbf{0'} \rangle_I$, is now frequency-dependent, explicitly scaling with $\eta_{j,j'}$. This implies, the higher the frequency in the excited state, the larger will be the maximum overlap. The alteration in spread is further elucidated by examining the dependence of $|\langle \mathbf{0} | \mathbf{0'} \rangle_{II}|^2$ on the corresponding Huang-Rhys factor (S) in Figure 4.2c. From a qualitative perspective, the decay of overlap magnitude as a function of the Huang-Rhys factor becomes steeper when transitioning from negative to positive frequency differences ($\omega' - \omega$).

The FCF expression relevant for FEIR, that is, $\langle \mathbf{1}_j | \mathbf{0}' \rangle$ will then be expressed as

$$\langle \mathbf{1}_j | \mathbf{0}' \rangle_{II} = \left(\frac{1}{\sqrt{2}} \right) \delta_j \eta_{j,j'} \langle \mathbf{0} | \mathbf{0}' \rangle_{II} \tag{4.20}$$

Comparing this to $\langle \mathbf{1}_j | \mathbf{0}' \rangle_I$ from Eq. 4.17, the impact of frequency changes become apparent through the incorporation of the elements of the η and ζ matrices. The consequence is that, the distribution of the FCFs as a function of displacements become narrower with increasing magnitude of $\omega' - \omega$, as shown in Fig. 4.2d. This can also be visualized from the Poissonian distribution of the squares of the FCFs as a function of the corresponding Huang-Rhys factors, as shown in panel e, where the distribution gets narrower as the curvature of the excited state potential increases. Furthermore, a similar effect on the maximum amplitude as the $\langle \mathbf{0} | \mathbf{0}' \rangle_{II}$ is seen here.

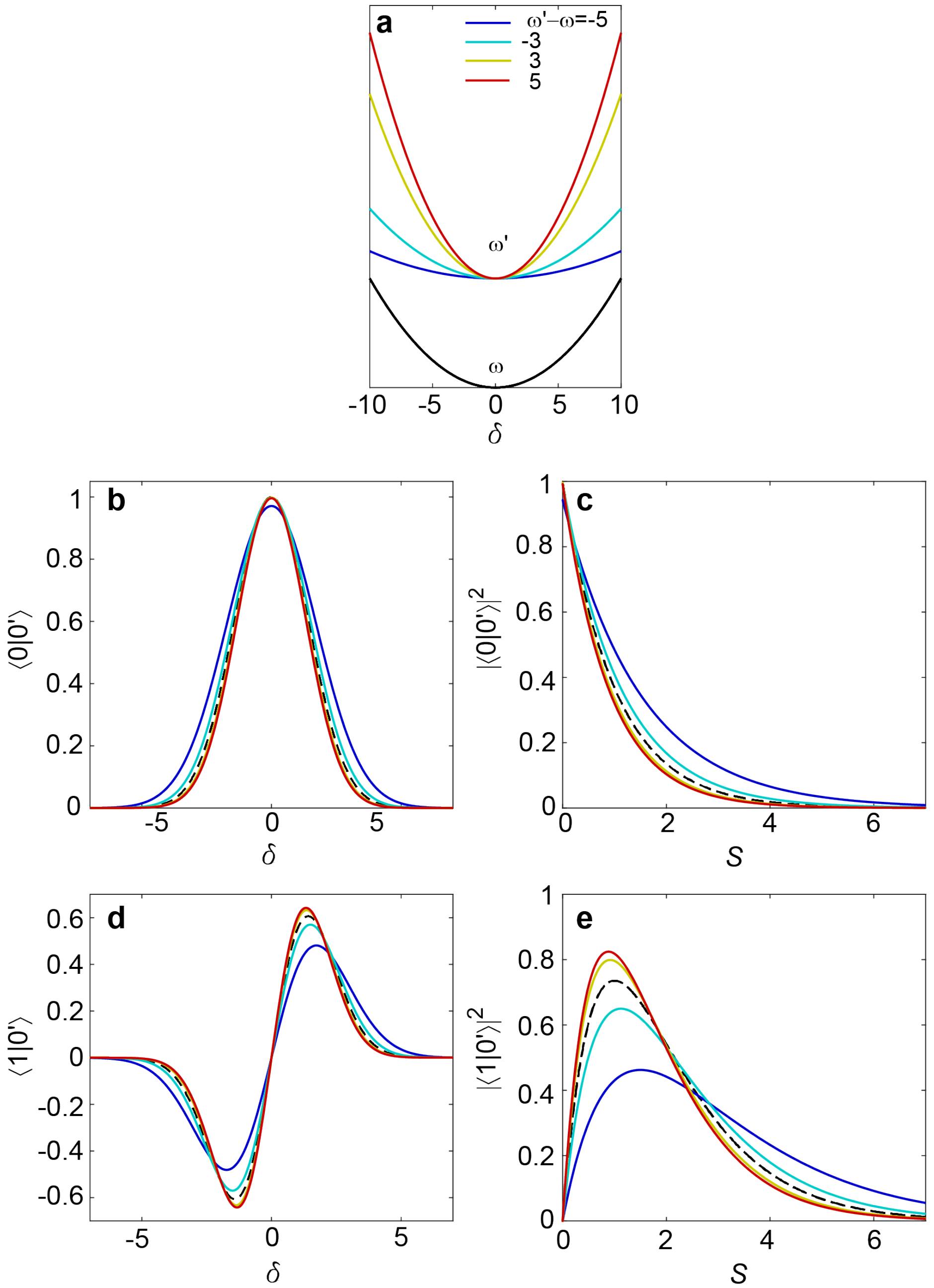

Figure 4.2: Modulation of vibronic coupling by vibrational frequency change in the excited electronic state. Vibrational frequency change manifests itself through (a) a change in the curvature of the excited state potential. (b),(d) Effect on distribution of $\langle 0|0'\rangle$ and $\langle 1|0'\rangle$ as a function of δ, relative to $\Delta\omega = 0$ (dashed black). (c),(e) Effect on the squares of the integrals as a function of Huang-Rhys factor.

4.2.2.3 Level III: Incorporating mode mixing

The dissimilarity in force constants between the ground and the excited electronic states results in distinct normal coordinates ($\mathbf{Q}$ and $\mathbf{Q}'$, respectively). Consequently, transitions between the electronic states can induce a rotation or mixing of normal modes from one electronic state into the basis of another, a concept initially explored by Duschinsky[108] when extending the Franck-Condon principle from diatomic to polyatomic molecules. This complicates the assessment of multidimensional Franck-Condon problems, preventing the reduction of these large multidimensional integrals to simple products of one-dimensional integrals, as applicable for the previous two levels of approximation (Eq. 4.14). Duschinsky suggested that a linear transformation, known as the Duschinsky transformation, involving a matrix and a displacement vector, relates the two sets of normal coordinates, as shown previously in Eq. 4.6. Here, the $\mathbf{J}$ matrix, also known as the Duschinsky matrix represents an overlap matrix between the normal modes of the two electronic states. The degree of similarity in form and energy of the normal modes is reflected in the squares of the diagonal elements, with large off-diagonal elements indicating a change in energy ordering or mixing between different normal modes, mathematically expressed as a Duschinsky rotation (Eq. 4.7). It is important to note that while the Duschinsky transformation is not universally applicable, as the relationship between the normal coordinates of different electronic states in a polyatomic molecule is generally neither linear nor orthogonal, the widely accepted linear/orthogonal transformation proposed by Duschinsky persists.

The qualitative effect of Duschinsky rotation on the magnitude of Franck-Condon factors has been illustrated by Whaley-Mayda in Ref. [93]. Briefly, it can be shown that mode mixing may result in "borrowing" of vibronic coupling from a more FC active to a relatively less active mode based on the relative rotation of the vibrational wavefunctions between the ground and excited electronic states. The relevant integrals are expressed using equations 4.11 and 4.12. Since $\mathbf{J} \neq \mathbf{I}$, and given its non-diagonal nature, the integrals can no longer be factorized into a product of one-dimensional integrals, making the treatment much more complicated than in approximations I and II. A relatively large rotation is required to bring about a significant difference between the FCF values from approximations II and III. To understand the difference between these three levels of approximation, we performed the FCF calculations for all the normal modes of a series of ten members from the coumarin family, structures of which are shown in Figure 3.5. We observed that the mode mixing is not sufficiently significant, resulting in a difference of $< 1\%$ from the approximation II values, and $< 2\%$ from the approximation I values. This is illustrated in Figure 4.3 shows the relative differences in FCF values obtained from the three levels of approximation. The details of how these calculations were performed are shared in the next section. Of practical interest are the high-frequency modes lying in the fingerprint region, where the differences are negligible, justifying that the Huang-Rhys factors by themselves are sufficient to describe the vibronic coupling for the vibrational modes of such organic polyatomics. This enables a fairly accurate description of the system using the widely popular displaced harmonic oscillator model (DHO). However, for its complete nature, we retain the values obtained from approximation III in the calculations of FEIR activities.

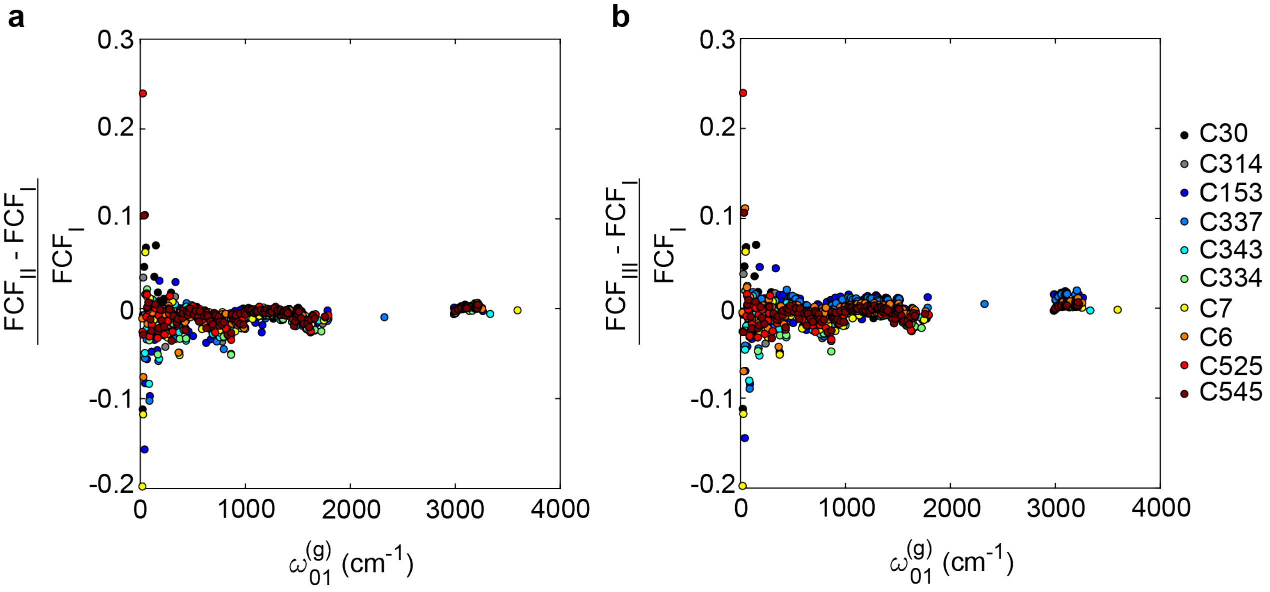

Figure 4.3: Difference in FCF magnitudes associated with computation at levels II (a) and III (b) relative to level I of approximation

4.2.3 Incorporating relative orientation of transition dipoles

The orientation of the vibrational and electronic transition dipole moments, described by the unit vectors $\hat{\mu}_j$ and $\hat{\mu}_{eg}$, respectively, also contribute to the overall transition probability through how they are projected onto the pulse polarization vectors in the laboratory frame and orientationally averaged.[95] Defining the polarization directions of the infrared and visible light fields through the unit vectors ε_{IR} and ε_{vis}, the orientational weighting of the excitation probability for a single vibrational mode can be expressed as $Y_{pol}^{(j)} = \langle [\hat{\mu}_j \cdot \varepsilon_{IR}]^2 [\hat{\mu}_{eg} \cdot \varepsilon_{vis}]^2 \rangle$, where the subscript $pol = \|, \perp$ indicates if the IR and visible fields are set parallel or perpendicular to each other, respectively, or in general denotes their relative angle. $Y_{pol}^{(j)}$ depends on the angle between the transition dipole moments,

$\cos\theta_j = [\hat{\mu}_j \cdot \hat{\mu}_{vis}]$, according to the following relations:[95,109]

$$\begin{aligned} Y_{\parallel} &= \frac{1}{15}(2\cos^2\theta + 1) \\ Y_{\perp} &= \frac{1}{15}(2 - \cos^2\theta) \end{aligned} \tag{4.21}$$

Taken together, we define the polarization dependent FEIR activity of the j^{th} vibration as the product of the previously described matrix elements and orientational factor describing the sequential infrared and visible encoding transitions,

$$A_j^{pol} = A_j \cdot Y_{pol}^{(j)} \tag{4.22}$$

In the context of the full response function theory in Ref. [95], this quantity represents the amplitude of the vibration's population pathways in the response function. The FEIR activity defined in this way depends on the choice of pulse polarization but is otherwise independent of all other experimental factors and can be assessed computationally from quantum chemical calculations. For simplicity, we will suppress the superscript ^{pol}, which unless otherwise noted will be taken to be parallel polarization and refer to the FEIR activity as A_j. The orientational factor $Y_{pol}^{(j)}$ at most modulates the activity by a factor of 3, and is therefore a minor contribution, although we note that all else being equal, parallel transition dipoles ($\theta_j = 0°$ or $180°$) will produce the largest FEIR activities upon optimizing the experimental polarization geometry.

4.3 Computational methodology

4.3.1 Electronic structure

This chapter focuses on the calculations performed on the structures of the ten members of the coumarin family (abbreviated C30, C314, etc.) shown in Figure 3.5. This set of chromophores was used in the experimental FEIR brightness and cross-section analysis presented in Ref. [90]. The spectroscopic constants and FEIR activities of the molecular vibrations were obtained from electronic structure calculations of the ground and first singlet excited state of the molecule using DFT and time-dependent DFT (TD-DFT), respectively.

Gaussian 09 CCP Revision B.01 was used to optimize the geometry in the electronic ground state and first singlet excited state and perform the corresponding frequency calculations. Calculations for all molecules were performed using the Becke, 3-parameter, Lee–Yang–Parr (B3LYP) hybrid functional[110,111] with 6-31G(d,p) double-zeta basis set with the default convergence criterion (i.e., RMS force threshold set to 3×10^{-4}) for geometry optimization. For all the structures, the polarizable continuum model (PCM) was used to account for the effect of acetonitrile as the solvent. Frequency calculations were performed at both optimized geometries using the same level of theory to determine the transition energies and transition dipole moments for the normal modes. The vibrational transition dipole moments were computed from the derivatives of the molecular dipole moment along the respective normal mode coordinates. The electronic transition dipole moments were computed from single-point energy calculations of the first excited state by using TD-DFT on the geometry-optimized ground state. The relative angles between the vibrational and electronic transition dipole moments obtained from the vectors in the cartesian space were used to calculate the orientational factors $Y_{\|}$ and $Y_{\perp}$ according to the Eq. 4.21.

Existing benchmark studies show that B3LYP demonstrates high levels of accuracy (or minimum % error) for TD-DFT calculations.[112] This encouraged us to use B3LYP uniformly for the excited state calculations for all coumarins. To test this, we repeated the calculations for C6 with a long-range corrected functional, ω`B97X-D`[113] and Def2-TZVP basis set, and found that the correlation of the computed IR intensities with the measured molar extinction coefficients for the normal modes worsened (See Appendix 5.A.3).

4.3.2 Franck-Condon Factors calculation

We used the FCClasses code (version 2.1) developed by Santoro and co-workers to compute the multidimensional FCFs from the DFT-optimized geometries of the ground and excited electronic states. Specifically, we used FCClasses to obtain the dimensionless displacement vectors and Duschinsky matrices and used these to compute FCFs using the expressions for $\langle \mathbf{1}_j | \mathbf{0}' \rangle$ and $\langle \mathbf{0} | \mathbf{0}' \rangle$ shown above, using home-written MATLAB scripts.

The dimensionality of the FCFs is dictated by the total number of normal modes of the molecule. Even at the simplest level of approximation (level I) where the FCFs can be written as a product of individual one-dimensional FCFs, the multidimensionality implements itself through the 0-0 overlap integral term. The low-frequency modes, typically below 100 cm^{-1} primarily contribute towards the broadening of the electronic lineshape.[114] The 0-0 overlap integrals are strongly affected by large displacements, if any, along the coordinates of these low-frequency modes. The influence of dimensionality on these integral values has been depicted in Figure 4.4 below, where the magnitudes of the 0-0 overlap integrals of all ten coumarins are shown as a function of the number of normal modes included in their calculation, starting with the highest frequency normal mode, gradually increasing the dimensions as we include the lower frequencies. Especially for C30, there are huge displacements of the excited state minimum along the coordinates of the low-frequency modes.

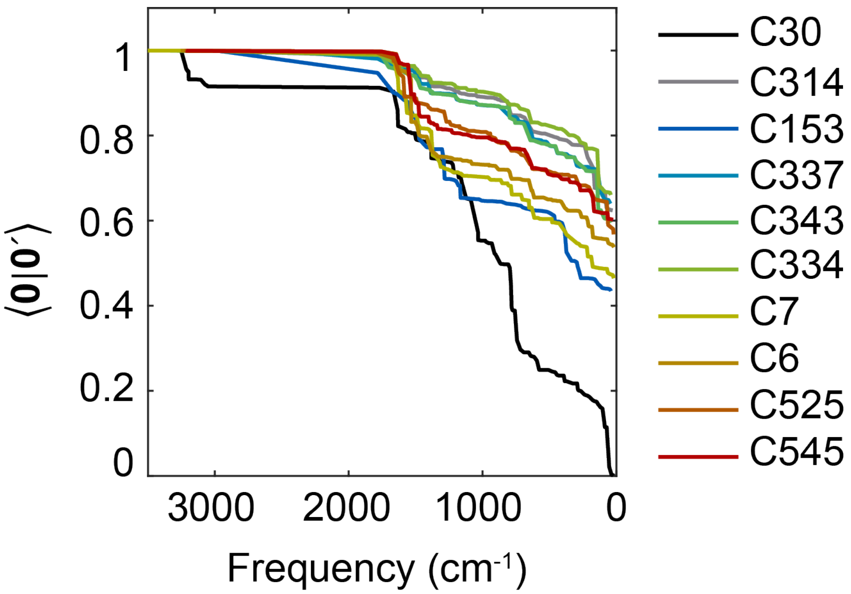

Figure 4.4: Magnitude of 0-0 overlap integrals as a function of dimension. Barring C30 (dark blue), the high-frequency normal modes have a negligible effect on the integral while the displacements along the low-frequency vibrations are large enough to bring down the value. The integrals used in the calculations are computed by reducing the dimension to the number of modes within the IR pulse envelope

To exclude the effect of displacements along the normal coordinates of these low-lying modes in our calculations, we have reduced the dimension of the involved matrices to the number of normal modes within the spectral window of our IR pump pulse. For instance, the FCFs of coumarin 6 are 123-dimensional integrals that are computed using a Duschinsky matrix of dimension 123×123, and a 123-dimensional displacement vector. There are 7 normal modes within the IR pump spectral window ($1450 - 1750$ cm^{-1}). Therefore, neglecting the effect of all other normal modes, the FCFs are calculated as 7-dimensional integrals from a truncated 7×7 Duschinsky matrix and a 7-dimensional displacement vector.

4.3.3 FEIR activity spectrum

We define a molecule's theoretical FEIR activity spectrum

$$A(\omega_{IR}, \omega_{vis}) = \sum_{j=1}^{N} |\mu_{eg}|^2 \; |\mu_j|^2 \; |\langle \mathbf{1}_j | \mathbf{0}' \rangle|^2 \; Y_{pol}^{(j)} \; \delta(\omega_{IR} - \omega_j)\delta(\omega_{eg} - \omega_{vis} - \omega_{IR}) \tag{4.23}$$

as a stick spectrum where each of the N modes has intensity given by its FEIR activity A_j. The integrated FEIR cross-section a reflects the response of all the vibrations excited within the bandwidth of the IR pulse spectrum, and in principle, the fractional contribution a_j for each vibration may be calculated from its relative peak area in the FEIR spectrum measured at the same encoding delay. Our approach is to connect these mode-specific cross-sections a_j to the theoretical activities A_j.

However, this procedure is complicated by the influence of the finite spectra and durations of the excitation pulses as well as vibrational dynamics, most notably multimode coherences, which in many cases produce phase-modulated lineshapes of variable positive or negative sign. Even with measurements taken by the same instrument and experimental conditions, quantitative comparisons of broadband FEIR spectra with DFT calculations for different molecules requires efforts to account for these phenomena. As a first step, we account for the finite IR spectral bandwidth by making the substitution $|\mu_j|^2 \rightarrow |\mu_j|^2 I_{IR}(\omega_j)$ in Eq. 4.23, where $I_{IR}(\omega_j)$ is the normalized IR spectral intensity at the vibrational frequency. As discussed in Ref. [96], this procedure correctly treats the effects of finite pulses on the population response outside the pulse overlap region.

4.3.4 Computational unit of FEIR activity

The computational unit of the FEIR activity A_j is derived from the units of the vibrational and electronic transition dipole moments. In Gaussian, the vibrational transition dipole derivatives with respect to the normal coordinates, μ_j are computed in the unit of $\sqrt{km\ mol^{-1}}$ and the electronic transition dipole moments, μ_{eg} are reported in Bohr-electron or, ea_0, where, a_0 represents the Bohr radius. These units are related to the conventional units of decadic molar extinction coefficients through linear conversion factors. We report the computed FEIR activities in the units of $km\ mol^{-1}\ e^2a_0^2$.

4.3.5 Finite-pulse response function simulations

Finite-pulse response function simulations of FEIR spectra were carried out as described in Ref. [96]. Homogenous-limit expressions for the response function were used with the transition moments and dipole angles taken from the electronic structure calculations. The vibrations were taken to be lifetime- broadened, and the rates derived from the Lorentzian linewidths of the experimental FTIR spectra. For calculations on coumarins, the vibrational coherence dephasing between all pairs of modes were taken as 400 fs, and the electronic and vibronic dephasing times were set to 10 fs. The IR and visible pulses were simulated to have a Gaussian profile, chosen to match the experimental pulse characteristics. The simulated IR pulse had a center frequency $\omega_{IR} = 1620$ cm^{-1}, FWHM $\Delta(\omega_{IR}) = 140$ cm^{-1}, and second order dispersion coefficient of -7800 fs^2 to produce a chirped duration of 230 fs. The visible pulse was taken to be transform-limited with $\omega_{vis} = 19360$ cm^{-1} and $\Delta\omega_{vis} = 46.7$ cm^{-1}, producing a duration of 315 fs.

4.A Appendix: Protocol for performing the required computations

The primary calculations involved in computing the FEIR activities are the geometry optimization and corresponding frequency calculations of the ground and excited electronic states using the density functional theory (DFT). These results are further used to calculate the FCFs and Y values. Additionally, the electronic transition dipole moments are calculated by performing a single-point energy calculation on the optimized geometry of the ground electronic state by employing time dependendent density functional theory (TD-DFT). For all calculations presented in this work, we have used Gaussian 09 computational chemistry package (CCP) Revision B.01,[115] and tried to maintain consistency in the steps we took for the computational tasks, which we enumerate in the list below:

1. **Geometry optimization using classical force fields**

   First, we use Avogadro[116] to optimize the geometry of the molecule in its ground state using the Merck molecular force field (MMF94) as a preliminary step towards the quantum chemical calculations. The primary reason for using Avogadro is that it is open-source, has an attractive and easy-to-use interface for performing cross-platform computational calculations. It is conveniently extensible via a plugin architecture, and has several in-built functionalities that prove fairly useful for chemists. It allows geometry optimization using in-built classical force fields, followed by an export of the geometry coordinates of the optimized structure in the format of input files for several computational chemistry packages (CCP) such as GAMESS and GAUSSIAN. We use this feature to create the input geometry files for the subsequent GAUSSIAN calculations.

2. **Optimization of resultant geometry at the Hartree Fock level**

   Passing on the classical force-field optimized geometry to a DFT calculation incurs fairly large computational costs. To address this challenge, we perform an initial optimization at the Hartree Fock (HF) level of theory, which is computationally cheaper, and provides a more efficient route for subsequent geometry optimization at the DFT level. The input file for the HF level, directly exported from Avogadro, looks as follows:

```
%nprocshared=8
%chk=hf_c525_acn_s0_opt.chk
# opt uhf/6-31g(d,p) scrf=(solvent=<solvent name>)

<Input File Name>

<Charge> <Spin multiplicity>
Atom1          X1          Y1          Z1
Atom2          X2          Y2          Z2
Atom3          X3          Y3          Z3
.              .           .           .
.              .           .           .
.              .           .           .
AtomN          XN          YN          ZN
<Empty line>
```

   Here, "`%nprocshared`" indicates the number of shared processors used for the calculation, and "`%chk`" denotes the name of the checkpoint file. The third line is the main command line of the program, which is written as follows:

First, we specify the type of calculation. In case of a geometry optimization, as in the above example, the command is "opt". The geometry is adjusted until a stationary point on the potential surface is found. This is followed by the level of theory to be used, written as "functional/basis set". In the above example, `"uhf"` represents an unrestricted-spin Hartree Fock functional, and a 6-31G(d,p) basis set. The last part is to include the solvent effect by invoking the polarization continuum model or PCM. The rest of the syntax of the input file is straightforward and self-explanatory.

3. **Optimization of resultant geometry at DFT level**

The key decision-making step for initiating the DFT level calculations is the choice of the exchange-correlation energy functional (or, simply, functional) and basis set. While several functionals at various levels of theory are now available, some are widely popular in the computational chemistry realm, for example, B3LYP.[110,111]. Despite its drawback of severe inherent errors due to lack of London dispersion, giving rise to errors of 5 - >10 kcal mol^{-1} relative to the experimental energies,[117], relatively shorter computational times for B3LYP compared to more accurate hybrid, double hybrid, and coupled cluster functionals, makes it a popular choice for predictive applications like ours, where robustness and reliability gains emphasis over minimizing energy accuracy. Furthermore, existing benchmark studies show that B3LYP demonstrates high levels of accuracy (or minimum % error) for TD-DFT calculations, which are invoked for computations carried out on the excited states (See point no. 5).[112]

The input file for the DFT-level calculation is derived from the output file of the previous HF level calculation. To set up this calculation, the command line is altered with the desired DFT-level functional and basis set. The relevant geometry coordinates are found under the *last* "Standard Orientation" output.

4. **Frequency calculation on ground state optimized geometry**

   A vibrational frequency calculation in Gaussian is initiated by the "freq" keyword. It computes force constants and the resulting vibrational frequencies, along with IR intensities that are reported in km mol^{-1}. The force constants are typically determined analytically whenever feasible. For methods that provide only first derivatives, they are calculated through single numerical differentiation. For methods offering only energy values, double numerical differentiation is employed. Vibrational frequencies are calculated through the derivation of second derivatives of energy concerning the Cartesian nuclear coordinates, followed by a transformation into mass-weighted coordinates. The most important point to note here is that this transformation is only valid at a *stationary point*. Therefore, computing frequencies at any geometry other than a stationary point would be futile. Therefore, the input file for the frequency calculation is derived from the output file resulting from the geometry optimization mentioned in point 3. The atomic cartesian coordinates are obtained from the last "Standard Orientation" output. Note that to carry out a meaningful frequency calculation, the same functional and basis set as that employed for geometry optimization must be used. Additionally, the FCClasses program, that is subsequently used to perform the FCF calculations requires the cartesian coordinates to be calculated with high precision. To employ this, we must write `freq= hpmodes`. Furthermore, the calculation of the Y values require the individual x,y, and z components of the vibrational transition dipole moments for all normal modes. Gaussian can be prompted to print these in the frequency output file by using the option `iop(7/33=1)`. The command line then looks like:

```
# freq=(hpmodes, savenm) <functional>/<basis set>
  solvent=(scrf=<solventname>) iop(7/33=1)
```

Note that this is a single command line.

5. **Excited state optimization using TD-DFT**

   We have routinely carried out geometry optimizations for the first singlet excited state, on the optimized geometry of the ground state. This requires employing TD-DFT, which is done by introducing the keyword `"td"`, along with mentioning the DFT functional and basis set. The command line looks like

   ```
   # opt td=(root=1) <functional>/<basis set> scrf=(solvent=<solventname>)
   ```

   Here, the `"root"` keyword is used to specify the excited state on which the calculation is desired. Specifying `"root=1"` indicates a calculation on the first singlet excited state. Note that if no value is mentioned, by default, the geometry optimization is carried out on the first singlet excited state.

6. **Frequency calculation on excited state optimized geometry**

   The frequency calculation for the excited state is done in the same manner as desceibed in point no. 4, with the coordinates of the optimized geometry obtained from the calculation in point no. 5, using the same functional and basis set, and the `"td"` keyword.

7. **Calculation of electronic transition dipoles at both geometries**

   Calculating the electronic transition dipole moment is fairly much more straightforward than the previous calculations. Once we have the optimized geometries of the ground and excited states from the calculations described in point nos. 3 and 5 respectively, we carry out single-point energy calculations of the first singlet excited state on these optimized geometries. This does not require any additional keyword, except `"td"`.

```
# td <functional>/<basis set> scrf=(solvent=<solventname>)
```

8. **Calculation of FCFs**

   By now, we have all the results for creating the input file for FCF calculations. The FCClasses 2.1 package makes it simple to directly use the outputs from Gaussian calculations, that is, the number of atoms, number of normal modes, the atomic coordinates corresponding to the optimized geometry, and the coordinates with respect to each normal mode, for both the ground and excited states, to create the respective interim input files. These is then passed on to a short Fortran code to generate the FCClasses input files for the two states. A third input file is required, which has two lines of input. The first line contains the x,y,z components of the electronic transition dipole moment from the optimized geometry of the ground state, and the second line contains the same for the excited state geometry. If a Franck-Condon level calculation is requested, no further input is required. However, FCClasses is capable of performing calculations at higher levels, that is, the Herzberg-Teller approximation (HT). For this, the input file must additionally contain the dipole derivatives with respect to all the normal modes.

   These three input files are then fed into the master input file for the FCClasses program, alongwith specifying the type of approximation (FC or HT). From the output file that the program generates, we extract the two key matrices: the Duschinsky matrix ($\mathbf{J}$) and the dimensionless displacement vector ($\boldsymbol{\delta}$). These are then used to calculate the FCFs using a home-written MATLAB script.

9. **Calculation of Y values**

   The relative angles between the vibrational and electronic transition dipole moments are calculated from their scalar products, computed from the respective cartesian components obtained from the calculations described in point nos. 4 (vibrational) and 7 (electronic). These angles are then used to calculate the Y values using Eq. 4.21.

The FEIR activities A_j are then calculated according to Eq. 4.23 using a home-written MATLAB script. The next chapter presents these computational results, and through correlations with the corresponding experimental observables, we comment on the reliability of the computational strategy in predicting FEIR activities of individual normal modes within a chromophore.

Chapter 5

Modulation of FEIR activity by molecular factors

The material in this chapter is adapted from:

Guha, A; Whaley-Mayda, L; Lee, S.Y.; Tokmakoff, A. "Molecular factors determining brightness in Fluorescence-Encoded Infrared Vibrational Spectroscopy" *J. Chem. Phys.* **2024**, *160*, 104202.

5.1 Introduction

This chapter showcases the results of the computational predictions of FEIR activities of ten coumarins using the theory and computational methodology described in Chapter 4, and draws correlations between the computational predictions and corresponding experimental measurements. We begin with discussing the roles played by the various molecular factors—the vibrational and electronic transition dipole moments, their geometric orientation in space, and, most importantly, vibronic coupling, in determining the FEIR activities of the normal modes of Coumarin 6, our best FEIR candidate so far, based on the optimal balance of brightness and contrast. We also briefly discuss the influence of the dynamics of population and coherence pathways, and finite pulse effects on the mode-specific FEIR activities, using response function simulations described in Refs. [95] and [96]. Having established a compelling computational treatment of the normal modes of Coumarin 6, we extend the computational analysis to the other members of the coumarin family that we studied (Figure 3.5). Based on the correlations between the experimentally measured FEIR cross-sections and the corresponding computationally predicted FEIR activities of the normal modes of these molecules, we discuss the extent to which we can use the computational models to predict FEIR activity of individual vibrations in a candidate molecule. The results discussed here provide the groundwork for computational strategies for choosing an FEIR vibrational probe or informing the structure of designer chromophores for single-molecule applications.

5.2 Role of vibronic coupling and orientational factors in FEIR activity of Coumarin 6 normal modes

5.2.1 DFT calculations of normal mode frequencies in the ground state

We begin with detailed results for Coumarin 6 (C6), the FEIR chromophore with the best combination of brightness and contrast measured to this time.[71,90] Figure 5.1 compares the measured FTIR absorption spectrum of C6 in the frequency region $1450 - 1800$ cm^{-1} with the stick spectrum obtained from DFT normal mode calculations on the optimized ground state.

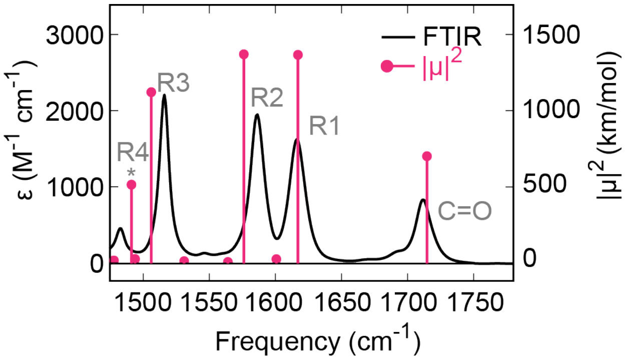

Figure 5.1: FTIR absorption spectrum of C6 in deuterated acetonitrile compared with the DFT normal mode calculations on the ground state in the spectral region of 1450 – 1800 cm^{-1}. Experimental spectrum is shown in black (left y axis), and calculated DFT spectrum is shown in magenta (right y axis). The experimental peaks at 1484, 1515, 1586, 1616 and 1712 cm^{-1} are denoted as R4, R3, R2, R1 and C=O respectively. The * indicates that the mode lies beyond the IR-pumped spectral region, and therefore, not observed in our FEIR experiments. The DFT frequencies are scaled by a factor of 0.973

Five distinct vibrational resonances are observed in the experimental spectrum: Four ring stretch modes with frequencies at 1484, 1515, 1586, and 1616 cm^{-1}, and the lactone carbonyl stretch mode at 1712 cm^{-1}, which we denote as R4, R3, R2, R1, and C=O respectively. Computed normal mode frequencies for C6 lie within ±10 cm^{-1} of experimental values when a scaling factor of 0.973 is applied (See Section 5.3), which is close to the empirical scaling factor of 0.96 for B3LYP/6-31G(d,p) level of calculation.[118] Figure 5.2 shows snapshots of the computed atomic displacement vectors, and the transition dipole moment vectors for these normal modes. The skeletal ring vibrations marked R1, R2, and R3 are the dominant contributors towards the FEIR activity of the molecule.[90] R4 is not sufficiently excited by our IR pump pulse to gauge its FEIR activity in our analysis.

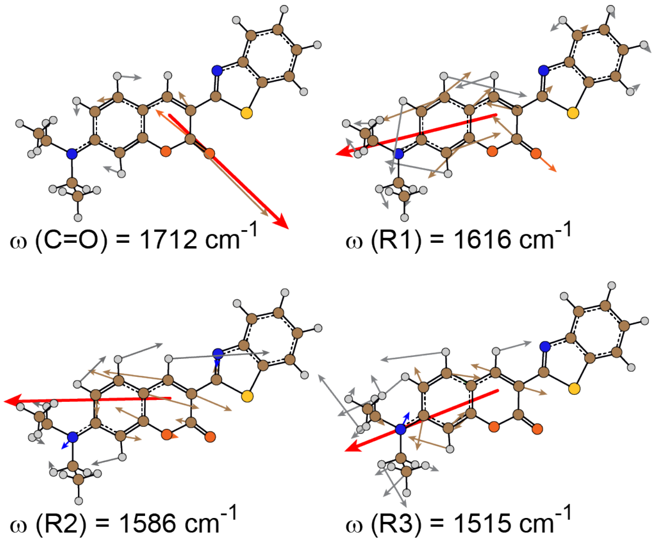

Figure 5.2: Snapshots of the normal mode displacement vectors for R3, R2, R1 and C=O from the DFT results. The arrows indicate atomic displacements, color-coded elementwise (H=grey, C=brown, N=blue, O=orange, S=yellow), scaled relative to the maximum displacement. The transition dipole moment vectors are indicated by red arrows (magnitudes are scaled for visual ease). The frequencies indicated are experimental values.

5.2.2 FEIR selection rules

One gains insight into FEIR selection rules by comparing the FEIR and FTIR spectra. Figure 5 shows the Fourier-transform FEIR spectrum of C6 at τ_{enc} = 600 fs overlaid on the pulse spectrum used to acquire it. This encoding delay represents a region outside pulse overlap. While the response from individual vibrations is still modulated by coherence in this region, such contributions are minimal for the case of C6. This is not true for a few other coumarins we studied, where coherence contributions to the FEIR response are quite significant. We discuss them in Section 5.3. In case of C6, the FEIR response at τ_{enc} = 600 fs primarily originates from population pathways. This allows a direct comparison of the FEIR spectrum with the FTIR spectrum of C6. Since the intensity of peaks in the FEIR spectrum is spectrally filtered by the IR pulse bandwidth, we compare it with the FTIR scaled by the same pulse spectrum. This reveals two important observations: First, the peak frequencies and lineshapes are the same in both spectra, as expected for ground-electronic-state vibrational spectroscopy. Second, the difference in the relative intensities of the resonances between FEIR and FTIR spectra indicate the different selection rules for these methods. While both methods require IR activity, FEIR also requires sufficiently large FCFs for the fluorescence encoding transition. Evidently, the R1, R3 and lactone C=O stretch modes are suppressed in FEIR activity relative to the intense R2 ring mode. Experimentally, it is indeed the most prominent mode in the single-molecule level FEIR spectrum.[71,90] This is qualitatively well-reproduced by the FEIR activity spectrum, calculated using Eq. 4.23 in the computational units of km mol^{-1} e^2 a$_0{}^2$.

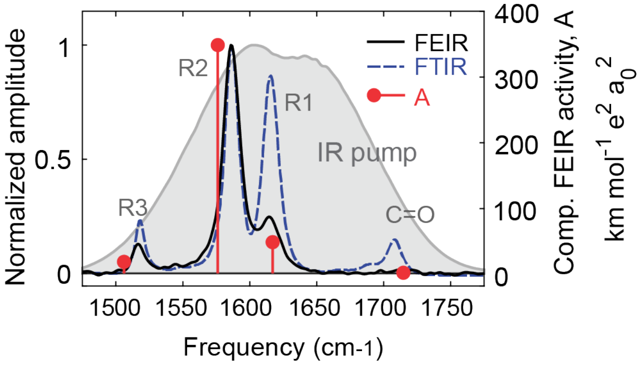

Figure 5.3: Comparison of FEIR intensities and computed FEIR activities of C6 in deuterated acetonitrile. FEIR spectrum (solid black) with the FTIR spectrum (dashed navy) scaled by the IR pump spectrum (grey shaded area) showing the suppression of R3, R1, and C=O relative to R2. The FEIR spectrum was acquired under the parallel polarization scheme at τ_{enc} = 600 fs, and normalized to the intensity of R2. The normalized amplitudes are read off the left y axis. The FEIR activity stick spectrum, calculated using Eq.4.23 in the computational units of km mol^{-1} e^2 a$_0{}^2$ is shown in red, and read off the right y axis. μ_{eg} = 17.53 ea$_0$.

As evident from Eq. 4.23, the product of the squares of FCF and the vibrational transition dipole shapes the FEIR activity for a normal mode. In the simplest approximation, FCFs are solely dependent on the Huang-Rhys factors (see approximation level I in Chapter 4). Furthermore, for the range $S \leq 0.1$ that applies for the normal modes we studied, $S = FCF^2$, as seen from Figure 4.1b of Chapter 4. Figure 5.4a shows a scatter plot of the squares of the vibrational transition dipoles ($|\mu|^2$) against the Huang-Rhys factor S for all normal modes of C6.

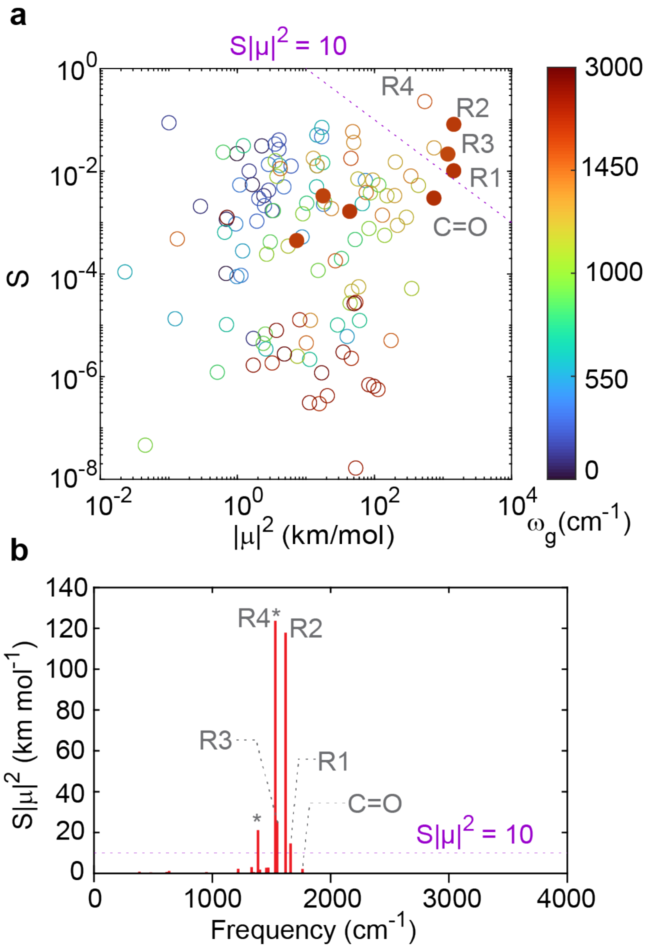

Figure 5.4: Demonstration of FEIR selection rule. (a) Correlation between the infrared intensities ($|\mu|^2$) and Huang-Rhys factors (S) for the 123 normal modes of C6 (circles). The color indicates its vibrational transition frequency (see color bar). The solid circles indicate the modes lying within the spectral window of the IR pump pulse. The detection threshold for our experimental studies, $S|\mu|^2 = 10$ is indicated with a dashed purple line. (b) The $S|\mu|^2$ product as a function of frequency for all normal modes of C6, demonstrating only 5 out of 123 modes have non-negligible contribution to the overall FEIR activity of C6. (*) indicates the modes lie outside our experimental window but are predicted to have large FEIR activity.

There is little correlation between these variables for different modes, but we see that the four prominent FEIR active normal modes in Figure 5.3, all lie in the top right quadrant of the correlation plot in the region bounded by $S|\mu|^2 = 10$ km/mol (marked by a dashed purple line). This indicates that there is a small number out of the 123 modes that dominate the FEIR activity of the molecule. The stringent requirements for FEIR activity become clearer in Figure 5.4b which shows the plot of the product of the two quantities $S|\mu|^2$ against the calculated frequencies. The plot identifies only 5 out of 123 normal modes that have a non-negligible ($S|\mu|^2 > 10$ km/mol), of which 3 are shown in Figure 5.2, along with C=O whose $S|\mu|^2$ value falls below the threshold of 10 km/mol. The other normal modes marked by (*) are the previously identified ring mode R4, and another ring stretching mode at 1387 cm^{-1} observed in the FTIR spectrum at 1358 cm^{-1}. They lie outside the IR pump spectral window. The atomic displacement snapshots for these are presented in the supplementary material. These results indicate that only ring skeletal stretching modes contribute to FEIR activity, whereas C-H ring stretching modes, high frequency C-H stretching and bending modes of the diethylamine and benzothiazole substituents (> 3000 cm^{-1}), and low frequency modes < 1300 cm^{-1} do not contribute. With this knowledge, we are in a position to look back at, and appreciate the observations Kaiser and co-workers made in their 1975 work,[59] where they concluded that the response from C6 excited with IR pulses centered at 3200 cm^{-1}, originated from C-H stretches, and upon further in-depth studies, in 1991,[61] deduced that the origin of the response was combination bands involving the ring stretches in the 1600 cm^{-1} region.

To look at the effect of frequency changes between ground and excited electronic states and Duschinsky mixing on the FCFs, we employ Eqs. 4.20 and 4.12 of Chapter 4 to calculate the FCFs at approximation levels II and III respectively. Comparing the values of FCFs under these approximations for R3, R2, R1 and C=O vibrations for C6 (Table 5.1), we observe that there is little difference ($< 1\%$) between them. This is true for all normal modes of all the members of the coumarin family presented in this chapter (See Figure 4.3of Chapter 4). This indicates that it is indeed the Huang-Rhys factor is sufficient to determine the magnitude of these integrals, while mode mixing and frequency changes play a negligible role, at least for this molecule. This is also in agreement with the calculated FCFs of C6 modes reported by Burghardt and co-workers.[103] This observation extends to all the coumarins reported in this chapter, and allows us to use the intuitive displaced harmonic oscillator model to understand FEIR activity.

Table 5.1: Experimental and calculated frequencies (scaled) of the four vibrational modes of C6, their extinction coefficients ε, calculated transition dipole moments $\lvert\mu\rvert$, magnitudes of Franck-Condon factors at three levels of approximation, relative angles between vibrational and electronic transition dipole moments from electronic structure and normal mode calculations θ, and the calculated and measured anisotropy values. Experimental anisotropies are obtained from the average value across the FWHM of individual peaks.

	ω_j (cm^{-1})		$\varepsilon/10^3$ (M^{-1}cm^{-2})	$\lvert\mu\rvert^2/10^3$ (km/mol)	FCF $\langle \mathbf{1}_j \vert \mathbf{0}' \rangle$			θ_j(°)	Anisotropy	
	expt.	calc.			I	II	III		calc.	expt.
R3	1515	1506	31.09	1.18	0.137	0.136	0.137	3.2	0.4	0.26
R2	1586	1576	36.07	1.44	0.268	0.264	0.266	19.1	0.33	0.28
R1	1616	1617	32.63	1.43	-0.094	-0.094	-0.094	6.7	0.39	0.35
C=O	1712	1714	18.86	0.74	-0.051	-0.051	-0.051	116.0	-0.08	-0.05

5.2.3 Relative orientation of transition dipoles

The geometric orientation of the vibrational and electronic transition dipoles plays a key role in modulating the overall FEIR response from the molecular vibrations, depending on the choice of polarization of the IR and visible pulses. The orientational factors (Y_{pol}) are discussed in detail in Ref. [95] They can be calculated from the computed angles between the vibrational and electronic transition dipoles (θ_j) using Eq. 4.21. To comment on the accuracy of the electronic structure calculations, we compare the anisotropies calculated from these computed angles with the anisotropy obtained from FEIR anisotropy experiments. The transition dipoles moment vectors computed for the R3, R2, R1, and C=O modes and the electronic transition dipole moment of C6 are pictured in Figure 5.5a, and are related to the anisotropy value according to:

$$r_{calc} = \frac{1}{5}(3\cos^2\theta_j - 1) \tag{5.1}$$

Note that this only holds when we neglect contribution from coherence pathways. Experimental anisotropies are determined from the parallel and perpendicular polarization FEIR spectra, $S(\omega)$, using

$$r_{expt} = \frac{S_{\parallel} - S_{\perp}}{S_{\parallel} + 2S_{\perp}} \tag{5.2}$$

Experimental measurements of the parallel and perpendicular FEIR spectra and the corresponding anisotropies are presented in Figure 5.5b and reported in Table 5.1. The reported values are averages over the corresponding linewidths. The FTIR spectrum is shown on the top panel for reference. R1, R2 and R3 have anisotropy values close to that expected for parallel or anti-parallel dipoles ($r = 0.4$), while the lactone C=O mode has an anisotropy close to zero, as expected for vibrational dipoles oriented close to the magic angle with the electronic transition dipole moment ($\theta_j \approx 54.7^\circ \texttt{ or } 125.3^\circ$). The errors associated with the measurements lie within $2 - 15\%$, the minimum being for R1 and maximum for R3. The anisotropy of the C=O mode, shown as a separate panel was determined from a separate experiment with the IR pump pulsetuned to $\sim$ 1720 cm^{-1}.

Computationally, the anisotropies were deduced from the DFT-calculated relative angles between the vibrational and electronic transition dipoles using Eq. 5.1. We will present a full correlation of the calculated and measured anisotropies of the normal modes of all ten coumarins in Section 5.3.

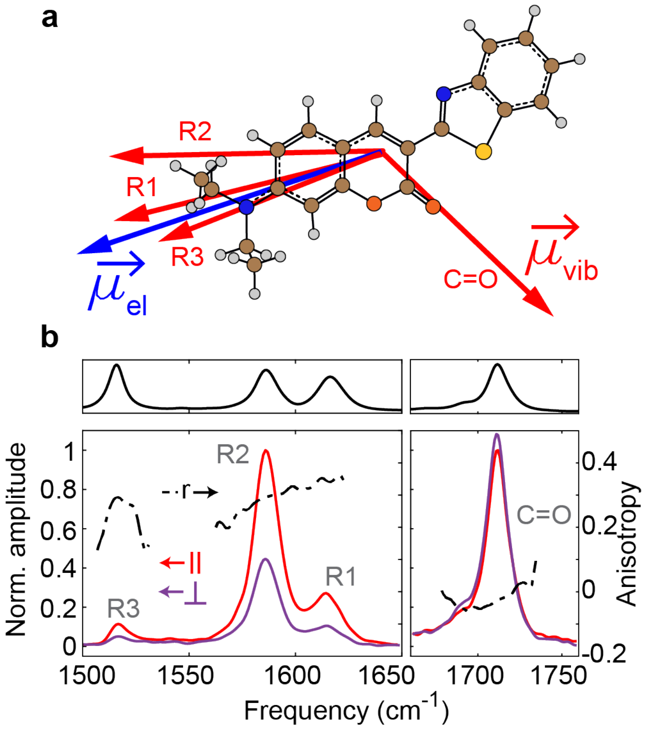

Figure 5.5: Relative orientations of transition dipoles for normal modes of C6 (a) Ground-state optimized geometry of C6 showing the relative angles between the vibrational (red arrow) and the electronic (blue arrow) transition dipoles for R3, R2, R1, and C=O. (b) Polarization dependent FEIR spectra and anisotropy of normal modes calculated using Eq. 5.2

5.2.4 Effects of vibrational coherence and finite pulses on FEIR spectra

As ultrafast nonlinear measurements, FEIR spectra are influenced by ground state vibrational dynamics initiated by the IR excitation fields, which can complicate the comparison against static parameters derived from electronic structure calculations. Vibrational coherences excited by the short IR pulses give rise to beats and phase distortions in FEIR spectra during a scan across the encoding delay, and finite pulse effects can introduce additional complexities, especially at early encoding delays. As shown in the two-paper series on the theory of FEIR spectroscopy,[95,96] response function simulations capture these phenomena and produce insight into the detailed shape and time evolution (τ_{enc}) of spectra. To discuss how these effects can be accounted for within our current analysis, we reproduce a part of the results from Ref. [96] in this section. Figure 5.6a shows the experimental FEIR spectrum of C6 as a function of encoding delay. The spectral intensities are observed to rise over several hundred femtoseconds before damping on picosecond timescales, and the R3 mode is particularly strongly modulated by coherent beats. Furthermore, negative contributions to the coherent signals are observed at early waiting times. The same FEIR spectrum simulated with DFT computed parameters and experimental variables is shown in Figure 5.6b. As input, we used the vibrational transition dipole moments, frequencies, FCFs and orientational factors (Y). Qualitatively we see that there is excellent agreement between the experimental and simulated spectral response, indicating that the calculation of the molecular factors will be very useful for interpreting experimental FEIR spectra. Beating amplitudes and peak growth and relaxation times are effectively simulated, as are the negative contributions to the signal for delays < 500 fs. The latter were shown to originate from coherences involving two FCFs and/or transition dipole projections that were of opposite sign. The only significant difference is an apparent τ_{enc} offset of 100 fs in the shape of the spectral response of the experiment relative to simulations, as highlighted by the dashed lines in the figure. The origin of this offset remains unclear but may be due to the counterpropagating beam configuration within the FEIR microscope, and thus we attribute this to an experimental uncertainty and consider the experimental spectra at encoding delays 600 fs and 100 fs for the purpose of comparing with simulations at encoding delays 500 fs and 0 fs respectively.

Other errors are present that are due to inaccuracies in the DFT calculations. The calculated frequencies do not accurately line up with the experimental values, and there are errors associated with the calculated vibrational transition dipole moments. When these ground state vibrational parameters are exchanged with the experimentally determined ones, we obtain the simulated spectrum in Figure 5.6c. For this, the linear FTIR spectrum was fit to a sum of Lorentzian functions, and the frequency and vibrational transition dipole values were extracted from the fit parameters.

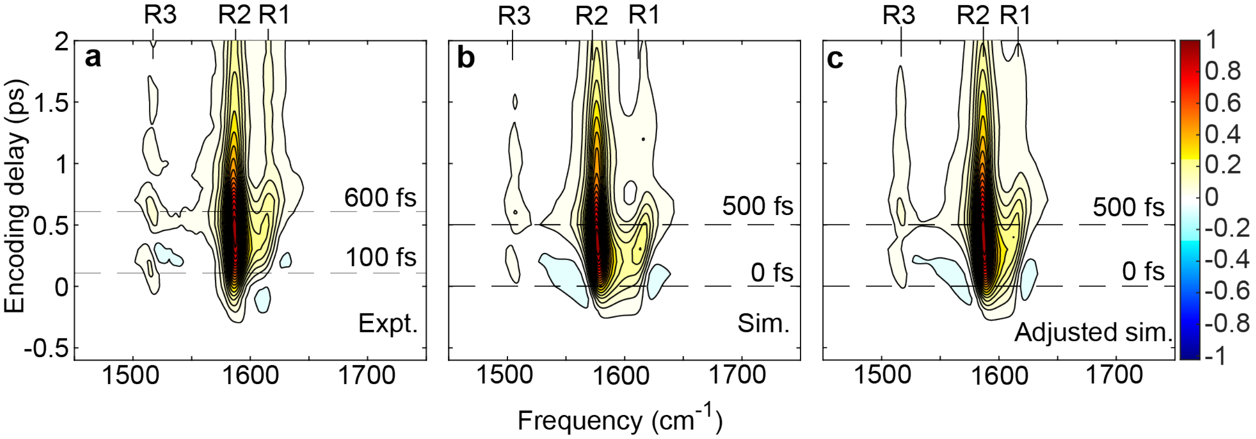

Figure 5.6: Qualitative comparison of experimental and computed FEIR intensities of C6 normal modes. FEIR spectra as a function of encoding delay, experimental (a) , simulated with all parameters from DFT (b), and simulated with vibrational transition dipoles and frequencies adjusted from FTIR (c).

Despite their promise, the computational complexity and cost of these simulations adds a substantial barrier to using them, and the outcome is specific to one experimental apparatus. This work is in part motivated by validating computational screening and design tools that can be readily applied to large numbers of FEIR chromophore candidates to determine their use in experimental design. As a result, we also investigated strategies for predicting peak intensities that account for coherence effects. Employing broadband IR pulses can also result in the simultaneous excitation of multiple vibrations. Consequently, both population and coherence pathways simultaneously influence the overall FEIR activity that cause deviations from, or even change the signs of the activities predicted using Eq. 4.23 of Chapter 4. To predict the FEIR activity of individual normal modes under broadband excitation, we use a modified version of the FEIR activity.

$$I_j = \sum_i |\mu_{eg}|^2 \mu_i \mu_j \langle \mathbf{1}_i | \mathbf{0'} \rangle \langle \mathbf{0'} | \mathbf{1}_j \rangle Y_{pol}^{(i,j)} \tag{5.3}$$

Here, i sums over the N vibrations with $i = j$ representing the population pathway, and all $i \neq j$ representing the different coherence pathways involving different pairs of normal modes. The relative signs of FEIR amplitudes can positive or negative, depending on the relative signs of the FCFs and orientational factors $Y^{(i,j)}$. The latter are now determined by the orientation of the two vibrational transition dipoles ($\hat{\mu}_i$ `and` $\hat{\mu}_j$) relative to the electronic transition dipole orientation ($\hat{\mu}_{eg}$). For the case of co-planar transition dipole moments, which is generally the case for all the chromophores studied as a part of this thesis, these expressions are given as[93]

$$\begin{aligned} Y_{\parallel}^{(i,j)} &= \frac{1}{15}(2\cos(\theta_i - \theta_j) + \cos(\theta_i + \theta_j)) \\ Y_{\perp}^{(i,j)} &= \frac{1}{15}(3\cos(\theta_i - \theta_j) - \cos(\theta_i + \theta_j)) \end{aligned} \tag{5.4}$$

For comparison to experiments in this case, we weight the individual IR transition dipole moments again by the spectral intensity of the IR light at the resonance frequency using the same treatment as mentioned in Chapter 4: $\mu_i \mu_j \rightarrow \mu_i \mu_i \sqrt{I_{IR}(\omega_i) I_{IR}(\omega_j)}$.

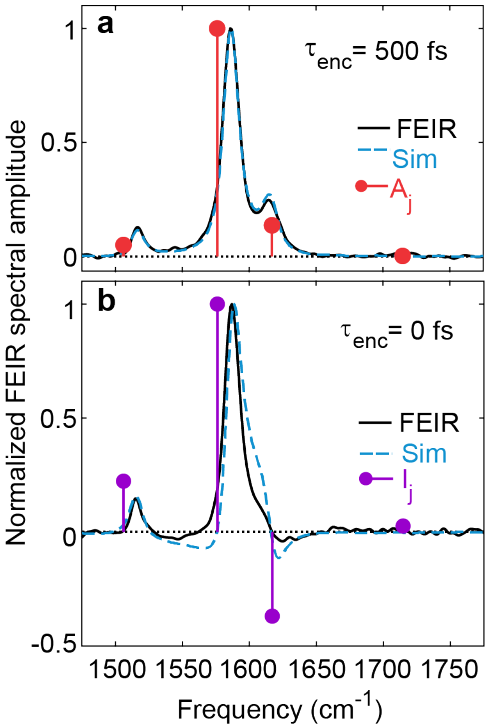

Figure 5.7: Comparison of experimental and simulated spectra at different encoding delays. (a) Comparison of the experimental spectrum at $\tau_{enc} = 600$ fs (black) with the simulated spectrum at $\tau_{enc} = 500$ fs (blue), overlayed by the FEIR activity spectrum (stick spectrum), derived from Eq. 4.23. (b) Comparison of the early-time FEIR spectra, $\tau_{enc} = 100$ fs for experimental (black) and $\tau_{enc} = 0$ fs for simulated spectra (blue), overlayed by the FEIR activity under broadband excitation, derived from Eq. 5.3 (stick spectrum).

To have a closer look at how broadband excitation and vibrational coherences influence FEIR spectra, we investigate the change in FEIR spectra between two encoding delays. Figure 5.7a shows a comparison between the experimental spectrum at $\tau_{enc} = 600$ fs and the simulated spectrum at 500 fs, where the peaks are absorptive. Comparing the simulated and experimental FEIR shows that the peak intensity pattern is identically reproduced by our simulation and qualitatively matches the FEIR activity predicted by static calculations in Eq. 4.23, indicating that the molecular response at this encoding delay originates primarily from population pathways. There are, however, contributions from multimode coherence, especially in the responses of R1 and R3, as seen from their deviations from the predicted DFT-calculated activities.

Next, in Figure 5.7b, we look at the spectra at $\tau_{enc} = 0$ fs (100 fs for experiment), which falls in the region most heavily affected by coherences. The response from R1 is significantly influenced by its coherence with R2. Given their FCFs have opposite signs (Table 5.1), the coherence pathways should have a negative contribution to the overall FEIR response. The FEIR amplitude of R1 indeed has a negative amplitude in the experimental spectrum and is correctly reproduced in the simulation. The FEIR activity spectrum (stick spectrum), calculated from the matrix elements alone using Eq. 5.3 also predicts the sign of R1 correctly, but is not able to capture the relative amplitudes well. However, when we invoke the simulation based on response function, and add in the finite pulse effects with the pulse characteristics taken from the experiment, the simulated spectrum predicts the relative intensities and signs fairly correctly, as shown in dashed blue. To summarize, our comparisons suggest that while the DFT calculations yield accurate results for the molecular factors, primarily, the signs of the FCFs and orientational factors (Y), multimode coherences and convolution with finite electric fields significantly modulate the amplitudes of the FEIR response, making it challenging to predict them using the matrix elements alone.

5.3 Comparing experiments to computational predictions across the coumarin family

5.3.1 Transition strengths and frequencies

We begin our investigating of the accuracy of computed FEIR activities by analyzing the vibrational and electronic transition frequencies and intensities. The method adopted to determine the experimental IR frequencies and intensities is outlined in Appendix 5.A. The $S_0 \rightarrow S_1$ transition frequencies are obtained from the maxima of the corresponding UV/Vis absorption spectra, and the oscillator strengths are determined from the area under the absorption spectra according to $f = 4.32 \times 10^{-9} \int \varepsilon(\omega) d\omega$.[90,119,120] The comparison between experiment and DFT calculations illustrated above with C6 are for the most part representative across the coumarin family. Figure 5.8 presents the comparison of the vibrational frequencies and computed IR intensities, electronic oscillator strengths and $S_0 \rightarrow S_1$ transition frequencies across members of the coumarin family. The harmonic computed frequencies across all molecules (ω_j) are highly correlated with experimental results ω_{vib} (expt), related by a scaling factor of 0.973 (Figure 5.8a). The squares of the vibrational transition dipole moments show a reasonable linear correlation with experimental integrated molar extinction coefficients (Figure 5.8b), and the error associated with the calculations of these absolute amplitudes directly carries into the prediction of FEIR activities. The experimental electronic oscillator strengths (determined previously in Ref. [90]) are also highly correlated with computed oscillator strengths for HOMO-LUMO transitions across all molecules, related by a scaling factor of 0.69 (Figure 5.8c). The experimental $S_0 \rightarrow S_1$ transition frequencies ω_{vis} (expt), derived from the absorption maxima in the UV/Vis spectra[90] also show a strong linear correlation with the corresponding TD-DFT calculated transition frequencies (ω_{eg}), related by a scaling factor of 0.942 (Figure 5.8d), with C314, C337, C343 and C334 treated as outliers. The relatively poor correlation of the electronic transition energies can be attributed to the errors in TD-DFT calculations, which are typically about $0.3 - 0.4$ eV[121]. For molecules like the coumarins, that involve bond length alteration and quinoidization as a result of conjugation, such errors have been reported previously.[112,118,122,123] The computed FCFs at Level I for vibrations > 1000 cm^{-1} lie within 2% of the Level II and Level III values (see Figure (4.3) in Chapter 4).

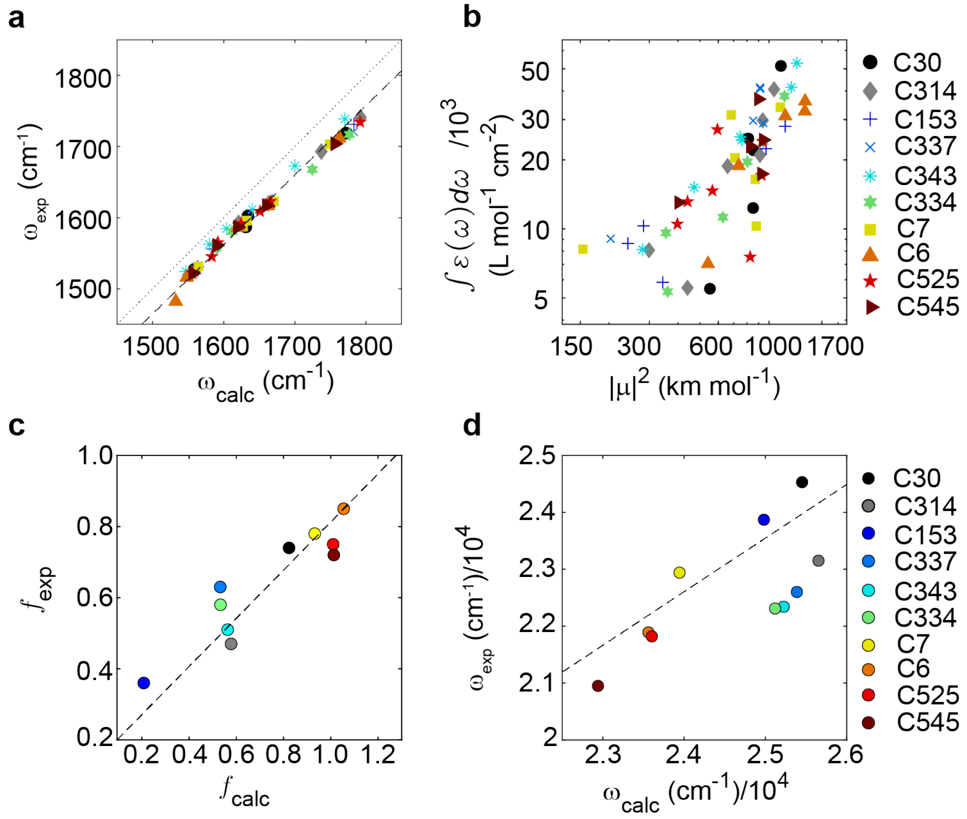

Figure 5.8: Comparison of experimental IR and electronic spectroscopy with computed values. (a) Correlation between the experimental and calculated IR vibrational frequencies. The correlation is fit to a linear function and yields a slope of 0.973, shown by the black dashed line. The grey dash-dot line, denoting $\omega_{exp} = \omega_{calc}$ is added for reference. (b) Correlation between the experimental IR molar extinction coefficients and corresponding calculated IR intensities for the normal modes of coumarins in the frequency range of $1450 - 1800$ cm^{-1}. (c) Correlation between TDDFT-calculated and experimental oscillator strengths for the $S_0 \rightarrow S_1$ transition, with a linear fit showing $f_{exp} = 0.69 f_{calc}$ (d) Correlation between TDDFT-calculated $S_0 \rightarrow S_1$ transition frequencies and the corresponding experimental A linear fit (dashed black line) establishes a relationship of $\omega_{exp} = 0.942\omega_{calc}$. The grey dash-dot line denoting $\omega_{exp} = \omega_{calc}$ is added for reference.

5.3.2 Polarization anisotropy

The methods described in detail above for C6 (Figure 5.5) were also applied to all the molecules within the coumarin family shown in Figure 3.5. The polarization dependent

FEIR spectra from which the anisotropies were deduced are shown in Figure 5.9. As in the case of C6, the anisotropy values are taken as average across the corresponding linewidth of the vibrational peaks.

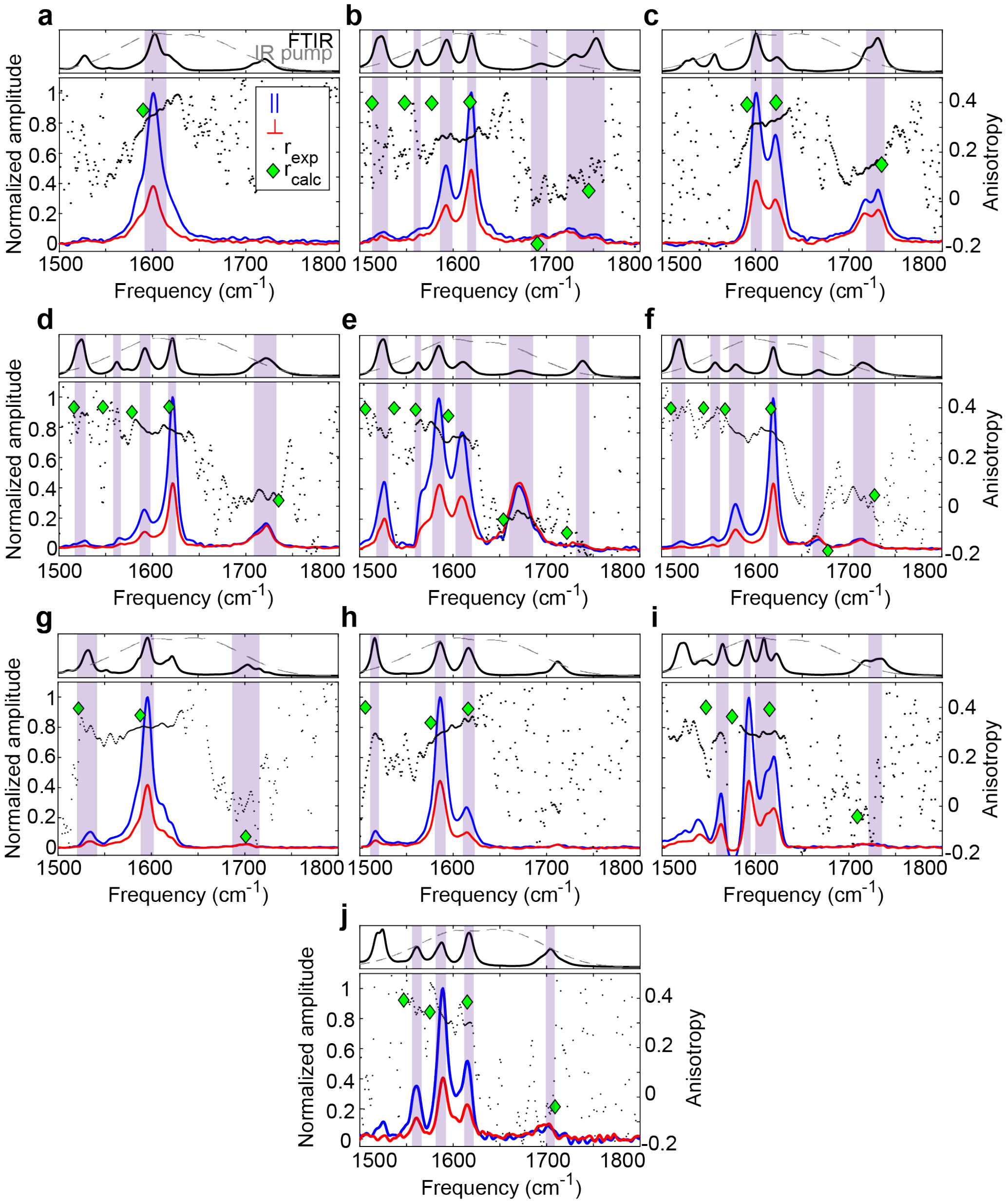

Figure 5.9: Experimental anisotropies of normal modes of coumarins determined from FEIR spectra acquired with relative parallel (blue) and perpendicular (red) polarization of IR and visible pulses. Anisotropies (black dots) are reported as average over respective linewidths (purple shaded areas). The corresponding FTIR (black) and IR pump spectra (grey) are shown for reference. The DFT-calculated anisotropy values are shown as green diamonds.

As a first comparison, the correlation between the calculated and experimental anisotropies for all FEIR active normal modes is shown in Figure 5.10. One observes an overall linear correlation, highlighting the accuracy to which the DFT calculations predict the relative orientation of the vibrational and electronic transition dipole moments. One key aspect to note here is that the variance associated with the experimental data points arise due to the polarization-dependent variation in the spectral intensities within the linewidths due to inhomogeneity within resonances, and therefore, cannot be eliminated by repeating the data acquisition.

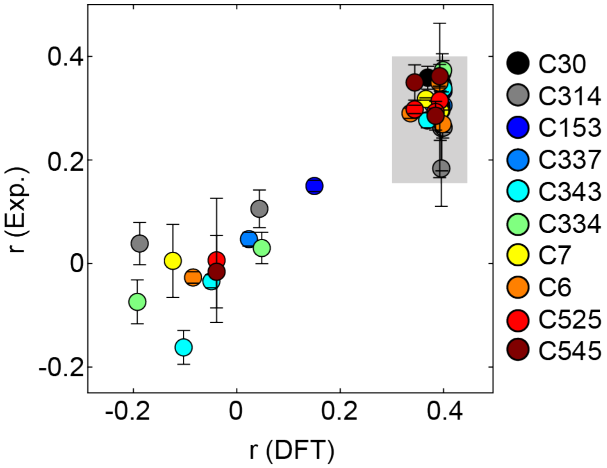

Figure 5.10: Correlation between calculated and experimental anisotropies for the normal modes of ten coumarin dyes. The error bars represent the uncertainty in the experimental anisotropies due to the respective lineshapes of the peaks in the FEIR spectra.

As seen from the plot, the transition dipoles for the ring modes of these chromophores, shown in a grey box, exhibit a near-parallel orientation with the electronic transition dipole, resulting in anisotropy values close to the theoretical maximum of 0.4. While the DFT results constantly predict anisotropies in the range of $0.3 - 0.4$, the corresponding experimental values are consistently low. One possible explanation for this discrepancy on the experimental side is the effect of impure linear polarization and out-of-plane components of the IR and visible fields, in particular resulting from the high numerical aperture focusing in the FEIR microscope, as discussed in Ref. [96]. The encouraging result lies in the linear correlation for the carbonyl modes, anisotropies of which lie in the range of -0.2 to 0.2. The lactone carbonyls of many of these coumarins have negligible FEIR activity. Therefore, the corresponding anisotropy measurements are accompanied by significantly large errors. For C153, C337, and C343, their FEIR activities are large, and their anisotropies are measured with much better accuracy. Also, the anisotropy for the lactone carbonyl of C6 was separately determined by tuning the IR pulse to 1720 cm^{-1}, directly pumping the mode. The correlation is particularly good for these data points. Moreover, coumarins like C314, C343, and C334 have two different carbonyls: a lactone carbonyl as a part of the coumarin core, and a carbonyl as a functional group (-COOC$_2$H$_5$, -COOH, and -COCH$_3$ respectively). The two carbonyl transition dipoles are oriented differently in space and are experimentally realized through their distinctly different anisotropy values. While the lactone carbonyls generally have an anisotropy close to zero, indicating that it is oriented at close to the magic angle of (54.7° or 125.3°) with the electronic transition dipole, the carbonyl in the functional group typically exhibits a value in the range of -0.1 to -0.2. This proves to be interesting when assigning the peaks to the two different carbonyls in a molecule. For instance, the carbonyls in the functional group resonate at $\sim$ 1660 cm^{-1}, while the lactone carbonyl peak primarily appears at 1720 cm^{-1}. For C343, we see intramolecular hydrogen bond formation between the -COOH group and the lactone carbonyl. This causes the frequency of the latter to red shift, so much that the order of their appearance in the vibrational spectrum is reversed (see normal mode snapshots in Figure 5.A.6 of Appendix 5.A.2). But, with the anisotropy values at hand, we can clearly identify one from the other. The DFT calculations do a fairly good job in capturing these values. Overall, this correlation serves as a proof of accuracy for the calculation of the vibrational and electronic transition dipoles, particularly their relative orientation in space.

5.3.3 Computational prediction of molecular FEIR brightness

Typically for the coumarins, $3-8$ normal modes significantly contribute to the total FEIR activity with $S|\mu|^2 > 10$ km mol^{-1}. Looking across the coumarin family, these modes are typically conjugated, delocalized ring modes involving C=C stretches, conjugated with C-H bends. Exceptions are the lactone carbonyl stretches of C153 and C337, that exhibit large $S|\mu|^2$ values of 128 and 26 km mol^{-1} respectively (see Table 5.A.1 in Appendix 5.A.2).

Now, we look at how the calculations work in predicting the FEIR brightness of these chromophores. On the experimental side, we have the molecular FEIR cross-section, which are determined from the FEIR brightness values derived from fluorescence photon count rates in the two-pulse FEIR measurements (Eq. 3.6 given in Chapter 3), and normalizing by the fluorescence quantum yield ($a = \frac{q}{\phi}$), and furthermore, by the value of the electronic lineshape function at the $vis + IR$ excitation frequency ($g(\omega_{vis} + \omega_{IR})$). We use the experimental data reported in Ref. [90]. On the computational side, the FEIR activity of the molecule is comprised of the individual FEIR activities of all the normal modes lying within the IR pump spectral window, or, $A = \sum_j A_j$, with the A_j's calculated using Eq. 4.23 (given in Chapter 4). Shown in Figure 5.11 is a correlation between these two quantities across the series of ten coumarins. Both are linearly correlated with a Pearson's correlation coefficient (ρ) of 0.7.

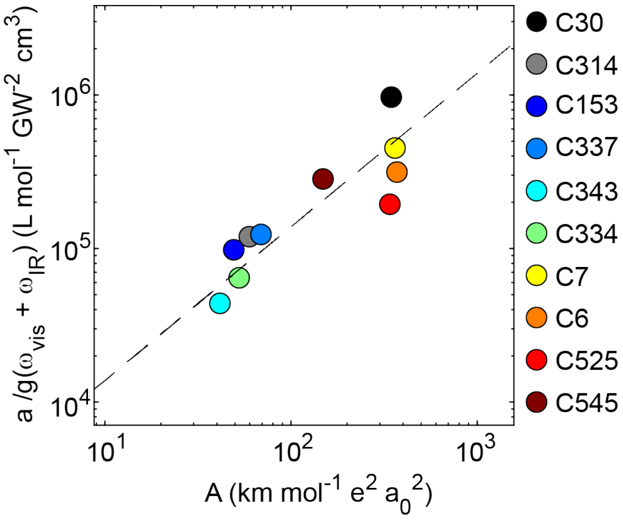

Figure 5.11: Correlation between the sum of computed FEIR activities of normal modes lying within the IR pump spectral window (A) and the lineshape-normalized experimental total FEIR cross-sections of molecules across the coumarin series.

An intriguing observation worth highlighting in this context is the spread in the experimental FEIR cross-sections across the coumarin series, underscoring the influence of molecular factors, particularly vibronic coupling. Despite possessing similar vibrational extinction coefficients, electronic oscillator strengths, and fluorescence quantum yields, there exists approximately a tenfold disparity between C343, one of the coumarins with the lowest FEIR brightness, and C6, among the FEIR-brightest coumarins. The dispersion observed in the plot can be attributed to the experimental variables describing the electric fields, resonance conditions, and vibrational dynamics. From a time-dependent perspective, several factors, namely (1) population relaxation, (2) multimode coherences, and (3) convolution with finite electric fields, introduce significant fluctuations in the FEIR response. These fluctuations, being time-dependent in nature, are not captured by the FEIR activities predicted using Eq. 4.23. On the computational front, errors associated with the determination of IR transition dipole amplitudes are directly transferred to the FEIR activity predictions. While such errors can be minimized through benchmark studies at various levels of theory, they cannot be eliminated. These factors collectively make the quantitative comparison of mode-specific FEIR activities with the experimental peak intensities challenging. Nevertheless, despite the observed scatter, the calculations predict substantial FEIR activities for C6, C7, C30, and C525. It is worth noting that, with our current experimental setup, we have validated these predictions for C6 and C7, confirming their single-molecule sensitivity as demonstrated in Ref. [90].

5.3.4 Effect of vibrational dynamics on the correlations of mode-specific FEIR activities

We have attempted to partially address the sources of errors by invoking the response function calculations to simulate the time-dependent FEIR spectra of nine of the coumarins shown in Figure 3.5 using the methodology developed in Ref.[96]. This allowed us to include the contribution from vibrational dynamics, finite pulses, and eliminate the errors from the DFT-calculated vibrational transition dipoles by using values extracted from the FTIR spectra. In this section we compare the experiments and computational predictions at $\tau_{enc} = 500$ fs. In Figure 5.12, we show the correlation between the experimental FEIR cross-sections and predicted FEIR activities of individual vibrations lying within the experimental IR pump spectral window. The experimental and simulated FEIR spectra at $\tau_{enc} = 500$ fs (600 fs for experiment) were fit to a sum of gaussians, and the areas under individual vibrational peaks were determined from the fit parameters. The mode-specific FEIR cross-sections (activities for simulation) are represented as these areas normalized by the total area under the spectra, shown as normalized FEIR cross-section and normalized FEIR activity on the vertical and horizontal axes respectively). Figure 5.12a demonstrates the correlation where the simulation results are calculated using Eq. 4.23 entirely from DFT-calculated matrix elements. Since this is a stick spectrum, the normalized FEIR activities are calculated as, $\frac{A_j}{\sum_{j=1}^{n} A_j}$, where n represents the total number of modes within the IR pump spectral window. The vibrational transition dipoles were scaled by the IR pump intensities at the corresponding experimental frequencies, as mentioned earlier in Chapter 4.

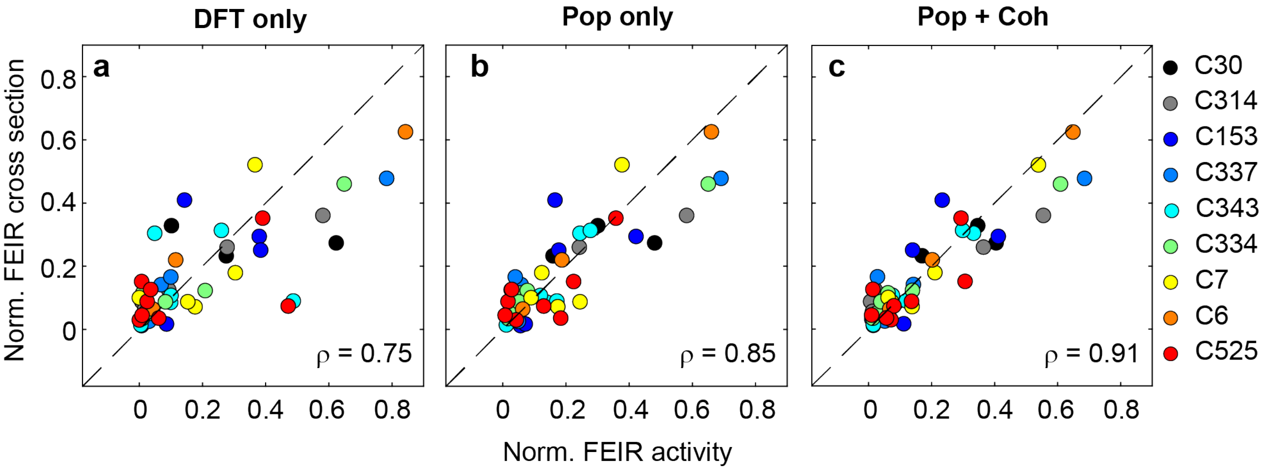

Figure 5.12: Effect of vibrational dynamics on the correlation of mode-specific computational predictions to the corresponding experimental FEIR response at $\tau_{enc} = 500$ fs (600 fs for experiment).(a) Correlation of the experimental normalized FEIR cross-sections of the vibrations of the coumarins with the normalized mode-specific FEIR activities computed using Eq. 4.23. (b) Improvement in the correlation with population relaxation and finite pulse effects are included in response function calculations, and DFT-calculated vibrational intensities replaced by values obtained from FTIR spectra. (c) Further slight improvement in correlation upon including the coherence pathways in the simulation, as seen from the qualitative reduction in scatter.

We suspect that the large scatter is attributed to the different factors we mentioned previously. Particularly, there are significant levels of error in DFT-calculated normal mode that contribute majorly to the scatter, impact of population relaxation, effect of finite excitation pulses, and contributions from coherence pathways as a consequence of broadband IR excitation. To demonstrate this, we first replace the DFT-calculated vibrational transition dipoles with those obtained from the FTIR spectra, incorporate population relaxation, and convolution with finite pulses to simulate the time-dependent FEIR spectra. In Figure 5.12b, we show a much-improved correlation between the normalized amplitudes of the vibrations from the experimental and “population only” simulation. Upon adding in the coherence between mode pairs to the simulation, we could improve the correlation even further, as shown in Figure 5.12c. The improvement in the linear correlation is seen as the Pearson’s correlation coefficient (ρ) increases from 0.75 in panel a to 0.85 in panel b to finally 0.91 in panel c. Qualitative comparisons between the spectra are shown in Figure 5.13.

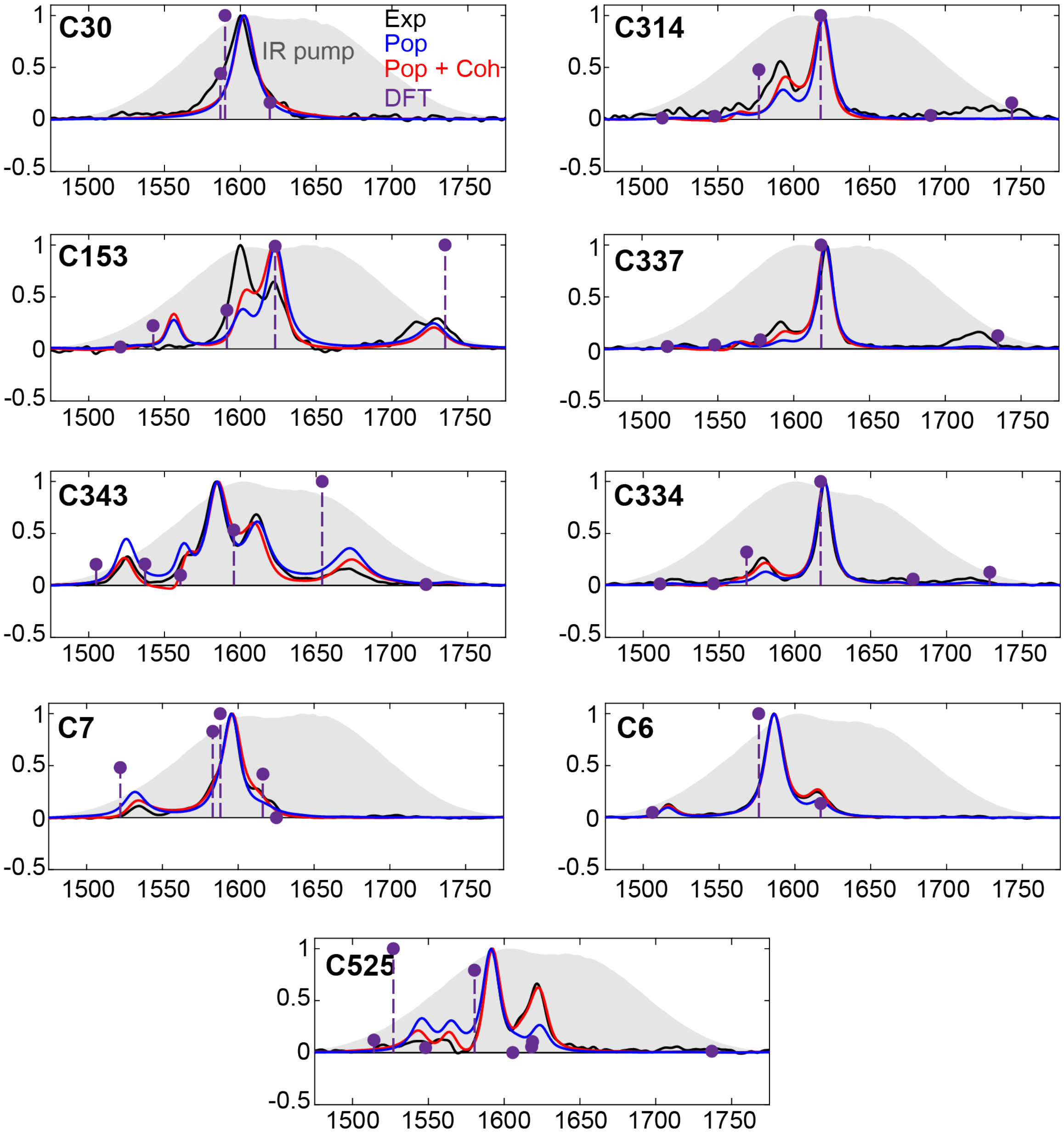

Figure 5.13: Qualitative comparison of the experimental and simulated FEIR spectra at τ_{enc} = 500 fs. The simulations with population pathways are shown in blue, population + coherence pathways in red, and for comparison, the stick spectra derived from DFT calculations (Eq. 4.23 of Chapter 4) are shown in purple. The experimental spectra are shown in black, and the IR pump spectra are shown as grey shaded areas.

The DFT calculations can reliably predict the relative signs of the FCFs and Y, that determine the overall sign of the FEIR response of the normal modes in the event of multimode excitation. This is the most prominent at the earliest encoding delays. The comparisons at $\tau_{enc} = 0$ fs (100 fs for experiment) are shown in Figure 5.14, where a similar relative improvement in correlation is observed. Particularly encouraging is the agreement in the signs of the responses between the experiment and simulation. Despite the near quantitative agreement, the simulations cannot predict the amplitudes of the characteristic broad continuous absorptive feature between the highest frequency ring mode and the lactone carbonyl mode of C153, C337, C334, and especially C343 shown in Figure 5.15, which we suspect to be originating from IR + visible two-photon absorption, as we have mentioned in our previous work.[96]

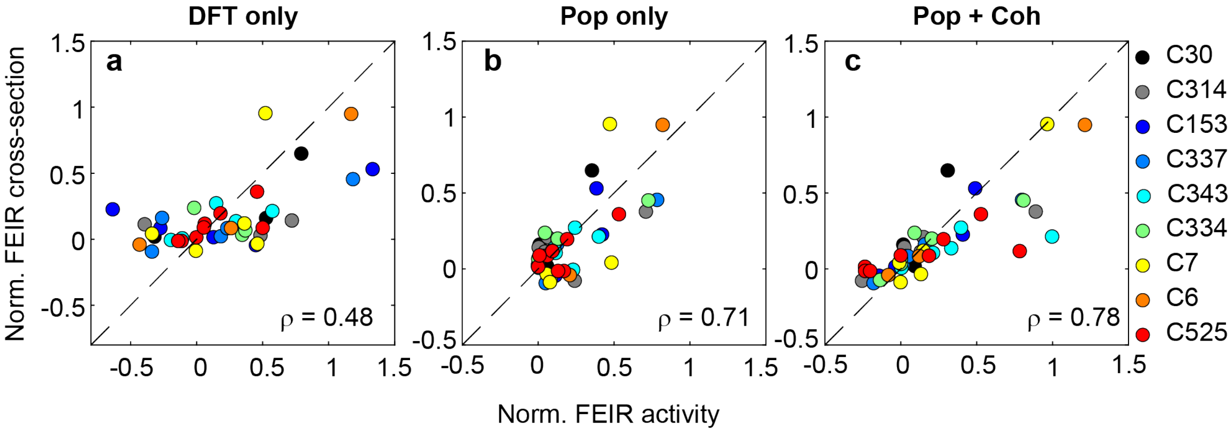

Figure 5.14: Effect of vibrational dynamics on the correlation of mode-specific computational predictions to the corresponding experimental FEIR response at $\tau_{enc} = 0$ fs (100 fs for experiment). (a) Correlation of the experimental normalized FEIR cross-sections of the vibrations of the coumarins with the normalized mode-specific FEIR activities computed using Eq. 5.3. (b) Improvement in the correlation with population relaxation and finite pulse effects are included in response function calculations, and DFT-calculated vibrational intensities replaced by values obtained from FTIR spectra. (c) Further slight improvement in correlation upon including the coherence pathways in the simulation.

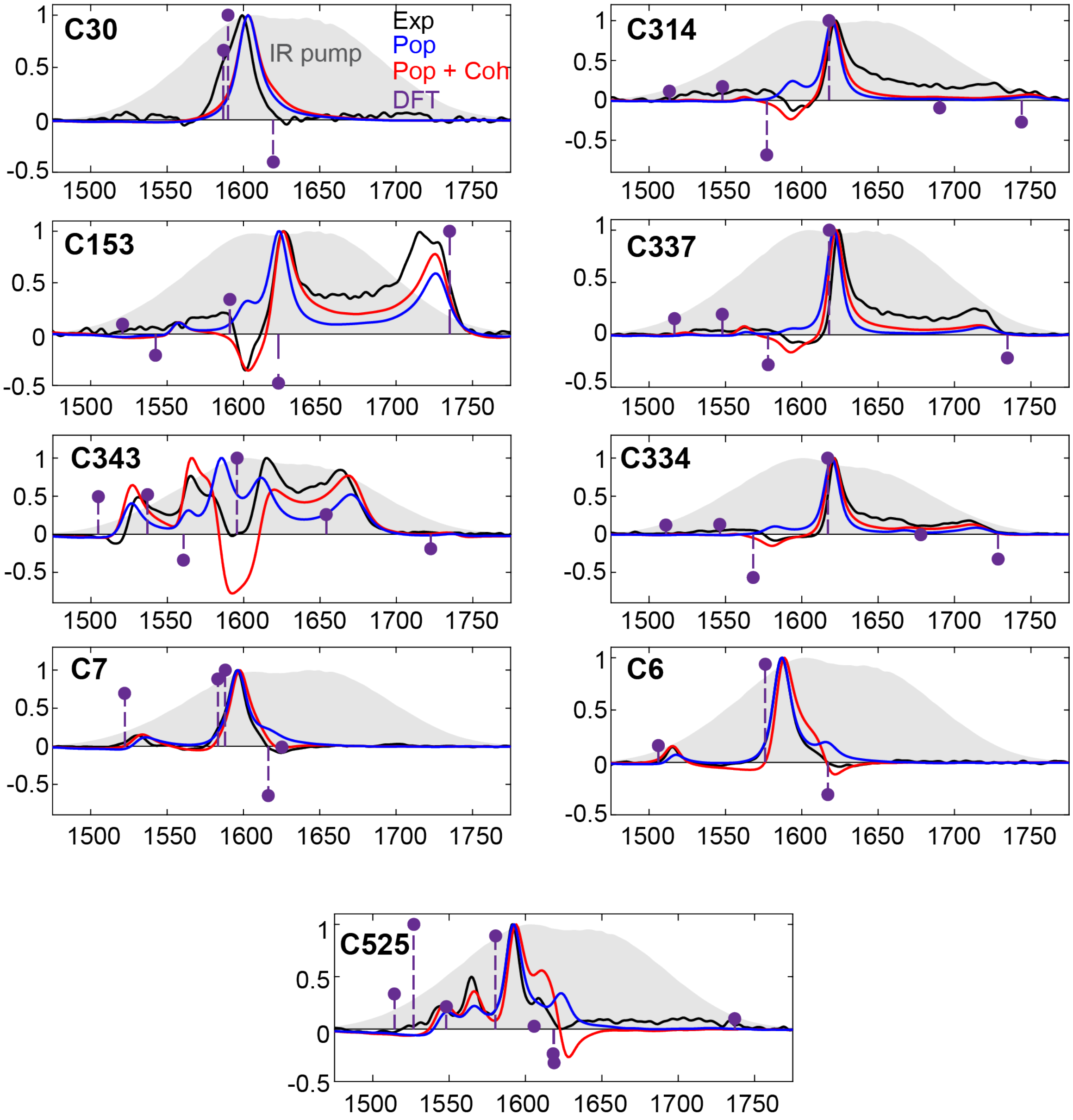

Figure 5.15: Qualitative comparison of the experimental and simulated FEIR spectra at $\tau_{enc} = 0$ fs. The simulations with population pathways are shown in blue, population + coherence pathways in red, and for comparison, the stick spectra derived from DFT calculations (Eq. 5.3) are shown in purple. The experimental spectra are shown in black, and the IR pump spectra are shown as grey shaded areas.

While the simulations can qualitatively reproduce the feature, they systematically underestimate the amplitude across the continuum. We also acknowledge the fact that these features arise primarily due to coherence pathways, which are a consequence of broadband IR excitation. They provide exciting avenues for understanding the intrinsic ultrafast vibrational dynamics. However, they will not play a role in the FEIR brightness of vibrations in the event of selective single-mode excitation, which is relevant for single-molecule FEIR spectroscopy.

5.3.5 Computational predictions of FEIR activities of carbonyl modes in coumarins

An ideal single-molecule FEIR probe would involve a vibrational mode that exhibits strong FEIR activity, and is an established reporter of chemical dynamics, such as the carbonyl or nitrile stretch. In our previous discussions, we have focused on predicting molecular and mode-specific FEIR activities. Among the most intense FEIR vibrations found in the brightest coumarins are primarily associated with conjugated C=C stretches, which collectively fall under the category of ring modes. These modes often remain unresponsive to chemical interactions, showing no discernible shifts in vibrational frequencies or intensities that would qualify them as effective FEIR probes. It is noteworthy that all the coumarins possess a lactone carbonyl group, which resonates in the spectral range of 1660 – 1730 cm^{-1}. Additionally, some coumarins, such as C314, C343, and C334, feature another carbonyl group as a ring substituent. In this context, we aim to compare the predictions of the FEIR activities associated with these carbonyl groups to the experimentally measured FEIR cross-sections across the coumarin series.

In Figure 5.16, we show the comparison between the DFT-calculated FEIR activities of the carbonyls (Eq. 4.23 without IR pump scaling) of all coumarins except C30 (unable to resolve carbonyl peak from noise), and their corresponding experimental FEIR cross-sections. The latter are obtained as fractional values of the overall FEIR cross-sections of the molecules, determined from two-pulse transients, averaged over the encoding delay range of $400 - 800$ fs. The fractions are determined as a ratio of the area under the carbonyl peak, obtained by fitting the peak to a Gaussian function to the total area under the spectrum. The spectrum used is also an average over the same range of encoding delays. These values are additionally normalized by the relative intensity of the IR pump pulse over the carbonyl, and the electronic lineshape value at $\omega_{vis} + \omega_{IR}$. While the correlation between the two quantities is not remarkable (fit shown as dashed line; $R^2 = 0.91$), there are a couple of aspects worth noting. First, there are consistent predictions of stronger FEIR activities of lactone carbonyls (circles) than the substituent carbonyls (rhombi). Furthermore, the model also predicts that C153 has the brightest lactone carbonyl, whose large FEIR activity is primarily attributed to its large Huang-Rhys factor as compared to the others (even larger than the C153 ring modes), and a strong vibrational transition dipole. The displacement of the excited electronic potential along the normal coordinates of a mode may have a correlation with the change in the electron density over the mode during the $\pi - \pi^*$ transition, as suggested tangentially in the literature.[124] We leave it at this speculation, due to the lack of any theory that suggests that these two quantities are indeed correlated.

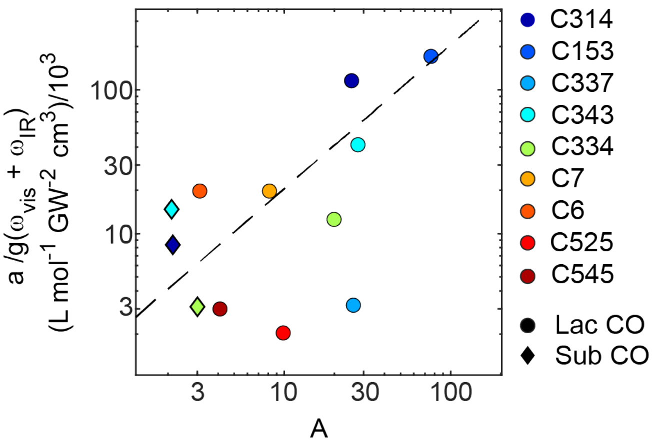

Figure 5.16: Correlation of the FEIR cross-sections of carbonyl modes in the coumarins to their predicted FEIR activities. The predictions suggest that lactone carbonyls systematically have larger FEIR activities than substituent carbonyls. Furthermore, the model correctly predicts the largest FEIR activity of C153 lactone carbonyl.

5.4 Conclusion

Following our analysis of the DFT-based computations of these matrix elements, one question that we ask ourselves is to what level of accuracy do they predict the FEIR activity since it is influenced by several time-dependent phenomena like vibrational population relaxation and multimode vibrational coherences, and the effect of finite light-matter interactions. We accounted for these through spectral simulations based on response function theory, building upon our prior work. These simulations provided valuable insights into the extent to which the calculations qualitatively capture the features observed in experimental spectra, serving as a testament to the accuracy of our Density Functional Theory (DFT)-based computation of FEIR activity, and also highlighting the challenges of predicting it, especially when confronted with time-dependent vibrational dynamics. The insights reveal how the electronic structure properties of a molecule can be used to anticipate its FEIR brightness, allowing us to classify it as a "good chromophore" for single-molecule

FEIR experiments. However, as previously mentioned, the FEIR-bright modes for most of these coumarins are conjugated, delocalized ring stretches, which are typically insensitive to molecular interactions. Consequently, they serve as poor vibrational reporters, posing a significant challenge in applying FEIR spectroscopy to probe chemical dynamics in solution. This is thought-provoking from the perspective of understanding the molecule. In the context of FEIR spectroscopy to probe chemical dynamics, a desirable vibrational reporter will possess a strong vibrational transition dipole, exhibit strong vibronic coupling, and is attached to a molecule with a high fluorescence quantum yield. Furthermore, it must be highly sensitive to structural changes through interactions with the environment. For example, a carbonyl mode that meets all these criteria will serve as a vibrational Stark probe at the single-molecule level, or a single-molecule probe to study hydrogen bonding interactions in solution, reporting on structural changes down at the length scale of a chemical bond. The computational methodology presented in this work leads us to carefully consider the molecular properties that can help predict the structure of designer chromophores for applications specific to studying such phenomena.

5.A Appendix: Supplementary material

5.A.1 Fit results for extracting integrated extinction coefficients of vibrations from FTIRs of coumarins

Each FTIR spectrum is fit to a sum of 'n' Lorentzian functions, 'n' is determined by the number of peaks in the spectrum with an ε value of > 500 M^{-1} cm^{-1}:

$$s(\omega) = \sum_{i=1}^{n} \frac{k^{(i)} \cdot b^{(i)}}{(\omega - \omega_0^{(i)})^2 + b^{(i)2}} \tag{5.A.1}$$

where b denotes the width of the Lorentzian function, and ω_0 represents the center frequency. The areas under individual Lorentzians are calculated from the fit parameter k, according to the relation $A = k\pi$. These areas represent the integrated molar extinction coefficients under peaks for individual normal modes, $A = \int \varepsilon(\omega) d\omega$, carrying the unit of L mol^{-1}cm^{-2} given the frequency is in cm^{-1}.

Figure 5.A.1 shows the FTIR spectra of the ten coumarins, along with the respective fits. The reconstructed Lorentzians are shown as shaded areas that represent the integrated extinction coefficients of the respective vibrations. The carbonyl modes for C153, C7, and C525 are spectrally well separated from the ring modes and are structured, probably due to Fermi resonance with a combination of low-frequency ring modes. The areas under them are calculated analytically by numerical integration. The lactone carbonyl of C314 shows a doublet centered around 1740 cm^{-1}. It is fit to two Lorentzians and the area under them is summed to obtain its total integrated ε.

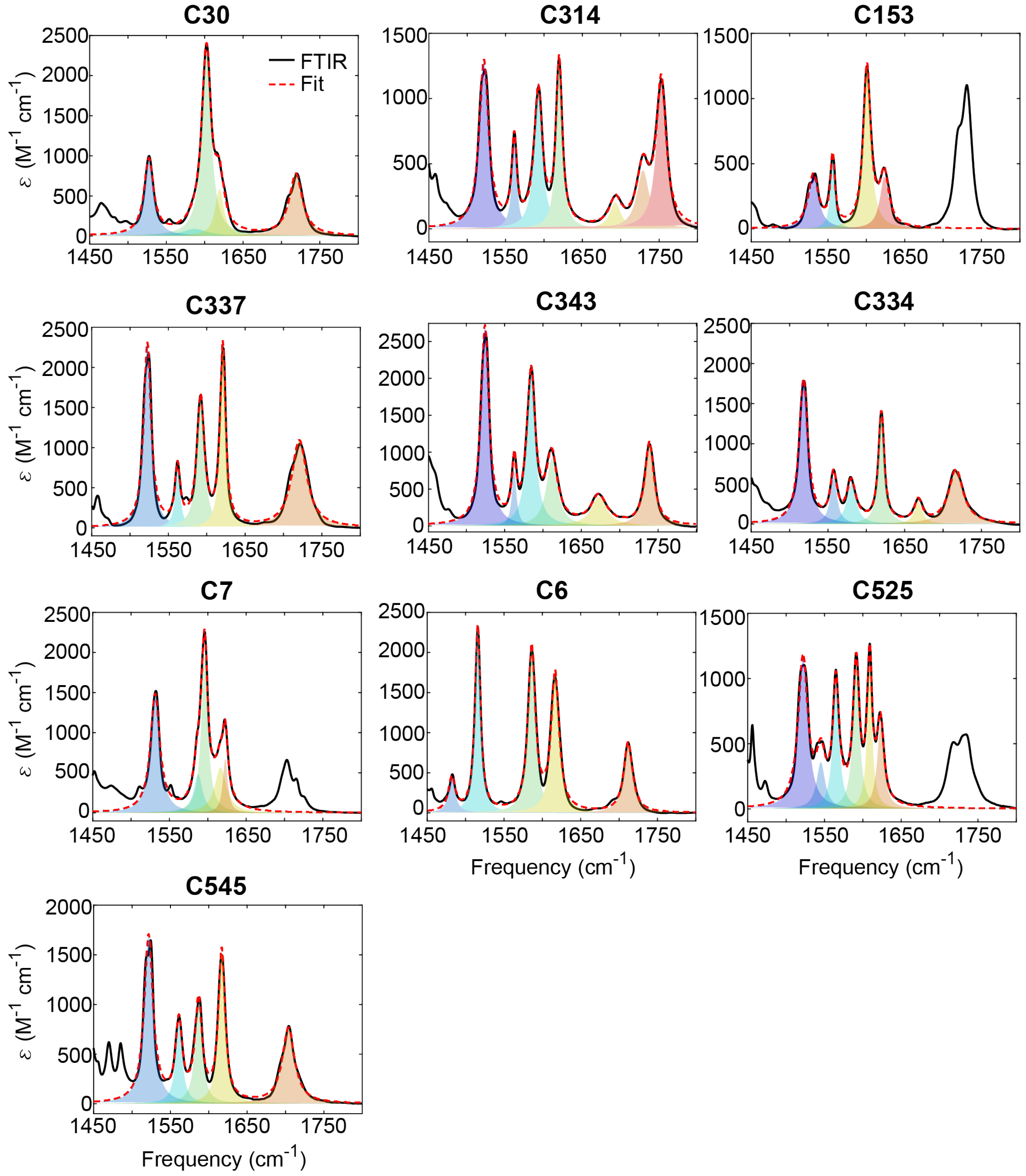

Figure 5.A.1: FTIRs of coumarins (black) fit to sum of ‘n’ Lorentzians (dashed red). ‘n’ is determined by the number of FTIR peaks with $\varepsilon > 500$ L mol^{-1}cm^{-2}. The shaded area under the Lorentzians represents the integrated molar extinction coefficient of the individual normal modes. For C153, C7, and C525, the area is determined analytically by numerical integration. For C314, the lactone carbonyl is fit to two Lorentzians, and their areas are summed.

5.A.2 IR intensities and Huang-Rhys factors of coumarin normal modes in the 6 µm region

This section contains the results of geometry optimization, frequency calculation, calculation of Huang-Rhys factors and their correlation with the squares of vibrational transition dipoles for all normal modes of all the coumarins studied. The snapshots of the normal modes shown for each coumarin (Figures 5.A.2 - 5.A.11) are the ones that lie within the spectral window of the IR pump pulse and have a significant $S|\mu|^2$ ($>$ 10 km/mol). The exception is Figure 5.A.9 that shows the two normal modes of C6 which are predicted to have strong FEIR activity but are not experimentally verified since they lie outside the spectral window of the IR pump used in the FEIR experiments. The C6 normal modes contributing to its FEIR response under our experimental conditions are shown in Figure 5.2 of the main text. The color-coded arrows in each snapshot denote the respective atomic displacements corresponding to the normal mode and the red arrow represents the vibrational transition dipole. The lengths of the red arrows are arbitrary, and not to be quantitatively mapped to the IR intensity. The lengths of the color-coded arrows are also arbitrary, but the relative lengths are directly proportional to the corresponding atomic displacements.

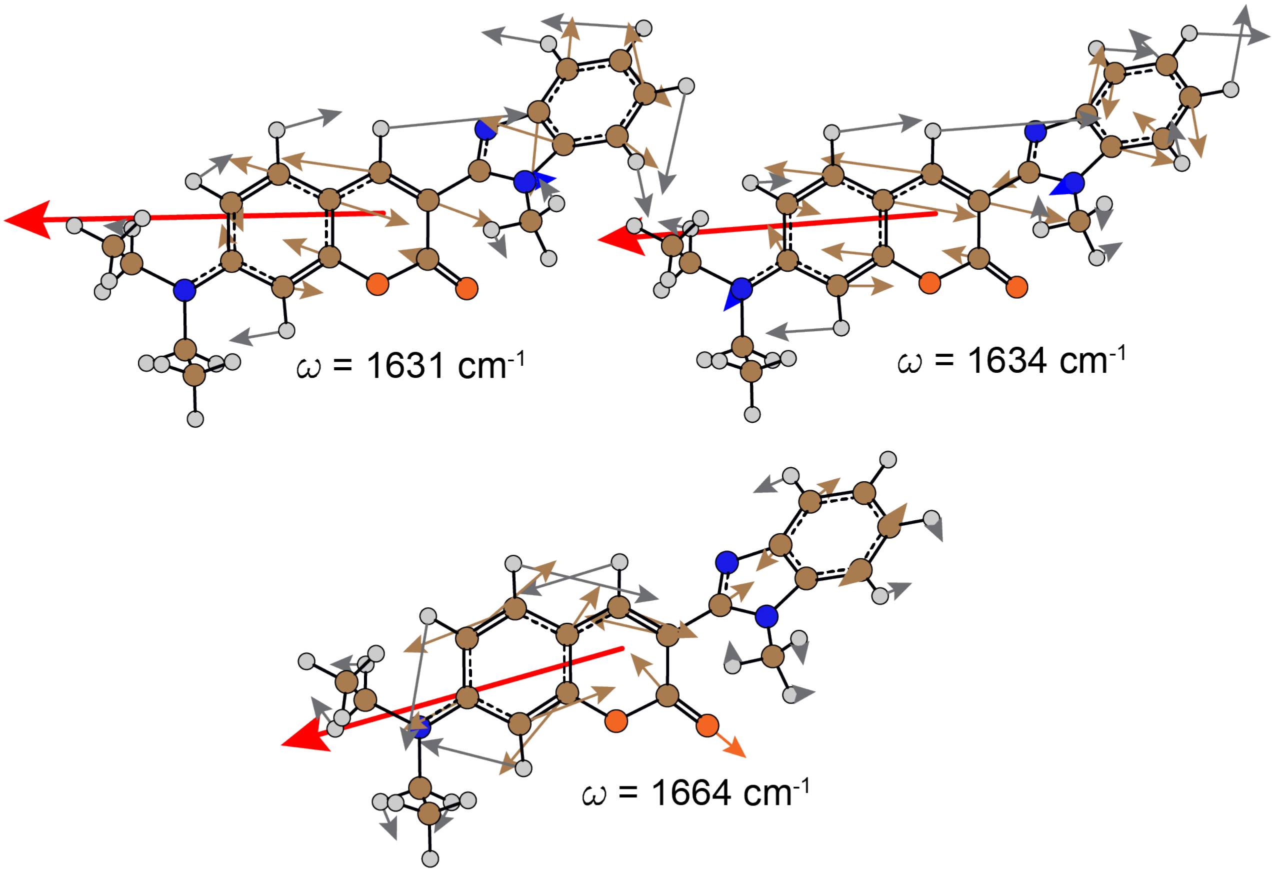

Figure 5.A.2: Snapshots of the normal modes of coumarin 30 in the spectral window of the IR pump pulse

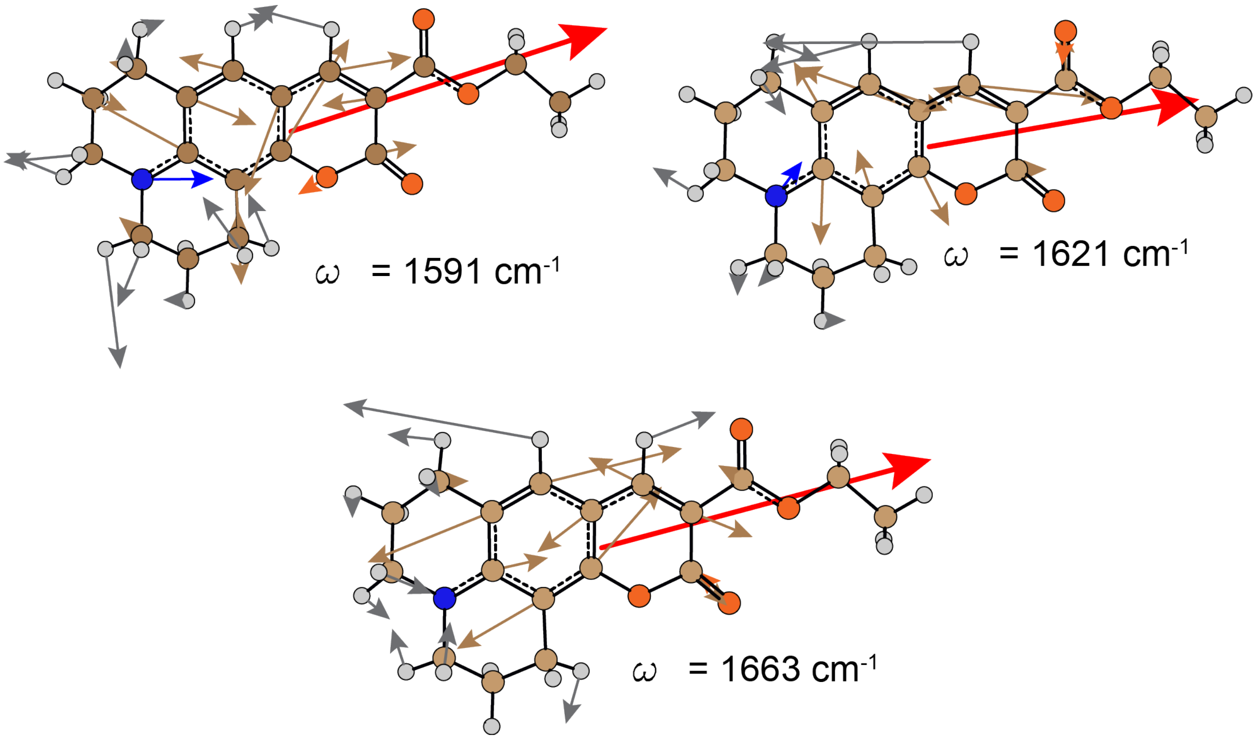

Figure 5.A.3: Snapshots of the normal modes of coumarin 314 in the spectral window of the IR pump pulse

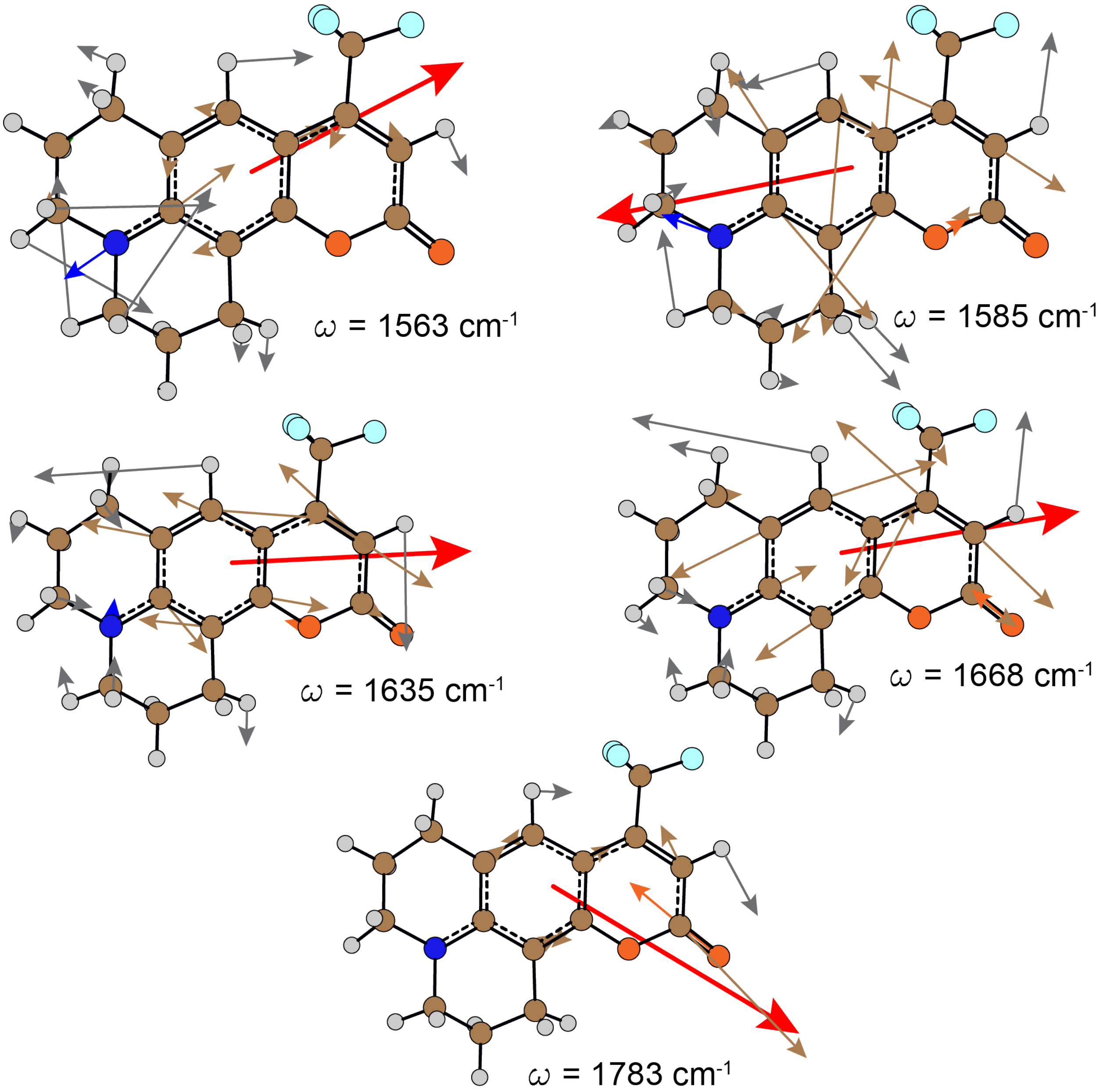

Figure 5.A.4: Snapshots of the normal modes of coumarin 153 in the spectral window of the IR pump pulse

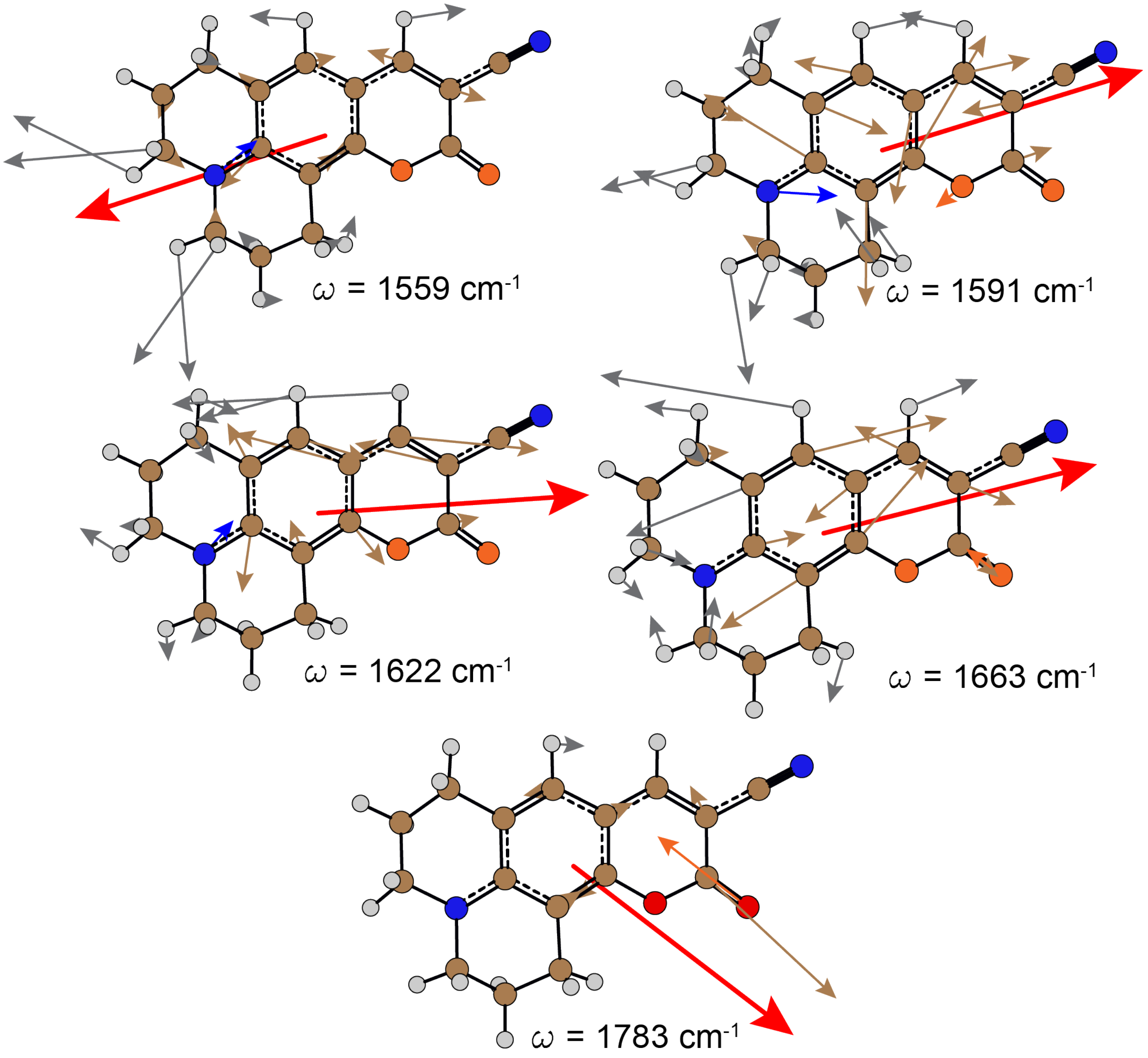

Figure 5.A.5: Snapshots of the normal modes of coumarin 337 in the spectral window of the IR pump pulse

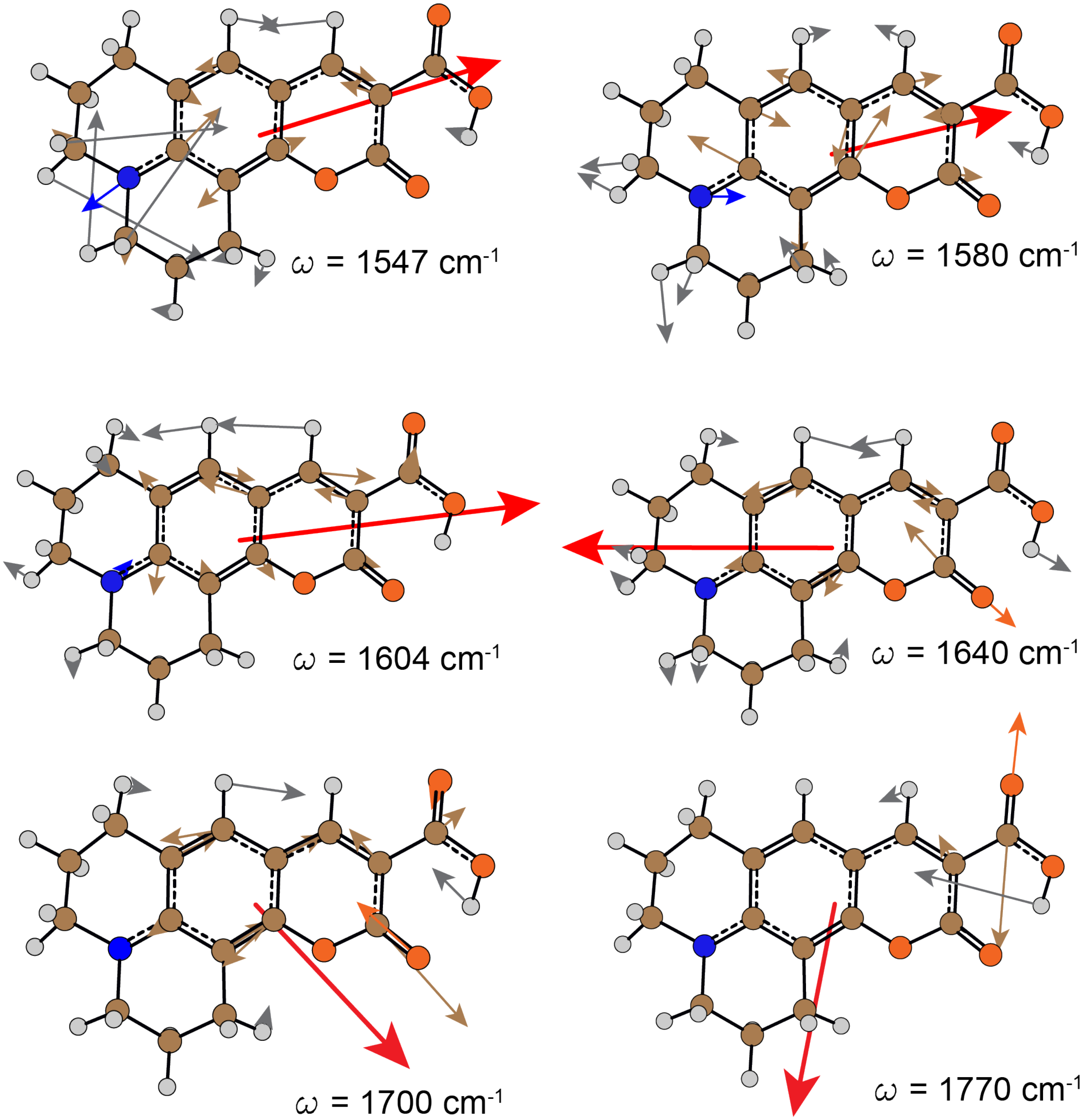

Figure 5.A.6: Snapshots of the normal modes of coumarin 343 in the spectral window of the IR pump pulse

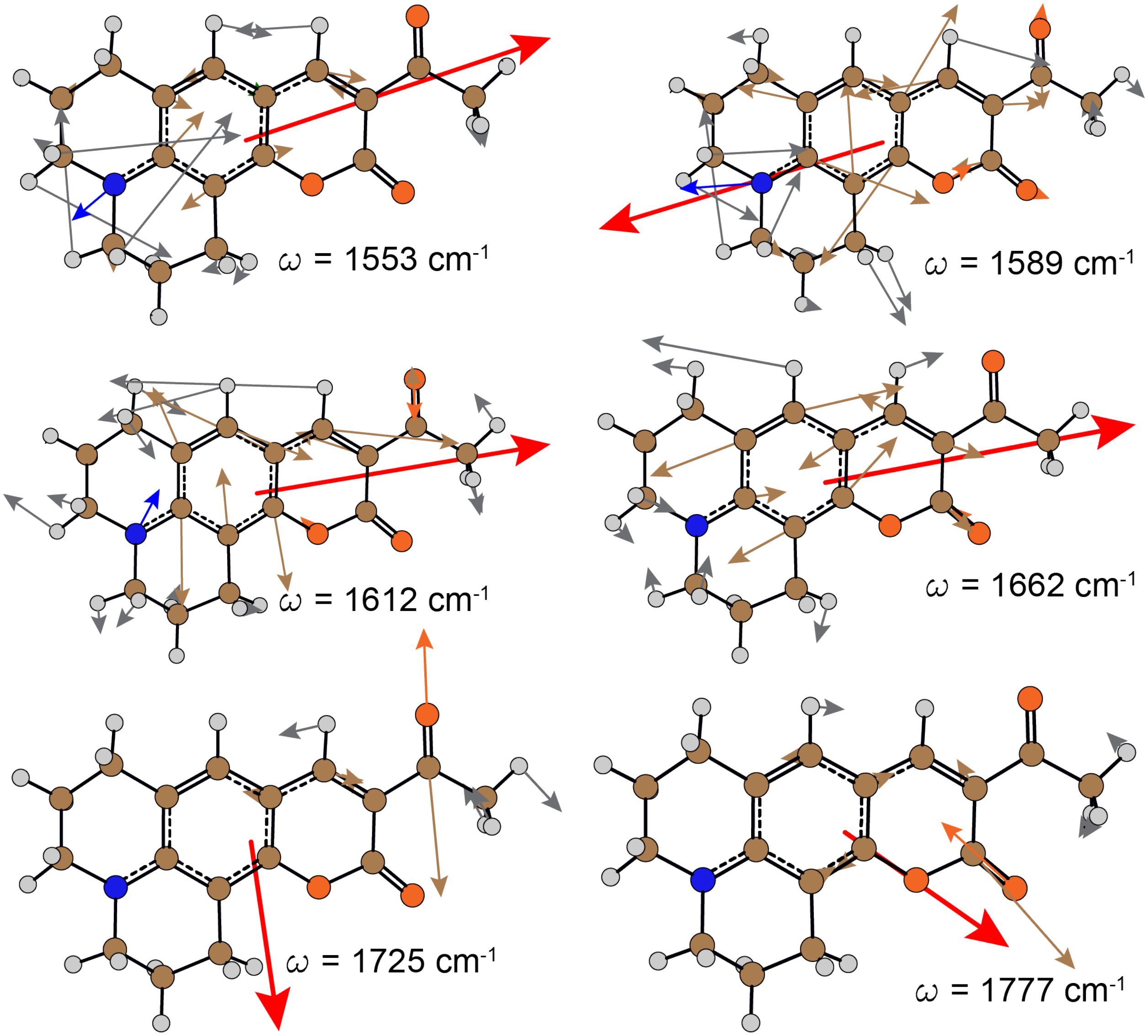

Figure 5.A.7: Snapshots of the normal modes of coumarin 334 in the spectral window of the IR pump pulse

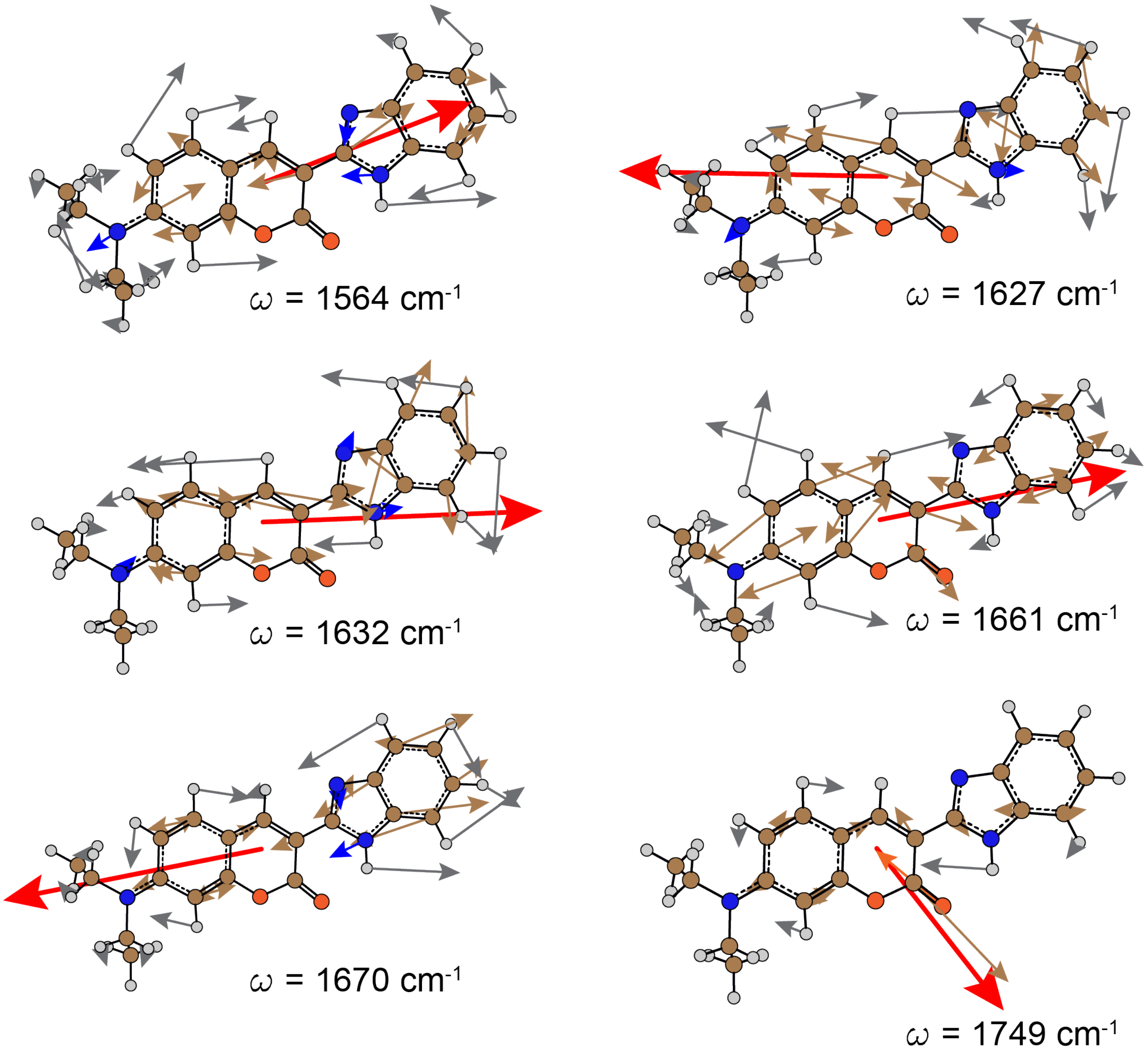

Figure 5.A.8: Snapshots of the normal modes of coumarin 7 in the spectral window of the IR pump pulse

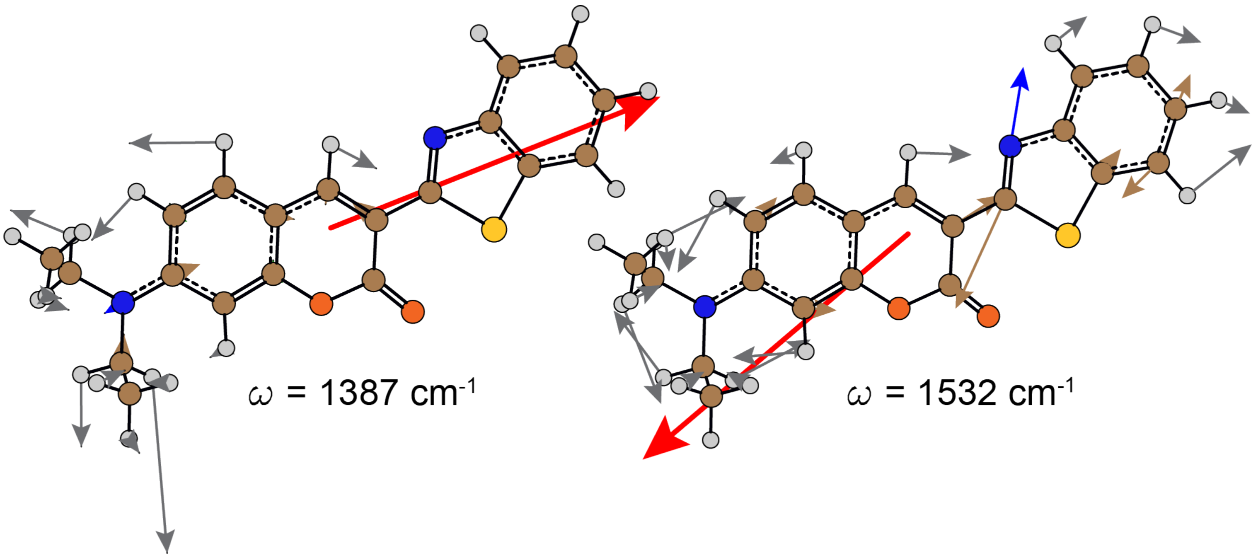

Figure 5.A.9: Snapshots of the two low-frequency ring modes of C6 that demonstrate a non-negligible FEIR activity but lie outside the spectral window of the IR pump.

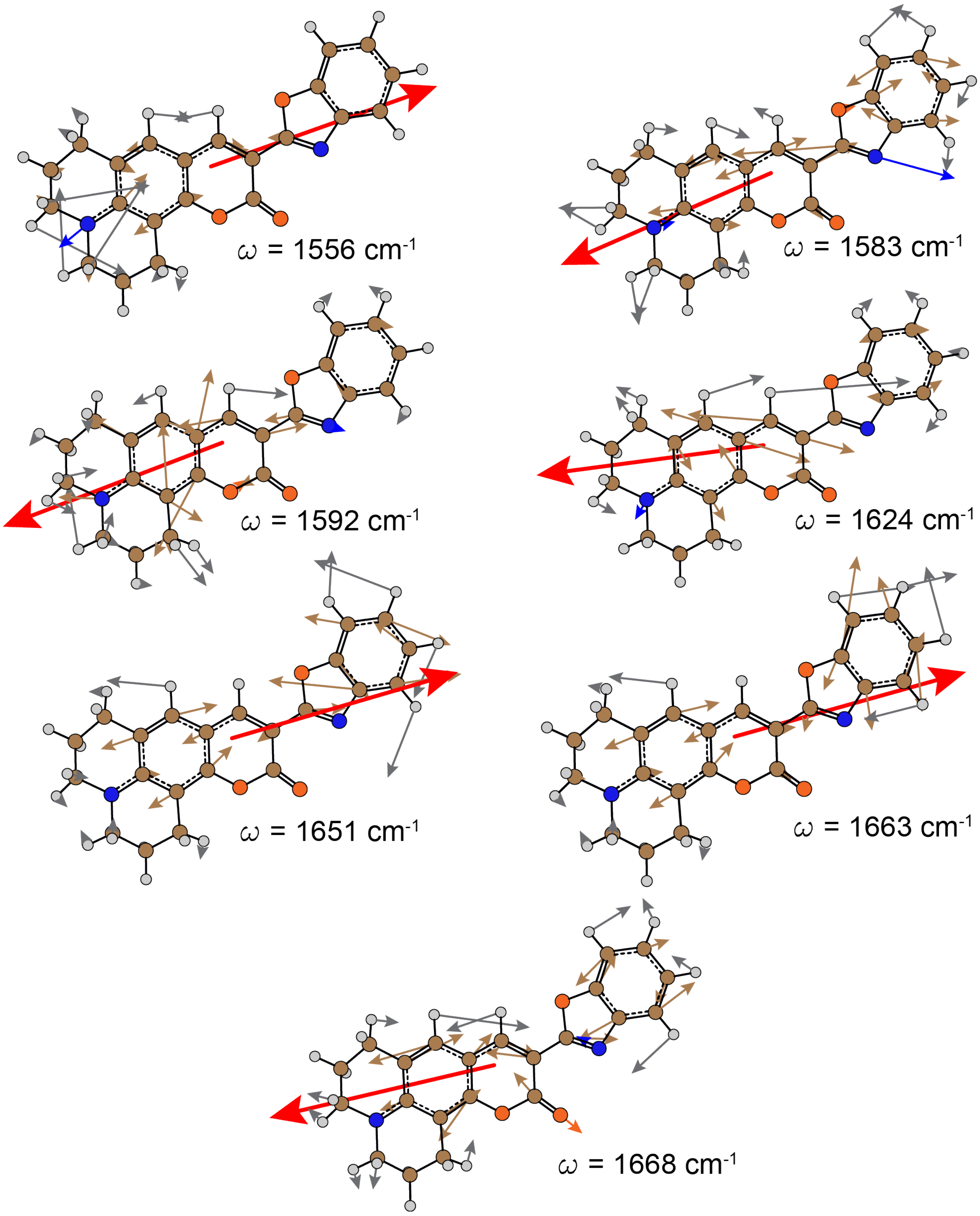

Figure 5.A.10: Snapshots of the normal modes of coumarin 525 in the spectral window of the IR pump pulse

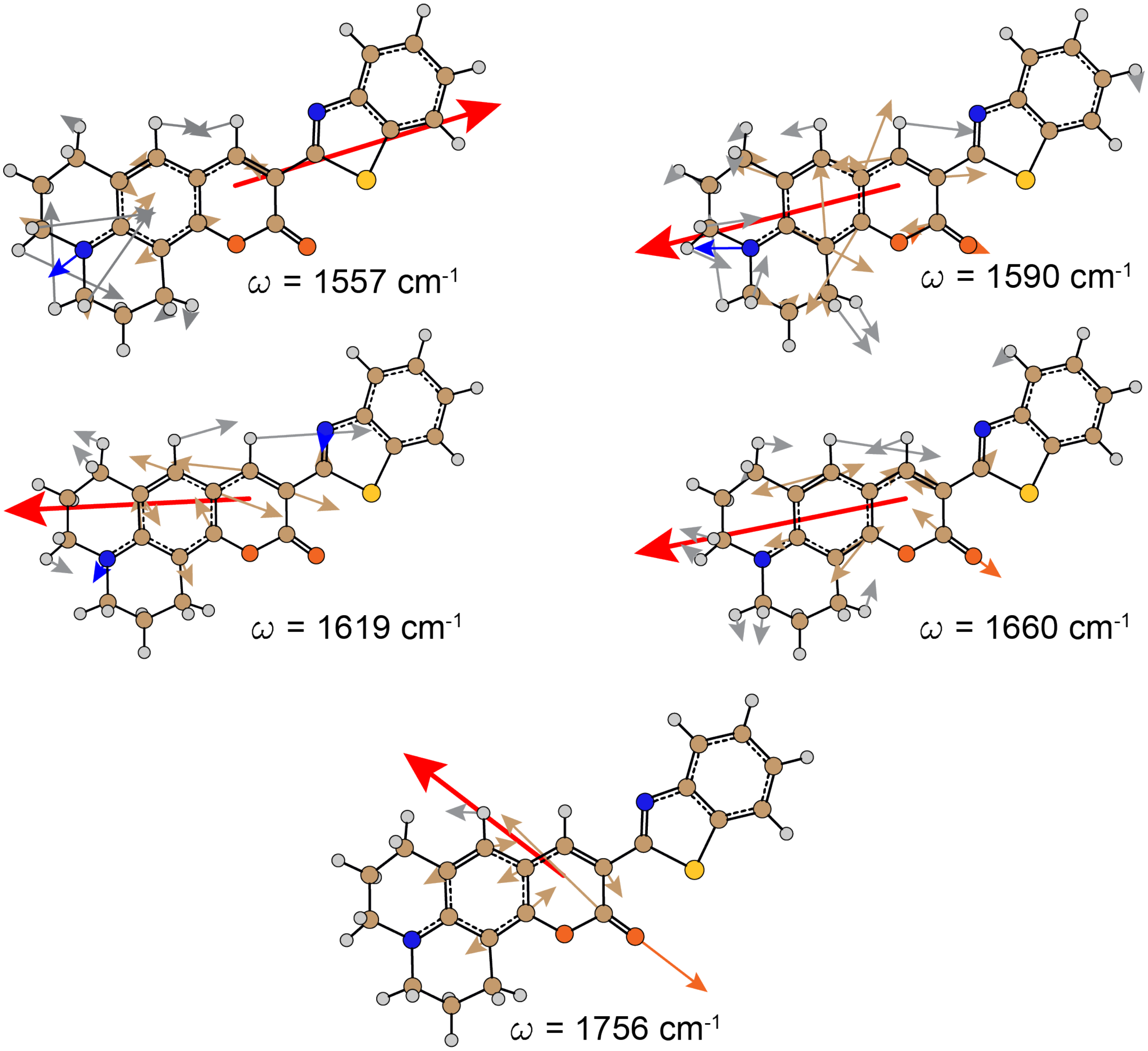

Figure 5.A.11: Snapshots of the normal modes of coumarin 545 in the spectral window of the IR pump pulse

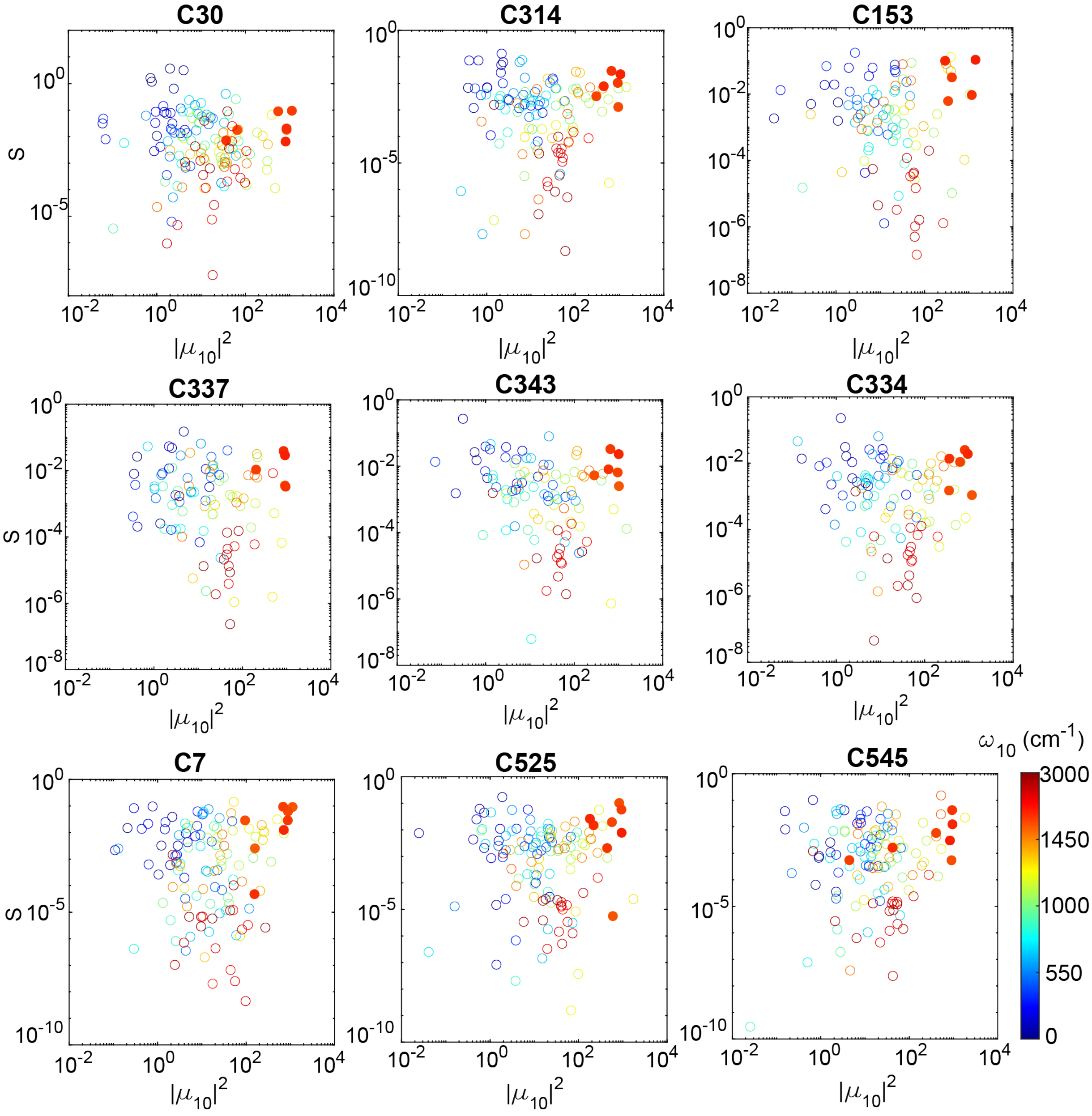

Figure 5.A.12: Correlation between the vibrational transition probabilities and the corresponding Huang-Rhys factors for coumarins. The plot for C6 can be found in Figure 5.4. Each circle represents a normal mode. The color indicates the corresponding vibrational resonance frequency, and the solid circles indicate the modes within our IR pulse envelope. For all the coumarins, the normal modes excited in FEIR experiments satisfy both the criteria of high transition probability and large Huang-Rhys factors, indicating strong vibronic coupling during the encoding transition. Consequently, coumarins behave as good FEIR probes.

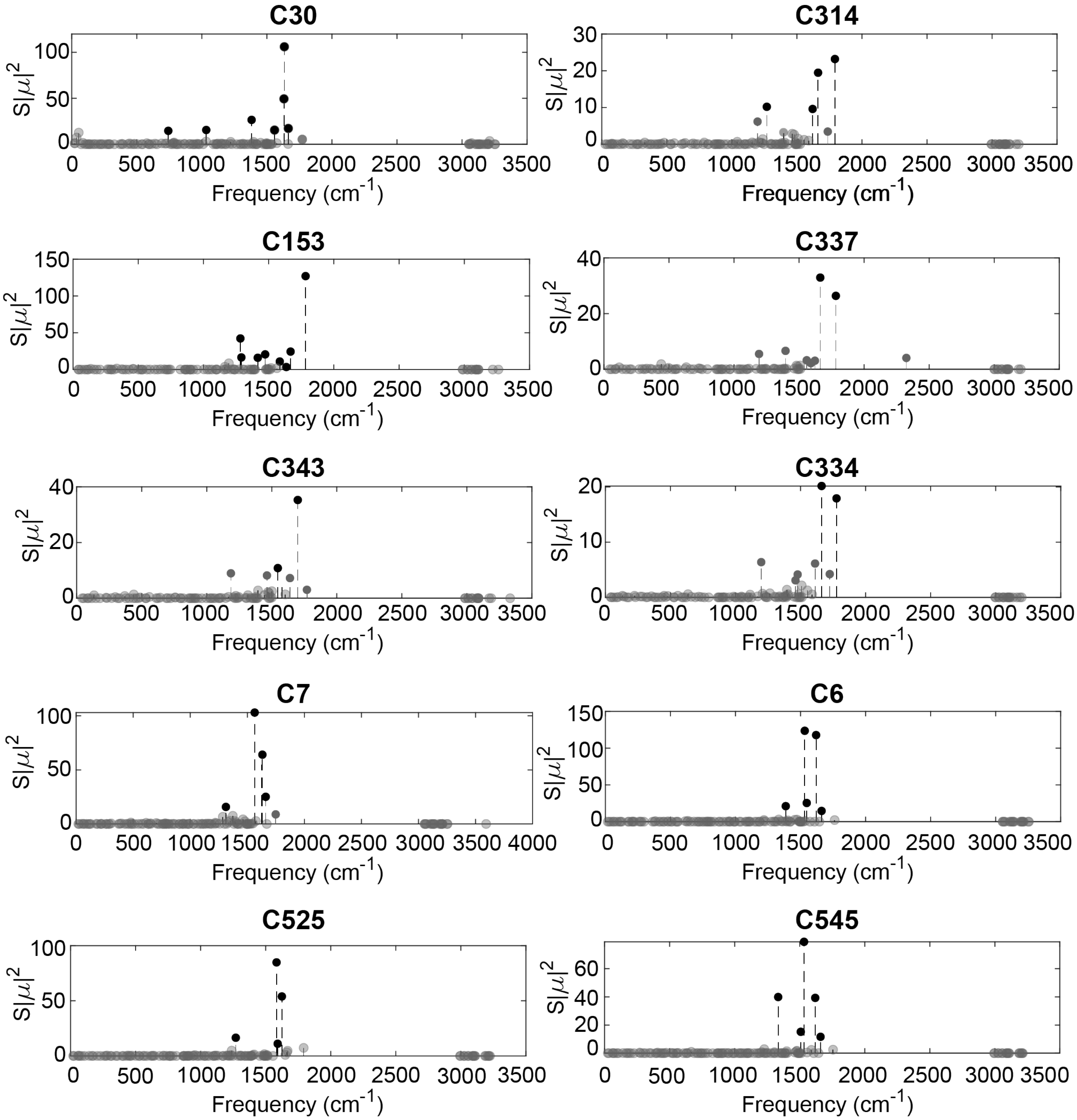

Figure 5.A.13: $S|\mu|^2$ plots of coumarins. The normal modes with $S|\mu|^2 > 10$ km/mol are shown in black and the ones shown in grey fall below this threshold.

Table 5.A.1 below shows the calculated ground state frequencies, vibrational transition dipole moments, and Huang-Rhys factors for the vibrations lying within the spectral window of the IR pump pulse, with $S|\mu|^2 > 10$ km/mol for all the coumarins studied. The corresponding values for the lactone carbonyls and any other carbonyl mode, if present, are also given, regardless of their $S|\mu|^2$ magnitude.

Table 5.A.1: Calculated frequencies, vibrational transition dipole moments, and Huang-Rhys factors of the vibrations lying within the IR pump spectral window, for coumarins. (*) indicates the vibrations lie beyond the bandwidth of IR pump, hence, their FEIR cross-sections have not been measured.

Dye	ω (cm^{-1})	$\lvert\mu\rvert^2$ (km/mol)	S	Dye	ω (cm^{-1})	$\lvert\mu\rvert^2$ (km/mol)	S
C30				**C334**	1553	1168	0.001
	1631	552	0.089		1589	355	0.001
	1634	1126	0.094		1612	629	0.011
	1664	852	0.020		1662	804	0.025
	1772	812	0.006		1725	361	0.014
					1777	943	0.019
C314	1591	299	0.003	**C7**	1564	1197	0.092
	1621	913	0.01		1627	880	0.063
	1663	659	0.029		1632	684	0.094
	1737	441	0.008		1661	871	0.029
	1792	1051	0.022		1670	154	4.7 x 10^{-5}
					1749	710	0.013
C153	1563	283	0.006	**C6**	*1387	741	0.029
	1585	344	0.032		*1532	541	0.228
	1635	970	0.009		1548	1177	0.022
	1668	242	0.1		1620	1437	0.082
	1783	1175	0.108		1662	1433	0.01
					1762	737	0.003
C337	1559	914	0.0003	**C525**	1556	595	5.6 x 10^{-6}
	1591	203	0.011		1583	827	0.103
	1622	943	0.003		1592	566	0.02
	1663	852	0.039		1624	928	0.058
	1783	915	0.029		1651	441	0.002
					1663	218	0.015
					1668	180	0.026
					1792	938	0.008
C343	1547	1322	0.008	**C545**	1557	898	5.4 x 10^{-4}
	1580	280	0.016		1590	403	0.006
	1604	1250	0.001		1619	927	0.042
	1640	760	0.009		1660	944	0.012
	1700	471	0.075		1756	828	0.003
	1770	750	0.004				

5.A.3 Comparison of results using different functionals (Coumarin 6)

To test the dependence of the choice of functional on the calculated FEIR activities, we performed electronic structure calculations on C6 using the long-range corrected functional ωB97XD with Def2TZVP triple zeta basis set. The same functional and basis set were used for calculations on the ground and first singlet excited states of the molecules. Table 5.A.2 summarizes the comparison of the energies in the ground and excited state minima, and electronic transition dipole moments for C6 using B3LYP/6-31G(d,p) (used in the main results) and ωB97XD/Def2TZVP. Table 5.A.3 shows the comparison of calculated frequencies of the four normal modes R1, R2, R3 and C=O, their IR intensities, Huang-Rhys factors and relative angles with the electronic transition dipole.

Both levels of theory result in optimized geometries in the ground and excited states with similar energies. The electronic transition dipole moments are also comparable. The new calculations show that there are two normal modes within the linewidth of R3, as compared to one. If we approximate the calculated anisotropy as the mean of the anisotropies of these two normal modes, it gives a value of 0.31, which is closer to the measured value of 0.27 than the calculated value of 0.39 given by B3LYP/6-31G(d,p) level of theory. This may hint at an improvement over the previous calculations. However, the IR intensity of R1 is underestimated by the long-range corrected functional. Keeping the degree of inconclusivity in mind, and considering that the optimized geometries are very similar for both levels of theory, we retain the results of B3LYP/6-31G(d,p) level of theory in the discussion in the main text.

Table 5.A.2: Comparison of energies of the minima of S_0 and S_1 electronic states, and transition dipole moments of C6 using two different functionals and basis sets

B3LYP/6-31G(d,p)			ωB97XD/Def2TZVP		
E (S_0) hartree	E(S_1) hartree		E (S_0) hartree	E(S_1) hartree	
-1431.18	-1431.09		-1430.83	-1430.72	
μ_{eg}(x)	μ_{eg} (y)	μ_{eg}(z)	μ_{eg} (x)	μ_{eg} (y)	μ_{eg} (z)
4.18	-0.25	-0.09	4.01	-0.33	-0.09

Table 5.A.3: Comparison of frequencies, IR intensities, Huang-Rhys factors, and relative orientations of transition dipoles of the normal modes of C6 from calculations using B3LYP/6-31G(d,p) (A) and ωB97XD/Def2TZVP (B) levels of theory

	ω_g (cm^{-1})		$\lvert\mu\rvert^2$(km/mol)		S		θ (relative angle with μ_e)	
	A	B	A	B	A	B	A	B
R3	1548	1574 1582	1177	1758 345	0.022	0.093 0.224	3.2	2.5 33.2
R2	1620	1662	1437	2158	0.082	0.195	19.0	18.3
R1	1662	1695	1433	770	0.010	0.014	6.7	1.4
C=O	1762	1813	737	842	0.003	3.3×10^{-4}	116.0	119.4

Chapter 6

Symmetry considerations for chromophore brightness in FEIR spectroscopy

Overview

The FEIR brightness of a normal mode in a chromophore is primarily governed by the strengths of the vibrational transition dipole and vibronic coupling. The latter is largely dependent on the symmetry of the normal mode in question. This causes the selection rules of FEIR spectroscopy to be closely related to those of resonance Raman spectroscopy (RRS). Briefly, for a molecule with a set of totally symmetric and non-totally symmetric normal modes, the excited state minimum is displaced only along the coordinates of the totally symmetric ones. Therefore, only those have a non-zero Franck-Condon factor, and consequently, a non-zero resonance Raman scattering cross-section. Owing to the vibronic nature of the encoding transition, this holds true for FEIR activity as well. In this chapter, we will discuss the FEIR selection rules from the perspective of group theory, and illustrate how they are shaped by the symmetry of the normal modes through a comparative study of

FEIR activity for coumarin 7, an asymmetric molecule, and proflavin, a molecule with C_{2v} point group symmetry, to argue about the substantial disparity in their FEIR brightness despite a striking similarity in their FEIR resonance conditions, and comparable vibrational transition dipole strengths and fluorescence quantum yields.

6.1 Introduction

We have presented a detailed description of the Franck-Condon factors (FCFs) in Chapter 4, and have demonstrated their role in shaping the FEIR selection rules in Chapter 5. Thus far, we have seen that the skeletal ring modes of organic chromophores like the coumarins, along with the lactone carbonyls of a few like C153, C337, and C343, exhibit strong FEIR activities. These are characterized by strong vibrational transition dipoles, together with large FCFs. In Chapter 5, we have shown that the FCFs are primarily determined by the excited state displacements along the normal coordinates, manifested through the Huang-Rhys factors. From the perspective of group theory, we know that these displacements only occur along totally symmetric normal coordinates, and therefore, only those normal modes have a non-zero FCF. This ties FEIR selection rules closely with those of resonance Raman spectroscopy (RRS).[125–127] However, our discussion in chapter 5, and Ref. [97], is entirely based on a set of chromophores from the coumarin family, which are asymmetric molecules. Therefore, by triviality, all their normal modes are totally symmetric. On the contrary, for a molecule with a higher order of symmetry, both totally symmetric and non-totally symmetric vibrations are present. One question that we might ask ourselves is, how does the symmetry of a normal mode influence its FEIR activity? To that end, in Section 6.2, we present a formal description of FEIR activity from the principles of group theory, arriving at a qualitative description of symmetry-allowed and symmetry-forbidden FEIR transitions. To illustrate this, in Section 6.3 we present a comparative study of the experimental FEIR brightness and cross-section, and computationally predicted FEIR activities for an asymmetric molecule, Coumarin 7 or C7 (C_1 point group), whose normal modes are all totally symmetric, and a molecule with a higher order of symmetry, Proflavin or PF (C_{2v} point group), which has a set of totally symmetric and non-totally symmetric normal modes. The key reason for choosing this particular pair of chromophores is that they exhibit a striking similarity in their FEIR resonance condition, and possess comparable electronic oscillator strengths. Both molecules are strongly fluorescent. The IR transition dipole moments corresponding to their normal modes are also comparable. Despite these, they exhibit a striking difference in their FEIR brightness, with C7 being ~ 16 times brighter than PF. The motivation for this chapter is to help identify FEIR-active vibrations from the character table of a molecule, in a way IR active and Raman active vibrations are identified. The discussion is expected to make the FEIR selection rules straightforward to comprehend across the Chemistry community, owing to the wide usage of character tables in molecular analysis.

6.2 FEIR selection rules from the perspective of group theory

From the perspective of group theory, for any transition to be symmetry allowed, the product of the irreducible representations of the initial state, the operator, and the final state, must be totally symmetric, or, in other words, must be the same as the highest symmetry representation of the point group (A in case of C_1, A_1 in case of C_{2v} and so on). This statement is summarized in the equation below, for a generic transition from an initial state to a final state brought about by the operator μ

$$\mu_{fi} = \langle i|\mu|f\rangle \tag{6.1}$$

For the transition moment integral μ_{fi} to be non-zero, the direct product of the irreducible representations of the individual terms in the integral must be totally symmetric.

$$\Gamma(i) \times \Gamma(\mu) \times \Gamma(f) = \Gamma(\text{Totally symmetric}) \tag{6.2}$$

In the context of FEIR spectroscopy, there are two consecutive transitions, beginning with the vibrational excitation $|g,0\rangle \rightarrow |g,1\rangle$, brought about by interaction with the IR pulse, followed by the encoding transition $|g,1\rangle \rightarrow |e,0'\rangle$ upon subsequent interaction with the visible or encoding pulse. The resulting FEIR transition dipole moment integral can therefore be represented as a product of three different integrals as shown in Equation 6.3

$$\mu_{\text{FEIR}} = \langle 0_g|\mu|1_g\rangle \cdot \langle 1_g|0_e\rangle \cdot \langle g|\mu|e\rangle \tag{6.3}$$

where, the first term represents the vibrational transition moment integral, and the second and third terms are factored out from the electronic transition moment integral, following the Born-Oppenheimer approximation. The second term represents the vibronic overlap integral (or, the Franck-Condon factor), and the third term is the pure electronic transition moment integral.

For μ_{FEIR} to be non-zero, the direct products of the irreducible representations for the individual integrals, that is, $\Gamma(vib) = \Gamma(0_g) \times \Gamma(\mu) \times \Gamma(1_g)$, $\Gamma(vibr) = \Gamma(1_g) \times \Gamma(0_e)$, and $\Gamma(el) = \Gamma(g) \times \Gamma(\mu) \times \Gamma(e)$ must be individually totally symmetric. Whether a vibrational transition is symmetry allowed will then depend on the product

$$\Gamma(vib) = \Gamma(0_g) \times \Gamma(\mu) \times \Gamma(1_g) \tag{6.4}$$

The vibrational ground state of a molecule is always totally symmetric because it must be invariant under all symmetry operations of the molecule, ensuring its stability and lowest energy configuration. Therefore, the symmetry of the vibrational transition matrix element is determined by the product of the symmetry of the operator (μ) and the final state ($\Gamma(1_g)$). To illustrate this, let us take a look at the C_{2v} point group character table:

Table 6.1: Character table of C_{2v} point group

	E	C_2	$\sigma_v(xz)$	$\sigma_v(yz)$		
A_1	1	1	1	1	z	x^2, y^2, z^2
A_2	1	1	-1	-1	R_z	xy
B_1	1	-1	1	-1	x , R_y	xz
B_2	1	-1	-1	1	y , R_x	yz

The multiplication rules are: $A \times A = A$, $A \times B = B$, $B \times A = B$, $B \times B = A$, and, for the subscripts, $1 \times 1 = 1$, $1 \times 2 = 2$, $2 \times 2 = 1$. From the table, we deduce the symmetry of μ_z, μ_x and μ_y to be A_1, B_1 and B_2 respectively. Applying the multiplication rules stated above to each kind of normal mode, we have the following results:

- Normal modes with A_1 symmetry

  $A_1 \times A_1 + A_1 \times B_1 + A_1 \times B_2 = A_1 + B_1 + B_2$

  We see that the product has at least one totally symmetric component, arising from the interaction between the vibrational states and the z component of the dipole moment operator, making vibrational transitions of A_1 normal modes symmetry allowed.

- Normal modes with A_2 symmetry

  $A_2 \times A_1 + A_2 \times B_1 + A_2 \times B_2 = A_2 + B_2 + B_1$

  No component is totally symmetric, and therefore vibrational transitions for A_2 normal modes are symmetry forbidden.

- Normal modes with B_1 symmetry

  $B_1 \times A_1 + B_1 \times B_1 + B_1 \times B_2 = B_1 + A_1 + A_2$

  There is at least one totally-symmetric component, now arising from the interaction with the x component of the dipole moment operator, making these vibrational transitions symmetry allowed.

- Normal modes with B_2 symmetry

  $B_2 \times A_1 + B_2 \times B_1 + B_2 \times B_2 = B_2 + A_2 + A_1$

  This time the totally-symmetric component arises from the interaction with the y component of the dipole moment operator, making vibrational transitions of B_2 normal modes symmetry allowed.

Up to now, we have successfully used the character table to select the normal modes that can undergo symmetry-allowed IR transitions. What follows is the encoding transition, which brings about even more stringent selectivity based on symmetry arguments, eventually shaping the FEIR selection rules. To understand this, let us take a look at the symmetry of the matrix elements representing the encoding transition: $\langle g, 1_g|\mu|e, 0_e\rangle$. Under the Born-Oppenheimer approximation, this factors into the Franck-Condon factor $\langle 1_g|0_e\rangle$ and the electronic transition dipole moment μ_{eg}. Note that for this transition to be symmetry allowed, $\Gamma(vibr) = \Gamma(1_g) \times \Gamma(0_e)$ and $\Gamma(el) = \Gamma(g) \times (\Gamma(\mu) \times \Gamma(e)$ must individually be totally symmetric. In the case of the C_{2v} point group, they must be individually A_1. The symmetries of the vibrational states in the ground and excited electronic states together determine the irreducible representation of the vibronic coupling term. Assuming that the electronic transition is symmetry allowed ($\Gamma(g) \times \Gamma(\mu) \times \Gamma(e) = \Gamma(\text{totally symmetric})$), and knowing that the ground vibrational state of any given electronic state is totally symmetric, the symmetry of the encoding transition is entirely determined by the symmetry of the vibrationally excited state of the ground electronic state ($\Gamma(1_g)$). For instance, in the case of C_{2v} symmetry, amongst the IR active normal modes A_1, B_1 and B_2, it is only the A_1 modes that yield a totally symmetric representation for $\Gamma(enc)$, thereby, surviving the encoding transition moment integral.

This analysis can be generalized to any point group to identify the normal modes that can undergo symmetry-allowed FEIR transitions. The generalization also ties the FEIR selection rules closely with those of resonance Raman spectroscopy (RRS),[125] where, under the Condon approximation, the magnitude of the polarizability tensor is primarily shaped by the Albrecht A term, which is non-zero only for totally symmetric vibrational modes, implying that it is only along the normal coordinates of these modes that the electronically excited state potential is displaced, giving rise to a non-zero FCF.

6.3 Comparative study of FEIR brightness of Coumarin 7 and Proflavin

As stated before, the results presented in Chapter 5 show that coumarins, in general, are good FEIR candidates. This is because coumarins are asymmetric molecules (i.e. belong to the C_1 point group), and therefore, all normal modes are trivially totally symmetric. As a result, the FEIR transitions are all symmetry allowed. The quantitative FEIR activity, however, is shaped by an interplay of the molecular factors. Naturally, a question that arises at this point is about the fate of prospective FEIR candidates that have a higher order of symmetry. In such cases, the molecule will possess both totally and non-totally symmetric normal modes. To illustrate the role that normal mode symmetry plays in determining the overall FEIR brightness of a molecule, we present a comparative study of FEIR cross-sections and predicted FEIR activities of the asymmetric C7, and the C_{2v} symmetric PF. The molecular structures are shown in Figure 6.1.

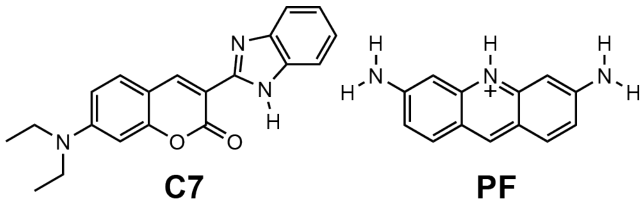

Figure 6.1: Molecular structures of C7 and PF.

6.3.1 Steady-state characterization

We begin our discussion with the motivation for choosing this pair of chromophores for this work. Shown in Fig. 6.2a are the UV/Vis absorption spectra of C7 and PF. With the visible and IR excitation frequencies tuned to 19360 cm^{-1} (or, 516.5 nm) and 1600 cm^{-1}, respectively, the absorption spectra show a striking similarity in their FEIR resonance condition. The values of the electronic lineshape function ($g(\omega)$) at $\omega_{vis}+\omega_{IR}$ are 7.23×10^{-5} cm and 8.45×10^{-5} cm for C7 and PF respectively. The fluorescence quantum yield of C7 in acetonitrile was measured to be 0.86,[90] while that of PF was measured as 0.47, with C7 in methanol as the reference standard. The lower quantum yield of PF is evident in their fluorescence spectra, shown in panel b, normalized with respect to the maximum intensity for C7.

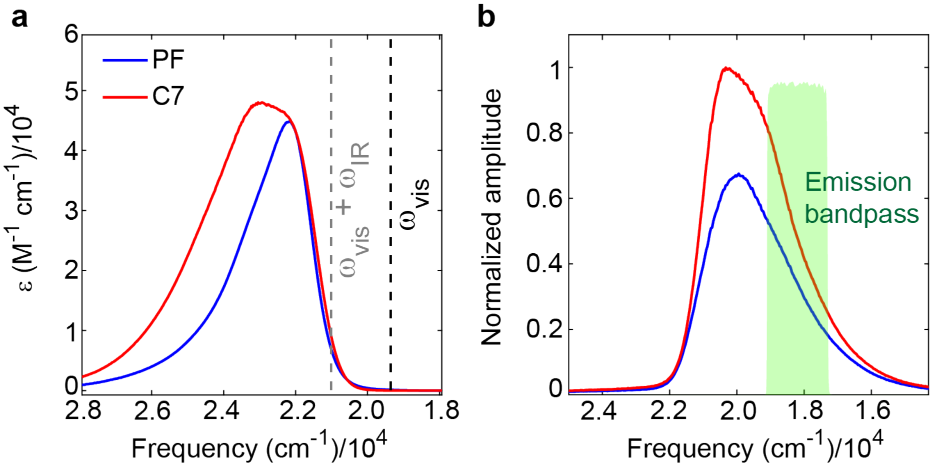

Figure 6.2: UV/vis and fluorescence measurements of C7 and PF. (a) UV/Vis absorption spectra of C7 (red) and PF (blue) exhibit a striking similarity in FEIR resonance condition with visible excitation tuned to 19360 cm^{-1} (black dotted line). The visible + IR double excitation frequency is shown as a grey dotted line (IR pump tuned to 1620 cm^{-1}). (b) Fluorescence spectra of C7 and PF, normalized with respect to the maximum intensity of C7. The transmission spectrum of the fluorescence bandpass filter used is shown as a green-shaded area.

Figures 6.3a-b show the FTIR spectra of C7 and PF, respectively, overlaid with the respective frequency stick spectra from DFT calculations. The latter were performed on the ground state optimized geometries shown in panels c-d. The details of the functionals and basis set used for the calculations are shared in Section 6.5. Both the FTIR and the DFT-calculated spectra are normalized with respect to the maximum amplitude in the 1450 - 1750 cm^{-1} region. The absolute computed values of μ^2 for the normal modes are given in Table 6.2. The results for C7 have already been reported in the supplementary material of Ref. [97], where we have also reported the predicted FEIR activities of the normal modes. For PF, we identified 7 normal modes in the 1550 - 1750 cm^{-1} region, based on the DFT-calculated frequencies. Out of these, four normal modes are distinguishable in the FTIR spectrum as peaks at 1575 cm^{-1}, 1605 cm^{-1}, the highest amplitude peak at 1637 cm^{-1}, and a shoulder at 1650 cm^{-1}. The remaining three normal modes have negligible amplitude, and we suspect that they are convoluted within the broad lineshapes of the four distinguishable peaks. The snapshots of these normal modes are shown in Figure 6.4. Panels a-b collectively represent the FTIR peak R4. Panel c represents the R3. Panels d-e collectively represent the broad FTIR peak R2, and f-g represent the shoulder R1. The DFT frequencies are scaled by 0.973, the slope of the fit for the correlation between the calculated and experimental frequencies (see Appendix 6.A.1).

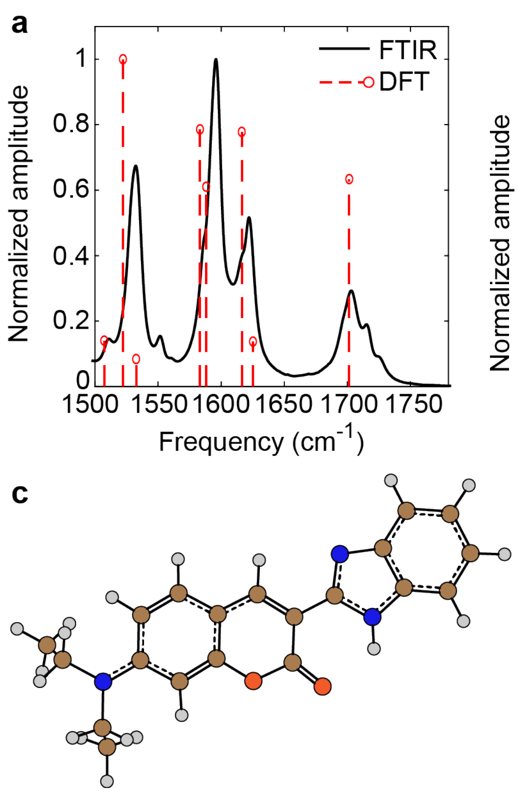

Figure 6.3: Vibrational measurements of C7 and PF. The FTIR spectra of C7 (a) and PF (b), both acquired in deuterated acetonitrile solvent, are shown in black, and the DFT-calculated stick spectra are shown in red. All spectra are normalized with respect to the maximum amplitude in the 1450 - 1750 cm^{-1} region. The DFT-calculated frequencies are scaled by a factor of 0.973. c - d show the optimized geometries of the ground state for C7 and PF. Atoms are color-coded as grey (H), brown (C), orange (O), and blue (N).

For organic chromophores like the ones discussed in this thesis, the magnitudes of

FCFs are primarily determined by the displacement of the excited state potential relative to the ground state along the normal mode coordinates, with vibrational frequency changes in the excited electronic state, and Duschinsky mixing playing insignificant roles. The dimensionless displacements are conveniently expressed as Huang-Rhys factors (S) according to Eq. 4.15, which serve as a fairly reasonable approximation for $\texttt{FCF}^2$ for $S < 0.1$. Therefore, the magnitude of $S|\mu|^2$ serves as a metric for FEIR activity of normal modes within a chromophore. For this product to be large, the normal mode must possess a strong IR transition dipole and, simultaneously, a large Huang-Rhys factor. At this point, we draw an analogy between the selection rules of FEIR and resonance Raman spectroscopy (RRS). The Raman polarizability tensor is expressed as the sum of Albrecht terms, $\alpha_{if} = A_{if} + B_{if} + C_{if}$. The Albrecht A term accounts for description under the Condon approximation and the remaining terms B and C represent the non-Condon contributions.[125,128,129] In his paper on the theory of Raman intensities[125], Albrecht has established that for molecules that do not undergo a change of symmetry between the ground and the excited electronic states, the excited state potential is displaced only along the coordinates of the totally symmetric normal modes, therefore, being the only ones with a non-zero FCF. Consequently, the selection rule for resonance Raman spectroscopy is strongly tied to the normal mode symmetry. The same argument holds for the encoding transition of FEIR, owing to its vibronic nature.

Symmetric molecules like PF (C_{2v}) have a set of totally symmetric and non-totally symmetric vibrations. PF has 78 normal modes in total, out of which 67 are IR active. Belonging to the C_{2v} point group, these are denoted by the symbols A_1, B_1, and B_2. The remaining 11 belong to A_2 symmetry, and their IR transitions are symmetry forbidden. From the character table, it can be assessed that A_1 labeled normal modes involve atomic displacements along the z axis, shown in Figure 6.4a, which is coincidentally the principal axis of symmetry for PF (C_2). These are totally symmetric, and there are 27 such modes.

The remaining 40 are non-totally symmetric (B_1 and B_2). Out of these, 26 normal modes involve atomic displacements along the long molecular axis, marked as x in Figure 6.4a. The remaining 14 modes involve out-of-plane ring bending motions. Figure 6.4 shows the snapshots of atomic displacements corresponding to the normal modes on the ground state optimized geometry of PF which lie within the spectral window of the IR pump pulse used in our experiments.

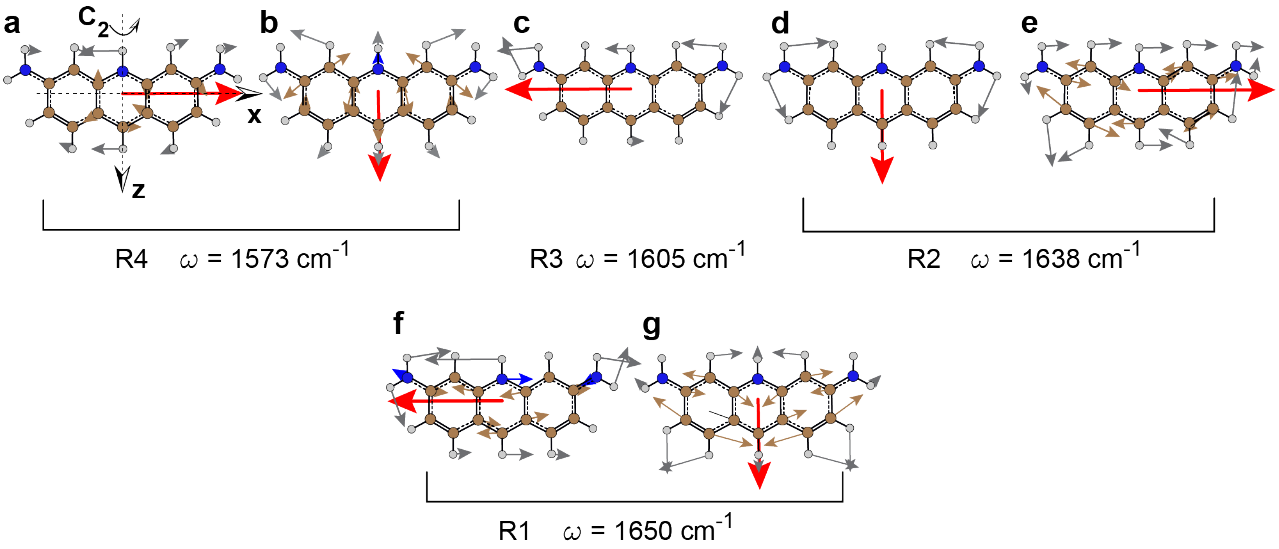

Figure 6.4: Atomic displacement snapshots corresponding to PF normal modes lying within the IR pump spectral window. Atoms and the corresponding displacement vectors are color-coded as grey (H), brown (C), and blue (N). The transition dipole moments are shown in red. The magnitude of the vectors are relatively scaled.

Due to the constraints imposed by the molecular structure, the totally symmetric vibrations involve relatively small atomic displacements along the principal axis of symmetry. These are characterized by large Franck-Condon factors but weak vibrational transition dipoles. The 26 B_1 modes involve fairly large atomic displacements along the long molecular axis (x). Consequently, these have strong vibrational transition dipoles, but, owing to their non-totally symmetric nature, are characterized by weak FCFs. The B_2 modes are non-totally symmetric and, therefore have weak FCFs, and small atomic displacements result in fairly weak vibrational transition dipole moments. The ones shown in panels a, c, e, and f are non-totally symmetric modes, while b, d, and g are totally symmetric. These are summarized in Table 6.2.

Table 6.2: DFT-calculated characteristics of PF and C7 normal modes lying within the IR pump spectral window

	ω_{exp} (cm^{-1})	ω_{calc} (cm^{-1})	S	$\|\mu\|^2$ (km mol^{-1})	Symmetry
PF	1573	1625	1.4×10^{-10}	711	B_1
		1628	0.037	72	A_1
	1605	1657	2.7×10^{-11}	1063	B_1
	1637	1666	9.5×10^{-4}	115	A_1
		1668	7.1×10^{-12}	2293	B_1
	1655	1694	3.6×10^{-13}	764	B_1
		1708	1.6×10^{-3}	151	A_1
C7	1531	1564	0.092	1120	A
	1587	1627	0.663	880	A
	1596	1632	0.094	684	A
	1617	1661	0.029	871	A
	1623	1670	4.7×10^{-5}	154	A
	1703	1749	0.012	710	A

6.3.2 Correlation between Huang-Rhys factor and IR transition dipole

While the magnitudes of the IR transition dipoles are of the same order as reported for the coumarins,[97] the Huang-Rhys factors of the non-totally symmetric vibrations are negligible. The totally symmetric vibrations, like the one at $\omega_{calc} = 1628$ cm^{-1}, despite having comparatively larger Huang-Rhys factors, have relatively weak transition dipole moments. On the contrary, all normal modes of C7 are totally symmetric, and, consequently, have fairly large Huang-Rhys factors. Furthermore, the modes lying in the $6\mu m$ region involve conjugated ring stretches extending along the length of the molecule, and are associated with strong IR transition dipoles. These values have been previously reported in Ref. [97], and also in Table 6.2 for a direct comparison with PF. The consequence of normal mode symmetry in determining FEIR activity is further highlighted in the scatter plots of S vs. $|\mu|^2$ for C7 and PF in Fig. 6.5

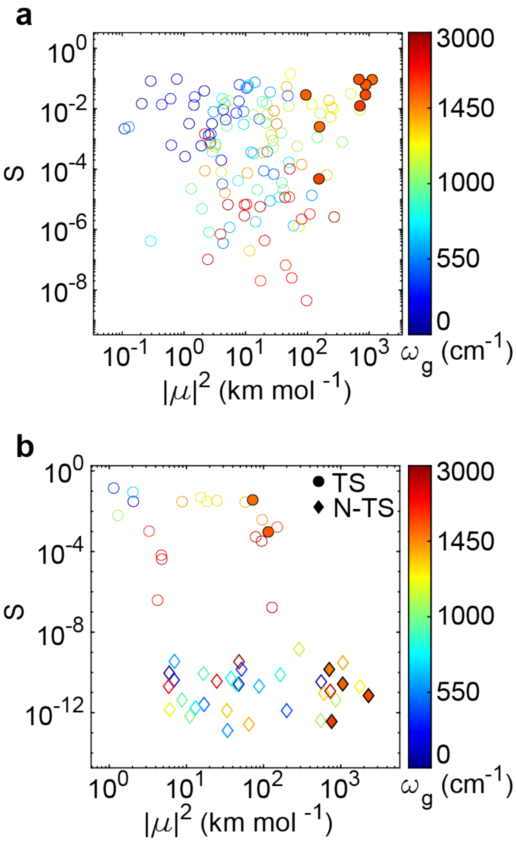

Figure 6.5: Scatter plots of S vs. $|\mu|^2$ for C7 and PF. Each point represents a normal mode, color-coded according to their resonance frequencies.The modes lying within the IR pump spectral window are shown in solid. (a) For C7, all modes are totally symmetric. (b) For PF, the totally symmetric modes are shown in circles, and the non-totally symmetric modes are shown in diamonds.

The single-molecule sensitivity of C7[90] is a consequence of its large FEIR cross-section, which is in turn a result of all its normal modes being totally symmetric, resulting in a barely-nil correlation between the Huang-Rhys factors and the IR transition dipole moments, as evident from Figure 6.5a. However, the normal modes within the IR pump spectral window all lie in the top right quadrant, implying that they simultaneously satisfy the requisites of large FCFs and strong vibrational transition dipole moments. On the contrary, for PF (Figure 6.5b) we notice an anti-correlation between S and $|\mu|^2$. The totally symmetric modes (A_1) have large characteristic S values (consequently, large FCFs), while the B_1 modes, primarily involving ring stretches along the long molecular axis, have large $|\mu|^2$ values. As a result, not one vibration can simultaneously satisfy both the requisites for high FEIR activity.

6.3.3 Comparison of FEIR cross-sections and predicted FEIR activities of C7 and PF

Despite having similar FEIR resonance condition, vibrational transition dipole moments, and comparable electronic oscillator strengths (1.13 for C7 and 0.87 for PF, computed using TDDFT), the FEIR cross-section of PF is measured to be ~ 16 times smaller than that of C7. This is shown in Figure 6.6b, where the bar chart represents the FEIR cross-sections of PF and C7, normalized with respect to the respective values of lineshape functions at $\omega_{vis} + \omega_{IR}$. These values are derived from the corresponding two-pulse FEIR transients shown in panel a, averaged over a 400 fs window containing the maxima. Although the fluorescence quantum yield of C7 (0.86) in deuterated acetonitrile is roughly double that of PF (0.47), it cannot alone account for this ~ 16 factor difference. The disparity in the FEIR cross-section between these two dyes is qualitatively reproduced in the prediction of their FEIR activities, shown as a bar chart comparison in Figure 6.6b. The overall FEIR activity of the molecule is calculated as $A = \sum_i A_i$, with the sum representing all the modes lying within the IR pump spectral window.[97] A_i's represent FEIR activities of individual normal modes, calculated according to Eq. 4.23. In accordance with the experimental conditions, we have used $Y_{pol} = Y_{\parallel}$.

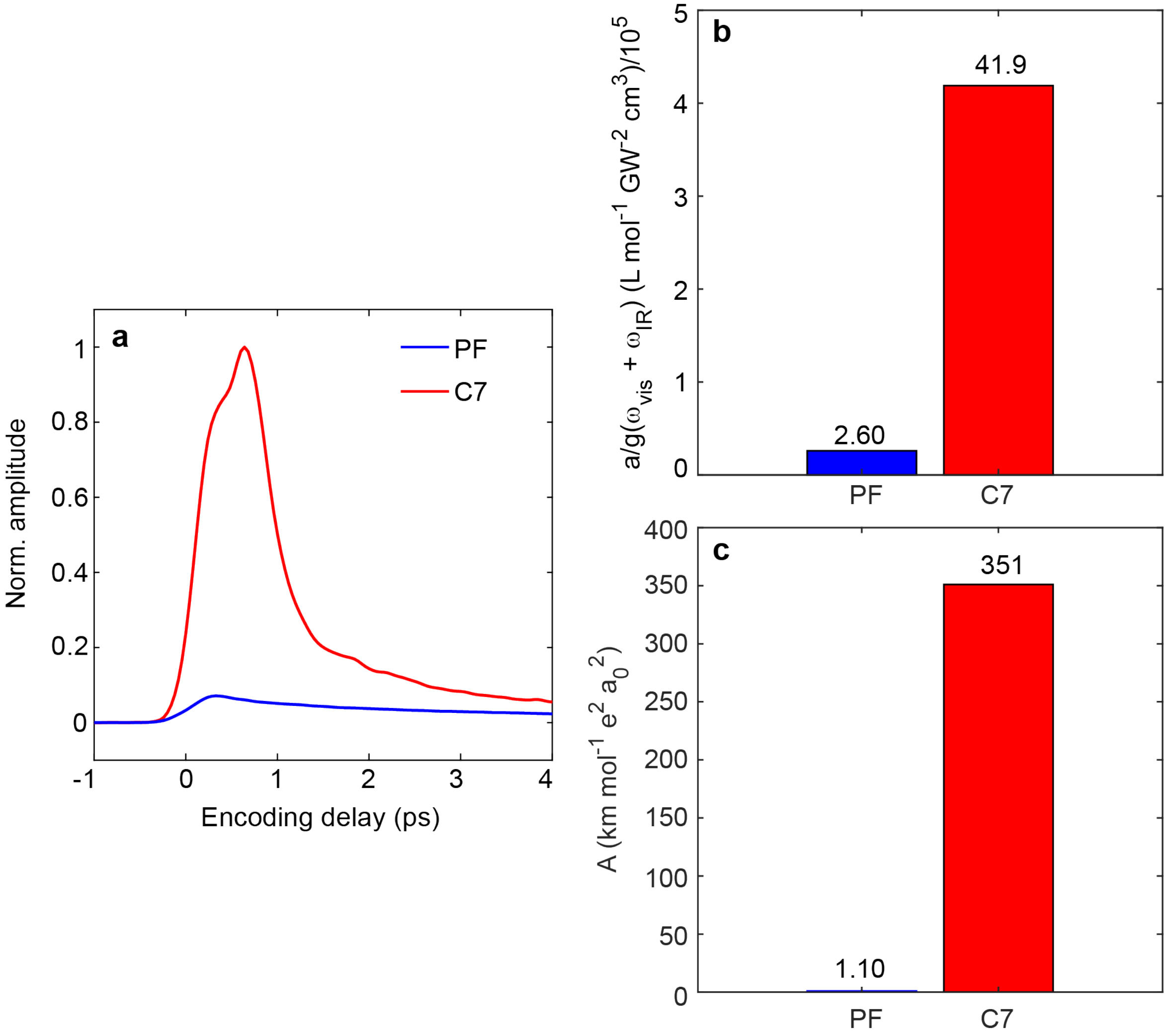

Figure 6.6: Comparison of FEIR cross-sections and computed FEIR activities of PF and C7. (a) Two-pulse transients of PF and C7, normalized with respect to the latter. (b) Experimental FEIR cross-sections derived from two-pulse FEIR transients. (c) Total FEIR activities $A = \sum_i A_i$ calculated from DFT-based computations.

The manifold difference in their predicted FEIR activities emphasizes that no normal mode of PF satisfies both the requisites of strong FC coupling and vibrational transition strength simultaneously. However, we have observed that while the calculations do a fairly good job in predicting the mode-specific FEIR activities of C7,[97] we do not get the same quality of agreement for PF (see Appendix 6.A.2 for a full mode-specific analysis of their

FEIR activities). The experimental FEIR spectrum of PF shows R2 to be the brightest mode, while the other modes are relatively suppressed. On the contrary, our calculations tremendously underestimate the FEIR activity of R2, while overestimating the value for R4. We suspect that this anomaly is attributed to the following factors:

First, IR intensities are influenced by both the harmonic force field and electron distribution through dipole moment derivatives. Achieving precision in dipole moment calculations necessitates a precise representation of molecular orbitals across all spatial regions. Therefore, it is not surprising that obtaining accurate estimations of related IR intensities requires extensive basis sets comprising both contracted and diffuse functions. Calculations of IR intensities, or the squares of the IR transition dipole moments using DFT are often associated with errors as high as $20 - 40\%$.[97,130]. Next, the calculated FCFs reflect those for a symmetric geometry in the ground and the excited electronic states. In reality, PF has 5 H-bond donor sites that interact explicitly with acetonitrile solvent molecules that causes loosening of the symmetry constraints. A more rigorous prediction of true FCFs would involve DFT computations with explicit solvent interactions, adding levels of complications that are beyond the scope of this work. The non-Condon effects may simultaneously play a significant role in determining the strength of vibronic coupling, as seen for spectroscopic techniques sharing similar selection rules as FEIR[131,132]. Especially, in Ref. [132], it has been shown that excluding the non-Condon effects while simulating the Resonance Hyper-Raman spectrum results in a drastic disagreement with the experimental result, while incorporating them yields a near-quantitative agreement. Modeling FEIR spectra by calculating these complicated non-Condon terms adds layers if complexity that go beyond the scope of this chapter. We suspect that the enhanced FEIR activity of R2 is primarily a result of such non-Condon contributions to its vibronic coupling. Furthermore, we also neglect the contribution from coherence pathways that arise as a consequence of broadband IR excitation.[96,97]

Despite the scatter in the correlation between the experimental cross-sections and the calculated activities, what is intriguing is that the most FEIR-intense vibration of PF (R2) has a brightness comparable to one of the least intense peaks of C7.

6.4 Conclusion

The description of FEIR selection rules from the perspective of group theory presented in this chapter, along with the illustrative example of C7 vs PF gives is expected to aid in the search for a "good" FEIR candidate. Furthermore, one can simply make use of the character table of any generic molecule to assess the FEIR-modes, making it easy to screen through a vast number of prospective candidates. While such treatment allows for labeling a normal mode as "symmetry allowed" or "symmetry forbidden", getting a quantitative prediction of the FEIR activity will still require the full treatment described in Chapters 4 and 5. The key takeaway from this analysis is that for a molecule of higher order of symmetry, like PF, where there is a distinct division of totally symmetric and non-totally symmetric normal modes, satisfying the criteria for large FEIR activity becomes more stringent than for a molecule that lacks any symmetry. This becomes a crucial point to consider in the event of choosing an FEIR probe.

One question that naturally arises here –In view of the above discussion, are asymmetric molecules the only choice for a "good" FEIR candidate? While FEIR-relevant transitions of all normal modes for an asymmetric molecule are theoretically symmetry allowed, it will be wrong to state that symmetric molecules cannot serve as FEIR candidates. The case of PF is special because of the restrictions imposed by its geometry, such that the atomic displacements corresponding to the totally symmetric normal modes are confined along the short molecular axis, leading to weak IR transition dipoles. Hypothetically, to think about a symmetric molecule as an FEIR candidate, one must ensure that the atomic displacements for the totally symmetric vibrations are confined along the long molecular axis to simultaneously ensure a large Huang-Rhys factor and a strong vibrational transition dipole moment, besides having a large electronic oscillator strength and a high fluorescence quantum yield, which are the basic requisites for any molecule to be considered for FEIR. Examples of such candidates include perylene-based derivatives, whose totally symmetric modes involve atomic displacements along the long molecular axis, and, therefore, should in principle be able to conform with the FEIR selection rules. Another strategy one can adopt is to break the symmetry by appropriate substitutions in either the chromophoric core or in the form of functional groups. We share a few examples of such calculations in Chapter 7. Unfortunately, we do not have any supporting experimental data, and therefore, will leave it at the level of a speculation.

6.5 Materials and Methods

The computational methodology used in this work has been previously documented in Ref. [97] and provided in detail in Chapter 4. Specifically, all calculations on C7 were carried out at B3LYP/6-31G(d,p) level of theory, and those on PF were performed using the long-range-corrected hybrid functional ωB97X-D with Def2-TZVP triple-zeta basis set. The experimental procedure is the same as followed for our previous works.[71,90,97], and outlined in Chapter 2. For the experiments shared in this work, the second harmonic of the 1033 nm fundamental (i.e., 516.5 nm) was used as the visible excitation source.

6.A Appendix: Supplementary material

6.A.1 Correlation between experimental and DFT-calculated IR frequencies of PF

Shown below is the correlation between the experimental and DFT-calculated IR frequencies for the normal modes of PF lying within the IR pump window. The DFT results suggest that the modes labeled R2 and R4 in the main text are a convolution of two closely spaced modes each. Hence, for those, the calculated frequency is taken as the average value of the two.

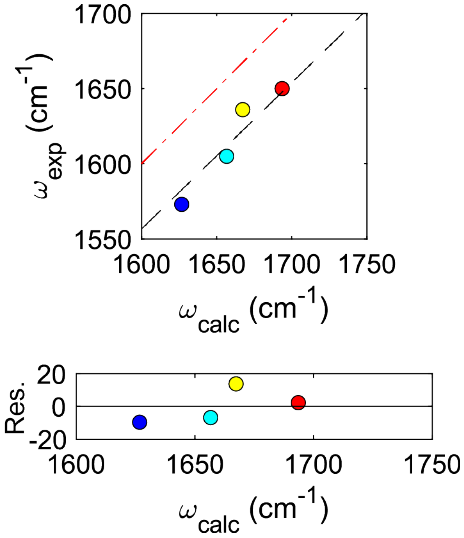

Figure 6.A.1: Correlation between DFT-calculated and experimentally determined frequencies of PF normal modes. A linear fit, shown by black dashed line gives $\omega_{exp} = 0.973\ \omega_{calc}$. The red dashed line corresponds to a 1:1 correlation, and is shown for reference.

6.A.2 Mode-specific FEIR cross-sections and activities of PF and C7

In this section, we present the mode-specific analysis of the experimentally determined FEIR cross-sections and computationally predicted FEIR activities of PF and C7. The results corresponding to C7 have previously been reported in Chapter 5.

The frequency resolved FEIR spectra in Figure 6.A.2a show the normal modes contributing to the FEIR response. They are averaged for encoding delays -0.6 ps to 2.6 ps. Figure 6.A.2b shows the correlation between the calculated FEIR activities and measured FEIR cross-sections of the normal modes for the two molecules. The measured values are determined following the same procedure as described in Ref. [97] and Chapter 5. Although the correlation exhibits significant scatter, it clearly shows that the normal modes of C7 (squares) exhibit larger FEIR cross-sections, as well as predicted FEIR activities than PF. In fact, the brightest PF vibration has an FEIR cross-section similar in magnitude to one of the least bright C7 vibrations.

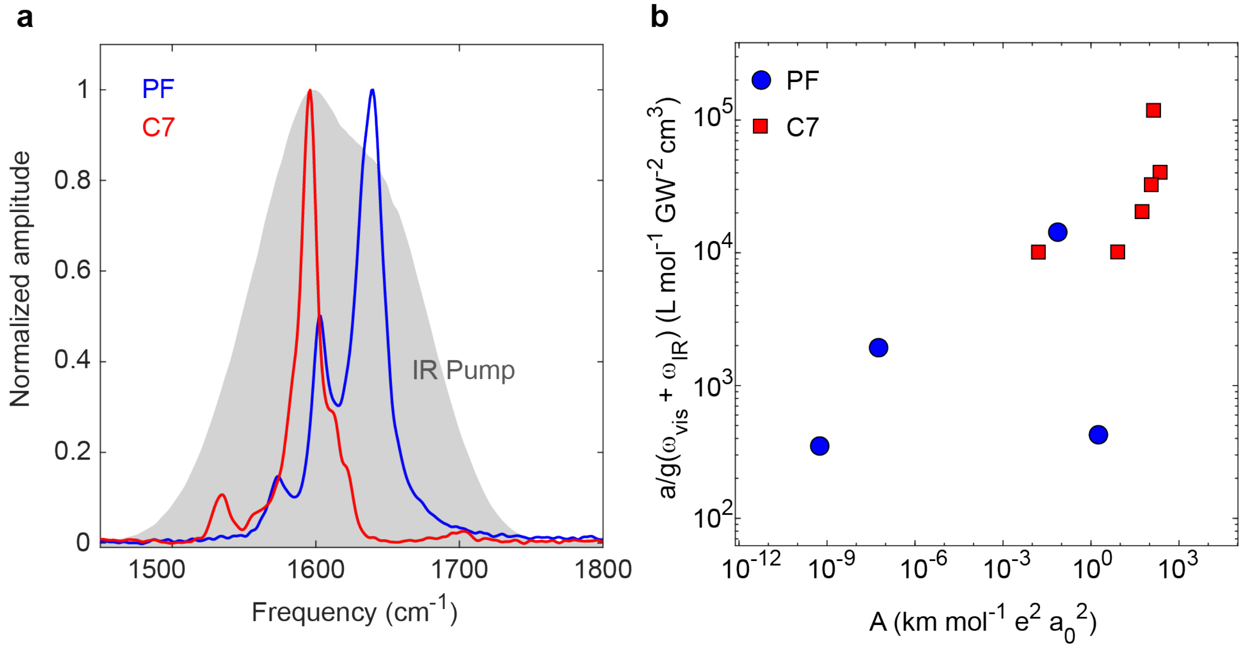

Figure 6.A.2: Comparison of mode-specific FEIR cross-sections of PF and C7. (a) The frequency resolved FEIR spectra of PF (blue) and C7(red), acquired with the IR pulse tuned to ~ 1600 cm^{-1}, showing the vibrations that contribute towards the overall FEIR cross-section of the molecules. The spectra are averaged over $\tau_{enc} = -0.6$ 2.6 ps. (b) Correlation between the mode-specific FEIR cross-sections determined from the two-pulse FEIR transients and the spectra using previously established methodology[97].

Chapter 7

Outlook: Search for "good" FEIR candidates for single-molecule vibrational spectroscopy in solution

7.1 Introduction

One of the primary objectives driving the advancement of FEIR spectroscopy lies in the meticulous investigation of chemical dynamics at the single-molecule level in solution, employing molecular vibrations as innate investigative tools. These vibrational signatures serve as adept probes, facilitating the discernment of subtle alterations within molecular architectures induced by interactions with surrounding species, which often elude detection through conventional molecular fluorescence techniques. Such nuanced variations materialize as dynamic fluctuations within real-time single-molecule FEIR trajectories, furnishing a rich source of kinetic and dynamic insights into these intricate interactions within the solution phase.

In the concluding discourse of Chapter 5, we commented on the attributes that qualify a chromophore as proficient for FEIR spectroscopy. Our present endeavor in this chapter is to revisit the notion of a "good FEIR candidate," elucidating the criteria that guide our quest in this domain. Drawing upon a set of computational predictions and experimental measurements, this chapter is poised to equip the reader with a rough guideline to identify individual chromophores, or classes/families thereof, conducive to the exploration of a diverse array of physicochemical phenomena in solution, that are amenable to FEIR spectroscopic investigations.

For probing single-molecule chemical dynamics, a good FEIR candidate is a molecule that meets the following three criteria: (1) must possess a high fluorescence quantum yield, (2) at least one of its vibrations must be FEIR-active, and (3) to be successfully employed as a vibrational reporter of chemical dynamics, the FEIR-active vibration must be sensitive to interactions in solution, materializing through either a vibrational frequency shift or a sharp change in the FEIR activity. Thus far, we have come across two different kinds of chromophores in the context of FEIR spectroscopy at the single-molecule level. The first set of chromophores includes candidates like, for example, the majority of the coumarins, naphthalimides, and a few cyanines that are expected to possess strongly FEIR active vibrations in the fingerprint region, thus making them sufficiently bright for single-molecule applications. However, in most cases, the vibrations responsible for their high FEIR brightness are conjugated C=C stretches that extend across the chromophore skeleton. These vibrations are often insensitive to any structural changes due to interactions. Therefore, they fail to satisfy criterion (3) listed above. Satisfying all three requisites simultaneously makes the chromophore search even more daunting, but, at the same time, the stringent selectivity criteria imposed by them allow for effective screening of chromophores that constitute the second set. Examples of molecules belonging to this set include, but are not limited to a few coumarins, acridines, xanthenes, and perylene derivatives. All these families include an extensive list of molecules whose excitation and emission spectra span across the visible region.

The choice of a chromophore is guided by the nature of the application: the phenomenon to study, the vibrational reporter probes, and the level of FEIR activity desired. FEIR can be applied to probe a plethora of dynamic interactions, examples of which include bimolecular reaction dynamics mediated through hydrogen-bonding interactions, ion-transport in electrolytic media reported by interactions between the metal ion and a vibrational mode of the chromophore, chemical exchange dynamics (for example, Hydrogen-Deuterium exchange) probed through shifts in the frequencies of chromophore vibrations, sensing local electric field around a molecular probe at the single-molecule level using vibrational stark spectroscopy, and many more. Besides probing chemical dynamics using vibrational reporters, it has been recently shown that FEIR is successfully used for chemical bond-selective imaging applications.[75] For such applications, any vibrational mode that is FEIR-bright can serve as a good candidate. Based on these scopes of application, we discuss a few chromophores in the light of "prospective FEIR candidates".

7.2 Probing chemical dynamics in solution with single-molecule sensitivity: The concept of FEIR-Correlation spectroscopy

A real single-molecule FEIR experiment would involve obtaining real-time trajectories from individual single molecules confined in space over time, and analyzing them for information about the details of the system otherwise masked by a synchronous ensemble-averaged measurement. This involves several complex steps including sample preparation ensuring immobilization of the molecule in space. Furthermore, single-molecule trajectories require high signal-to-noise ratios, and to ensure that, a general practice is to perform the experiment at a high repetition rate of excitation pulses. In our experiments, we use ultrafast pulses at 1 MHz repetition rate, while techniques similar to FEIR, which have demonstrated vibrational signals from individual single molecules, use rates as high as 80 MHz.[65,75] Furthermore, the subpicosecond IR pulses we employ in our experiments are about 120 cm^{-1} broad, which makes it challenging to selectively excite a vibration within a molecule, the typical linewidth of which is roughly $\sim 8-10$ cm^{-1}. This suggests that to perform real-time FEIR trajectory acquisitions, the future generation FEIR setup will need a high repetition rate laser source, and a new IR pulse generation device, capable of delivering tunable narrowband IR pulses.

With our current experimental setup, we can use the FEIR fluctuation trajectory to derive the autocorrelation function, same as in the case of fluorescence correlation spectroscopy (FCS),[133]

$$G(\tau) = \frac{\langle F(t)F(t+\tau)\rangle}{\langle F(t)\rangle^2} \tag{7.1}$$

For a molecule undergoing diffusion through a Gaussian focal volume, one can represent the correlation function in terms of the physical parameters as follows:

$$G_{diff}(\tau) = \frac{1}{\langle N\rangle}\frac{1}{1+\frac{\tau}{\tau_D}}\sqrt{\frac{1}{1+\frac{\tau}{\tau_D}+\left(\frac{\omega_0}{\omega_z}\right)^2}} \tag{7.2}$$

where, $\langle N\rangle$ is the avarage number of molecules in the focal volume, τ_D is the diffusion time constant of the molecule, and $\frac{\omega_0}{\omega_z}$ is the ratio of the short and long radii of the Gaussian focal volume. We realize that lower the value of $\langle N\rangle$, larger is the relative fluctuation, and therefore, higher is $\tau = 0$ amplitude of the correlation function. Therefore, while an ensemble-averaged measurement in the truest sense, fluctuation correlation spectroscopy is performed with single-molecule sensitivity. It is because of this reason, we project FEIR correlation spectroscopy (or, FEIR-CS) as a steppingstone towards real single-molecule measurements.[93]

In the event of a reaction occuring at a timescale faster than diffusion, the correlation function takes the form,

$$G(\tau) = G_{diff}(\tau)\left(1 + K\exp\left(-\frac{\tau}{\tau_R}\right)\right) \tag{7.3}$$

Here, K represents the equilibrium constant associated with the reaction, and τ_R denotes the reaction time constant, the reciprocal of which is the effective rate constant of the reaction. Since the fluctuation in an FEIR trajectory arises due to shifts in the vibrational frequency, in theory, FEIR-CS can be used to probe chemical interactions involving minute changes in the molecular structure, for example, H-D exchange, that FCS is insensitive to. In such case, FCS would solely report on the diffusive properties of the molecule, while FEIR-CS can resolve the part of the fluctuation that arises from reaction. Thus, one can envision FEIR-CS as FCS with a vibrational tag.

7.3 Chromophores with promising normal mode activity for single-molecule FEIR applications

In this section, we highlight representatives from a few of the most popular fluorophore families, namely, naphthalimides, perylenes, xanthenes, and coumarins that can serve as potential FEIR candidates for various application purposes. Our claim that these molecules are "FEIR-active" is based on the FEIR activity threshold ($(S|\mu|^2 > 10$ km/mol) outlined in Chapter 5. However, ensuring sufficient signal-to-noise at the single-molecule level is dependent on how well the instrumental factors are optimized (see Chapter 2).

7.3.1 Molecular probes without efficient vibrational reporters

As mentioned previously, we classify FEIR probes under two broad categories. The first includes molecules with predictions of strong FEIR-active normal modes, but not good enough vibrational reporters for probing dynamic interactions. These modes primarily involve C=C stretches across the molecular skeleton, and are mostly insensitive to any molecular interaction. We have already looked at a few coumarins that fall under this category, namely, Coumarin 30, Coumarin 7, Coumarin 6, Coumarin 525 and Coumarin 545. Besides these, we present the computational predictions for two other molecules belonging to the naphthalimide (Fluorol 555) and cyanine (DCM) families. Figure 7.1 below shows the predicted FEIR activity spectrum of Fluorol 555, overlaid with its experimental FEIR spectrum (panel a). The optimized ground state geometry and the atomic displacements corresponding to the most FEIR active normal mode (1580 cm^{-1}) are shown in panel b.

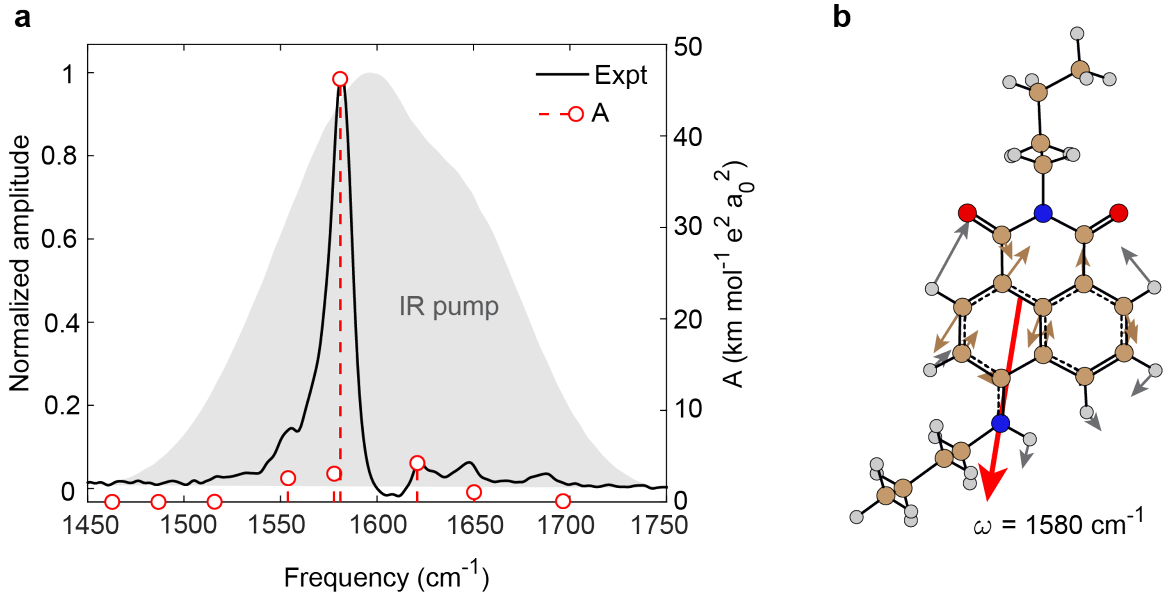

Figure 7.1: FEIR activity prediction for Fluorol 555. (a) FEIR activity spectrum (dashed red) calculated using Eq. 4.23 with $|\mu|^2$ values scaled by the relative IR pump intensities at the corresponding frequencies. The values are read off the right y axis. The experimental FEIR spectrum under relative parallel polarization of IR and visible pulses is shown in black. The IR pump spectrum is shown as grey shaded area. (b) Optimized geometry of the electronic ground state of Fluorol 555, calculated using DFT, and the atomic displacements corresponding to the most FEIR-bright ring mode, derived from frequency calculation on the optimized geometry. The atoms and the corresponding displacement vectors are color-coded as C=Brown, O=Red, N=Blue, H=Grey. The red arrow denotes the vibrational transition dipole moment vector. The lengths of the arrows do not indicate the absolute magnitude of the vectors, but are scaled relative to each other.

This is an example where the molecule as a whole is asymmetric, but the chromophoric core, that is, the naphthalimide core belongs to the C_{2v} symmetry point group. The highlighted mode is totally symmetric, therefore exhibits a large Huang-Rhys factor. Moreover, the molecular geometry forces the atomic displacements to be along the long molecular axis, which, in this case, is the C_2 axis itself, resulting in a simultaneously strong vibrational transition dipole. This molecule could have been a useful FEIR candidate using its symmetric and asymmetric carbonyl stretches as vibrational reporters for chemical dynamics. However, these modes exhibit extremely weak vibronic coupling, and therefore, are not FEIR-bright, as represented by the small peaks in the 1650 - 1700 cm^{-1} region.

The second example in this category is 4-(Dicyanomethylene)-2-methyl-6-(4-dimethylaminostyryl)-4H-pyran or DCM. Unfortunately, we do not have any experimental data to support the computational predictions. However, the popularity of DCM as a Franck-Condon active dye,[134,135] provides a foundation to trust its computational prediction. Shown in Figure 7.21 below is its frequency resolved $S|\mu|^2$ spectrum (panel a) together with the optimized geometry of its ground state (panel b). The atomic displacements corresponding to the most FEIR active normal mode is shown as color-coded arrows. This mode, like Fluorol 555, involved conjugated C=C stretches across the length of the molecule, and similar to the carbonyls of Fluorol 555, the symmetric and asymmetric nitrile stretches, that could have been excellent vibrational reporters for probing chemical dynamics, exhibit very weak vibronic coupling resulting in their FEIR activity falling below the threshold of $S|\mu|^2 = 10$ km/mol.

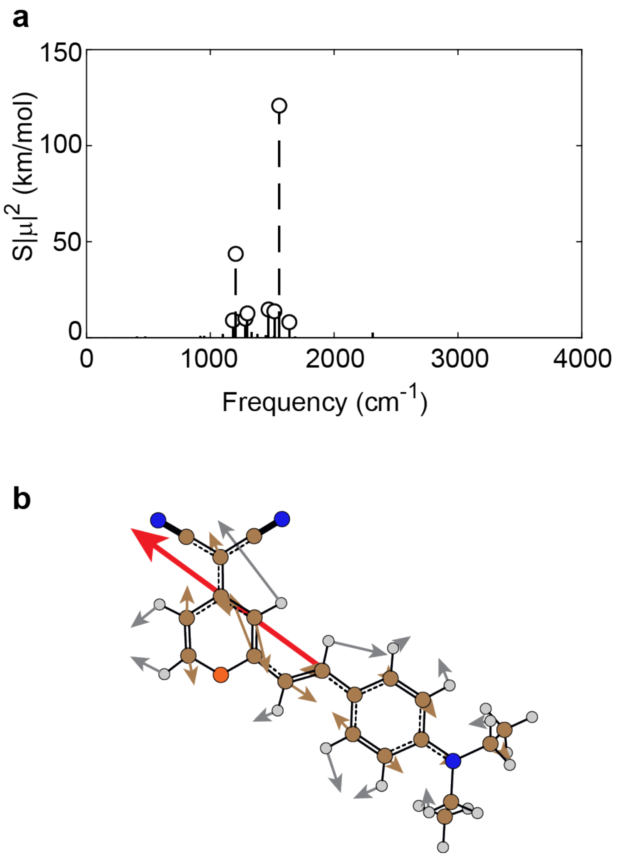

Figure 7.2: FEIR activity prediction for 4-(Dicyanomethylene)-2-methyl-6-(4-dimethylaminostyryl)-4H-pyran (DCM) (a) The $S|\mu|^2$ spectrum of DCM predicts large FEIR activity of the ring modes of the molecule. (b) Atomic displacements corresponding to the most FEIR active ring mode shown on the optimized geometry of the ground state. The atoms and the corresponding arrows are color-coded as follows: C=Brown, H=Grey, O=Orange, N=Blue. The red arrow denotes the vibrational transition dipole moment.

7.3.2 Molecular probes with FEIR active vibrational reporters

This section contains descriptions of fluorophores that satisfy the criterion that their FEIR active vibration is also simultaneously sensitive to fine changes in molecular structure, thereby qualifying them as efficient vibrational reporters to probe chemical dynamics with single-molecule sensitivity in solution. While one can potentially think of a wide range of questions pertaining to chemical dynamics in solution, we divide the section into a few subsections based on a few illustrative types of application, and discuss the FEIR candidates that satisfy the criteria therein.

7.3.2.1 Probing chemical exchange at the single-molecule level in solution

Hydrogen/Deuterium (H/D) exchange is a pivotal chemical exchange phenomenon that elucidates molecular dynamics, structure, and interactions, particularly in biomolecules like proteins and nucleic acids.[136,137] This process involves the substitution of hydrogen atoms with deuterium, a heavier isotope, in a molecule. The rate and extent of H/D exchange are highly dependent on the molecular environment, offering insights into solvent accessibility, hydrogen bonding, and conformational dynamics. The key to understanding H/D exchange is recognizing how differential exchange rates across a molecule reveal its dynamic landscape. For instance, hydrogen atoms in a protein's core or engaged in stable hydrogen bonds exhibit slower exchange rates, indicating structural rigidity or protected regions. Conversely, rapid exchange rates in other regions signal solvent-exposed sites or structural flexibility. H/D exchange is commonly analyzed using mass spectrometry (H/D exchange-MS)[138], nuclear magnetic resonance (NMR) spectroscopy,[139] or 2D-IR spectroscopy[140] that allow detailed investigation of the dynamics of protein folding, structural fluctuations in membranes, and a myriad of other physicochemical and biophysical phenomena.

Being a purely nuclear phenomenon, the H/D exchange has no impact on the electronic properties of the molecule, and therefore, the dynamics associated with it is not resolvable by molecular fluorescence. This serves as an ideal system for a proof-of-principle single-molecule FEIR experiment, where the fluctuations in a single-molecule fluorescence trajectory are entirely due to changes in the vibrational spectrum of the molecule. To this end, we discuss two prospective FEIR candidates for investigating the dynamics of H/D exchange phenomena at the single-molecule level.

As the first example, we choose Rhodamine 6G (R6G), a widely popular fluorescent probe from the xanthene family. The molecular structure is shown in Figure 3.8a in Chapter 3, and in Figure 7.3 below. It exhibits excellent fluorescence quantum yield (~ 0.9) in most aqueous and organic solvents,[141], and a sharp absorption profile that allows for high contrast with suitable resonance condition in an FEIR experiment, as demonstrated in Section 3.5.2 in Chapter 3. From preliminary FEIR experiments, we have determined that with an electronic pre-resonance set to 570 nm, and the IR pulse tuned to 1550 $\mathrm{cm^{-1}}$, effectively pumping six ring modes (Figure 7.4), the FEIR cross-section of R6G is 2.48×10^4 L $\mathrm{mol^{-1}}$ $\mathrm{GW^{-1}}$ $\mathrm{cm^2}$, which is approximately double in magnitude to that of Coumarin 6.[90] under a visible preresonance at 516.5 nm with the IR pulse tuned to 1600 $\mathrm{cm^{-1}}$. This indicates that R6G will be sufficiently bright at the single-molecule level. Figure 7.3 below shows the molecular structure of R6G with two protons, one on each amino group (marked H_a and H_b) that are labile to exchange.

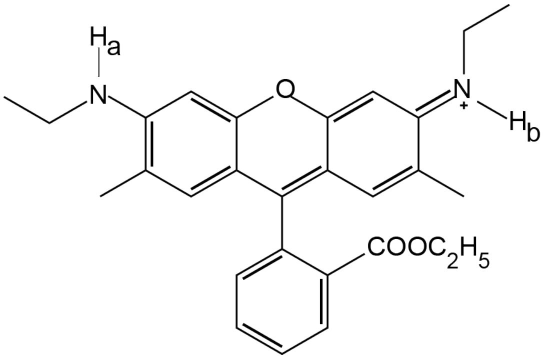

Figure 7.3: Molecular structure of Rhodamine 6G

To demonstrate the effect of H/D exchange on the FEIR spectrum of the molecule, two samples of R6G were prepared. In one, R6G was dissolved in deuterated acetonitrile ($\mathrm{ACND_3}$), and for the other, 3% (v/v) of deuterated ethanol ($\mathrm{C_2H_5O\text{-}D}$) was added, that plays the role of the deuterium exchange partner. The FEIR spectra of the two samples at the 6 µm region are shown in Figure 7.4a. Using DFT-based frequency calculations, we identify six ring modes in this region. Both the spectra are normalized to the intensity of the mode at 1608 cm^{-1}. It is clear that the modes lying in the red side of the spectrum (< 1585 cm^{-1}), that is R3, R4 and R5 are drastically affected by H/D exchange, exhibiting red shifts by $\sim 34, 27$ and 33 cm^{-1} respectively. The shift of R5 by 33 cm^{-1} causes it to coincide with the sixth ring mode of protonated R6G, apparently making it appear to gain intensity in the event of H/D exchange. The DFT calculation of the normal mode frequencies suggests that R3, R4, and R5 are constituted of conjugated ring stretches involving N-H bend on the amino groups on either end of the xanthene core, as seen in the corresponding snapshots in panels c-e. Upon H/D exchange of the two labile protons, a similar qualitative shift in their frequencies are observed, as shown in the DFT-calculated stick spectra in panel b.

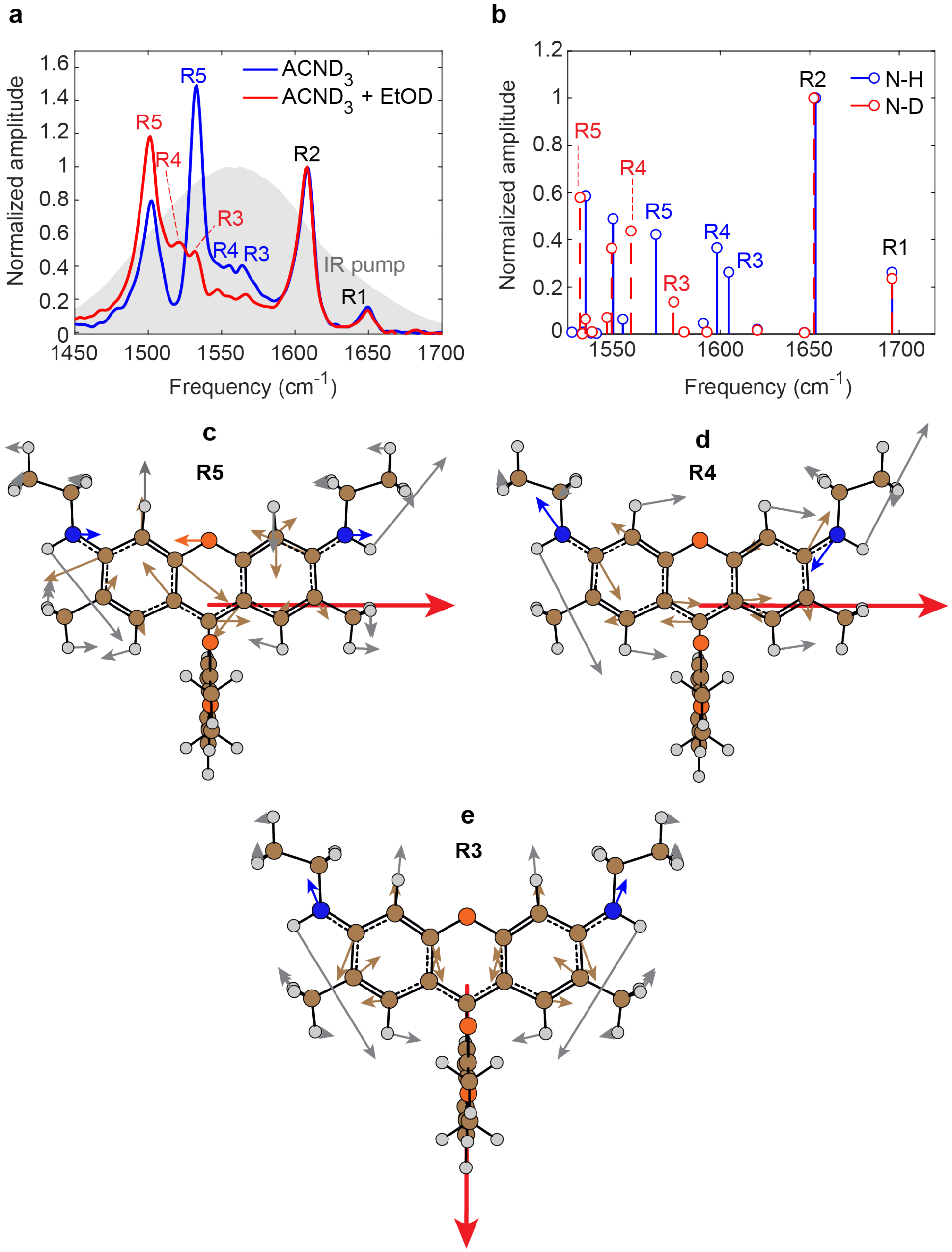

Figure 7.4: Impact of H/D exchange on R6G vibrations. (a) FEIR spectra of R6G in ACND$_3$ (blue) and ACND$_3$ + C_2H_5OD (red), indicating frequency red shifts for R3, R4 and R5, while R1 and R2 are unaffected. Both spectra are normalized with respect to the intensity of R2. (b) DFT-calculated IR spectra of protonated (blue) and deuterated (red) R6G, showing similar qualitative red shift of the frequencies of R3, R4 and R5. (c-e) Normal mode snapshots of R5, R4 and R3, showing the coupling of N-H bend coupled with the ring stretches in each.

This provides an exciting avenue for a proof-of-principle FEIR-CS experiment to investigate the dynamics of the chemical exchange in solution with single-molecule sensitivity. From our preliminary 2-pulse FEIR transients shown in Figure 7.5, acquired under the same experimental conditions, we observed that the FEIR cross-section of R6G (1.3×10^4 L mol^{-1} GW^{-1} cm^2, measured as an average over $400\texttt{fs} < \tau_{enc} < 800\texttt{fs}$)dropped to approximately half its value (6.5×10^3 L mol^{-1} GW^{-1} cm^2). This modulation in the fluorescence photon count rate occurs solely due to vibrational effects since the electronic properties of the molecule are unchanged upon H/D exchange.

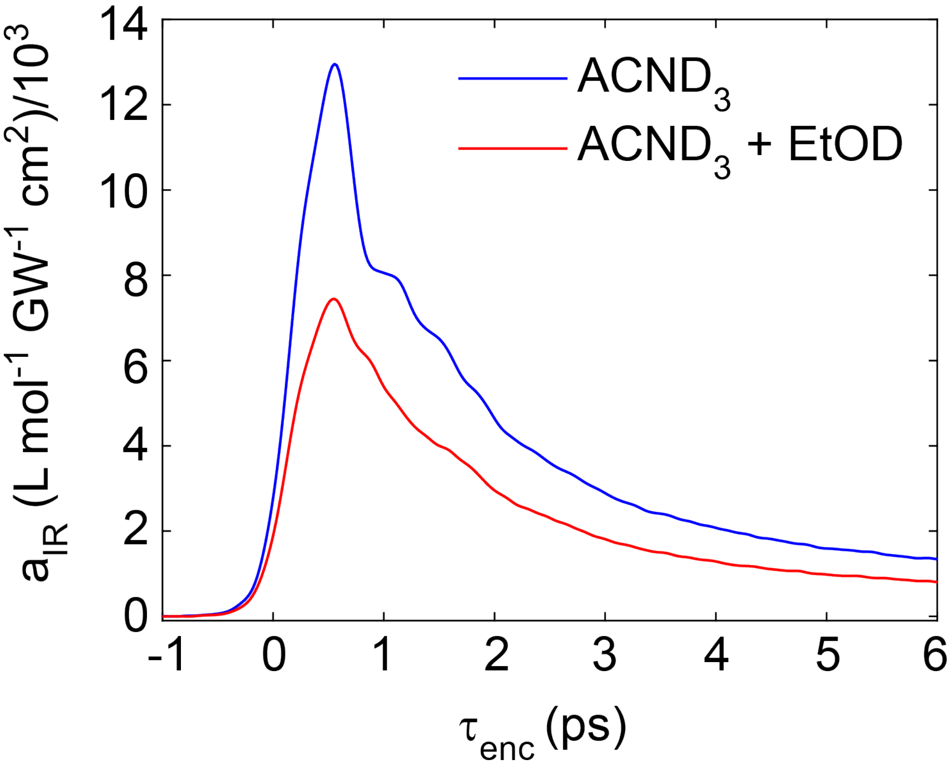

Figure 7.5: Two-pulse FEIR transients of protonated and deuterated R6G showing the drop in the FEIR cross-section of the molecule upon exchanging the labile protons for deuterons.

Despite the sharp contrast in their FEIR brightness, it is true that the broadband IR pulse, shown as the grey shaded area in Figure 7.4a, simultaneously excites both the protonated and the deuterated species. It is our hypothesis that we can bring about even better contrast between the two states by performing a selective vibrational excitation of one of the two. For this, we plan to tweak the time delay between the IR pump pulses to generate an IR excitation pulse characterized by alternating interferometric bright and dark fringes. By choosing an appropriate time delay between the two pulses, we can make the bright fringe overlap with the peak for the protonated species, as shown in the illustration in Figure 7.6 ($\tau_{IR} = 848\texttt{fs}$), while the peak for the deuterated species coincides with one of the dark fringes, thus bringing about selective FEIR-excitation of the protonated state. The future goal of this project is to perform an FEIR-CS experiment to resolve the kinetics of H/D exchange from that of molecular diffusion, depending on the difference in the respective timescales of their occurrence. Note that a typical FCS experiment would only be able to report on the diffusive properties of the molecule while the H/D exchange will remain undetected, thereby making this model system perfectly suitable for a proof-of-principle FEIR-CS measurement.

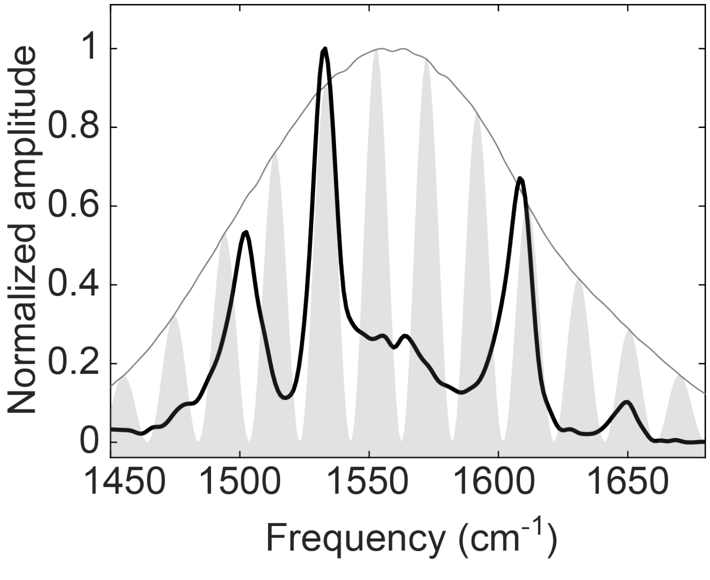

Figure 7.6: Illustration of selective excitation of R6G vibrations with spectral interferometry ($\tau_{IR} = 848\ \texttt{fs}$).

7.3.2.2 Probing dynamics of interactions mediated through non-covalent bonding in solution

One can potentially apply FEIR to answer unresolved questions regarding the transport of molecules in solutions and the accuracy of the hydrodynamic model described by the Stokes-Einstein equation. This includes inquiries about changes in the local molecular interactions as molecules move through a fluid, much of which occurs through non-covalent bonding. It questions whether the fundamental molecular movements adhere to the anticipated Markovian random walk patterns, and if they do, the nature of these steps. Additionally, it explores how the mesoscale organization within complex environments affects the transport mechanisms. Recently, single-molecule fluorescence has been instrumental in uncovering similar types of data,[142] such as identifying voids within polymers and analyzing the varied dynamics within glass-like structures.[143]

The few examples given below illustrate the utilization of a carbonyl mode attached to a chromophore as a vibrational reporter for molecular interactions in solution. The involvement of the carbonyl mode in the formation of complexes with the binding partner results in distinct shift in its resonance frequency. By appropriately choosing the IR excitation frequency such that it is resonant with one out of the two states (free or bound carbonyl), one can ensure that the fluctuations in the real-time FEIR trajectory reflects the changes in molecular structure.

Interaction between FEIR vibrational probe and metal ions in electrolytic solutions

To this end, first, we look at the example of probing the interaction of metal ions in an electrolytic solution with the carbonyl mode attached to a chromophore. In this example, we have chosen Coumarin 153 as the FEIR probe. Its lactone carbonyl is has the largest

FEIR activity, as compared to the other coumarins we have studied. The example illustrates the prospect of using C153 to probe the transport of metal ions (Zn^{2+} in this case) through a concentrated electrolytic solution (Zinc bis(trifluoromethane)sulfonimide or $Zn(TFSI)_2$) (Figure 7.7).

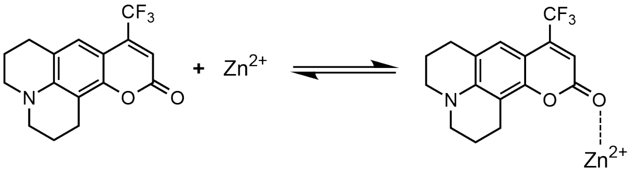

Figure 7.7: Schematic depicting non-covalent bonding interaction between C153 and Zn^{2+}

Shown in Figure are the FTIR spectra of C153 in acetonitrile in the absence and presence of Zn^{2+}. The carbonyl mode interacts with Zn^{2+} ions in solution to form an adduct, and in the process, its resonance frequency red-shifts by $\sim$ 50 cm^{-1}.

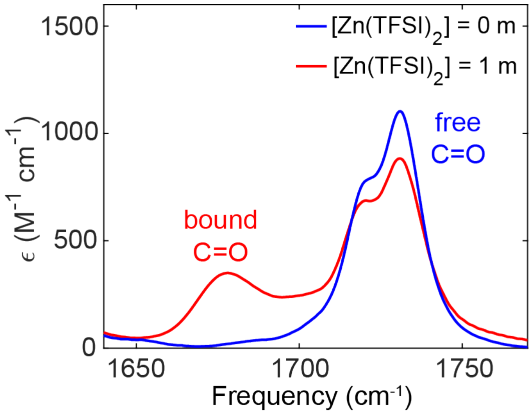

Figure 7.8: FTIR of C153 in acetonitrile in the absence and presence of $Zn(TFSI)_2$, showing a $\sim$ 50 cm^{-1} red shift in the frequency of the lactone carbonyl upon interaction with the metal ion.

With our prior knowledge that the lactone carbonyl of C153 is has the largest FEIR cross-section amongst all the coumarins we studied,[97], we can utilize the contrast in the vibrational resonance frequencies of the free vs the bound carbonyl to selectively FEIR-excite one of the two states in the process of probing the dynamics of motion of Zn^{2+} ions through the electrolytic solution, at the single-molecule level.

Bimolecular heterodimerization dynamics mediated by hydrogen bonding interactions

Since carbonyls are excellent reporters for H-bond mediated molecular interactions, it is always useful to have an FEIR-active vibration in a candidate that involves the C=O stretch. The following example is of Fluorescein, a member of the xanthene family. Fluorescein is a well-known dye with excellent fluorescence quantum yield.

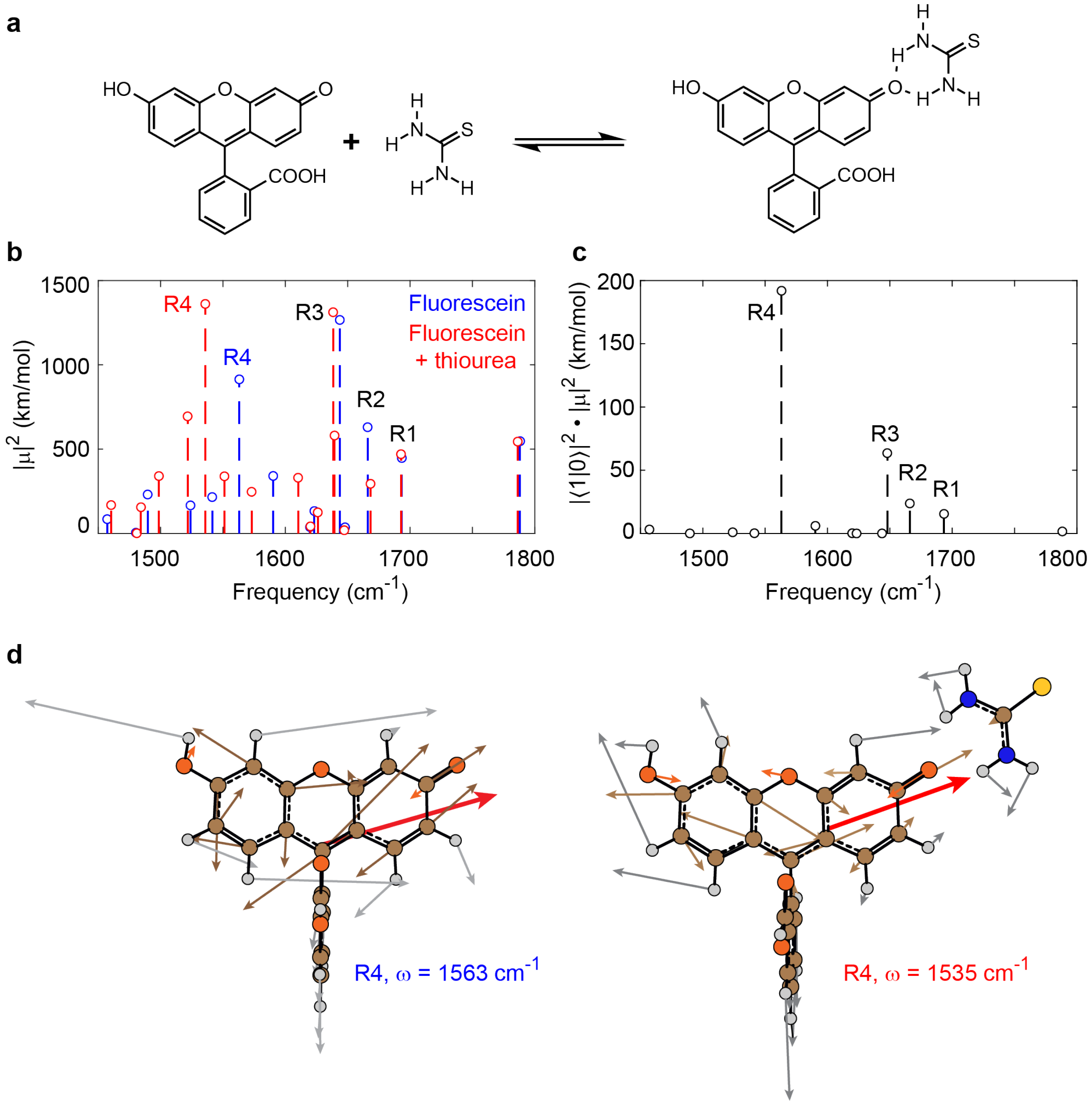

Figure 7.9: Fluorescein as a promising probe for studying bimolecular reaction dynamics. (a) The equilibrium reaction between fluorescein and thiourea mediated by hydrogen-bonding interactions between the H atoms on the thiourea molecule and the ring carbonyl of fluorescein. (b) Ground state frequencies fluorescein (blue) and the fluorescein-thiourea heterodimer(red) predicting a ∼ 30 cm^{-1} red shift in R4 frequency of fluorescein upon binding. (c) The FCF-scaled vibrational intensity spectrum of fluorescein suggesting strong FEIR activity of R4 (d) Normal mode snapshots of R4 for free and bound fluroescein. The atoms and the corresponding arrows are color-coded as follows: C=Brown, H=Grey, O=Orange, S=Yellow. The red arrow denotes the vibrational transition dipole moment.

The xanthene core has a carbonyl mode conjugated with it, which may act as a reported for bimolecular interactions mediated through hydrogen bonding, as shown in the equilibrium between fluorescein and a thiourea molecule in Figure 7.9a. The ground-state frequency calculations shown in Figure 7.9b suggest the fluorescein is characterized by 4 prominent normal modes in the infrared absorption region of 1500-1800 cm^{-1}. These involve skeletal ring stretches. Out of them, R4 involves the carbonyl stretch conjugated with the stretching motion of the xanthene core. Upon the formation of the heterodimer, this mode undergoes a red shift by $\sim$ 30 cm^{-1}, demonstrating its sensitivity towards probing the interaction. We performed the FEIR activity calculations on the molecule, and the results predict a strong FEIR activity for this mode, as shown in the $|\langle 1|0\rangle|^2 \cdot |\mu|^2$ plot in Figure 7.9c. The normal mode snapshots of the mode in the free and the bound species are shown in Figure 7.9d. The conjugated motion of the N-H bonds of the thiourea molecule is suggestive of the hydrogen bonding interaction that couples the two molecules.

7.4 Concluding remarks

The discussions presented in this thesis are aimed at providing a comprehensive framework for identifying and understanding the quintessential attributes of proficient chromophores for FEIR spectroscopy, paving the way for discerning single-molecule dynamics in solution by interrogating molecular vibrations. This thesis delineates the stringent yet essential criteria for a molecule to qualify as a "good FEIR candidate", underscoring the delicate interplay between the different factors intrinsic to the electronic structure of the molecule. While the search for ideal chromophores that satisfy all necessary conditions is an arduous journey, it is also one of discernment and precision. The computational tools elaborated in this thesis is intended to serve the purpose of guiding one to choose a suitable FEIR candidate, or predict the structure of a designer candidate with promising FEIR activity for applications at the single-molecule level. The examples discussed herein not only showcase the diversity of chromophoric families suitable for FEIR spectroscopy but also highlight the nuanced roles they can play in unveiling the intricate tapestry of chemical interactions at the single-molecule level. From hydrogen bonding to ion transport, to bond-selective imaging, there is a vast scope to explore the versatility of FEIR spectroscopy in the realm of physical, chemical, biological, and materials sciences. With a suitable chromophore with a FEIR-bright vibrational reporter, a precise control over resonance condition, high-throughput data acquisition, and a sophisticated photon detection architecture, it is expected that one can successfully study molecular dynamics at the single-molecule level in real time, probing bond-specific structural changes, with an aim to unravel the intricate details of molecular interactions in solution.

Bibliography

(1) Moerner, W. E.; Orrit, M. Illuminating Single Molecules in Condensed Matter. *Science* **1999**, *283*, 1670–1676, DOI: `10.1126/science.283.5408.1670`.

(2) Curran, S. C.; Angus, J.; Cockroft, A. L. The Beta-Spectrum of Tritium. *Phys. Rev.* **1949**, *76*, 853–854, DOI: `10.1103/PhysRev.76.853`.

(3) Falk, G.; Fatt, P. Passive electrical properties of rod outer segments. *The Journal of Physiology* **1968**, *198*, 627–646.

(4) Cova, S.; Longoni, A.; Andreoni, A. Towards picosecond resolution with single-photon avalanche diodes. *Review of Scientific Instruments* **1981**, *52*, 408–412.

(5) McIntyre, R. Recent developments in silicon avalanche photodiodes. *Measurement* **1985**, *3*, 146–152, DOI: `https://doi.org/10.1016/0263-2241(85)90024-7`.

(6) Rarity, J.; Tapster, P.; Jakeman, E. Observation of sub-poissonian light in parametric downconversion. *Optics communications* **1987**, *62*, 201–206.

(7) Moerner, W. E.; Kador, L. Optical detection and spectroscopy of single molecules in a solid. *Phys. Rev. Lett.* **1989**, *62*, 2535–2538, DOI: `10.1103/PhysRevLett.62.2535`.

(8) Xie, X. S.; Trautman, J. K. Optical Studies of Single Molecules at Room Temperature. *Annual Review of Physical Chemistry* **1998**, *49*, 441–480, DOI: `https://doi.org/10.1146/annurev.physchem.49.1.441`.

(9) Betzig, E.; Chichester, R. J. Single Molecules Observed by Near-Field Scanning Optical Microscopy. *Science* **1993**, *262*, 1422–1425, DOI: `10.1126/science.262.5138.1422`.

(10) Rigler, R.; Mets, Ü.; Widengren, J.; Kask, P. Fluorescence correlation spectroscopy with high count rate and low background: analysis of translational diffusion. *European Biophysics Journal* **1993**, *22*, 169–175.

(11) Funatsu, T.; Harada, Y.; Tokunaga, M.; Saito, K.; Yanagida, T. Imaging of single fluorescent molecules and individual ATP turnovers by single myosin molecules in aqueous solution. *Nature* **1995**, *374*, 555–559.

(12) Orrit, M.; Bernard, J. Single pentacene molecules detected by fluorescence excitation in a p-terphenyl crystal. *Physical review letters* **1990**, *65*, 2716.

(13) Lu, H. P.; Xun, L.; Xie, X. S. Single-molecule enzymatic dynamics. *Science* **1998**, *282*, 1877–1882.

(14) Ha, T.; Enderle, T.; Ogletree, D. F.; Chemla, D. S.; Selvin, P. R.; Weiss, S. Probing the interaction between two single molecules: fluorescence resonance energy transfer between a single donor and a single acceptor. *Proceedings of the National Academy of Sciences* **1996**, *93*, 6264–6268, DOI: `10.1073/pnas.93.13.6264`.

(15) Kusumi, A.; Sako, Y.; Yamamoto, M. Confined lateral diffusion of membrane receptors as studied by single particle tracking (nanovid microscopy). Effects of calcium-induced differentiation in cultured epithelial cells. *Biophysical journal* **1993**, *65*, 2021–2040.

(16) Zhuang, X.; Bartley, L. E.; Babcock, H. P.; Russell, R.; Ha, T.; Herschlag, D.; Chu, S. A Single-Molecule Study of RNA Catalysis and Folding. *Science* **2000**, *288*, 2048–2051, DOI: `10.1126/science.288.5473.2048`.

(17) Weiss, S. Fluorescence spectroscopy of single biomolecules. *Science* **1999**, *283*, 1676–1683.

(18) Bruchez Jr, M.; Moronne, M.; Gin, P.; Weiss, S.; Alivisatos, A. P. Semiconductor nanocrystals as fluorescent biological labels. *science* **1998**, *281*, 2013–2016.

(19) Weiss, S. Measuring conformational dynamics of biomolecules by single molecule fluorescence spectroscopy. *Nature structural biology* **2000**, *7*, 724–729, DOI: `10.1038/78941`.

(20) Betzig, E.; Patterson, G. H.; Sougrat, R.; Lindwasser, O. W.; Olenych, S.; Bonifacino, J. S.; Davidson, M. W.; Lippincott-Schwartz, J.; Hess, H. F. Imaging Intracellular Fluorescent Proteins at Nanometer Resolution. *Science* **2006**, *313*, 1642–1645, DOI: `10.1126/science.1127344`.

(21) Tolić-Nørrelykke, S. F.; Rasmussen, M. B.; Pavone, F. S.; Berg-Sørensen, K.; Oddershede, L. B. Stepwise bending of DNA by a single TATA-box binding protein. *Biophys. J.* **2006**, *90*, 3694–3703.

(22) Yildiz, A.; Forkey, J. N.; McKinney, S. A.; Ha, T.; Goldman, Y. E.; Selvin, P. R. Myosin V Walks Hand-Over-Hand: Single Fluorophore Imaging with 1.5-nm Localization. *Science* **2003**, *300*, 2061–2065, DOI: `10.1126/science.1084398`.

(23) Ha, T.; Rasnik, I.; Cheng, W.; Babcock, H. P.; Gauss, G. H.; Lohman, T. M.; Chu, S. Initiation and re-initiation of DNA unwinding by the Escherichia coli Rep helicase. *Nature* **2002**, *419*, 638–641, DOI: `10.1038/nature01083`.

(24) Betzig, E.; Patterson, G. H.; Sougrat, R.; Lindwasser, O. W.; Olenych, S.; Bonifacino, J. S.; Davidson, M. W.; Lippincott-Schwartz, J.; Hess, H. F. Imaging Intracellular Fluorescent Proteins at Nanometer Resolution. *Science* **2006**, *313*, 1642–1645, DOI: `10.1126/science.1127344`.

(25) Kapanidis, A. N.; Weiss, S. Fluorescent probes and bioconjugation chemistries for single-molecule fluorescence analysis of biomolecules. *Journal of Chemical Physics* **2002**, *117*, 10953–10964.

(26) Branton, D. et al. The potential and challenges of nanopore sequencing. *Nature Biotechnology* **2008**, *26*, 1146–1153, DOI: `10.1038/nbt.1495`.

(27) Thiele, S.; Balestro, F.; Ballou, R.; Klyatskaya, S.; Ruben, M.; Wernsdorfer, W. Electrically driven nuclear spin resonance in single-molecule magnets. *Science* **2014**, *344*, 1135–1138, DOI: `10.1126/science.1249802`.

(28) Lounis, B.; Orrit, M. Single-photon sources. *Reports on Progress in Physics* **2005**, *68*, 1129, DOI: `10.1088/0034-4885/68/5/R04`.

(29) Rust, M. J.; Bates, M.; Zhuang, X. Sub-diffraction-limit imaging by stochastic optical reconstruction microscopy (STORM). *Nature Methods* **2006**, *3*, 793–796, DOI: `10.1038/nmeth929`.

(30) Dekker, C. Solid-state nanopores. *Nature Nanotechnology* **2007**, *2*, 209–215, DOI: `10.1038/nnano.2007.27`.

(31) Manzo, C.; Garcia-Parajo, M. F. A review of progress in single particle tracking: from methods to biophysical insights. *Rep. Prog. Phys.* **2015**, *78*, 124601.

(32) Yeou, S.; Lee, N. K. Single-molecule methods for investigating the double-stranded DNA bendability. *Mol. Cells* **2022**, *45*, 33–40.

(33) Huang, B.; Bates, M.; Zhuang, X. Super-Resolution Fluorescence Microscopy. *Annual Review of Biochemistry* **2009**, *78*, 993–1016, DOI: `https://doi.org/10.1146/annurev.biochem.77.061906.092014`.

(34) Michalet, X.; Pinaud, F. F.; Bentolila, L. A.; Tsay, J. M.; Doose, S.; Li, J. J.; Sundaresan, G.; Wu, A. M.; Gambhir, S. S.; Weiss, S. Quantum dots for live cells, in vivo imaging, and diagnostics. *Science* **2005**, *307*, 538–544.

(35) Zhuang, X.; Rief, M. Single-molecule folding. *Current Opinion in Structural Biology* **2003**, *13*, 88–97, DOI: `https://doi.org/10.1016/S0959-440X(03)00011-3`.

(36) Ha, T. Single-molecule fluorescence resonance energy transfer. *Methods* **2001**, *25*, 78–86.

(37) Sönnichsen, C.; Franzl, T.; Wilk, T.; von Plessen, G.; Feldmann, J.; Wilson, O.; Mulvaney, P. Drastic Reduction of Plasmon Damping in Gold Nanorods. *Phys. Rev. Lett.* **2002**, *88*, 077402, DOI: `10.1103/PhysRevLett.88.077402`.

(38) Schlierf, M.; Li, H.; Fernandez, J. M. The unfolding kinetics of ubiquitin captured with single-molecule force-clamp techniques. *Proceedings of the National Academy of Sciences* **2004**, *101*, 7299–7304, DOI: `doi:10.1073/pnas.0400033101`.

(39) Schwille, P.; Kummer, S.; Heikal, A. A.; Moerner, W. E.; Webb, W. W. Fluorescence correlation spectroscopy reveals fast optical excitation-driven intramolecular dynamics of yellow fluorescent proteins. *Proceedings of the National Academy of Sciences* **2000**, *97*, 151–156, DOI: `10.1073/pnas.97.1.151`.

(40) Widengren, J.; Schwille, P. Characterization of Photoinduced Isomerization and Back-Isomerization of the Cyanine Dye Cy5 by Fluorescence Correlation Spectroscopy. *The Journal of Physical Chemistry A* **2000**, *104*, 6416–6428, DOI: `10.1021/jp000059s`.

(41) English, B. P.; Min, W.; van Oijen, A. M.; Lee, K. T.; Luo, G.; Sun, H.; Cherayil, B. J.; Kou, S. C.; Xie, X. S. Ever-fluctuating single enzyme molecules: Michaelis-Menten equation revisited. *Nature Chemical Biology* **2006**, *2*, 87–94, DOI: `10.1038/nchembio759`.

(42) Hamm, P.; Zanni, M., *Concepts and methods of 2D infrared spectroscopy*; Cambridge University Press: 2011.

(43) Loparo, J. J.; Roberts, S. T.; Tokmakoff, A. Multidimensional infrared spectroscopy of water. I. Vibrational dynamics in two-dimensional IR line shapes. *J. Chem. Phys.* **2006**, *125*, 194521.

(44) Petersen, P. B.; Tokmakoff, A. Source for ultrafast continuum infrared and terahertz radiation. *Opt. Lett.* **2010**, *35*, 1962–1964, DOI: `10.1364/OL.35.001962`.

(45) Paesani, F.; Voth, G. A. The properties of water: insights from quantum simulations. *J. Phys. Chem. B* **2009**, *113*, 5702–5719.

(46) Fayer, M. D. Dynamics of water interacting with interfaces, molecules, and ions. *Accounts of chemical research* **2012**, *45*, 3–14.

(47) Peng, C. S.; Baiz, C. R.; Tokmakoff, A. Direct observation of ground-state lactam–lactim tautomerization using temperature-jump transient 2D IR spectroscopy. *Proceedings of the National Academy of Sciences* **2013**, *110*, 9243–9248.

(48) Ashwood, B.; Jones, M. S.; Radakovic, A.; Khanna, S.; Lee, Y.; Sachleben, J. R.; Szostak, J. W.; Ferguson, A. L.; Tokmakoff, A. Direct monitoring of the thermodynamics and kinetics of DNA and RNA dinucleotide dehybridization from gaps and overhangs. *bioRxiv.*

(49) Ashwood, B.; Jones, M. S.; Lee, Y.; Sachleben, J. R.; Ferguson, A. L.; Tokmakoff, A. Molecular insight into how the position of an abasic site modifies DNA duplex stability and dynamics. *Biophysical Journal* **2024**, *123*, 118–133.

(50) Lee, Y.; Ashwood, B.; Wu, Y.; Dhayalan, B.; Gagnon, I.; Sosnick, T. R.; Tokmakoff, A. Direct observation of protein-peptide folding and binding in the formation of ribonuclease S. *Biophysical Journal* **2024**, *123*, 461a–462a.

(51) Jeanmaire, D. L.; Van Duyne, R. P. Surface Raman spectroelectrochemistry: Part I. Heterocyclic, aromatic, and aliphatic amines adsorbed on the anodized silver electrode. *Journal of electroanalytical chemistry and interfacial electrochemistry* **1977**, *84*, 1–20.

(52) Fleischmann, M.; Hendra, P. J.; McQuillan, A. J. Raman spectra of pyridine adsorbed at a silver electrode. *Chemical physics letters* **1974**, *26*, 163–166.

(53) Albrecht, M. G.; Creighton, J. A. Anomalously intense Raman spectra of pyridine at a silver electrode. *Journal of the american chemical society* **1977**, *99*, 5215–5217.

(54) Wessel, J. Surface-enhanced optical microscopy. *JOSA B* **1985**, *2*, 1538–1541.

(55) Kneipp, K.; Wang, Y.; Kneipp, H.; Perelman, L. T.; Itzkan, I.; Dasari, R. R.; Feld, M. S. Single molecule detection using surface-enhanced Raman scattering (SERS). *Physical review letters* **1997**, *78*, 1667.

(56) Nie, S.; Emory, S. R. Probing single molecules and single nanoparticles by surface-enhanced Raman scattering. *science* **1997**, *275*, 1102–1106.

(57) Stöckle, R. M.; Suh, Y. D.; Deckert, V.; Zenobi, R. Nanoscale chemical analysis by tip-enhanced Raman spectroscopy. *Chemical Physics Letters* **2000**, *318*, 131–136.

(58) Neugebauer, U.; Rösch, P.; Schmitt, M.; Popp, J.; Julien, C.; Rasmussen, A.; Budich, C.; Deckert, V. On the Way to Nanometer-Sized Information of the Bacterial Surface by Tip-Enhanced Raman Spectroscopy. *ChemPhysChem* **2006**, *7*, 1428–1430, DOI: `https://doi.org/10.1002/cphc.200600173`.

(59) Laubereau, A.; Seilmeier, A.; Kaiser, W. A new technique to measure ultrashort vibrational relaxation times in liquid systems. *Chemical Physics Letters* **1975**, *36*, 232–237, DOI: `10.1016/0009-2614(75)87023-0`.

(60) Seilmeier, A.; Kaiser, W.; Laubereau, A.; Fischer, S. F. A Novel Spectroscopy Using Ultrafast Two-Pulse Excitation of Large Polyatomic Molecules. *Chemical Physics Letters* **1978**, *58*, 225–229.

(61) Hübner, H. J.; Wörner, M.; Kaiser, W.; Seilmeier, A. Subpicosecond vibrational relaxation of skeletal modes in polyatomic molecules. *Chemical Physics Letters* **1991**, *182*, 315–320, DOI: `10.1016/0009-2614(91)80221-I`.

(62) Wright, J. C. Double Resonance Excitation of Fluorescence in the Condensed Phase—An Alternative to Infrared, Raman, and Fluorescence Spectroscopy. *Applied Spectroscopy* **1980**, *34*, 151–157.

(63) Lee, S.; Nguyen, D.; Wright, J. Double resonance excitation of fluorescence by stimulated Raman scattering. *Applied Spectroscopy* **1983**, *37*, 472–474.

(64) Winterhalder, M.; Zumbusch, A.; Lippitz, M.; Orrit, M. Toward far-field vibrational spectroscopy of single molecules at room temperature. *The Journal of Physical Chemistry B* **2011**, *115*, 5425–5430.

(65) Xiong, H.; Shi, L.; Wei, L.; Shen, Y.; Long, R.; Zhao, Z.; Min, W. Stimulated Raman excited fluorescence spectroscopy and imaging. *Nature Photonics* **2019**, *13*, 412–417, DOI: `10.1038/s41566-019-0396-4`.

(66) Xiong, H.; Qian, N.; Miao, Y.; Zhao, Z.; Min, W. Stimulated Raman Excited Fluorescence Spectroscopy of Visible Dyes. *Journal of Physical Chemistry Letters* **2019**, *10*, 3563–3570, DOI: `10.1021/acs.jpclett.9b01289`.

(67) Xiong, H.; Min, W. Combining the best of two worlds: Stimulated Raman excited fluorescence. *The Journal of Chemical Physics* **2020**, *153*, 210901–210901, DOI: `10.1063/5.0030204`.

(68) Mastron, J. N.; Tokmakoff, A. Two-Photon-Excited fluorescence-Encoded infrared spectroscopy. *Journal of Physical Chemistry A* **2016**, *120*, 9178–9187, DOI: `10.1021/acs.jpca.6b09158`.

(69) Mastron, J. N.; Tokmakoff, A. Fourier transform fluorescence-encoded infrared spectroscopy. *The Journal of Physical Chemistry A* **2018**, *122*, 554–562.

(70) Whaley-Mayda, L.; Penwell, S. B.; Tokmakoff, A. Fluorescence-Encoded Infrared Spectroscopy: Ultrafast Vibrational Spectroscopy on Small Ensembles of Molecules in Solution. *Journal of Physical Chemistry Letters* **2019**, *10*, 1967–1972, DOI: `10.1021/acs.jpclett.9b00748`.

(71) Whaley-mayda, L.; Guha, A.; Penwell, S. B.; Tokmakoff, A. Fluorescence-Encoded Infrared Vibrational Spectroscopy with Single-Molecule Sensitivity. *J. Am. Chem. Soc.* **2021**, *143*, 10–14.

(72) Takahashi, H.; Oue, T.; Sakai, M. Resonance IR spectroscopy in aqueous solution by combining IR super-resolution with TFD-IR method. *Chemical Physics Letters* **2020**, *758*, 137942, DOI: `https://doi.org/10.1016/j.cplett.2020.137942`.

(73) Chikkaraddy, R.; Arul, R.; Jakob, L. A.; Baumberg, J. J. Single-molecule mid-infrared spectroscopy and detection through vibrationally assisted luminescence. *Nature Photonics* **2023**, *17*, 865–871, DOI: `10.1038/s41566-023-01263-4`.

(74) Yan, C.; Wang, C.; Wagner, J. C.; Ren, J.; Lee, C.; Wan, Y.; Wang, S. E.; Xiong, W. Multidimensional Widefield Infrared-Encoded Spontaneous Emission Microscopy: Distinguishing Chromophores by Ultrashort Infrared Pulses. *Journal of the American Chemical Society* **2023**, *146*, 1874–1886.

(75) Wang, H.; Lee, D.; Cao, Y.; Bi, X.; Du, J.; Miao, K.; Wei, L. Bond-selective fluorescence imaging with single-molecule sensitivity. *Nature Photonics* **2023**, *17*, 846–855, DOI: `10.1038/s41566-023-01243-8`.

(76) Limpert, J.; Schreiber, T.; Clausnitzer, T.; Zöllner, K.; Fuchs, H.-J.; Kley, E.-B.; Zellmer, H.; Tünnermann, A. High-power femtosecond Yb-doped fiber amplifier. *Opt. Express* **2002**, *10*, 628–638, DOI: `10.1364/OE.10.000628`.

(77) Li, X.; Reber, M. A. R.; Corder, C.; Chen, Y.; Zhao, P.; Allison, T. K. High-power ultrafast Yb:fiber laser frequency combs using commercially available components and basic fiber tools. *Review of Scientific Instruments* **2016**, *87*, 093114, DOI: `10.1063/1.4962867`.

(78) Luther, B. M.; Tracy, K. M.; Gerrity, M.; Brown, S.; Krummel, A. T. 2D IR spectroscopy at 100 kHz utilizing a Mid-IR OPCPA laser source. *Opt. Express* **2016**, *24*, 4117–4127, DOI: `10.1364/OE.24.004117`.

(79) Heiner, Z.; Petrov, V.; Mero, M. Compact, high-repetition-rate source for broadband sum-frequency generation spectroscopy. *APL Photonics* **2017**, *2*, 066102, DOI: `10.1063/1.4983691`.

(80) Grupp, A.; Budweg, A.; Fischer, M. P.; Allerbeck, J.; Soavi, G.; Leitenstorfer, A.; Brida, D. Broadly tunable ultrafast pump-probe system operating at multi-kHz repetition rate. *Journal of Optics* **2017**, *20*, 014005, DOI: `10.1088/2040-8986/aa9b07`.

(81) Donaldson, P.; Greetham, G.; Shaw, D.; Parker, A.; Towrie, M. A 100 kHz Pulse Shaping 2D-IR Spectrometer Based on Dual Yb:KGW Amplifiers. *The Journal of Physical Chemistry A* **2018**, *122*, PMID: 29250947, 780–787, DOI: `10.1021/acs.jpca.7b10259`.

(82) Heiner, Z.; Wang, L.; Petrov, V.; Mero, M. Broadband vibrational sum-frequency generation spectrometer at 100 kHz in the 950-1750 cm^{-1} spectral range utilizing a LiGaS2 optical parametric amplifier. *Opt. Express* **2019**, *27*, 15289–15297, DOI: `10.1364/OE.27.015289`.

(83) Farrell, K. M.; Ostrander, J. S.; Jones, A. C.; Yakami, B. R.; Dicke, S. S.; Middleton, C. T.; Hamm, P.; Zanni, M. T. Shot-to-shot 2D IR spectroscopy at 100 kHz using a Yb laser and custom-designed electronics. *Opt. Express* **2020**, *28*, 33584–33602, DOI: `10.1364/OE.409360`.

(84) Hamm, P. Transient 2D IR spectroscopy from micro- to milliseconds. *The Journal of Chemical Physics* **2021**, *154*, 104201, DOI: `10.1063/5.0045294`.

(85) Homann, C.; Schriever, C.; Baum, P.; Riedle, E. Octave wide tunable UV-pumped NOPA: pulses down to 20 fs at 0.5 MHz repetition rate. *Opt. Express* **2008**, *16*, 5746–5756, DOI: `10.1364/OE.16.005746`.

(86) Schriever, C.; Lochbrunner, S.; Krok, P.; Riedle, E. Tunable pulses from below 300 to 970 nm with durations down to 14 fs based on a 2 MHz ytterbium-doped fiber system. *Optics letters* **2008**, *33*, 192–194.

(87) Penwell, S. B.; Whaley-Mayda, L.; Tokmakoff, A. Single-stage MHz mid-IR OPA using LiGaS$_2$ and a fiber laser pump source. *Opt. Lett.* **2018**, *43*, 1363–1366, DOI: `10.1364/OL.43.001363`.

(88) Calendron, A.-L.; Çankaya, H.; Cirmi, G.; Kärtner, F. X. White-light generation with sub-ps pulses. *Opt. Express* **2015**, *23*, 13866–13879, DOI: `10.1364/OE.23.013866`.

(89) Isaenko, L.; Yelisseyev, A.; Lobanov, S.; Titov, A.; Petrov, V.; Zondy, J.-J.; Krinitsin, P.; Merkulov, A.; Vedenyapin, V.; Smirnova, J. Growth and properties of LiGaX2 (X = S, Se, Te) single crystals for nonlinear optical applications in the mid-IR. *Crystal Research and Technology* **2003**, *38*, 379–387, DOI: `https://doi.org/10.1002/crat.200310047`.

(90) Whaley-Mayda, L.; Guha, A.; Tokmakoff, A. Resonance conditions, detection quality, and single-molecule sensitivity in fluorescence-encoded infrared vibrational spectroscopy. *The Journal of Chemical Physics* **2022**, *156*, 174202, DOI: `10.1063/5.0088435`.

(91) Huber, R.; Satzger, H.; Zinth, W.; Wachtveitl, J. Noncollinear optical parametric amplifiers with output parameters improved by the application of a white light continuum generated in CaF2. *Optics Communications* **2001**, *194*, 443–448, DOI: `https://doi.org/10.1016/S0030-4018(01)01324-4`.

(92) French, R. H.; Ling, J. W.; Ohuchi, F. S.; Chen, C. T. Electronic structure of β-BaB_2O_4 and LiB_3O_5 nonlinear optical crystals. *Phys. Rev. B* **1991**, *44*, 8496–8502, DOI: `10.1103/PhysRevB.44.8496`.

(93) Whaley-Mayda, L. Fluorescence-Encoded Infrared Spectroscopy for Single-Molecule Vibrational Investigation in Solution. 437, DOI: `https://doi.org/10.6082/uchicago.5274`.

(94) Mertz, J., *Introduction to optical microscopy*; Cambridge University Press: 2019.

(95) Whaley-Mayda, L.; Guha, A.; Tokmakoff, A. Multimode vibrational dynamics and orientational effects in fluorescence-encoded infrared spectroscopy. I. Response function theory. *The Journal of Chemical Physics* **2023**, *159*, DOI: `10.1063/5.0171939`.

(96) Whaley-Mayda, L.; Guha, A.; Tokmakoff, A. Multimode vibrational dynamics and orientational effects in fluorescence-encoded infrared spectroscopy. II. Analysis of early-time signals. *The Journal of Chemical Physics* **2023**, *159*, DOI: `10.1063/5.0171946`.

(97) Guha, A.; Whaley-Mayda, L.; Lee, S. Y.; Tokmakoff, A. Molecular factors determining brightness in fluorescence-encoded infrared vibrational spectroscopy. *The Journal of Chemical Physics* **2024**, *160*, 104202, DOI: `10.1063/5.0190231`.

(98) Arlt, J.; Tyndall, D.; Rae, B. R.; Li, D. D.-U.; Richardson, J. A.; Henderson, R. K. A study of pile-up in integrated time-correlated single photon counting systems. *Review of Scientific Instruments* **2013**, *84*, 103105, DOI: `10.1063/1.4824196`.

(99) McHale, J., *Molecular Spectroscopy*; Prentice Hall: 1999.

(100) Wilson, E. B.; Decius, J. C.; Cross, P. C., *Molecular vibrations : the theory of infrared and Raman vibrational spectra*; McGraw-Hill New York: New York, 1955.

(101) Kupka, H.; Cribb, P. H. Multidimensional Franck–Condon integrals and Duschinsky mixing effects. *The Journal of Chemical Physics* **1986**, *85*, 1303–1315, DOI: `10.1063/1.451216`.

(102) Santoro, F.; Lami, A.; Improta, R.; Barone, V. Effective method to compute vibrationally resolved optical spectra of large molecules at finite temperature in the gas phase and in solution. *Journal of Chemical Physics* **2007**, *126*, DOI: `10.1063/1.2721539`.

(103) Von Cosel, J.; Cerezo, J.; Kern-Michler, D.; Neumann, C.; Van Wilderen, L. J. G. W.; Bredenbeck, J.; Santoro, F.; Burghardt, I. Vibrationally resolved electronic spectra including vibrational pre-excitation: Theory and application to VIPER spectroscopy. *Journal of Chemical Physics* **2017**, *147*, DOI: `10.1063/1.4999455`.

(104) Ruhoff, P. T. Recursion relations for multi-dimensional Franck-Condon overlap integrals. *Chemical Physics* **1994**, *186*, 355–374, DOI: `10.1016/0301-0104(94)00173-1`.

(105) Sharp, T. E.; Rosenstock, H. M. Franck—Condon Factors for Polyatomic Molecules. *The Journal of Chemical Physics* **1964**, *41*, 3453–3463, DOI: `10.1063/1.1725748`.

(106) Lermé, J. Iterative methods to compute one- and two-dimensional Franck-Condon factors. Tests of accuracy and application to study indirect molecular transitions. *Chemical Physics* **1990**, *145*, 67–88, DOI: `https://doi.org/10.1016/0301-0104(90)80119-I`.

(107) Palma, A.; Morales, J. Franck–condon factors and ladder operators. I. harmonic oscillator. *International Journal of Quantum Chemistry* **1983**, *24*, 393–400, DOI: `https://doi.org/10.1002/qua.560240843`.

(108) Duschinsky, F. The importance of the electron spectrum in multi atomic molecules. Concerning the Franck-Condon principle. *Acta Physicochim. URSS* **1937**, *7*, 551–566.

(109) Gaynor, J. D.; Weakly, R. B.; Khalil, M. Multimode two-dimensional vibronic spectroscopy. I. Orientational response and polarization-selectivity. *The Journal of Chemical Physics* **2021**, *154*, DOI: `10.1063/5.0047724`.

(110) Becke, A. Density-functional thermochemistry. III. The role of exact exchange. *J. Chem. Phys* **1993**, *98*, 5648.

(111) Stephens, P. J.; Devlin, F. J.; Chabalowski, C. F.; Frisch, M. J. Ab Initio Calculation of Vibrational Absorption and Circular Dichroism Spectra Using Density Functional Force Fields. *The Journal of Physical Chemistry* **1994**, *98*, 11623–11627, DOI: `10.1021/j100096a001`.

(112) Jacquemin, D.; Wathelet, V.; Perpete, E. A.; Adamo, C. Extensive TD-DFT benchmark: singlet-excited states of organic molecules. *Journal of Chemical Theory and Computation* **2009**, *5*, 2420–2435.

(113) Chai, J.-D.; Head-Gordon, M. Systematic optimization of long-range corrected hybrid density functionals. *The Journal of Chemical Physics* **2008**, *128*, 084106, DOI: `10.1063/1.2834918`.

(114) Sorour, M. I.; Marcus, A. H.; Matsika, S. Modeling the Electronic Absorption Spectra of the Indocarbocyanine Cy3. *Molecules* **2022**, *27*, 4062.

(115) Frisch, M. J. et al. Gaussian09 Revision B.01, Gaussian Inc. Wallingford CT 2009.

(116) Hanwell, M. D.; Curtis, D. E.; Lonie, D. C.; Vandermeersch, T.; Zurek, E.; Hutchison, G. R. Avogadro: an advanced semantic chemical editor, visualization, and analysis platform. *Journal of Cheminformatics* **2012**, *4*, 17, DOI: `10.1186/1758-2946-4-17`.

(117) Bursch, M.; Mewes, J.-M.; Hansen, A.; Grimme, S. Best-Practice DFT Protocols for Basic Molecular Computational Chemistry**. *Angewandte Chemie International Edition* **2022**, *61*, e202205735, DOI: `https://doi.org/10.1002/anie.202205735`.

(118) Jacquemin, D.; Adamo, C. Bond length alternation of conjugated oligomers: wave function and DFT benchmarks. *Journal of chemical theory and computation* **2011**, *7*, 369–376.

(119) Birks, J., *Photophysics of Aromatic Molecules*; Studies in the History of American Education Series; Wiley-Interscience: 1970.

(120) Tarleton, A. S.; Garcia-Alvarez, J. C.; Wynn, A.; Awbrey, C. M.; Roberts, T. P.; Gozem, S. OS100: A benchmark set of 100 digitized UV–visible spectra and derived

experimental oscillator strengths. *The Journal of Physical Chemistry A* **2022**, *126*, 435–443.

(121) Jacquemin, D.; Mennucci, B.; Adamo, C. Excited-state calculations with TD-DFT: from benchmarks to simulations in complex environments. *Physical Chemistry Chemical Physics* **2011**, *13*, 16987–16998, DOI: `10.1039/C1CP22144B`.

(122) Liu, X.; Xu, Z.; Cole, J. M. Molecular Design of UV–vis Absorption and Emission Properties in Organic Fluorophores: Toward Larger Bathochromic Shifts, Enhanced Molar Extinction Coefficients, and Greater Stokes Shifts. *The Journal of Physical Chemistry C* **2013**, *117*, 16584–16595, DOI: `10.1021/jp404170w`.

(123) Manzhos, S.; Segawa, H.; Yamashita, K. Computational dye design by changing the conjugation order: Failure of LR-TDDFT to predict relative excitation energies in organic dyes differing by the position of the methine unit. *Chemical Physics Letters* **2012**, *527*, 51–56.

(124) Du, J.; Tao, X.; Begušić, T.; Wei, L. Computational Design of Molecular Probes for Electronic Preresonance Raman Scattering Microscopy. *The Journal of Physical Chemistry B* **2023**, *127*, PMID: 37226966, 4979–4988, DOI: `10.1021/acs.jpcb.3c00699`.

(125) Albrecht, A. C. On the Theory of Raman Intensities. *The Journal of Chemical Physics* **1961**, *34*, 1476–1484, DOI: `10.1063/1.1701032`.

(126) Strommen, D. P.; Nakamoto, K. Resonance raman spectroscopy. *Journal of Chemical Education* **1977**, *54*, 474, DOI: `10.1021/ed054p474`.

(127) Resonance Raman Scattering In *Modern Raman Spectroscopy*; John Wiley & Sons, Ltd: 2019; Chapter 4, pp 101–117, DOI: `https://doi.org/10.1002/9781119440598.ch4`.

(128) Gong, Z.-Y.; Tian, G.; Duan, S.; Luo, Y. Significant Contributions of the Albrecht's A Term to Nonresonant Raman Scattering Processes. *J. Chem. Theory Comput.* **2015**, *11*, Publisher: American Chemical Society, 5385–5390, DOI: `10.1021/acs.jctc.5b00761`.

(129) Myers Kelley, A. Resonance Raman and Resonance Hyper-Raman Intensities: Structure and Dynamics of Molecular Excited States in Solution. *J. Phys. Chem. A* **2008**, *112*, Publisher: American Chemical Society, 11975–11991, DOI: `10.1021/jp805530y`.

(130) Fan, L.; Ziegler, T. Application of density functional theory to infrared absorption intensity calculations on main group molecules. *The Journal of Chemical Physics* **1992**, *96*, 9005–9012, DOI: `10.1063/1.462258`.

(131) Horz, M.; Masood, H. M. A.; Brunst, H.; Cerezo, J.; Picconi, D.; Vormann, H.; Niraghatam, M. S.; van Wilderen, L. J. G. W.; Bredenbeck, J.; Santoro, F.; Burghardt, I. Vibrationally resolved two-photon electronic spectra including vibrational pre-excitation: Theory and application to VIPER spectroscopy with two-photon excitation. *The Journal of Chemical Physics* **2023**, *158*, 064201, DOI: `10.1063/5.0132608`.

(132) Milojevich, C. B.; Silverstein, D. W.; Jensen, L.; Camden, J. P. Probing Two-Photon Properties of Molecules: Large Non-Condon Effects Dominate the Resonance Hyper-Raman Scattering of Rhodamine 6G. *Journal of the American Chemical Society* **2011**, *133*, PMID: 21851085, 14590–14592, DOI: `10.1021/ja2054622`.

(133) Krichevsky, O.; Bonnet, G. Fluorescence correlation spectroscopy: the technique and its applications. *Reports on Progress in Physics* **2002**, *65*, 251, DOI: `10.1088/0034-4885/65/2/203`.

(134) Oliver, T. A. A.; Lewis, N. H. C.; Fleming, G. R. Correlating the motion of electrons and nuclei with two-dimensional electronic–vibrational spectroscopy. *Proceedings of the National Academy of Sciences* **2014**, *111*, 10061–10066, DOI: `10.1073/pnas.1409207111`.

(135) Wu, E. C.; Arsenault, E. A.; Bhattacharyya, P.; Lewis, N. H. C.; Fleming, G. R. Two-dimensional electronic vibrational spectroscopy and ultrafast excitonic and vibronic photosynthetic energy transfer. *Faraday Discuss.* **2019**, *216*, 116–132, DOI: `10.1039/C8FD00190A`.

(136) Englander, S. W.; Kallenbach, N. R. Hydrogen exchange and structural dynamics of proteins and nucleic acids. *Quarterly Reviews of Biophysics* **1983**, *16*, 521–655, DOI: `10.1017/S0033583500005217`.

(137) Bai, Y.; Milne, J. S.; Mayne, L.; Englander, S. W. Primary structure effects on peptide group hydrogen exchange. *Proteins: Structure, Function, and Bioinformatics* **1993**, *17*, 75, DOI: `https://doi.org/10.1002/prot.340170110`.

(138) Zhang, Z.; Smith, D. L. Determination of amide hydrogen exchange by mass spectrometry: A new tool for protein structure elucidation. *Protein Science* **1993**, *2*, 522, DOI: `https://doi.org/10.1002/pro.5560020404`.

(139) Loria, J. P.; Rance, M.; Palmer, A. G. A Relaxation-Compensated Carr-Purcell-Meiboom-Gill Sequence for Characterizing Chemical Exchange by NMR Spectroscopy. *Journal of the American Chemical Society* **1999**, *121*, 2331.

(140) DeFlores, L. P.; Tokmakoff, A. Water Penetration into Protein Secondary Structure Revealed by Hydrogen-Deuterium Exchange Two-Dimensional Infrared Spectroscopy. *Journal of the American Chemical Society* **2006**, *128*, PMID: 17177399, 16520–16521, DOI: `10.1021/ja067723o`.

(141) Magde, D.; Wong, R.; Seybold, P. G. Fluorescence Quantum Yields and Their Relation to Lifetimes of Rhodamine 6G and Fluorescein in Nine Solvents: Improved Absolute Standards for Quantum Yields. *Photochemistry and Photobiology* **2002**, *75*, 327–334, DOI: `https://doi.org/10.1562/0031-8655(2002)0750327FQYATR2.0.CO2`.

(142) Wöll, D.; Braeken, E.; Deres, A.; De Schryver, F. C.; Uji-i, H.; Hofkens, J. Polymers and single molecule fluorescence spectroscopy, what can we learn? *Chem. Soc. Rev.* **2009**, *38*, 313–328, DOI: `10.1039/B704319H`.

(143) Paeng, K.; Kaufman, L. J. Single Molecule Experiments Reveal the Dynamic Heterogeneity and Exchange Time Scales of Polystyrene near the Glass Transition. *Macromolecules* **2016**, *49*, 2876–2885, DOI: `10.1021/acs.macromol.6b00097`.